Università degli Studi di Padova

UNIVERSITÀ DEGLI STUDI DI PADOVA

Dipartimento di Fisica e Astronomia

Scuola di dottorato in Scienza ed Ingegneria dei Materiali

XXV CICLO

TESI DI DOTTORATO

Microdroplets: fabrication of microdevices for interfacial phenomena studies

Direttore della scuola: Prof. Gaetano Granozzi

Supervisore: Dott. Matteo Pierno

Co-supervisore: Prof. Giampaolo Mistura

Dottorando: Davide Ferraro

Alla mia famiglia

Contents

Riassunto

Quando i fluidi vengono confinati in canali microfluidici, di dimensioni caratteristiche dell'ordine della decina o centinaia di micron, le loro proprietà possono risultare significativamente diverse da quelle tipicamente osservate negli stessi fluidi, ma nella cosiddetta condizione massiva. Ciò è dovuto principalmente al fatto che la miniaturizzazione di qualsiasi sistema porta a un rapporto superficie / volume grande, in cui tipicamente le forze volumetriche sono trascurabili rispetto a quelle superficiali. Questo effetto si verifica ad esempio quando due fluidi immiscibili vengono mescolati per formare emulsioni di gocce. Negli ultimi dieci anni, l'idea di utilizzare gocce in dispositivi microfluidici si è diffusa soprattutto perché permette di ridurre le tipiche dimensioni coinvolte in questi sistemi, comportando un notevole numero di applicazioni in chimica, in biologia ed in fisica. Tuttavia, nonostante la loro grande notorietà, per la complessità dei fenomeni interfacciali coinvolti, i sistemi microfluidici che utilizzano gocce non sono stati ancora pienamente compresi. Lo scopo di questa tesi è, quindi, quello di caratterizzare i sistemi di gocce comunemente utilizzati in dispositivi microfluidici. In particolare, abbiamo lavorato con gocce confinate sia in sistemi aperti che in sistemi chiusi, focalizzandoci sulla loro produzione, il loro controllo e la loro manipolazione. Per fare ciò abbiamo realizzato vari tipi di micro-dispositivi che presentano diverse caratteristiche geometriche e di bagnabilità.
Per quanto riguarda i sistemi aperti, nel Capitolo 3, abbiamo paragonato la forma di gocce d'acqua confinate su strutture aventi sezioni circolari e quadrate, osservando che la condizione di "pinning" della linea di contatto è fortemente influenzata dalla geometria della struttura. In particolare, nel caso del profilo circolare, la linea di contatto è bloccata lungo tutto il bordo della struttura, confermando

il criterio di Gibbs, mentre nel caso del profilo quadrato, la linea di contatto può scendere lungo le pareti verticali, perché sostenuta dagli angoli.
Nel capitolo 4, siamo passati ad indagare la transizione morfologica tipica di gocce confinate su strutture allungate: da uno stato di "filamento", dove il liquido è distribuito uniformemente sulla struttura, a un stato "gonfiato", dove esso forma una protuberanza al centro della struttura stessa. Questo effetto era già noto in letteratura, ma non era mai stato quantificato in termini di geometria della struttura e del volume delle gocce. Abbiamo quindi considerato strutture con profilo rettangolare, aventi diversi rapporti di aspetto ℓ (rapporto tra lunghezza L e larghezza W). Aumentando e diminuendo progressivamente il volume dell'acqua sulla superficie delle strutture, abbiamo osservato che la transizione morfologica si verifica per tutti i rapporti di aspetto ℓ, ma che soltanto per $\ell > 16$, vi è una bistabilità dei due stati allo stesso volume. Inoltre, abbiamo iniziato a studiare la transizione sotto l'aspetto dinamico, cercando di indurla mediante delle oscillazioni, osservando che questo è possibile solo per strutture con $\ell > 16$.
Inoltre, al fine di controllare il movimento delle gocce, nel capitolo 5, abbiamo studiato il loro diverso comportamento di scorrimento su superfici omogenee e strutturate chimicamente. Per fare questo abbiamo realizzato superfici con microstrisce idrofile e idrofobe, mediante la tecnica del "microcontact printing". Osservando lo scivolamento di gocce d'acqua su queste superfici, abbiamo riscontrato che esse presentano un moto denominato "stick-slip", che provoca la loro deformazione e introduce un nuovo attrito al sistema goccia-superficie, imputabile alla dissipazione di energia alla linea di contatto.
Con lo scopo di studiare la produzione e il controllo di gocce in canali microfluidici chiusi, nel Capitolo 6, abbiamo focalizzato la nostra attenzione per definire un protocollo affidabile per la produzione di gocce mediante giunzioni a T. Inoltre, abbiamo studiato il tipico problema del rigonfiamento del PDMS, che si verifica quando esso si trova a contatto con solventi organici. Confrontando microcanali con diversa sezione, abbiamo notato che le deformazioni dovute al rigonfiamento sono fortemente connesse con la geometria dei dispositivi. In particolare esse risultano più evidenti quando il rapporto di aspetto (altezza / larghezza) della sezione trasversale del canale è maggiore.
Infine, nel capitolo 7, abbiamo introdotto un nuovo metodo per modificare le proprietà di bagnabilità di resine tioleniche, che vengono comunemente usate in

microfluidica. In particolare abbiamo lavorato con il NOA, una resina disponibile in commercio, che mostra un angolo di contatto statico di 70 °. Utilizzando la chimica tipica dei clorosilani, abbiamo cambiato la bagnabilità della resina, portandola ad angoli di contatto più idrofili ed idrofobi. Inoltre abbiamo anche dimostrato che questa tecnica può essere utilizzata sia con sistemi microfluidici chiusi, sia con sistemi aperti.

Parole chiave:
Microfabbricazione, microfluidica, gocce, fenomeni interfacciali, bagnabilità, microfluidica delle gocce, PDMS, soft litografia, fotolitografia, linea di contatto.

Si desidera ringraziare la Fondazione Cassa di Risparmio di Padova e Rovigo (http://www.fondazionecariparo.net/) per aver finanziato il presente progetto di Dottorato di Ricerca, nell'ambito dell'iniziativa 'PROGETTO DOTTORATI DI RICERCA 2009', svoltosi in collaborazione con l'Università di Padova (Italia).

Abstract

When fluids are confined on the length scales of microfluidic channels, typically in the range of tens and hundreds microns, their behavior may results significantly different with respect to the so called "bulk" proprieties. This is mainly due to the fact that the miniaturization is always characterized by a large surface to volume ratio, where the body forces can be normally neglected in favor of the surface forces. Notable example of this kind of systems is observable when two immiscible fluids are mixed to form droplets of emulsions. In the last ten years, the idea to use droplets in microfluidics has been inspired mainly because it allows to further scale down the typical size involved in these systems, bringing to a huge number of applications in chemistry, biology and physics. However, despite a large notoriety, microfluidic systems using droplets are not yet fully understood for the complexity of the interfacial phenomena that are involved. Aim of this thesis is to characterize the droplet systems commonly used in microfluidic devices. In detail, we worked with droplets in both open and closed microfluidic systems, focusing with the problem of their generation, control and manipulation with suitable microdevices, in presence of defects having different geometry and wettability.

Regarding the open microfluidics, in Chapter 3,we first compared the shape of water droplets confined on posts having circular and square cross sections, observing that the pinning of the contact line is strongly influenced by the post shape. In particular, in the case of a circular profile, the contact line is pinned to the whole edge, confirming the Gibbs criteria, while on the square post, the contact line can spill along the vertical walls, because it is sustained by the corners.

Then, in Chapter 4,we moved to investigate the change of morphological config-

uration from filament to bulge state, typical of liquid droplets confined on posts with rectangular cross section. This effect was already know in literature, but it was not quantify in term of post geometry and volume of the water droplets. Therefore, we realized rectangular posts with different aspect ratio (ℓ), between length (L) and width (W). Changing the water volume on the posts, we observed that the morphological transition occurs for all the aspect ratios ℓ and that, for $\ell > 16$, there is a bistability of the two states at the same volume. Furthermore, we started to investigate the dynamic of the transition, induced by oscillations, founding that, for posts with $\ell > 16$, it is possible to induce the transition by the oscillation, without change the volume.

Next, in order to control the droplets motion, in Chapter 5, we studied the different behavior of sliding droplets on homogeneous and on chemically patterned surfaces. To do that we realized surfaces with hydrophilic and hydrophobic stripes by microcontact printing. On these surfaces, droplets show stick-slip motion, which causes the deformation of their shapes and introduces an extra friction imputable to the dissipation of energy at the contact line.

With the aim to study generation and control of droplets in closed microfluidic channels, in Chapter 6, we focused our attention to define a reliable protocol for the production of droplets by T-junctions. Moreover, we investigated the swelling problem, which occurs using organic solvent into PDMS microchannels. We noticed that the swelling deformation is strongly connected with the geometry of the devices, being more evident when the aspect ratio (high to width) of the channel cross section is higher.

Finally, in Chapter 7, we introduced a new method to change the wettability proprieties of thiolen resins, which are commonly used in microfluidics. In particular we worked with NOA, a commercial available resin, which shows a contact angle of 70°. Using chlorosilane chemistry, we changed its wettability to a more hydrophilic and to hydrophobic contact angles, showing that this technique can be used both to open and closed microfluidic devices.

Keywords:

Microfabrication, microfluidics, droplets, interfacial phenomena, wetting, droplet microfluidics, PDMS, soft-lithography, photo-lithography, contact line.

The bank foundation “Fondazione Cassa di Risparmio di Padova e Rovigo ” (http://www.fondazionecariparo.net/) is gratefully acknowledged for its financial support to this PhD in the frame of the PhD Program 2009 - ‘PROGETTO DOTTORATI DI RICERCA 2009’ in partnership with the University of Padova (Italy).

Introduction

Microfabrication usually refers to the set of processes needed for realizing structures having micrometer size. Historically, it was developed during the second half of the 20th century from the electronics industries, pushing the production of smaller and smaller devices that nowadays are at the basis of countless consumer products like radios, computers, phones, watches, etc. In the 1990s, the original concept of the transistor miniaturization, to drive electrons in small "channels", inspired the possibility to flow and manipulate small amounts of fluids (10^{-9} to 10^{-18} liters), using channels with dimensions from tens to hundreds of micrometers. This concept is commonly known as microfluidics and its goal is the realization of the Lab-on-a-chip, which consists in the miniaturization of all the processes normally performed on analysis laboratory, on the scale of an individual microfluidic device. When fluids are confined on the scales of microchannels and microdevices, their behavior may results significantly different with respect to the so called "bulk" proprieties. This is mainly due to the fact that the miniaturization is always accompained by a large surface to volume ratio, as shown in Figure 1b. A relevant example occurs when two immiscible fluids are mixed to produce emulsions, forming droplets of one phase dispersed in the other. Despite these are metastable systems, their lifetime may become significant enought (more than a year) that they are good candidates for many commercial applications, mainly with regard to food, cosemtics, drugs, oil, etc. [1]. Moreover, the use of droplets in microfluidic devices allows from one hand to further scale down the typical size involved in immiscible systems, and from the other hand to gather the control of the dispersed phases at the level of single droplet. In particular, in chemistry every droplet can be reviewed as a single small reactor where chemicals

may be mixed in more efficient way than in usual microchannels [2] and can be exploited for the synthesis of polymer and inorganic particles [3]. In biological applications, being the dimension scale of the droplets similar to the biological tissue, it is possible to reduce the liquid volume and better screen the biological assays, like for example DNA amplification by PCR [4]. In physics, droplets in microfluidic devices can be exploited to study the multi-phase systems, focusing on the non-obvious connection between micro- and macro-scale proprieties, which represents a challenging open problem [5–7]. Despite so large notoriety, microfluidic systems using droplets are not yet fully understood for the complexity of the interfacial phenomena that are involved. In fact, when an interface is considered, there are at list two phases involved and its response to a stimulus can depend from vary different factor, e.g. the dimension and geometry of the system, the proprieties of the bulk phases, etc. As a consequence, the higher is the number of the phases, the harder is the prediction of their interfaces behavior, and in droplet microfluidics are normally involved more than one solid, liquid and gas phases in the same system.

Aim of this thesis is to characterize the interfacial phenomena of droplets normally used in microfluidic devices, therefore focusing on their behavior when they are in confined conditions. In particular, we concentrated our attention on their manipulation, which is a key step for their applications, especially in biological and chemical fields [8,9]. It is largely used to refer to these systems as droplet or open microfluidics. The first definition concerns droplets confined in closed microchannels, while the second is used when they are confined on open surfaces, for example in direct contact with the air.

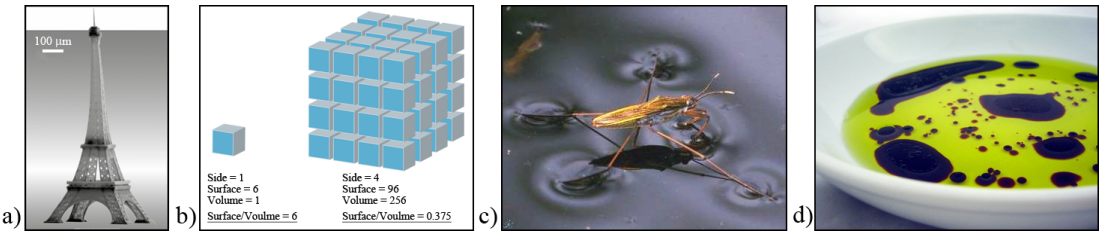

Figure 1: a) Example of microfabrication technique commercial available: two-photon polymerization [10]; b) scheme describing the scaling of surface to volume ratio of a cube with different sides; c) picture of a water bug standing on water's surface, for effect of the surface tension; d) Example of everyday emulsion: olive oil and balsamic vinegar [11].

Droplet microfluidics. In the second half of the 20th century a new strategy of fluid manipulation was developed: the droplet microfluidics, where discrete volumes of different phases are produced and manipulated [12]. Although this adds a new degree of complexity to the system, it presents many advantages compared to the single phase flow [2], which may be basically summerzed as follows:

- every droplet can be seen as a single reactor;
- a system can produce a large number of such reactors;
- there is no interaction between droplet and channel walls;
- inside the droplet there is no dispersion but, a more rapid mixing, related to the flow field due to interfaces.

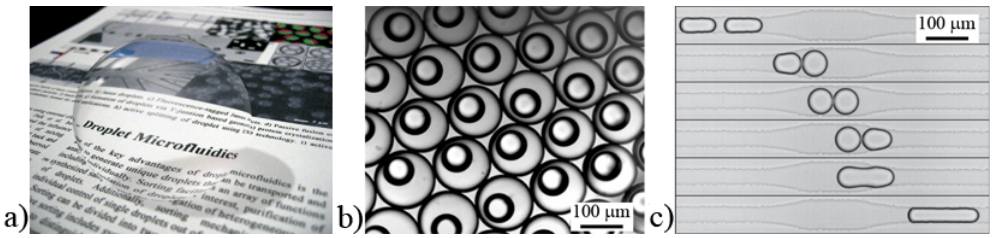

Figure 2: a) Droplet microfluidics [12]; b) microdroplets obtained using two organic phase (fluorinated oil/silicone oil) and water as the external phases [13]; c) time sequence showing the destabilization of a droplet pair passing through a symmetrical coalescence chamber and moving from left to right [14].

Moreover, droplets can be easily generated, transported and manipulated, playing with geometry of the devices. For this reason droplet microfluidics has become an excellent platform for innumereous applications of material science. Just to name a few, i) pharmaceutical and food industries include benefits from the realization of uniform emulsions. ii) Other applications include: synthesis of biomolecules, drug delivery and DNA amplification. iii) In Engineering (especially electronic) it is emerging the microfluidic bubble logic [15]: a bubble traveling in a channel represents a *bit* that transports materials and performs logic operations like AND/OR/NOT gates.

Open microfluidics. Microfluidic devices are usually a set of closed channels with a micrometer section. Even if they have a considerable potential utilization, closed microfluidics have some inconveniences: e.g. small channels easily clog, no accessibility to the liquids, flows through very small cross section pipes are extremely difficult because of the high fluidic resistance and the fabrication is more challenging [16]. A way to overcome these inconveniences is offered by open microfluidics: liquid drops are positioned on an open surface and have a free interface with air. The main goal of open microfluidics is the total control of the drops, including: formation, volume [17], morphology [18, 19] and above all, motion [20, 21].

A widely used method to generate and control drop motion is the electrowetting [22]: applying different electric potentials on a conductive surface, it is possible to change its wettability. For obtaining a better control of the droplet motion, they are usually positioned between two plates: a homogeneous top plate and a patterned bottom plate. When electric potentials are applied between them, changing the wettability, the droplets move [21]. This technology can be used in: dry blood spot analysis [21], extraction and quantification of estrogen in biological samples [23] and cell culture analysis [24]. This device may be positioned halfway between closed and open microfluidics, inheriting the fluid non accessibility of closed microfluidics. Anyway, considering also the open configurations, electrowetting presents some intrinsic limitations for non ionic liquids [25].

An alternative method for driving droplets is the application of surface acoustic waves (SAWs) to the substrate. SAWs are acoustic waves which travel coupled with the material surface, which over the past few decades, have been successfully employed in various applications: radio frequency (RF) communication, biochemical sensors and optical modulators [26]. In recent years, SAW has been attracting attentions from microfluidics research communities to drive droplets. As a matter of fact, owing to the mismatch of sound velocities between substrate and liquid, SAWs can be efficiently transferred into the liquid, to create significant inertial force and flow velocity. Therefore, this mechanism can be exploited to drive liquid actions such as pumping, mixing, jetting [20]. Generally, SAW devices consist in interdigitated transducer (IDT) fabricated on a piezoelectric substrate, using standard photo-lithography and etching processes.

Instead of using complex devices, which need expensive lithographic techniques,

it is possible to cause the droplets movement with vibration, by putting in oscillation the substrate where they are placed. In particular, Brunet et al. [27] observed that applying vertical vibrations on a flat surface tilted at 45°, a droplet, initially pinned, can slide down, as if it is without friction and slide up in antigravity direction. This happens because the vibration changes the local contact angles of the droplet and for particular amplitudes and frequencies, the contact angle hysteresis can overcame the condition of sliding, allowing the drop to move up or down.

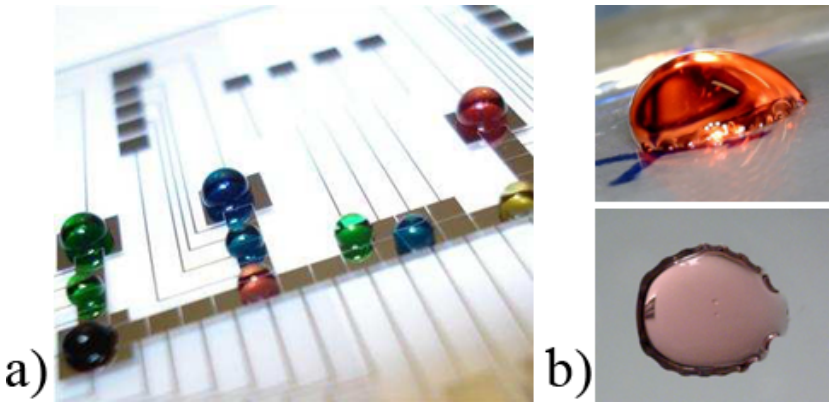

Figure 3: a) Open microfluidic device can measure estrogen levels in very small samples of tissue. The device uses electrowetting, in which discrete droplets (colored with dyes in the picture) are manipulated by application of electrical potentials to an array of electrodes. [28]; b) Side and bottom views of a colored droplet sliding on patterned surface.

Thesis outline. Regarding the interfacial phenomena of droplets in both open and closed microfluidic configurations, a key parametrer is the wettability at the solid/liquid interface, which is determined either by the chemical nature of the surfaces or the physical patterning. Full control of the wetting properties can be achieved only by aqcuiring the ability of realizing devices in a versatile way. For this reason, a consistent part of this thesis is devoted on the exanimation of the *microfabrication strategies*, for finding the best solutions for a given investigation: for every activity we have scrupulously tested the best experimental technique, sometimes through trials and errors of procedure. Then, only after the optimization of the microfabrication step, we started with the experiment. Additionally, the apparatus setups described, were assembled in the laboratory

during the PhD. This choice is largely motivated by the possibility to overcome limitations of commercial setups, that are usually hardly versatile.

This thesis is structured for guiding the readers to the comprehension of the studies described. Chapter 1 and Chapter 2 represent respectively an introduction to the physical proprieties and on the microfabrication techniques, which play an important role in open and closed microfluidics. Particular attention is focused on the useful concepts to understand the works described in the following chapters. Chapter 3 and 4 describe experimental and numerical studies of droplets confined on different types of posts, having various wetting proprieties and geometries. In the first case, the pinning effect is analyzed, while in the second case the morphological transition of a film of water is described. Chapter 5 presents a dynamic observation of droplets which slide on open inclined surfaces. For the first time, the different behaviors of sliding between patterned and homogeneous surfaces are considered. Chapter 6 shows a preliminary study of droplet microfluidics in microchannels, developed with the aim to understand how to generate droplets in closed systems and how to develop their manipulation with obstacles eventually present in the microchannels. In parallel to this study, we quantitatively studied also the behavior of a water/air meniscus that fills a microchannel patterned with different posts. The results are illustrated in the Appendix B. Finally, in Chapter 7 is described a stable and versatile method to functionalize a surface of thiolene resin, which are a common material in microfluidics.

Chapter 1

Surface properties in microdevices

The behavior of fluids in microchannels is strongly influenced by the high surface-to-volume ratio highlighting the surface properties of the materials, to the point that the body forces can usually be neglected. Sometimes this brings to unexpected behaviors, which go against the physical intuition.
This Chapter introduces basic concepts for describing fluid proprieties under confinement. At First, we review the concept of laminar flow, which dominate the flow in microfluidic devices. Then, we introduce the more important interfacial phenomena which are involved in the open microfluidic systems and in particular, which are described in the studies discussed in this thesis. Finally, the specific filed of droplet microfluidics is illustrated, to give an overview of the state of the art of these microfluidic devices.

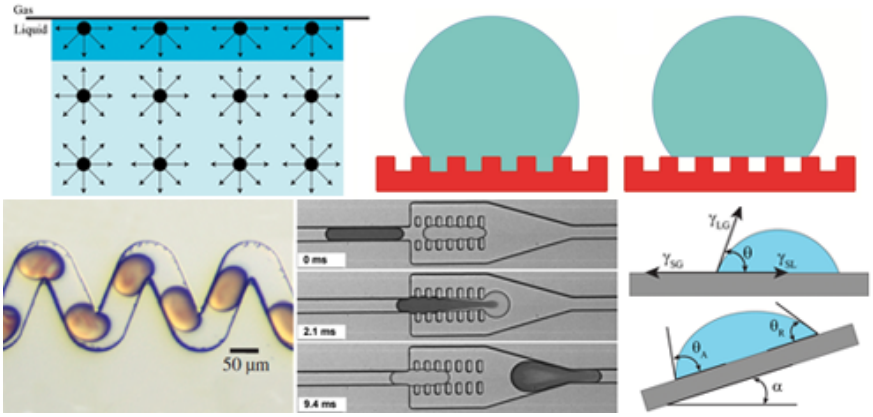

1.1 Introduction

The typical microfluidic devices are composed of a serial of microchannels connected with each other and having dimensions in the order of tens and hundreds of microns. These small dimensions strongly affect the fluid dynamics of such systems and one of the most important consequences is that the flow in microchannels is laminar [29]. This allows a very good control of the fluid transport and moreover, the possibility to generate controlled droplet emulsions [2, 9, 12]. The laminar flow in microchannels can be numerically derived solving the Navier-Stokes equations, which generally describes the motion of fluids [29]. In the following section, this and other base concepts to explain the laminar flow in microchannels are reviewed.

1.2 Laminar flow in microchannels

Let us consider the velocity field $\mathbf{u}$ of a Newtonian (viscosity does not change with the velocity) and incompressible fluid with density ρ and viscosity μ. It can be described with the Navier-Stokes (Equation 1.1) and the conservation of mass (Equation 1.2) equations:

$$\rho(\frac{\delta \mathbf{u}}{\delta t} + \mathbf{u} \cdot \nabla \mathbf{u}) = -\nabla p + \eta \nabla^2 \mathbf{u} + \mathbf{f}, \tag{1.1}$$

$$\frac{\delta \rho}{\delta t} + \nabla \cdot (\rho \mathbf{u}) = 0, \tag{1.2}$$

where p is the pressure and $\mathbf{f}$ is the external force per unit volume. In particular the Equation 1.1 rappresents Newton's second law for unit volume, where the inertial term appears on the left and forces on the right. Therefore, considering the fluid incompressibility, which is valid if the velocity is much lower than the sound speed, the velocity field is uniquely determined by the boundary conditions: the slip length on the border is very small compared to the typical channel size. Moreover, if the walls are waterproof, also the normal component of the velocity to them is zero. Integrating Equation 1.1 and taking in to account these considerations, the velocity field assumes the well known Hagen-Poiseuille parabolic profile where the maximum velocity is in the center of the channel [30]:

$$\Delta p = \frac{8\,\mu\,L\,Q}{\pi\,r^4} \tag{1.3}$$

where Q is the volumetric flow rate that passes the channel, r is the radius and $\Delta p = p_2 - p_1$ is the pressure difference between two points of the channel separated by the distance L, as shown in Figure 1.1. Equation 1.3 is valid only

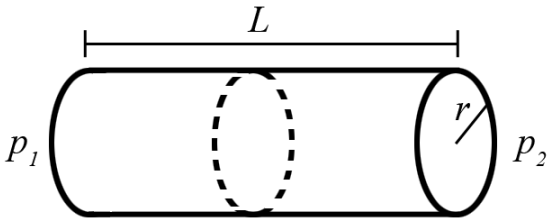

Figure 1.1: Geometry used for the Hagen-Poiseuille equation, described in Equation 1.3.

for circular cross sections and for rectangular cross sections, there is no exact analytical solution. One way to solve this problem is considering the approximation of the hydraulic radius in Equation 1.3. This quantity is defined considering a theoretical circular channel having the same area as the rectangular real channel. According to Equation 1.3 the flow rate Q in the channel depends linearly on the pressure gradient Δp. In analogy to Ohm's law, the hydrodynamic resistance of a microfluidic channel can be introduced. In this analogy the pressure corresponds to the electric voltage and the flux to the electric current. The hydrodynamic resistance R is defined by the Equation 1.4 [30].

$$\Delta p = R\,Q, \qquad \text{with} \qquad R = \frac{8\,\mu\,L}{\pi\,r^4} \tag{1.4}$$

The resistance of the channel is linear with the dynamic viscosity and small changes in the hydrodynamic diameter significantly affects the hydrodynamic resistance. This consideration is examined in detail in Chapter 6, where some measures of microchannel resistance are described.

It must be specified that all these considerations are valid for a laminar flow, that occurs when all the path lines of a fluid are parallel. To define if a flow inside a channel is laminar or turbulent, it is normally used a dimensionless parameter, Reynolds number Re:

$$Re = \frac{\rho\,v\,L}{\mu} = \frac{[\text{inertia forces}]}{[\text{viscous forces}]} \tag{1.5}$$

where ρ is the fluid density, μ the dynamic viscosity, v the velocity and L the typical length scale (for instance the channel diameter). In particular, Re relates inertia to viscous forces and considering a flow into circular pipe, it was experimentally found that when $Re < 3000$, the flow is laminar [29]. In microfluidics, a typical dimension channel (about 100 μm) fills of water (ρ=1000 Kg/m^3, μ=10^{-3} Pa s) which moves at velocity of a few mm/s, shows a Re of about 0.1.
The laminar flow in microfluidic systems, allows to control in a very precise way the fluids inside the channels. This is the main characteristic that pushes microfluidics to several application in biological, chemical and engineering fields. Nevertheless, at the same time, it is also the cause of one of the most important problems: the mixing of different fluids inside the channel. As a matter of fact, two fluids which flux in parallel can mix together only by standard diffusion at the interface, where usual diffusion coefficients have an order of magnitude of 10^{-6} cm^2 /s [31]. With a typical flow rate of about 1 mm/s, the complete mixing is reached after tens centimeters scale. This problem can be overcomed by inserting suitable obstacles inside the channels, introducing turbulence [32] or by using droplet microfluidic strategies [33].

1.3 Interfacial phenomena

The surface-to-volume ratio is much higher (by several orders of magnitude) in microsystems, rather than in decimetric systems. This implies that interfaces play a crucial role with respect to "bulk" systems, also referred as systems of "ordinary" size. In this section, some quantity and phenomena occurring at interfaces are presented, like the surface tension and the Plateau-Rayleigh instability. These are crucial for the analysis of experimental situations shown in this thesis.

1.3.1 Surface tension and Laplace's law

It is well know that, the surface tension is an energy density associated with any surface, usually indicated by the symbol γ and measured in J/m^2 or N/m [30]. In detail, the energy of an interface (Gibbs energy, G) is given by this surface energy multiplied by the area A of the interface itself:

$$\gamma = (\frac{\delta G}{\delta A})_{p,T} \tag{1.6}$$

where the partial derivative is calculated at fixed pressure p and temperature T. The physical origin of γ can be explained considering the intramolecular forces of two surfaces in contact in vacuum: to detach them it is necessary to apply an energy of $E = 2\,\gamma$. Another way to explain the surface tension is considering that the atoms or molecules which constitute an interface are not coordinated as those inside a massive material [34]. Taking into account a liquid contained in an open container, most of the part of its molecules are surrounded by other molecules that, on average, are distributed symmetrically, so that the forces applied have zero resultant. This is not true for the molecules on the surface, because they can interact only with the molecules underlying, at least by neglecting interactions with air and container. Therefore, the resultant of the forces is different from zero and it is directed inside the liquid, as shown in Figure 1.2. As a result the surfaces are like elastic membranes. To give an idea, the order of magnitude of the surface energies for metal/air interface is about 500 mJ/m^2, while for an oil/air or teflon/air interface it is about 20 mJ/m^2. For the water/air interface, notably the most important interface in this thesis, γ is 73 mJ/m^2.

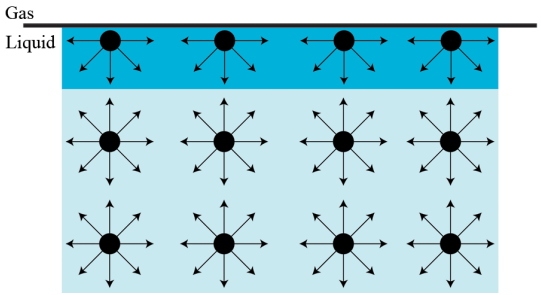

Figure 1.2: Scheme of the interacting forces at liquid/gas interface, which is represented by the black top line.

Additionally, the surface tension regulates the dynamics related to the shape of a liquid/air meniscus. In particular, Laplace's Law demonstrates that, in order to maintain a curved interface in mechanical equilibrium, it is necessary to exert a pressure P at the interface proportional to γ:

$$P = \gamma \left(\frac{1}{R_1} + \frac{1}{R_2} \right) \tag{1.7}$$

where R_1 and R_2 are the two radii of principal curvature of the surface depicted in three dimensions [30].

1.3.2 Capillary number and capillary length

Since the typical size of a microfluidic channel is of the order of few tens of microns, up to hundreds of microns, another phenomenon to take into account in microfluidic scales, is the capillarity. The capillary number Ca is a dimensionless number used to compare the viscous forces with the surface tension γ, and is defined as:

$$Ca = \frac{\mu U}{\gamma} = \frac{[\text{viscous forces}]}{[\text{interfacial tension}]} \tag{1.8}$$

where μ and U are the viscosity and the velocity of the liquid, respectively. In microdevices, the capillary number is small, meaning that capillary effects tend to dominate over the viscous effects. However, this estimation is not always acceptable. For example, generation of droplets in microfluidic closed channels, is usually performed by adding surfactants to reduce γ and stabilize the droplets against coalescence. This implies an increase of the contribution of the viscous forces. As a matter of fact, it is possible to observe a dependence of the droplet formation regime from the capillary number [35].

Another important dimensionless number in microsystems is the capillary length κ^{-1}, beyond which the gravity becomes important [34]. It compares the Laplace pressure (written as γ/κ^{-1}) with the hydrostatic pressure $\rho g \kappa^{-1}$ at a depth κ^{-1} in a liquid of density ρ and submitted to gravity g:

$$\kappa^{-1} = \sqrt{\frac{\gamma}{\rho g}} \tag{1.9}$$

The distance κ^{-1} is generally of the order of a few mm (for water it is about 2.7 mm). Therefore, considering a droplet placed on a surface and keeping r as its radius, gravity is negligible and capillary effects dominate for sizes $r < \kappa^{-1}$. While for $r > \kappa^{-1}$ the system is affected by gravity.

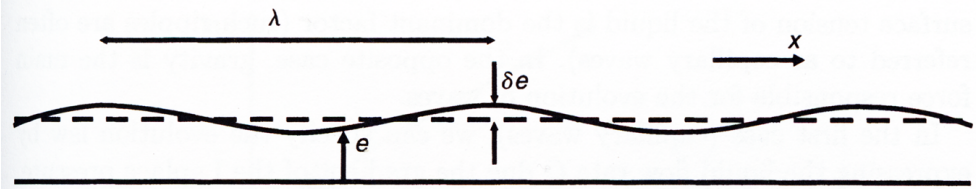

Figure 1.3: Ripples of wavelength λ on the surface of a thin liquid film, having average thickness e_0 and variation of δe. Dashed line represents the average position of the liquid's surface [34].

1.3.3 Horizontal liquid films

Considering a liquid film placed on a horizontal substrate and supposing that the free upper surface has been perturbed, for example with air flow, it should be possible to observe some waves on it, as shown in Figure 1.3. This perturbation will disappear in a certain time, under the combination of gravity effects and the surface tension [34] . In particular, the fluid tends to flow from crests to troughs because of its weight, for gravity effect and for the different Laplace pressure, in case of surface tension. If we are interested on the main contribution, it has to be considered the wavelength of the perturbation: if the ripples have short wavelength ($\lambda < \kappa^{-1}$), surface tension is the dominant factor, while in the opposite case, gravity is the main force responsible of the system evolution. For $\lambda < \kappa^{-1}$, the ripples are also called capillary waves, a concept that will prove relevant for explaining some results described in Chapter 4.

Plateau-Rayleigh Instability

In the previous case the instability on a flat surface, caused by an external agent was considered. Let us take into consideration a fiber (e.g. hair with a typical diameter of 100 μm) wetted by a liquid. Condensing more liquid on the fiber, the system develops some instabilities and in particular it forms a wavy profile, as shown in Figure 1.4. The wave-like structure keeps on growing in amplitude until it eventually breaks up into a necklace of droplets. The pressure within the hairy film includes both hydrostatic (P_h) and Laplace (P_L) contributions:

$$P_h = \rho g R, \qquad P_L = \frac{\gamma}{R}, \qquad \text{with} \qquad R = b + e_0 \tag{1.10}$$

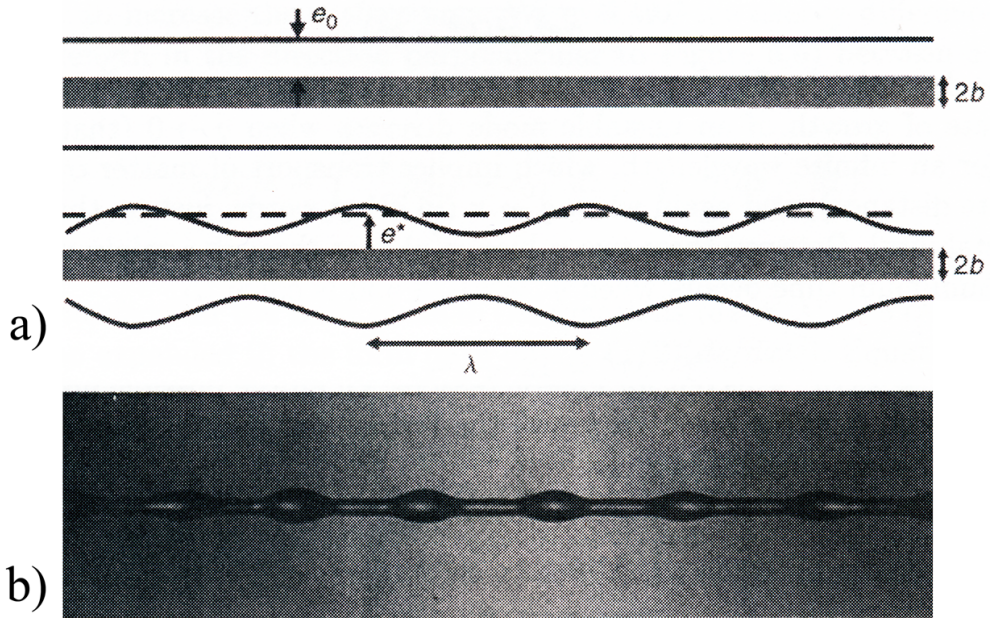

Figure 1.4: a) Liquid film on fiber before and after the destabilization. b) Necklace of droplets resulting from the instability of a liquid film on a fiber with radius of 100 μm.

where b is the fiber radius and e_0 the initial thickness of the liquid film, as shown in Figure 1.4a. A dimensionless parameter, known as the Bond number Bo, can be used to compare the two pressures:

$$Bo = \kappa^2 R^2 = \frac{\rho g R^2}{\gamma} = \frac{\text{[body pressure]}}{\text{[interfacial pressure]}} \tag{1.11}$$

For a liquid cylinder ≈100 μm in diameter, Bo is about 0.01 and the gravity is clearly negligible.

These types of instabilities, where the liquid film changes the shape following a stimulus, are known in literature as morphological transitions [19]. Working with droplets on open microfluidic devices, interfacial tension effects are dominant. Therefore, motivated both by practical applications and by fundamental questions, interfacial shapes and instabilities of small liquid droplets wetting chemically or topographically structured surfaces have been widely studied in recent years. As a matter of fact, they can be utilized to control small amounts of liquid passively, by specifically designed wettability patterns [17,19,36] or surface topographies [18]. It has also been demonstrated in electrowetting experiments that morphological transitions of droplets can be utilized to actuate liquids in microfluidic applications [37–39]. Moreover, condensation experiments on hy-

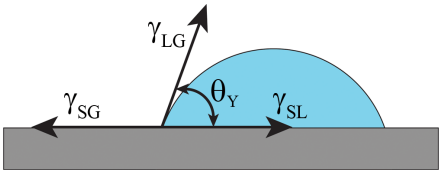

Figure 1.5: Droplet on a flat surface with a static contact angle θ resulting from the balance between γ_{SG}, γ_{SL} and $\gamma_L G$, which are the surface tensions of solid-gas, solid-liquid and liquid-gas interfaces, respectively.

drophilic stripes reported a transition between a liquid filament with a homogeneous cylindrical cross section and a flat filament with a single bulge located in the center of the rectangular domain [19]. In Chapter 4 an extensive experimental and numerical work on this transition is presented.

1.4 Wetting

Speaking about surface phenomena, it is not possible take no notice of the wetting that concerns the behavior of the contact line between a liquid and a surface. Considering a droplet placed on a surface, as shown in Figure 1.5, there are three interfaces in the system: i) solid/gas, ii) liquid/solid and iii) liquid/air. On each of these interfaces there is an associated surface energy γ_{SG}, γ_{SL} and γ_{LG}, respectively. Generally they can be related each other by the Young's equation [40]:

$$\gamma_{SG} - \gamma_{SL} = \gamma_{LG} \cos\theta_Y \tag{1.12}$$

where the static contact angle θ_Y is the results of the balance between the three surface tensions and it is the angle shown from a droplet profile in proximity of the contact line, see Figure 1.5. If the liquid is water, the surface is called hydrophilic when $10°<\theta_Y<90°$, or hydrophobic when $90°<\theta_Y<150°$, superhydrophilic when $\theta_Y \leq 10°$ and superhydrophobic when $\theta_Y \geq 150°$.
All the experimental contact angle values presented in this thesis have been measured by a homemade apparatus described in Appendix A and are indicated with the symbol θ.

1.4.1 Wetting on heterogeneous surfaces

Real surfaces are usually heterogeneous both chemically and topologically. On rough surfaces the local contact angle may change from one point to another. To understand the relation between the apparent macroscopic contact angle θ^* and Young contact angle θ_Y of a surface, two models can be considered: the Wenzel [41] and Cassie-Baxter [42] models.

Wenzel model. It is used to understand the influence of a physical roughness on a surface, when it is completely wetted (see Figure 1.6a). The apparent contact angle θ^* can be described as:

$$\cos\theta^* = r\cos\theta_Y \tag{1.13}$$

where θ_Y is the Young contact angle and r the roughness of the surface ($r>1$). This last parameter always magnifies the original wetting proprieties: if $\theta_Y<90°$ (hydrophilic), it will have $\theta^*<\theta_Y$, likewise if $\theta_Y>90°$ (hydrophobic), it will have $\theta^*>\theta_Y$.

Cassie-Baxter model. It can be applied for flat but chemically heterogeneous surfaces. Considering a surface composed by two species, each characterized by its own contact angles θ_1 and θ_2. The surface fraction occupied by the two species are defined as f_1 and f_2, therefore $f_1+f_2=1$, as shown in Figure 1.6b. The apparent contact angle θ^* can be described as:

$$\cos\theta^* = f_1\cos\theta_1 + f_2\cos\theta_2 \tag{1.14}$$

Therefore, θ^* is indeed restricted to the interval $\theta_1 \div \theta_2$.
A particular case is when one of the species is air. This is common working with rough surfaces, where air can be trapped between the liquid and the surfaceas, as shown in Figure 1.6c. In this case the Cassie-Baxter equation is:

$$\cos\theta^* = r_f \cdot \cos\theta_Y + f - 1 \tag{1.15}$$

where f is the fraction of wetted area and r is the roughness ratio of the wetted area. This is the case of superhydrophobic surfaces [34], where the water droplets are not able to wet completely the surface. This behavior is due to the presence

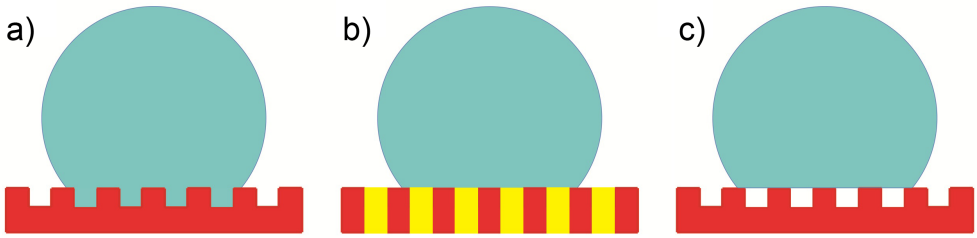

Figure 1.6: Scheme of Wenzel and Cassie-Baxter models: different colors represent different static contact angles. a) Scheme of roughness surface related to Wenzel state. Scheme of surfaces related to Cassie-Baxter state: b) in cases of flat, but chemically patterned and c) roughness substrate. This last particular case is used to explain the superhydrophobicity.

of micro- and nano-structures on the surface. The most common example of superhydrophobic surface in nature, is the lotus leaf, famous for the self-cleaning propriety [43]. In this condition the droplet shows a very weak adhesive force on the surface.

1.4.2 Pinning of the contact line

When the water/air meniscus finds a defect, it can stay blocked on it until a critical value of the contact angle is reached. This behavior is predicted by the Gibbs criteria, described in Figure 1.7 and from the below Equation 1.16:

$$\theta_{max} = \theta_Y + (180 - \phi), \tag{1.16}$$

where θ_{max} and θ_Y are the critical contact angle and the Young contact angle, respectively and ϕ is the aperture of the defect.

Roughness, wettability and pinning are three of the most important parameters

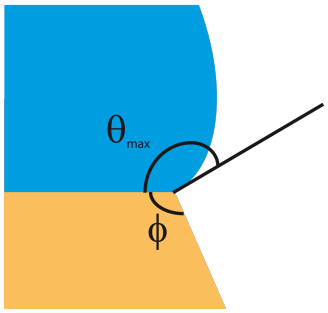

Figure 1.7: Pinning on a structure with corner angle ϕ. θ_{max} is the maximum contact angle predicted by the Gibbs criteria.

to control the droplets motion in open microfluidic devices. Indeed, to do that it is essential to know the physical and chemical proprieties of the surfaces. In Chapter 3 we will present a work with the aim to investigated the pinning of the contact line of a water droplet placed on pillars having different geometry and wettability properties.

The pinning effect can be observed also in closed patterned microchannels [44–46]. As a matter of fact, obstacles and defects in microchannels can induce the pinning of the liquid/air meniscus and this represents a very delicate aspect for their filling. For this reason, in recent years the filling of microchannels patterned with posts or ridges has been the subject of intense studies. For example, different geometric patterns inside microchannels have been analyzed by simulations based on the algorithm of the Lattice-Bolzman by Yeomans et al. [44]. In this article they show how the capillary filling of hydrophilic microchannels is affected by posts on the sides of the channels. Figure 1.8 summarizes their results: θ_Y is the static contact angle of the channel border, θ_p is the pinning contact angle and α is the characteristic post angle. Considering rectangular and isosceles triangle posts, the pinning condition is preserved for $\theta_p<\theta_Y$ and $\theta_Y<90°-\alpha/2$, respectively (Figure 1.8a,b). While, in the case of asymmetric triangles the behavior depends from the flow direction: the pinning is observed only for meniscus which moves from right to left, at the condition of $45°<\theta_Y<90°-\alpha/2$. Moreover, the simulations reported

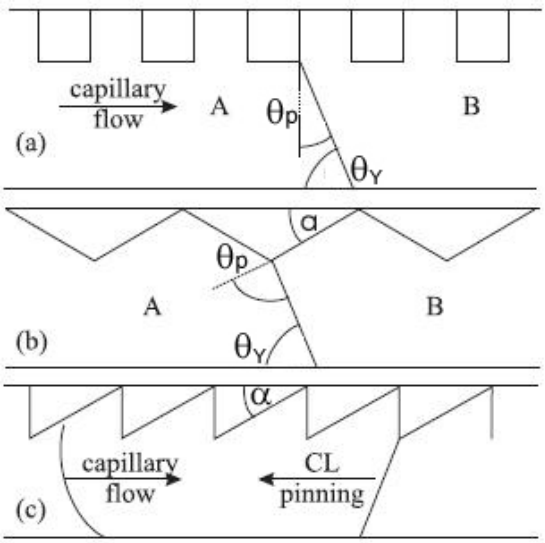

Figure 1.8: Pinning of the contact line during capillary filling when the top wall is patterned with a) squares, b) triangles and c) ratchets. θ_Y and θ_p are the static and the pinning contact angles, respectively [44].

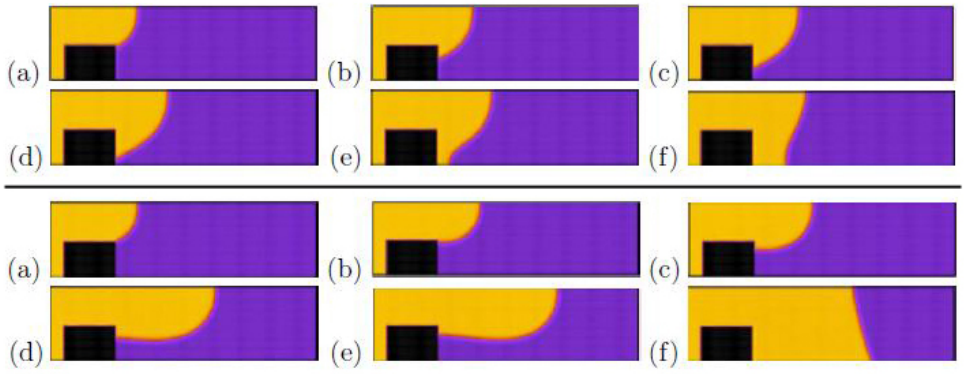

Figure 1.9: Simulations of pinning in hydrophilic (top) and hydrophobic (bottom) channels, with liquid flowing from left to right [47].

in Figure 1.9 compare the pinning difference between hydrophilic and hydrophobic channels [47]. In the hydrophilic case the meniscus follows the channel border, while in the hydrophobic, it increases the curvature until to collapse.

Despite a rich literature of numerical simulation results, until now, the pinning in microchannels has not been analyzed quantitatively from the experimental point of view. Therefore, we started to observe the behavior of a water/air meniscus moving in patterned microchannels and some results are described in the Appendix B.

1.4.3 Contact angles on inclined surfaces

When the surface is inclined with a slope angle α, water droplet looses the symmetric shape [20]. The front assumes a blunt shape and the rear becomes thinner. The contact angles are no longer equal and are therefore distinguished in advancing contact angle (θ_A) and receding contact angle (θ_R), respectively, as shown in Figure 1.10. As the surface inclination increases, the advancing contact angle

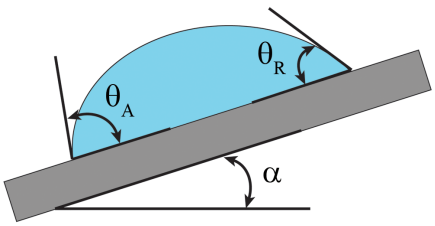

Figure 1.10: Droplet on a plane inclined of α, which shows the advancing θ_A and the receding θ_R contact angles.

increases, while the receding contact angle decreases. As a consequence, the contact angle hysteresis ($\Delta\theta = \theta_A - \theta_R$) increases. For small inclinations, a droplet can remain at rest because the adhesion to the surface is stronger than the gravitational force: this occurs for α lower than a critical angle called sliding angle α_S. Sliding angle (α_S) and contact angle hysteresis are related together by the equation [48]:

$$\frac{mg\sin\alpha_S}{w} = \gamma_{LG}(\cos\theta_{R,s} - \cos\theta_{A,s}) \tag{1.17}$$

where m and w are the weight and the width of the drop, g is the gravitational acceleration and $\theta_{A,s}$ and $\theta_{R,s}$ are advancing and receding critical contact angles in the limit of zero velocity. Equation 1.17 holds also for $\alpha > \alpha_s$, if $\theta_{A,s}$ and $\theta_{R,s}$ are respectively replaced by θ_A and θ_R assumed for such surface inclination.
Sliding droplets on inclined plane are subject to three forces [49]:

- gravitational pull along the plane, of the order of $\rho V g \sin\alpha$;
- viscous drag on the surface, of the order of $-\eta U V^{1/3}$;
- interfacial forces, of the order of $-\gamma V^{1/3}\Delta_\theta$.

where ρ and η are the droplet density and viscosity, respectively, γ is the surface tension between the droplet and the fluid which surrounds it, V and U are the droplet volume and velocity, respectively, α is the plate inclination and Δ_θ is a non dimensional factor depending on the contact angle distribution along the contact line and on the perimeter shape.
Initial motion can be either, accelerated or kept at constant velocity, depending on many surface properties, such as: chemical composition, surface roughness or affinity with water [50]. However the process is dissipative in the sense that after a transient phase, forces balance, and the droplet reaches a steady state with a constant velocity and almost a constant shape [51–53].
Force balance implies a scaling law of the form:

$$Ca \simeq Bo_\alpha - Bo_c, \qquad \text{with} \qquad Bo_\alpha = Bo\,\sin\alpha \tag{1.18}$$

where Ca is the capillary number, Bo_α is the effective Bond number based on the component of gravity parallel to the plane and Bo_c is a constant depending on

Δ_θ. An estimation of terminal velocity can be found by means of computational simulations, containing also predictions about droplet contact line and profile shape [52, 54].
These studies are very interesting for possible applications in open microfluidic devices, where droplets are moved on open surfaces. Taking inspiration from them, we realized a study of sliding water droplets on inclined surfaces having a regular chemical pattern. Experimental results are shown in Chapter 5.

1.5 Droplet microfluidics

Two-phase flow is generated when two immiscible fluids are put into contact. In comparison with the single phase flow, it adds a new degree of complexity to the system, but at the same time it offers many advantages related to applications in chemistry and biology. For example, high-throughput DNA sequencing [55], synthesis of polymer particles controlling their size and shape on the micrometer scale [56] or the production of highly gel emulsions and foams [57].
The two-phase flow properties in micro-devices are tied on three groups of parameters: the channel geometry, the fluid properties and the flow conditions.
The key of the droplet-based microfluidics is the control of the two-phase flow in a microfluidic device in order to produce and manage discrete volumes of fluids. In the most common situation there are two phases: the dispersed and the continuous phases. The first forms the droplets and the second carries the droplets downstream. Moreover, the continuous phase wets the channel borders and prevents that the dispersed phase interacts with them. In the case of a hydrophobic channel, water is the dispersed fluid and an organic phase, usually called "oil", constitutes to the continuous phase: this is the so called W/O condition, that means Water-in-Oil droplets. Vice versa O/W condition (Oil-in-Water droplets) is obtained when the channels are hydrophilic.
As a subcategory of microfluidics, droplet microfluidic inherits the same features of standard microfluidics, but presents also new dynamic problems. First of all, microfluidic devices operate at low Reynolds numbers that assure a laminar flow. In droplet microfluidics the presence of interfacial tension, deformable interfaces and the complexity of singular events as droplets merging or splitting, introduce elements of instability and nonlinearity, not present in standard microfluidics [58].

The proof of that, it is the presence of different regimes that can appear in the same channel, upon varying the flow parameters in the experiments. In the transition from one regime to the other, small changes in the conditions produce great differences on the output: this is a typical example of instability [2]. The presence of instabilities does not enable to predict the system behavior in an easy way, but despite that, the experimental droplet production is possible also in controlled and reproducible manner [2]. Stability droplet production means especially to obtain droplets with constant size and frequency. As a matter of fact, these are the capital proprieties for potential applications in chemistry, biology and material science.

1.5.1 Droplet generators

Direct agitation of immiscible fluids produces the traditional top-down method of droplet production or emulsion, but it causes a broad size droplet distribution [12]. On the other hand, geometry constraints of devices have shown to generate highly monodispersed droplets with size variation smaller than 2% [59]. The three main methods to produce droplets in channels are: i) Co-flowing system, ii) T-junction and iii) Flow-focusing devices. In all of these cases, the dispersed phase is injected in the device where it comes in contact with the continuous phase that is independently driven. The junction zone is particularly important, its design should optimize the reproducibility of droplet production. The shape of the channel influences the local flow field, that can deform the interface causing the droplet break-up. The size of the droplet is the result of the competition between the viscous shear stress and the pressure of the external flow on the one hand and the capillary pressure resisting deformation on the other [2]. The frequency is related to the volumetric flow rate of the dispersed fluid. Usually T-junction devices are exploited to produce droplets with low frequency rate ($1\text{Hz} \div 1\text{kHz}$), while Flow Focusing devices are used for high frequency rate ($1\text{kHz} \div 10\text{kHz}$). Let us now resume the main features of these methods.

Co-flowing system. As it can be seen in Figure 1.11 this configuration is obtained using two concentric capillaries: the dispersed phase is injected via a needle into another co-flowing immiscible fluid. This geometry was first proposed by Cramer et al. in 2004 [35]. With this set up two different regimes are distinguished: dripping and jetting. In the former, droplets are generated close to the capillary (Figure 1.12a), while in the latter they break-up downstream from an extended liquid jet (Figure 1.12b).

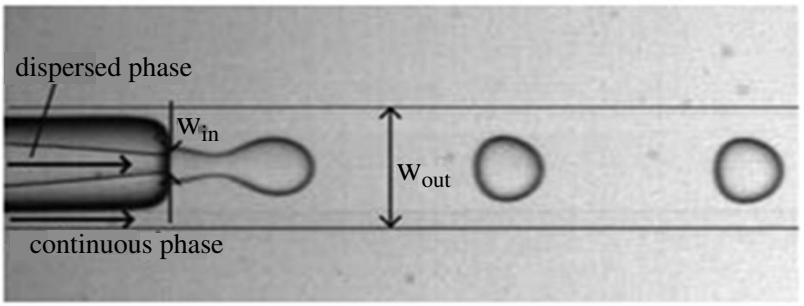

Figure 1.11: Droplet production in a co-flowing geometry [2]. W_{in} and W_{out} are the diameters of the capillaries which transport the dispersed and the continuous phase, respectively.

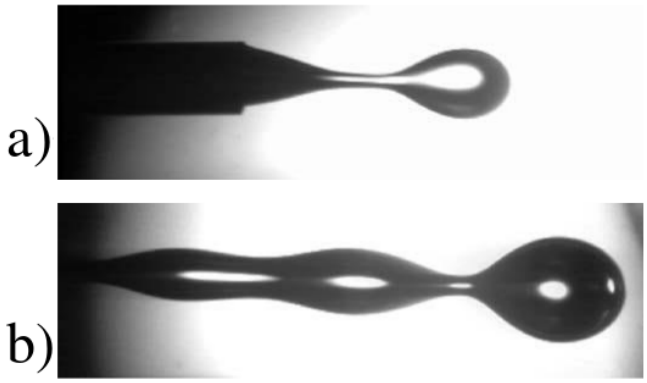

Figure 1.12: Two different regimes of droplet break-up in a co-flowing configuration: a) dripping and b) jetting [35].

T-junction. A typical example of T-junction is shown in Figure 1.13. It was first proposed by Thorsen et al. [58] and it consists in two perpendicular channels, one for each phase, forming a T-shaped junction. With this junction three different regimes can be generally obtained, as shown in Figures 1.14: i) squeezing, ii) dripping and iii) jetting. The first regime occurs when the dispersed phase obstructs the channel as the droplet grows, thus restricting the flow of the continuous phase. This restriction produces an increase of the dynamic pressure upstream of the droplets, that generates a force, necking the interface and pinching off the droplets [2]. In the dripping regime, droplets break up when the shear stress overcomes the interfacial tension. Finally, the jetting regime occurs when both phases (oil and water) have high velocities and they appear as stable parallel flowing streams. In this configuration droplets are formed by the instability at the flat interface and their size is not controlled. As this junction is the one used in this thesis, a more detailed description of the T-junction can be found in the following section.

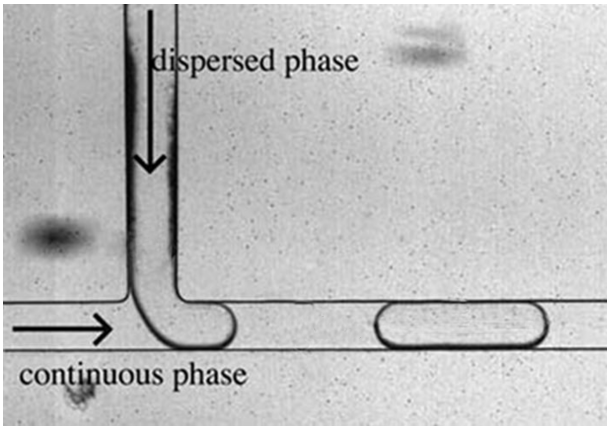

Figure 1.13: Example of a T-junction device [2].

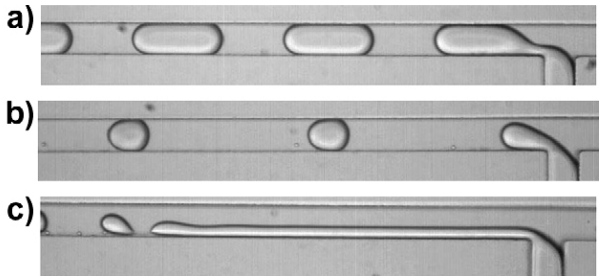

Figure 1.14: Droplet formation mode in a T-junction device: a) Squeezing, b) Dripping, c) Jetting [60].

Flow-focusing device. As shown in Figure 1.15, in this kind of geometry the dispersed phase is squeezed by two opposite streaming flows of the continuous phase. The flow-focusing device was first proposed by Anna et al. [61] where both monodisperse and polydisperse emulsions were produced. The large number of possible configurations does not allow the development of simple scaling laws. Four main regimes can be identified: i) squeezing, ii) dripping, iii) jetting and iv) thread formation.

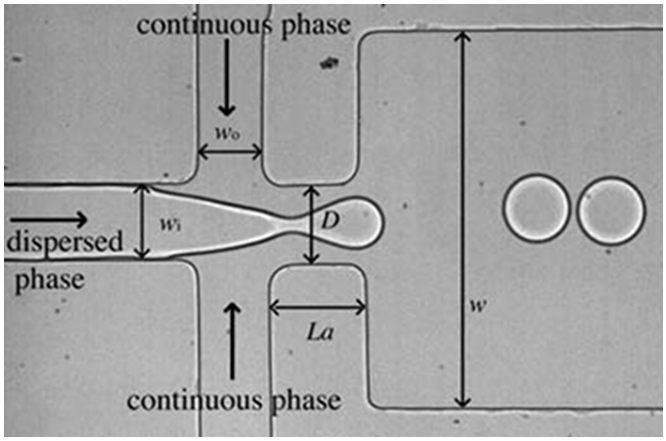

Figure 1.15: Example of droplet production in a flow focusing device. w_0, w_1 and w are the channel widths, which transport continuous phase, dispersed phase and droplets, respectively. The ratio between them and the aperture D can be changed obtaining different droplet sizes [2].

1.5.2 Droplet formation in a T-junction device

One of the most common methods to produce droplets is the T-junction device, mainly because of using that, the droplet formation is periodic and regular over a wide range of flow rates. The break-up of droplets strongly influences their final size and several numerical [62–64] and experimental studies [65, 66] discuss models of the pinch-off mechanism, analysing the strength of the forces involved. In general the process of droplet formation is characterized by the competition between the local fluid shear stress τ acting to deform the interface and the Laplace's pressure Δp, which resists to that deformation, as shown in Figure 1.16. The viscous stress τ due to the continuous phase can be estimated by the product of the viscosity μ_c with the the average velocity u_c of the continuous fluid

divided by the width w_c, so that:

$$\tau = \frac{\mu_c \cdot Q_c}{h \cdot w_c^2}, \qquad \text{with} \qquad Q_c = u_c h w_c \tag{1.19}$$

where h is the depth of the channel. The Laplace pressure at the interface is proportional to the local curvature and in this case can be written as

$$\Delta p \approx \frac{2\gamma}{r} \tag{1.20}$$

being r the characteristic radius of curvature of the liquid-liquid interface. The most important dimensionless number involved in the breaking process is the capillary number Ca. Indeed for T-junction, it describes the relative magnitude of these two forces and can be written as:

$$Ca = \frac{\mu_c Q_c}{\gamma\, w_c\, h}, \tag{1.21}$$

where γ is the surface tension between the continuous and the discontinuous phases.

If w_d is the width of the dispersed-channel, there is a first classification of the process related to the channel width ratio $\Lambda = w_d/w_c$: when $\Lambda < 1/5$ the emerging droplets do not interact with the downstream microchannel walls and remain unconfined by the channel [5]. In this configuration the dependence of the droplet size on the dispersed phase flow rate is less consistent and it should depend solely on the capillary number. When $\Lambda \geq 1/2$ or $\Lambda \sim 1$ the emerging droplet is

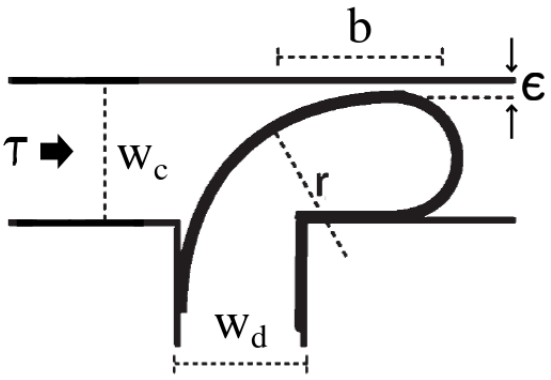

Figure 1.16: Scheme of droplet break-up in a T-junction. w_c and w_d are the channel widths, which transport continuous and dispersed phases, respectively; τ is the shear stress applied, r is the radius of curvature of the droplet during the break-up, b is the length of the liquid film between droplet and channel wall and ϵ is the relative thickness.

influenced by the confinement within the microchannel. The obstruction of the channel by the droplet gives an additional force F_R exerting on the interface due to the increasing resistance of the continuous flow in the region between the droplet and the wall [66]. F_R scales width ϵ^{-2} being ϵ the distance between the droplet and the channel wall (see Figure 1.16) and causes a difference of pressure:

$$\Delta P_R \approx \frac{\mu_c \, Q_c \, w_c}{h^2 \, \epsilon^2}, \tag{1.22}$$

that is the Hagen-Poiseuille pressure for a typical film of thickness ϵ and of length $b \sim w_c$. The corresponding force acting on the droplet is

$$F_R = \Delta P_R \, w_c \, h \approx \frac{\mu_c \, Q_c \, w_c^2}{h \, \epsilon^2} \tag{1.23}$$

Depending on Ca, two regimes can be found: the squeezing regime when $F_R > F_\tau$ ($\epsilon \ll w_c$) and the dripping regime when $\epsilon \sim w_c$ and the droplets pinch off before obstructing the channel because the shear stress is comparable and acts deforming the droplet. The transition from the two regimes is found at a critical capillary number $Ca^* \approx 0.015$ [65].

1.5.3 Droplets transport

After that a droplet breaks up, it is carried downstream by the oil. If the droplet diameter is larger than the channel diameter, the droplet shape is determined by both surface tension, acting to minimize the surface, and geometry constraints. For a circular channel the plug assumes a circular cross section with a film of oil of constant thickness wetting the walls. If the channel has a rectangular cross section, this thickness in not constant and the oil fills the corners like in Figure 1.17. The presence of oil prevents the direct contact between plugs and walls. Both experiments [67] and numerical simulations [68] confirm that the thickness which separates droplets from the walls, is of the order of 1%÷5% of the channel's radius. The oil layer influences also the velocity of the droplet along the channel: in circular channels the droplet moves faster than the oil [67], while in rectangular channels it moves slower than the carrier fluid. Usually the velocity difference is below 6%. [69].

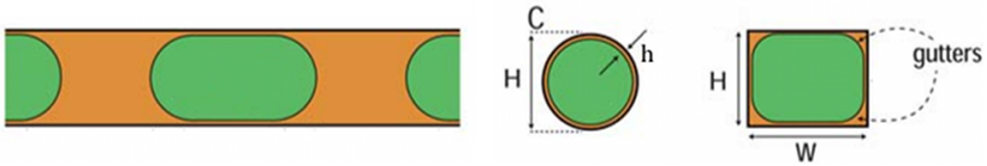

Figure 1.17: Typical shape of a droplet in a microfluidic circular and square channels from front and cross section perspectives, where h is the continuous phase film in the circular case and H and W are the geometric channel parameters [2].

Another important feature of confined droplets is related to the fast self mixing induced inside the droplet volume and the possibility of droplet handling by active or passive methods. The mixing inside of micro-droplets can be tuned directed by channel geometry, inducing internal vortex circulation, as shown in Figure 1.18a [33]. Many efforts are aimed to manipulate the droplets and in the recent years several interesting methods were proposed, for example to merge [70] or to split droplets [71] using suitable obstacles in microfluidic devices (see Figure 1.18b,c).

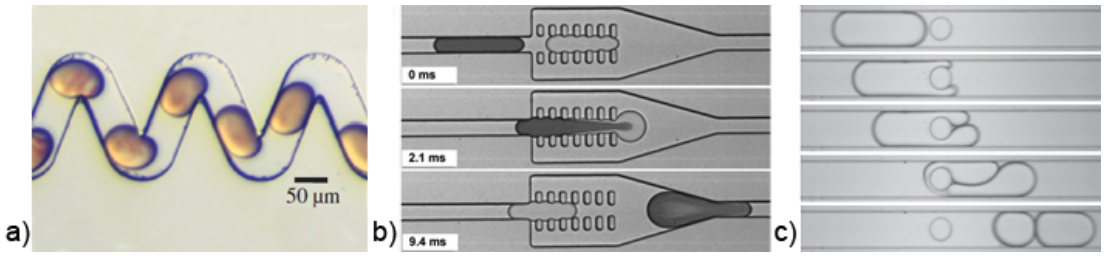

Figure 1.18: Examples of microfluidic devices produced a) to mix the liquid inside droplets, b) to merge different droplets and c) to split one droplet in two smaller.

Chapter 2

Microfabrication techniques

To study the interfacial phenomena described in Chapter 1, the realization of samples with different wetting and geometry proprieties is fundamental. Since the second half of the last century several microfabrication techniques were developed for various applications (e.g. microelectronics, sensing, micromechanics, etc.).This Chapter describes the microfabrication techniques used during the PhD, which are also the most important for microfluidic applications. These techniques are generally introduced, while the details for every sample produced will be illustrated in following Chapters.

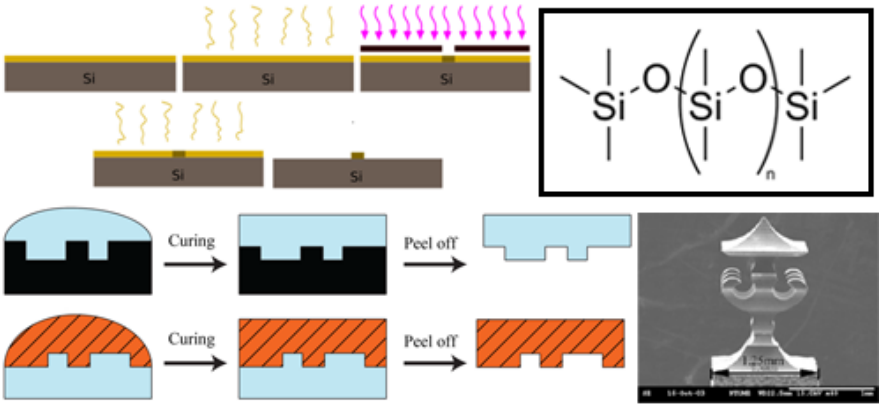

2.1 Introduction

The devices described in this thesis are made using a double step approach. First, a master piece is produced using two different techniques: micro-EDM and photolithography. This master is then replicated to obtain the final structure using soft-lithography. The micro-EDM is an electro-mechanical technique, while photo- and soft- lithography are two common lithographic techniques normally used to create different kinds of patterned surfaces.
To better understand the microfabrication processes described in the experiment sections, these three techniques are fully introduced in this Chapter.

2.2 Micro Electrical Discharge Machining (micro-EDM)

Electric discharge machining (EDM) is a manufacturing process, where a desired shape is obtained using electrical discharges. Micro-EDM is a technological development of this technique, which allows working on micrometer scales.
The origin of EDM is dated back to the first years of the last century, inspired by the behavior of a lightning striking a conductive material: this is a form of natural EDM [72]. During the 1930s, for the first time attempts were made to machine metals and diamonds with electrical discharge. V.E. Matulaitis and H.V. Harding of Elox (USA) developed the "Disintegrators" to remove broken taps from valuable workpiece materials: the erosion was created by intermittent arc discharges occurring in air between the tool electrode and the workpiece connected to a DC power supply. During World War II two physicists B.R. and N.I. Lazarenko in Moscow conducted studies on the minimisation of wear on electric power contacts. They tested different materials with discharges of defined energy. This started the development of Electrical Discharge Machining (EDM), using controlled discharge conditions, for achieving precision machining. Figure 2.1 shows the modern concept of EDM. Pulsed arc discharges occur in the "gap" between tool electrode and workpiece. The gap is filled with an insulating medium, preferably a dielectric liquid like hydrocarbon oil or de-ionized water. The ignition of the discharge is initiated by a high voltage, overcoming the dielectric breakdown strength of the small gap. A channel of plasma is formed between the electrodes

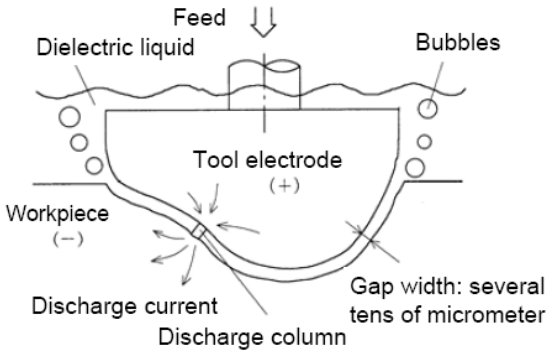

Figure 2.1: Concept of standard EDM [72].

and develops further with discharge duration. As a result, a small crater is generated both on the tool electrode and workpiece surfaces. Removed materials are cooled and resolidified in the dielectric liquid forming several hundreds of spherical debris particles, which are then flushed away from the gap by the dielectric flow. At the end of the discharge period, the temperature of the plasma and the electrode surfaces rapidly decreases. To obtain stable conditions in EDM, it is essential that the next pulse discharge occurs at a spot distanced sufficiently far away from the previous discharge location.

In recent years, several developments in EDM were studied for the production of microstructures. One of these developments brought to the micro-Electrical Discharge Machining (or micro-EDM) [73]. In particular, current micro-EDM technology can be categorized into four different types:

1. Micro-wire EDM: a small wire of diameter 0.02 mm is used to cut through a conductive workpiece;

2. Die-sinking micro-EDM, an electrode with micro-features is employed to produce mirror image on the workpiece;

3. Micro-EDM drilling, micro-electrodes (diameter of 5-10 μm) are used to drill micro holes on workpiece;

4. Micro-EDM milling, micro-electrodes (diameter of 5-10 μm) are employed to produce 3D cavities by adopting a movement strategy similar to the conventional milling.

These new strategies of microfabrication all use the same principle of the standard EDM, as shown in Figure 2.2: a potential difference applied between

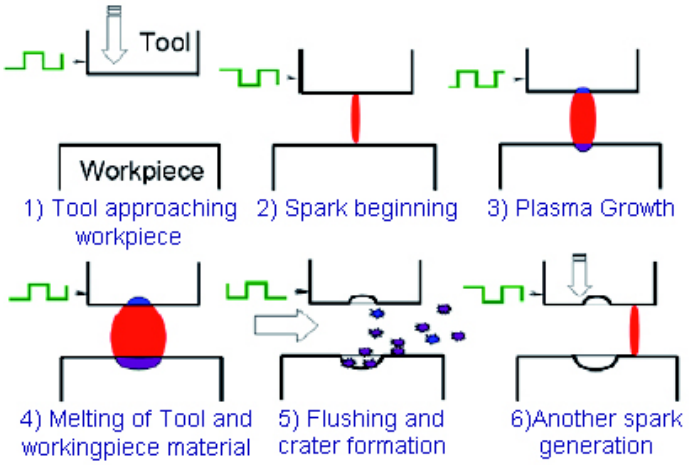

Figure 2.2: micro-EDM process mechanism [74].

the tool and the workpiece creates plasma which melts the surface of the material and the resulting debris are removed by the dielectric flow [74]. At variance with the standard EDM, here energy discharges are less than 100 µJ (typically of 0.1-1 µJ), in order to reduce the material removal and to increase the quality of the final piece. The tools for micro-EDM require high heat conductivity, high melting point and boiling point. For these reasons tungsten is the predominant tool material. An important role during the process, is the different polarization applied between the electrode and the workpiece. By appling a positive potential to the tool, a higher dissipation of energy is observed on it and the carbon released by the discharge is pushed to deposit on it. In this way, the thin layer of carbon protects the electrode during the plasma, which therefore will wear less than the workpiece. Anyway, as the tool is damaged during the process it is important to have a control system to balance the erosion. An example of the capability of the micro-EDM is fully exploited in the machining of a complex Chinese pagoda reported in Figure 2.3.

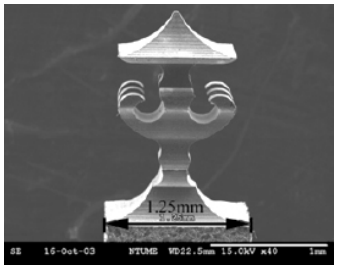

Figure 2.3: Pagoda machined by micro wire EDM [74].

2.3 Lithography

The word lithography, which derives from Greek words stone [lithos] and to write [graphein], refers to a process invented by Aloys Senefelder in 1796 [75]. He was a German actor and playwrighter who decided to print himself his plays. He found that stone (he used Bavarian limestone), when properly inked and treated with chemicals, could transfer a carved image onto paper. Due to the chemical treatment of the stone, image and nonimage areas became oil receptive (water repellent) and oil repellent (water receptive) respectively, attractiving ink onto the image area and attracting water on nonimage areas. This was the first lithographic process in the printing history. Nowadays, lithography is the most important technique for fabricating microscale structures. It is divided into photolithography, electron lithography, X-ray lithography, ion lithography and the most recent soft-lithography.
In next sections the attention will be focused on photo- and soft-lithography, which are the main techniques used in this thesis.

2.4 Photolithography

Photolithography [75] is a lithography technique that uses UV-radiation to transfer a geometric pattern from a photomask to a light-sensitive chemical photoresist (or resist) on the substrate. The father of the photolithography is Nicéphore Niépe, who in 1822 obtained the first image drawn by the light. He covered a copper substrate with a mixture of bitumen dissolved in oil and, after some hours of exposure under the sunlight, the exposed part hardened compared to the unexposed part, which remained soluble and could be washed away. Now we can call Niépe's mixture "negative photoresist". Despite the so old origin, photolithography found an application only after the Second World War, with the first printed circuit boards. During the second part of the 20th century, the development of photolithography increased the performances and reduced the costs in the electronic industries. In 1965 Gordon Moore, co-founder of Intel, observed that in the period between 1959-1965 the electronic components composed a chip, duplicated every year. Therefore, he assumed that the performance of microprocessors would be duplicated every 18 months. Today this prediction is known as the first

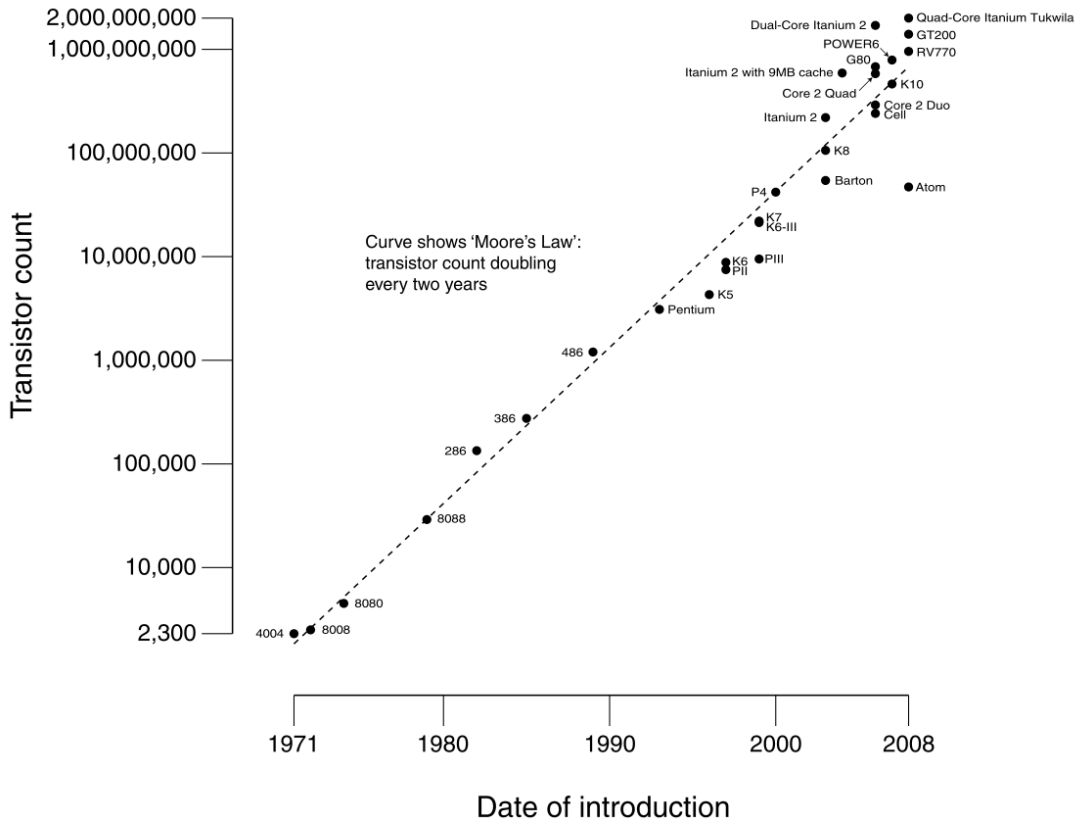

Figure 2.4: Plot of CPU transistor counts against dates of introduction. Note the logarithmic vertical scale; the line corresponds to exponential growth with transistor count doubling every two years.

Moore's law and it was quite well satisfied, as it is possible to observe from Figure 2.4.

The modern photolithography consists in a multi step procedure summarized in Figure 2.5: 1) Photoresist deposition, 2) Pre exposure bake (or soft-bake), 3) Exposure, 4) Post exposure bake, 5) Development.

1) Photoresist deposition

Photoresist is deposited on a cleaned substrate (usually a silicon wafer) by spin-coating to obtain a homogeneous film. The resulting polymer thickness, T, is directly proportional to the solution concentration, the viscosity and inversed proportional to the spin speed. Unlucky, the expression which relates all these parameters must be deduced only empirically. The cleanness of the substrate is very important for the quality of the polymer film [75]. To clean the wafer two different approaches are normally used: oxygen plasma or strong acid solution, also

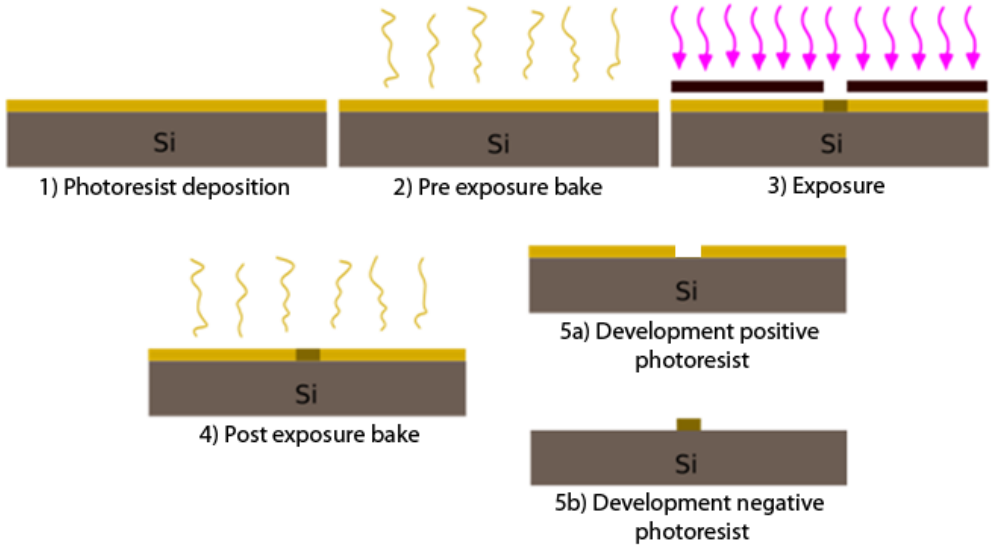

Figure 2.5: Steps of photolithographic process.

calls Piranha solution. This is a mixture of sulfuric acid (H_2SO_4) and hydrogen peroxide (H_2O_2), that removes organic matter and hydroxylated, or activated, the silicon surface.

2) Pre exposure bake (or soft-bake)

To remove the solvent that is still contained in the photoresist after the spin coating and to promote the adhesion between polymer and substrate, the sample is baked at 60-100°C for few minutes (5-15min). The exact parameters depend on the type of photoresist.

3) Exposure

The film of photoresist is exposed by an UV-radiation through a mask, which presents transparent and opaque parts. If we are working with a Negative photoresist (for example the SU-8), the radiation promotes the random cross-linkage of the chains of the polymer and only the areas exposed will reticulate. The unexposed part could be easily removed by an appropriate solvent. Conversely with a Positive resist (for example the Microposit^{TM} and PMMA), the radiation induces the weakening or the braking of the polymer chains; therefore, the exposed areas will be removable, while the unexposed ones remains attached to the silicon wafer. The wavelengths of the light used in photolithography depend on

the characteristic of photoresist. After the exposure step it is possible to observe a latent image of the mask on the surface of the photoresist.
During the exposure step, the quality of the mask plays a crucial role. To obtain the best resolution, the masks are usually composed by a quartz plate which is transparent to deep UV, covered with an adsorber metal pattern, normally a chromium layer of tens nanometer. If it is not necessary to achieve high resolutions, it is possible to use a dark pattern printed by common laser printers on a standard transparent acetate sheet. There are different methods for interfacing the photoresist film with the mask: i) contact printing, ii) proximity printing and iii) projection printing. In the first case the mask and the film are put into contact, while in the second case a gap of about 10 μm is left between the two surfaces. Projection printing uses optics to demagnify images: in this case the feature resolution on the imaged wafer can be even finer than the resolution of the mask. Using both contact and proximity arrangements of mask and substrate, the resolution limit depends on various factors. These include the diffraction of the light at the edge of an opaque feature, the alignment of substrate respect to the mask, the not perfect flatness of the film and the dirty particles between mask and substrate. If we consider a periodic grating made of opaque and transparent stripes of equal width, b (see Figure 2.6), the theoretical resolution R, is given by:

$$R = b_{min} = \frac{3}{2}\sqrt{\lambda(s + \frac{z}{2})} \tag{2.1}$$

Where b_{min} is the minimum feature size transferable, s is the gap between the mask and the photoresist, λ is the radiation wavelength and z is the photoresist thickness. From this equation it is possible to observe that, smaller is the wavelength and the thickness of the film, higher is the possible resolution and that the contact printing, where s=0, should give higher resolution than the proximity printing. However, as the contact between the polymer and the mask could cause mask damage or contamination, sometimes it is better to avoid working in contact mode.

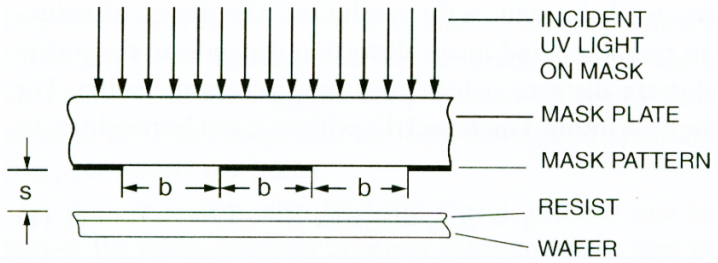

Figure 2.6: Photolithography with a grating mask having period b and placed at distance s from the resist [75].

4) Post exposure bake

The post exposure bake is usually necessary to complete the polymerization reactions initiated during the exposure. The first step of the reactions induced by the radiation takes place at room temperature and their rate is increased by a baking at about 100°C.

5) Development

Development procedure is a selective dissolving process where parts of unpolymerized resist are washed away. Therefore the developer transforms the latent image formed during the exposure into a relief image. Positive photoresist are typically developed in aqueous alkaline solutions and negative resists in organic ones.

2.4.1 Clean Room

One of the most important parameter to control is the cleanness, not only of the substrate, but also of the work environment and facilities. Normally, all the step of the photolithography take place inside a Clean Room, which is a special area that is controlled with respect to the airborne particulates, temperature, air pressure, humidity, vibration and lighting. There are different kinds of clean rooms, which are classified according to the number of particles per cubic meter at a specified particle size. To have an idea, a normal urban environment contains 35,000,000 particles per cubic meter of about 0.5 μm and larger, corresponding to an ISO 9 clean room, while an ISO 1 has only 10 particles per cubic meter of 0.1 μm and smaller. The choice of the clean room depends on the size of the structures that are necessary to realize. All the structures described in this thesis

are realized in a clean room ISO 7 (< 2,930 particles with size of >5 μm), which is sufficient for the fabrication of devices with typical dimensions of about 10-100 μm.

2.4.2 Negative photoresist: SU-8

SU-8 is one of the most common negative photoresist, for its capability of producing high aspect ratio structures. It is an epoxy-based photocurable resin. The maximum absorption occurs at a wavelength of 365 nm and, when exposed, its long molecular chains cross-link, causing the solidification of the material. The final aspect is the one of a strong polymer with a T_g higher than 200°C. The SU-8 was originally developed for the microelectronics industry for the fabrication of semiconductor devices. Today, it is mainly used for the fabrication of microfluidics devices. In particular it can be used for direct fabrication of microchannels [76] and to produce masters with relief patterns for molding devices in other materials [77], like polydimethylsiloxane (PDMS). All the photolithography activities described in this thesis are based on this last usage of SU-8. In detail, SU-8 2050 provided from MicroChem Corporation (Newton, Massachusetts) permits to realize structure with a thickness about 10-150 μm, was used.

2.5 Soft-lithography

Even if photolithography is one of the most diffused microfabrication techniques, it has some disadvantages. The sizes of the features are limited by optical diffraction and to use the required high energy radiation, complex facilities are necessary. It is quite an expensive technique and only a few types of material can be used. In addition, there is not a good control of the surface chemistry and this could be an important problem for chemical and biological applications. For all these reasons, at the end of the 20th century, a new microfabrication technique expanded rapidly: the soft-lithography [79]. This term is referred to a family of non-photolithographic techniques for fabricating of high-quality microstructures using elastomeric or soft materials; the most notable polymer is the polydimethylsiloxane, commonly known as PDMS. Soft lithographic techniques require little capital investments, because they can often be carried out in normal laboratory environment (the clean room is usually not necessary) and the typical materi-

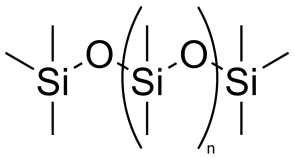

Figure 2.7: Chemical structure of PDMS.

als used are not expensive. The different techniques [79] which are included in the soft-lithography family are: microcontact printing (μCP), replica molding (REM), microtransfer molding (μTM), micromolding in capillaries (MIMIC) and solvent-assisted molding (SAMIM). In all of these techniques the PDMS is used as a mold or to produce the final sample. In following sections only the techniques used in this thesis will be detailed explained.

2.5.1 Polydimethylsiloxane - PDMS

The principal polymeric material used to produce elastomeric devices is polydimethylsiloxane (PDMS). It is composed of inorganic siloxane chains with organic methyl groups attached to the silicon, see Figure 2.7. This material is commercially available as a liquid pre-polymer (made by siloxane oligomers), that reticulates after mixing with a reticulant agent, containing a platinum catalyst. After curing time, that could be accelerated thermally, PDMS looks like a transparent flexible elastomer, which has a T_g around -120°C and a melting temperature higher than 200°C.

Several proprieties of PDMS are useful for the formation of high-quality microstructures in soft-lithography:

- Being an elastomer, PDMS conforms to the substrate over a large area. It is sufficiently deformable so that the conformal contact can be achieved also on not perfectly planar surfaces. Moreover, it can be released easily also from complex and rigid structures.

- PDMS surface has a low surface energy (ca. $21.6 \cdot 10^{-3} Jm^{-2}$ [79]) and is chemically inert, therefore usually not adhere irreversibly on other polymers. The surface proprieties can eventually be modified by treatment of oxygen plasma, to give an appropriate interfacial interaction with other materials or molecules [80].

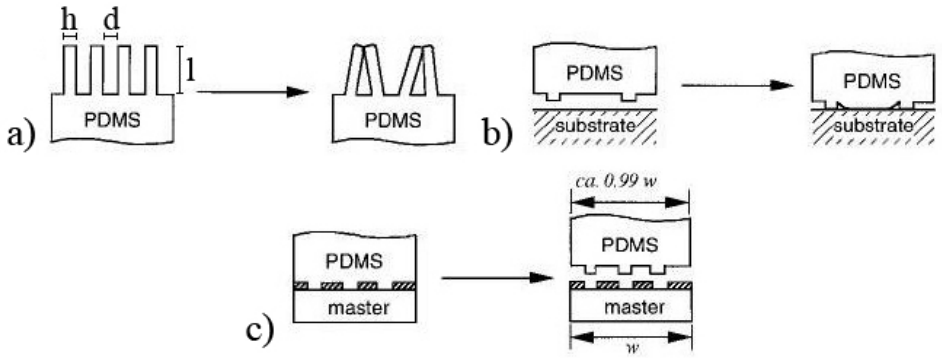

Figure 2.8: Schematic illustration of possible deformations and distortions of microstructures in the surfaces of elastomers such as PDMS [79]

- After the complete polymerization, it is homogeneous, isotropic and optical transparent down to 300 nm. Additionally, PDMS is permeable by oxygen and biocompatible, so it can be used for biological applications.
- The final structures in PDMS are durable in time. It is possible to use the same sample for several times and several months.
- PDMS is a low cost material (about 100 Euro/kg), if compared of a photoresist (e.g. SU-8 costs about 1000 Euro/Kg).

These pros makes PDMS the principal material for microfabrication and for microfluidics in the last 15 years. However there are some technical problems which must be considered for its utilization. First, adhesion and capillary forces exert stress on the elastomeric chains and can cause the collapse of the structures, in particular if the aspect ratio of the relief features is too large (see Figure 2.8a). Delamarche et al. [81] showed that the aspect ratios (l/h) of the structures on PDMS surfaces have to be between 0.2 and 2 in order to avoid this problem. Moreover, when the aspect ratio is too low, the relief structures are unable to sustain its weight. To avoid this problem it is better to do not work with too distant features ($d \leq 20$ h), as shown in Figure 2.8b. Next, during the curing, the shrinkage is about 1% [82] (see Figure 2.8c). Finally and probably the most important problem of the PDMS regards the applications in chemistry, since it can be readily swelled by non-polar solvents (in general organic solvents). When non-polar molecules are put in contact with PDMS surface, they have great affinity with the methyl groups that are commonly exposed by the polymer. This promotes adsorption and the penetration of the molecules into of the material, changing

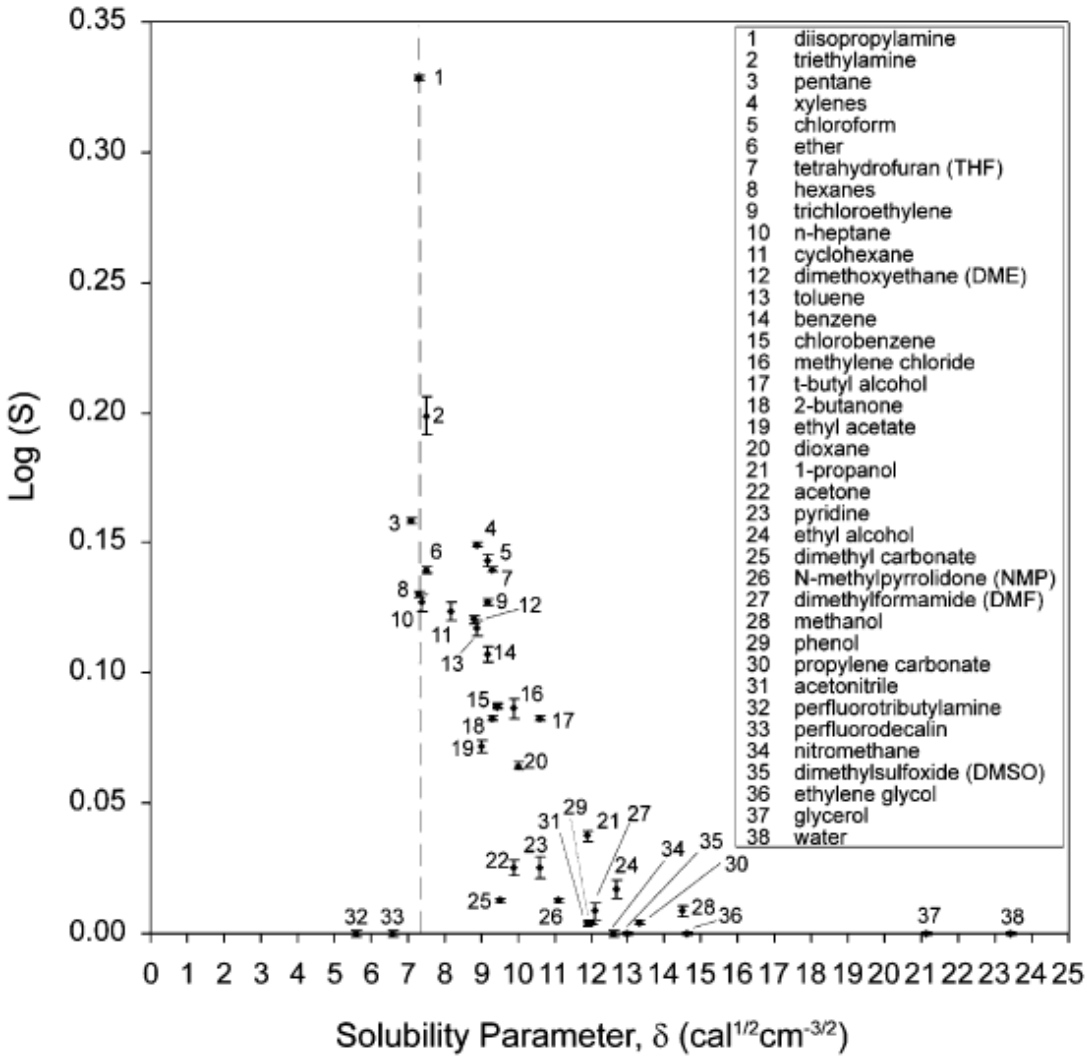

Figure 2.9: Graph with the swelling ratio $S = D/D_0$ with different solvents, having different cohesive energy δ [83].

the shape of the microstructures. This phenomenon was studied by Whitesides et al. [83], who put a piece of PDMS inside different solvents for a controlled time and then registered the length variation (and consequently the amount of solvent inside the polymer) while the polymer was still inside the solvent. Looking at Figure 2.9, using S as adimensional length variation parameter ($S = D/D_0$ with D=length of PDMS in the solvent and D_0=length of dry PDMS), it is possible to see that solvents with cohesive energy near to that of PDMS have a great tendency to cause swelling (here expressed as $\delta = (\text{cohesive energy})^{1/2}$) .

This last problem pushed people to look for other materials to use in soft-lithography or to find strategies to protect the PDMS from the non-polar agents.

For example, Weitz et al. [84] found a strategy to protect the inside border of a microchannel with a glass coating by sol-gel polymerization. The limit of this technique is that the final shape of the channel is rounded.
Regarding new polymers, Steven Quake's group studied the possibilities to use perfluoropolyethers (PFPEs) [85]. These materials are liquid in room temperature, exhibit low surface energy, low Young modulus, high gas permeability. The resulting polymer is transparent and compatible with many solvents (dichloromethane, acetonitrile and methanol). Other polymers with solvent compatibility are thermoset polyesthers (TPE). Fiorini et al. [86] produced devices with a resolution down to a few micrometers that are resistant to acids, bases and some common organic solvents, but not with the chlorinated.
Another possibility is to use thiolene resins (ThR), which are commercially available as optical adhesives by Norland Products. The commercial name is Norland Optical Adhesive (NOA) [87] and it exists with vary formulations that differ in their mechanical proprieties, curing time and viscosity. Thiolene resins are available as prepolymer that under UV radiation becomes hard. The reaction can be described as a four step radical process, as shown in Figure 2.10, which consists in the UV initiation, two propagations and termination processes. The final cured material is optically transparent in the visible range of electromagnetic spectrum, adheres to glass and metals and resists at temperature up to about 130°C. Regarding the stability with organic solvents, thiolene resins show good compatibility with not chlorinated solvents, as showed in Table 2.1, in which its volumetric swelling ratios (S) are compared to those of PDMS [88]. However, swelling ratio with chlorinated solvents is similar to the PDMS.

Solvent	S	S_{PDMS}
acetone	1.31	1.28
benzene	1.32	2.09
dichloromethane	1.87	1.97
ethanol	1.01	1.01
hexanes	1.01	2.40
n-butyl acrylate	1.03	1.93
tetrahydrofuran	1.49	2.29
toluene	1.13	2.18

Table 2.1: Swelling ratio (S) of NOA in organic solvent compare with PDMS.

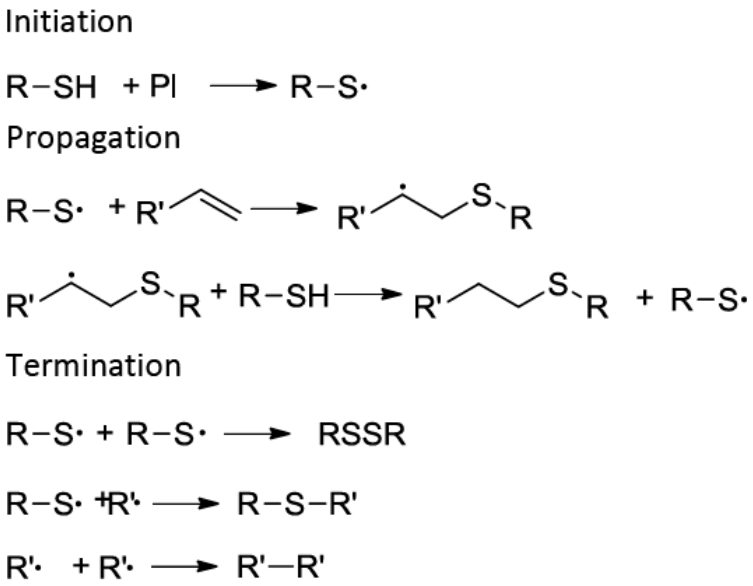

Figure 2.10: Polymerization by radical process of thiolene resins.

Thiolene resins (ThR) have been extensively used to fabricate microdevices because of their good solvent resistance, rapid curing procedures, biocompatibility and strong adhesion to metal and glass substrates [89]. Harrison et al. [90] showed the possibility to use thiolenic resins for microfluidics applications for the first time. They put thiolene resins between two glass slides and exposed them to UV curing using an appropriate mask to realize a microfluidic channels. Since thiolene is photopolymerizable, after an UV exposure the non cured prepolymer was washed away, obtaining the desired microchannel network. Moreover, thiolene resins can be used to produce devices with soft-lithographic techniques, generally in combination with PDMS [91].

2.5.2 Self assembled monolayer (SAM)

Self assembly is a spontaneous organization of molecules in a stable configuration generally driven by covalent and non-covalent forces. The key idea is that the final structure is close to a thermodynamic equilibrium and therefore is predetermined by the characteristics of the initial subunits. Various strategies have been developed to fabricate two and three dimensional structures and self assembled monolayers (SAMs) are the most widely studied.
SAMs of organic molecules are molecular assemblies formed spontaneously on sur-

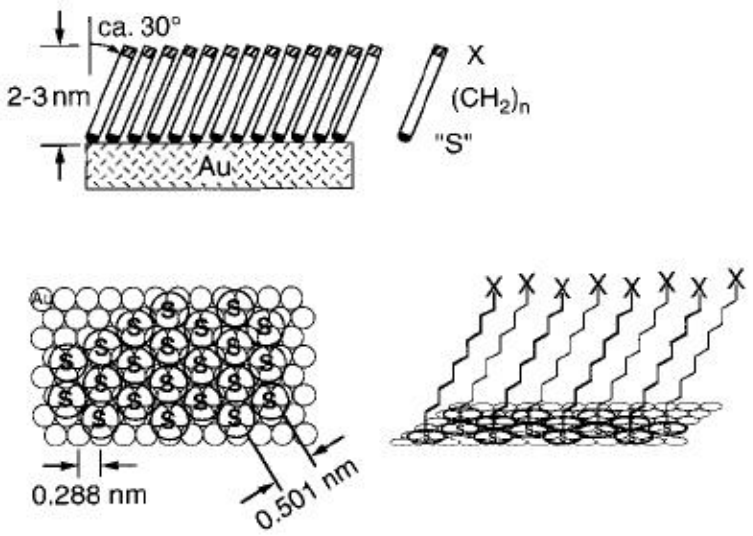

Figure 2.11: Representation of a highly ordered monolayer of alkanethiolate formed on a gold surface. The sulfur atoms form a commensurate overlayer on Au(111) with a structure, whose thickness is determined by the number of methylene groups (n) in the alkyl chain. The alkyl chains $(CH_2)_n$ extend from the surface are tilted approximately 30° from the normal to the surface. This configuration maximizes the van der Waals interactions between adjacent methylene groups [79].

faces by adsorption and organized in ordered domains. They are usually prepared by immersing the substrate in a solution containing the molecules reacting with the surface, or by a vapor exposition. The best characterized systems of SAMs are alkanethiolates $CH_3(CH_2)_nS^-$ on gold, where the sulfur atoms bonded to the gold surface bringing the alkyl chains into close contact, see Figure 2.11. The formation of ordered SAMs is a relatively fast process, for example in solution it takes few minutes. This ability to obtain ordered structures rapidly is one of the factors that increased the diffusion of the SAMs also to study model systems on wetting. SAMs are also well suited for fabricating chemical patterns and structures with lateral dimensions between nanometer and micrometer scales. One of the most popular techniques to pattern SAM on a flat surface is the microcontact printing (μCP).

2.5.3 Microcontact printing (μCP)

Microcontact printing (μCP) is a flexible, simple and non photolithographic method that uses the relief structures on the surface of a PDMS part as a stamp to transfer a pattern of self-assembled monolayers (SAMs) to the substrate surface by contact [92]. SAMs can be created by immersion of the substrate in a solution containing a ligand $Y(CH_2)_nX$ (named "ink"), where X is the head group and Y is the final group. The head group depends on the propriety of the substrate and Y determines the surface property of the monolayer. In microcontact printing, the stamp is wetted with the "ink" and pressed on the substrate surface, as shown in Figure 2.12. The use of PDMS as a stamp is very important for its swelling propriety in organic solvents. As a matter of fact, during the immersion step the PDMS absorbs part of the solution, helping the pattern transfer to the substrate. The possibility to realize very resolute patterns in short time (one print takes less than 1 minute) and in a not particular clean environment (it is not necessary to work in clean room conditions) push μCP to became very common.

Microcontact printing was first demonstrated for SAMs of alkanethiolates on gold and then it has been realized with a large variety both of substrates and molecules. For examples using SiO_2 [93], Al [94] and glass [95] as substrate and OTS (Octadecylthriclorosilane) [93], DTS (docosyltrichlorosilane) [96] and proteins [97] as functionalizing molecules.

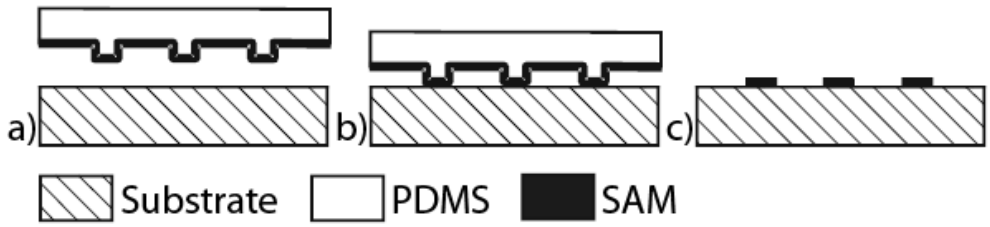

Figure 2.12: Step of process of μCP [92]

2.5.4 Replica Molding (REM)

The replica molding (REM), described in Figure 2.13a, is a microfabrication technique that allows to realize a negative copy of a initial master [75]. Unlike the standard strategies to make a mold, in this case an elastomeric polymer is used, which can be easily removed from the master: the prepolymer is poured on the master and, after a curing time, it is peeled off. REM is a procedure that accommodates a wide range of materials and the most used is still PDMS. As a matter of fact, it allows to produce very complex (two or three dimensions) [98] and resolute (nanometer scales) [99] structures in one single step. Moreover, using PDMS it is possible to make a "Double replica molding": using the first replica as a master to produce a second replica that will be the positive copy of the original master, as shown in Figure 2.13b. This evolution of REM allows to prepare devices using materials, like NOA, that would not be compatible with the standard replica molding: if a polymer, after the curing time, is not elastomeric, it will not be possible to peel it off from the master. At variance, if the master is made with PDMS, it will always be possible, to detach the two parts without damaging them. For all of these reasons, replica molding with PDMS is the most common techniques to realize also microfluidic devices. Starting from a master made by photolithographic or mechanical techniques, PDMS microchannels are produced by REM and can be closed with normal glass cleaned and activated by oxygen plasma exposition [100].

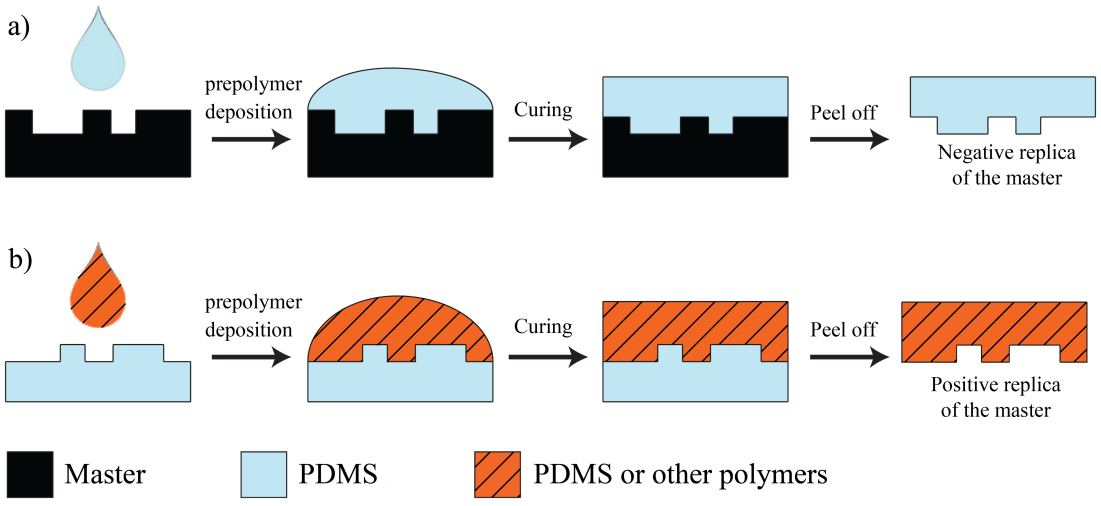

Figure 2.13: Soft-lithographic techniques: a) Replica molding and b) Double replica molding.

Chapter 3

Suspension of water droplets on individual pillars

This Chapter reports results of extensive experimental and numerical studies on the suspension of water drops deposited on cylindrical pillars having circular and square cross sections and different wettabilities. In the case of circular pillars, the drop contact line is pinned to the whole edge contour until the drop collapses due to the action of gravity. In contrast, on square pillars, the drops are suspended on the four corners and spilling along the vertical walls is observed. The Chapter is divided in two main parts: at first the experimental and simulation details are described and then, the results for each pillar geometry are presented.

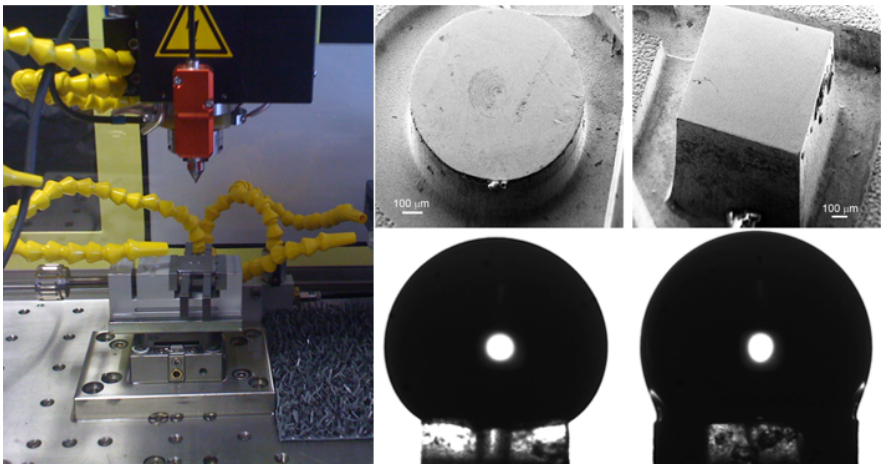

3.1 Introduction

One of the main goals regarding the open microfluidics is the control of the droplet motion. To achieve this purpose, it is very important to know the physical and chemical proprieties of the surfaces, like their roughness and wettability, as introduced in Chapter 1. For this reason, a very active field of research is the realization of surfaces controlling these parameters. As a matter of fact, by playing with their surface chemical composition and their morphology, it is possible to significantly enhance their hydrophobic or hydrophilic characters. In the past few years, a large variety of superhydrophobic and superhydrophilic surfaces have been realized which present a contact angle θ>150° [101–104] and θ<10° [105–107], respectively. More interesting for potential applications, is the realization of smart coatings which can change their wettability when subject to specific external stimuli, like light [108–110] or temperature [111–113]. An essential feature in all of these realizations is the presence of a rough surface. If the roughness is isotropic, a drop deposited on the surface assumes an almost hemispherical shape and the apparent contact angle is the same measured in any direction, as predicted by Wenzel [41] or Cassie-Baxter models [42]. If the roughness is not isotropic, e.g. parallel grooves, the drop is elongated and the apparent contact angles measured along the principal directions of the patterned surface are different. Recent studies have focused onto the wetting properties of anisotropic patterned surfaces. It was observed that even relatively simple surface topographies, such as grooves with a rectangular cross section, exhibit a large variety of different wetting morphologies [18]. Analogously, chemically heterogeneous flat surfaces formed by alternating hydrophilic/hydrophobic stripes [114–116] and geometrically structured surfaces characterized by parallel microscopic grooves [117–119] show pronounced anisotropic contact angle and elongated drops. To better analyze this anisotropy, Semprebon et al. investigated the wetting of a drop deposited on top of a single rectangular post having a length much longer than its width [120]. The orthogonal contact angle is found to increase with the drop volume, while the parallel angle does not change and coincides with the intrinsic values of the corresponding surface. To further characterize this phenomenology, we have extended the study to individual posts of sub-millimetric size having symmetrical cross section.
Classic experiments [121] on the equilibrium of liquid drops confined on macro-

scopic circular cylinders with sharp edges were already presented, confirming the validity of the Gibbs condition. These measurements have been recently extended to the study of the suspension of liquid drops by a single frustoconical asperity, having a top circular surface of millimeter size [122]. It was established that for the suspension of a drop, not only the contact line must be pinned but also that the vertical component of the surface tension must be of sufficient magnitude to hold unsupported liquid against the downward pull of gravity. The stability of drops at the edges was also investigated by pressing the drop with a superhydrophobic surface and was characterized in terms of the critical pressure necessary to depin the contact line [123]. More recently, the profile of liquid drops at the tip of a cylindrical fiber with a sub-millimiter radius was studied [124]. Additionally, the wetting behavior of individual nanostructures with diameters down to the sub-100 nm scale was quantified. It has been shown that the macroscopic pinning behavior is preserved for nanostructures with dimensions down to about 200 nm [125].
A common feature in all of these studies is the presence of asperities and posts having circular cross-sections [36, 121–127] and therefore the results may be directly deduced by the Gibbs criteria. The aim of the work described in this Chapter is to provide a first analysis of the profiles of water drops pinned on geometric posts with corners. Following we present the results of systematic experiments and numerical calculations of the shape of drops deposited on single posts having circular and square cross sections and various wettabilities.

3.2 Microfabrication of PDMS pillars

Following the general approach presented in Chapter 2, in this section the microfabrication process for posts with circular and rectangular cross section is described. It is developed in two parts: first, we prepared two masters of stainless steel by micro-EDM technique and then, we produced the final structures with PDMS by double replica molding.

3.2.1 Master production by micro-EDM

We produced two kinds of individual posts in stainless steel, by micro-EDM in milling mode. The posts, shown in Figure 3.1b,c, were produced with height of 200 μm and with cylindrical and square shapes having characteristics size of 800 μm (diameter D = 800 μm and side L = 800 μm, respectively). In details, at first we polished the metal surface and then we started the milling process. The machine used is the SARIX SX-200 (see Figure 3.2) available in the department of Mechanical engineering. We realized the 3D CAD draws of the structure, using Pro Engineering Wildfire 3.0 and then, we generated and simulated the manufacturing of workpieces by ESPRIT, a CAM software (Computer-aided manufacturing) provided by DP Technology. During the milling, we used a hydrocarbon oil (HEDMA111) as dielectric fluid and tungsten carbide rods with diameter of 300 μm as electrodes.

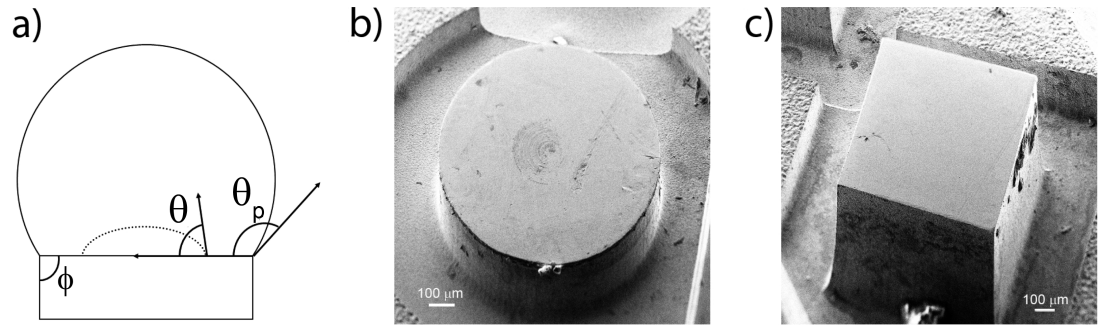

Figure 3.1: a) Scheme of a cross-section of a drop placed on top of single pillar showing characteristic angles. SEM views of b) the circular and c) the square pillars.

The final posts have been characterized by profile meter and by scanning electron microscopy (SEM). Figure 3.1b,c shows magnified views of two pillars. The root mean square surface roughness of the polished top face was less than 1 μm, the vertical walls about 3 μm, and finally, the contour edge 2 μm. After the machining, the pillars were washed using solutions of ethanol and acetone in ultrasonic bath and finally used as masters in double replica molding process.

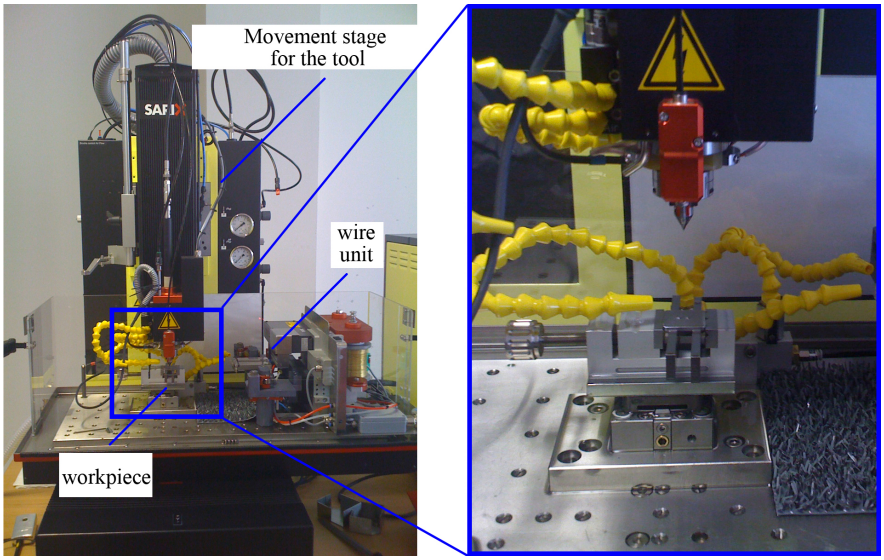

Figure 3.2: Picture of the SARIX machine for micro-EDM.

3.2.2 Double replica molding of stainless steel masters

The final samples were prepared by standard double replica molding process as positive copies in polydimethilsiloxane (PDMS) of the stainless steel masters. Referring to Figure 3.3, a negative copy in PDMS was firstly casted by simply pouring over the master a mixture of the pre-polymer and the curing agent and then, heating the whole system in an oven for 1 hour at 80°C (steps I and II). With the help of a microscope, thin stainless steel wires (diameter 130 µm) were vertically inserted at the center of each cavity (step III). Then, a second replica of PDMS was performed on this assembly in the same manner as the first process (step IV). Before casting, the first PDMS replica was functionalized with a monolayer of trichloroperfluorooctylsilane (FOTS). It was left in a silane atmosphere for at least 2 hours so that the whole surface is evenly coated. This works as an anti-stick layer which allows the detachment of the two PDMS parts. After solidification, the PDMS replica was peeled off, the wires were gently taken off and thin tubes were fixed at the extremity of each hole (step V). By connecting them to a syringe pump, a water flow could be induced through the central hole to form a small drop on top of the pillar (step VI). In this way it was possible to easily control the production of drops of known volume. We soon discarded the standard deposition of sessile drops for a series of drawbacks: i) the procedure was highly erratic given the small size of the post and its hydrophobic nature, ii)

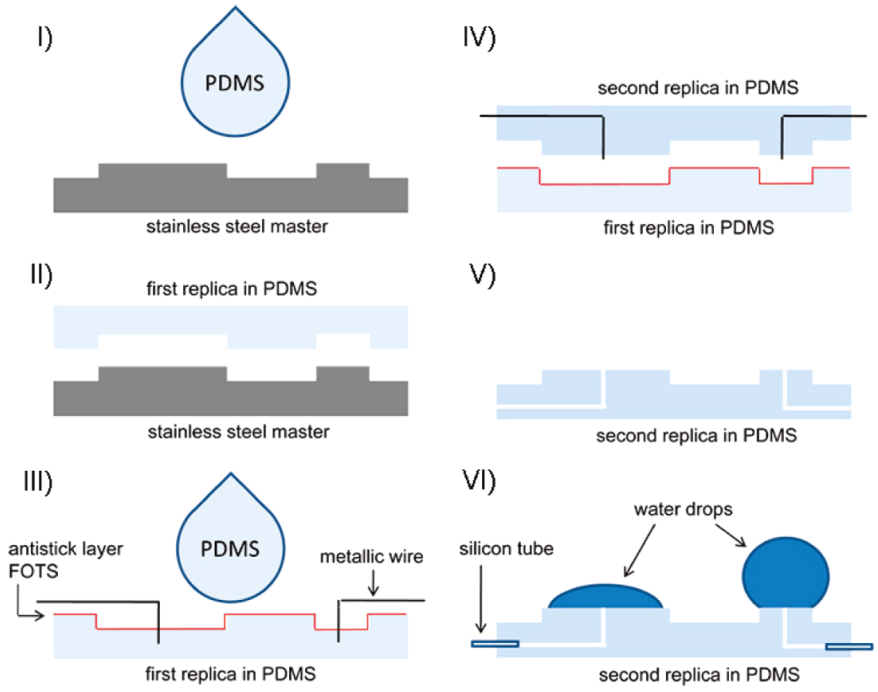

Figure 3.3: Double replica molding process to produce pillars with PDMS.

$$2\,O_2 \xrightarrow{\lambda = 184.9\ \text{nm}} O^* + O_3$$

$$O_3 + \underset{\text{residual}}{\text{organic}} \xrightarrow{\lambda = 253.7\ \text{nm}} CO_2 + H_2O$$

Figure 3.4: Oxidation process induced by UV lamps in UVO-cleaner.

the volume could not be varied continuously. A similar procedure was adopted in the original work by Mason and coworkers [121], the only difference being that they used much larger posts by a factor $\geq$10. The wettability of these posts was changed by exposure to oxygen plasma. The treatment of the PDMS surface was carried out in a commercial UVO-cleaner (by Jelight Inc), normally used to clean the surface from organic contaminants. The machine is composed by two UV lamps with different wavelengths of emission (184,9 nm and 253,7 nm): the first band excites the oxygen creating ozone and the second catalyzes the reaction to decompose the organic molecules to water and carbon dioxide, as shown in Figure 3.4. We found that after 45 minutes in the UVO-cleaner, the contact angle on flat, untreated PDMS samples decreased to around 80°, while after three hours of the same treatment, it decreased to about 60°. This change was stable only for a

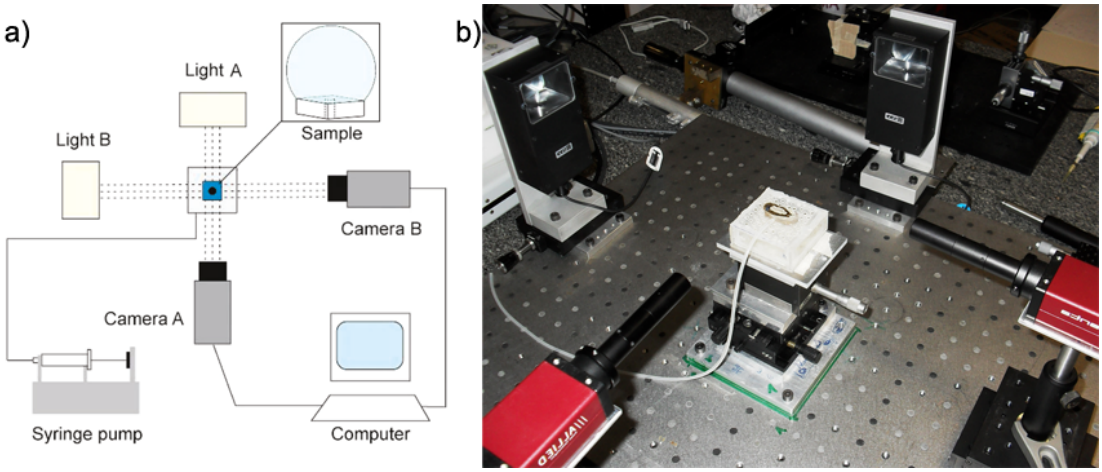

Figure 3.5: Schematic draw a) and picture b) of the optical setup used to observe the water drops.

couple of hours and then, the surface recovered its initial wetting character on a time scale of several days. The data on the treated surfaces were taken right after the extraction from the UVO and very quickly (within two hours) to bypass this recovery. Anyway, to be sure that the surface recovery was negligible, contact angle measurements on flat portions of the sample were taken before and after each acquisition sequence.

3.3 Experimental apparatus

Water drop profiles were recorded with the homemade apparatus shown in Figure 3.5. The sample was positioned in the middle and its vertical position could be finely adjusted with a manual translational stage. A small drop of increasing volume V of distilled water was produced on the top face of each pillar with a syringe pump, provided by Harvard Apparatus (PHD 22/2000-Infuse/Withdraw). The drop was illuminated by two back-light collimated led sources, Light A and B in Figure 3.5a. The drop profile was simultaneously viewed from two different orientations with telecentric lenses which guarantee a good contrast and a faithful reproduction of the drop shape, mounted on two high-resolution cameras (MANTA G-146B). In this study, they were oriented at right angles to probe the symmetry of the drop with the circular posts and at 45° with the square posts. In this way it was possible to view the drop from one side and from one corner of the square. In order to get statistically sound results, we typically recorded at

least five complete runs for each pillar, starting from the formation of a tiny drop at the center and increasing the volume till the final collapse of the enlarged drop due to gravity. After each sequence, the surface was dried by means of absorbing paper and subsequently, by blowing pure nitrogen. Typically images acquired during the measures are shown in Figure 3.6. The profile of each image was then analyzed off-line, using a program written by LabVIEW. For each volume, the contact angle was deduced from a fit of the profile. The profiles have been derived from differences in the grayscale values along the horizontal direction and the contact angles have been calculated from the slope of the fit in correspondence of the contact line, as shown in Figure 3.7. The corresponding error was estimated to be typically $\pm 3°$, unless otherwise stated.

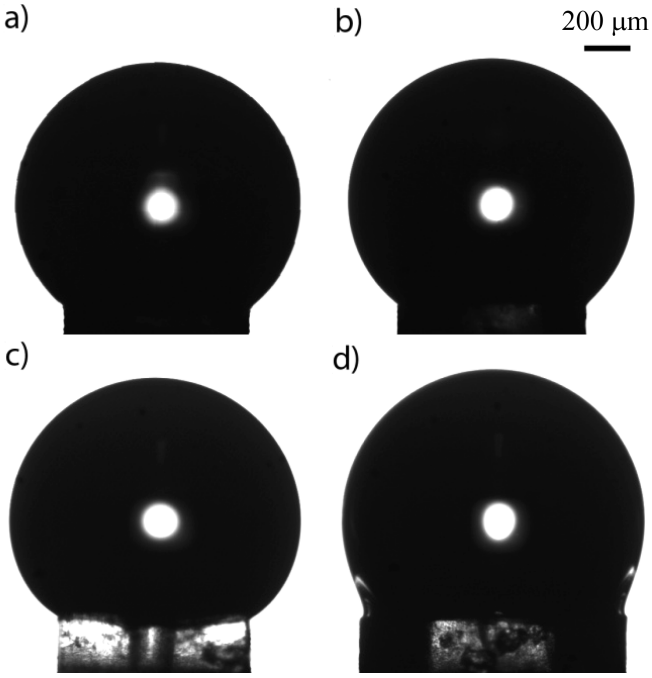

Figure 3.6: Typical images of water drops on a circular a), b) and on a square c), d) pillars taken from two different directions. Images a) and b) are taken along two orthogonal directions ($\theta = 64°$), while images c) and d) represent side and diagonal views respectively ($\theta = 68°$).

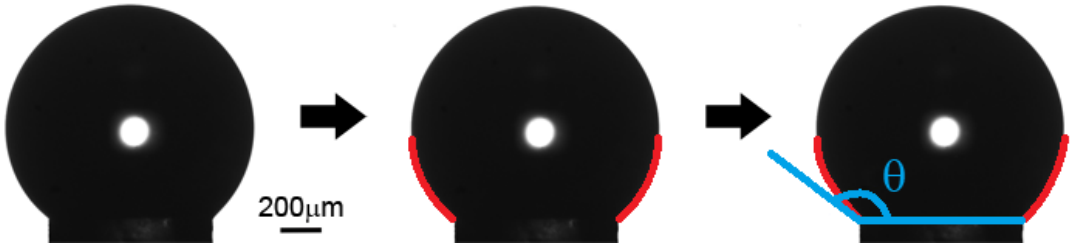

Figure 3.7: Schematic sequence of fitting procedure. First the drop profile is found from the contrast between droplet (dark) and background (bright) and then, the contact angle is calculated between the drop baseline and the fit slope.

3.4 Simulation details

Thanks to the collaboration with the Max Plank Institute "Dynamics of Complex Fluids" in Gottingen, it was possible compare the experimental profiles with the droplet shapes calculated using the public domain software Surface Evolver, developed by Ken Brakke [128]. This software allows to determine the equilibrium shape of the interface by minimizing the total interfacial energy. In this program the liquid-vapor interface is represented by a mesh of small triangles. For the purpose of these calculations we account only for liquid configurations which exhibit the same symmetry as the underlying post geometry, i.e. horizontal translation of the center of mass of the liquid are completely suppressed. The essential feature in the numerical calculation is that the contact line is always free to move on a surface until it reaches a pinning edge and then the Gibbs equation is applied. As long as the local contact angle on the pillar (θ_p) is less than the maximum angle (θ_{max}) derived from the Gibbs condition, the corresponding portion of the contact line is pinned to the edge (see Figure 3.1a). When the liquid volume is increased, θ_p increases until it reaches a value θ_{max}. After a further addition of liquid, $\theta_p > \theta_{max}$, the contact becomes free to move along the adjacent surface and eventually finds a new equilibrium position or keeps on moving, indicating a collapse of the drop along the vertical direction. In the latter case, the corresponding volume will represent the maximum liquid volume V_{max} which can be sustained by the post. We studied both the case of zero and non-zero gravity.

θ (°)	θ_{max} Experiment (°)	θ_{max} Gibbs criteria (°)
64±4	148±3	154
80±4	167±3	170
110±2	175±4	200

Table 3.1: θ is the contact angles of the post, θ_{max} Experiment, the maximum contact angles measure on the circular pillar and θ_{max} Gibbs criteria, the maximum contact angles calculated with Equation 1.16.

3.5 Data elaboration

First we analyzed the most symmetrical case of a drop deposited on a cylindrical post having a circular cross-section to compare our results with the Gibbs criteria. Then, we focused our attention on the original case of drop placed on square pillar.

3.5.1 Results with circular pillar

The symmetrical circular geometry was originally studied by Mason and coworkers in their classic work devoted to the stability of axis symmetric sessile drops of various liquids [121] and more recently by Extrand [122]. In these papers are describes that, when $\theta > 90°$, the maximum angle predicted by the Gibbs condition at a right edge ($\phi = 90°$) is $\theta_{max} > 180°$. In the absence of gravity, the contact angle on the post θ_p tends to the limiting value 180° at finite volumes V, while for macroscopic systems angles above 180° can be obtained because of the distortion induced by gravity. Actually, $\theta_{max} > 180°$ have been found even though they have been not measured directly [122]. When $\theta < 90°$, θ_{max} is expected to be less than 180° at a right edge. If the V exceeds the maximal volume corresponding to θ_{max}, the contact line suddenly jumps and spreads spontaneously down the vertical wall. Our results are consistent with such a phenomenology. Regardless of the surface wettability, the drops have a symmetric shape with the contact line pinned to the circular edge.

Figure 3.8 summarizes the contact angle measurements on a cylindrical post having a diameter D = 800 µm. It shows the contact angle on the post θ_p as a function of the drop volume divided by D^3 for three different wetting surfaces. The measured dependence of the contact angle on drop volume nicely follows the curves derived from the Surface Evolver taking gravity into account, see continuous lines.

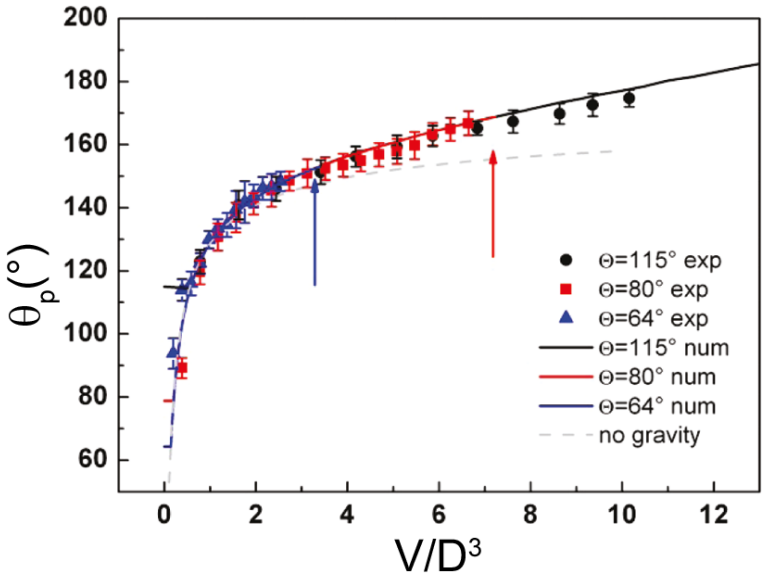

Figure 3.8: (color online) Contact angle as a function of the normalized volume of water drops on circular pillars having different surface wettabilities and a diameter D = 800 μm. Symbols refer to experiments, continuous line to numerical simulations, and dashed line to theoretical calculation for an hemispherical drop.

For each curve, the final point corresponds to the maximum volume of a stable sessile drop: at higher volumes the drops collapse. The corresponding contact angle values θ_{max} found experimentally are summarized in Table 3.1. Hydrophilic

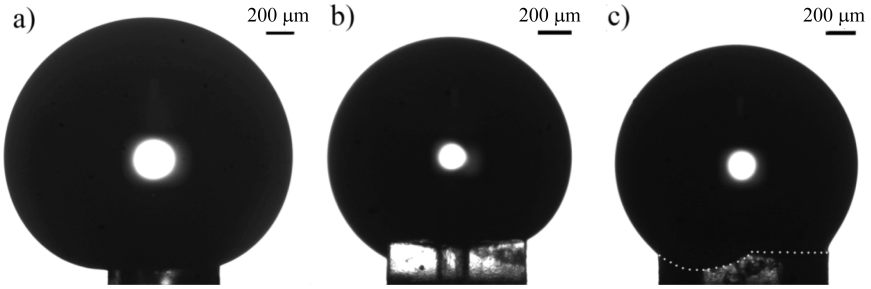

Figure 3.9: Images of asymmetric water drops on a circular pillar with $\theta = 115°$ a) and side view b) and diagonal view c) of a square pillar with $\theta = 68°$.

pillars ($\theta = 64°$ and $\theta = 80°$) are quite consistent with the Gibbs prediction, while on untreated post ($\theta = 110°$) we found $175° \pm 4°$, although the simulation yields a monotonic increasing θ with the normalized drop volume well above 180°. We believe that one reason for the observed difference is the difficulty of producing large symmetric drops. As already stated, lateral shifts in the center of mass of the drop have not been considered in the calculations. Actually, the quoted value

for θ_{max} corresponds to the largest volume which presents a symmetric profile. For larger drops, contact angles above 180° were observed only on one side of the post, as shown in Figure 3.9a. In the case of symmetric drops, it was impossible to directly measure contact angles above 180° because the depth of field of our objectives was much larger than the drop size.
As a useful comparison, in Figure 3.8 we have also plotted (see dashed line) the volume of a hemispherical drop having a circular contact line of diameter D and forming a contact angle θ_p as derived from the following geometric formula, valid in the absence of gravity [121]:

$$\frac{V}{D^3} = \frac{\pi}{24}\frac{(1-\cos\theta_p)^2}{\sin^3\theta_p}(2+\cos\theta_p), \tag{3.1}$$

where V,D,θ_p have been already defined. As expected, at small volumes the data agree with this estimate, while for $V/D^3 \geq 1.2$ Equation 3.1 underestimates the actual contact angles. In other words, gravity acts to flatten the central portion of the drop and increases the pinned contact angle.

3.5.2 Results with square pillar

Let me now consider the novel case of a geometric post with a square cross-section. Figure 3.10a shows the numerical and experimental profiles of drops of different volumes as viewed along the side (panel a, left) and the diagonal (panel a, right) of a hydrophilic post with a side L = 800 μm. The full symbols represent the experimental profiles for different volumes, while the continuous lines indicate the corresponding calculated profiles. The smallest drop displays the profile of a spherical cap with an angle θ indicating that the contact line has not reached the sides of the pillar and it is still circular. As V is increased, the liquid front reaches the side edges and pins. However, the regions close to the corners are still dry. On further increasing V, the liquid remains pinned to the lateral edges and the lateral contact angle increases. When this angle passes the Gibbs maximum angle, the contact line depins from the edge and slightly moves downward the vertical walls. When the contact line reaches the corners, the constrains of the boundary conditions are modified and the contact line is then allowed to move downwards along the corner edge. When this movement occurs, it is interpreted as the equivalent instability which takes place on the circular post leading to the

collapse of the droplet. Loosely speaking, we can say that the drop is suspended by the whole edge contour on the circular pillar and only by the four corners on the square pillar. A more detailed description of the shape evolution near the edges, as derived from the numerical calculations, as displayed in Figure 3.10b. The continuous lines represent the evolution of the lateral profile of a drop pinned to the edge. The dashed curves indicate the corresponding profiles as viewed along the diagonal. They show a non monotonic variation of the profile curvature near the solid surface. More interesting, the behavior observed in the side view clearly displays a pronounced spilling of the drop down the vertical wall.

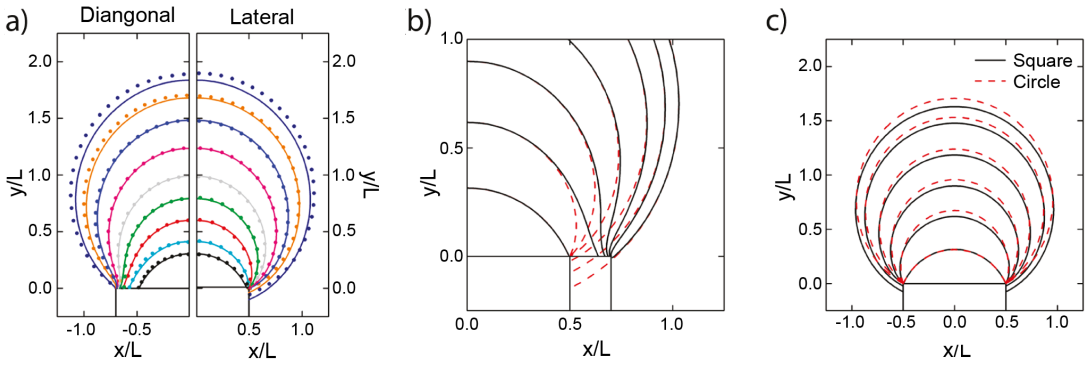

Figure 3.10: Profiles of drops of different volumes deposited on a pillar having a square section of side $L = 800$ μm and a contact angle $\theta = 68°$. a) Experimental (dotted lines) and numerical (continuous lines) profiles along the diagonal and lateral views. b) Evolution of the numerical profiles near a corner displayed along the side (red dashed lines) and diagonal (black continuous lines) views. c) Lateral view of whole numerical profiles of drops deposited on square and circular pillars having the same characteristic size (L or D).

The profiles shown in the graphs of Figure 3.10a indicate a very good agreement between the experimental and numerical data up to the intermediate volumes (blue data, $V/L^3 = 2.6$). For larger values (orange data, $V/L^3 = 3.5$), deviations from a symmetric shape start to be clearly observable in the experimental profiles. However, the main difference is the amount of spilling found: in the simulation the contact line moves downward the lateral wall much more than in the experiment. We think that this is due to two different factors. First of all, the fact that no symmetry breakings and other instability mechanisms related to in-plane shifts of the center of mass are considered in the calculations. As already stated, experimentally it is very difficult to produce a symmetric large drop. The

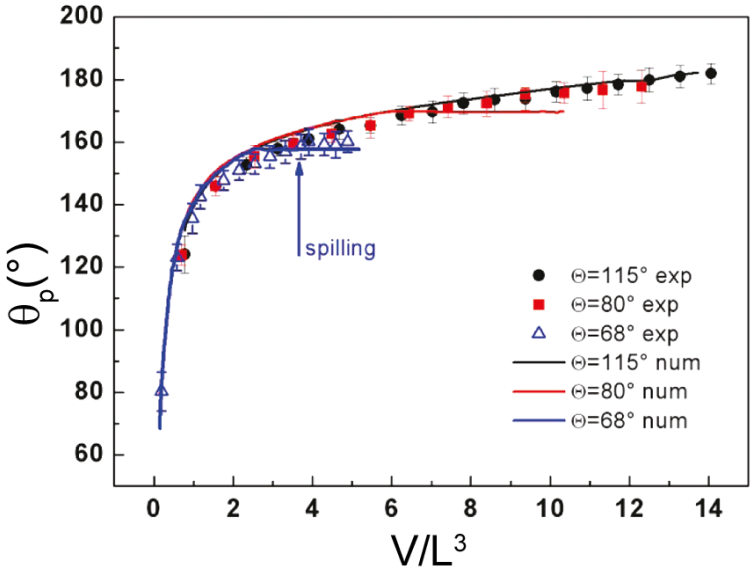

Figure 3.11: Lateral contact angle as a function of the normalized volume of water drops on a square pillar having different surface wettabilities and a side L = 800 μm. Symbols refer to experiments and continuous lines to numerical simulations.

profile shown in Figure 3.10a corresponds to one of the most symmetric drop we produced, the more common outcome being the asymmetric profile displayed in Figure 3.9b and 3.9c, characterized by significant spilling but only on one side. Secondly, vertical walls of the real posts are not smooth but present some roughness which favors the pinning of the contact line [126].

Although the spilling of the drop along the vertical walls is arguably the most evident difference between a drop sustained by a square post and a circular one, Figure 3.10c shows that it is also possible to distinguish the pinning behavior of the two posts by just looking at the lateral views of the drop profiles. In general, the flattening of a drop is caused by gravity and on a square post the drop is more flattened than on a circular one.

Another way to account for the pinning behavior is to use the contact angle. Figure 3.11 shows the contact angle θ_p measured laterally on a square post as a function of the drop volume divided by L^3 for three different wetting surfaces. Again, the continuous lines represent the results of the numerical simulations. At variance with the circular post, once θ_p reaches the critical value θ_{max} the drop does not fall down but it spills over the edge and the contact line gets pinned somewhere along the vertical sides as previously discussed. The drop remains suspended and further increases in volumes can be accommodated at the same

critical angle by simply moving the contact line downward. This explains the horizontal segment seen in the numerical curves. Eventually, the drop will fall down when the spilling region extends itself and touches the corners. The experimental points nicely agree for $\theta_p < \theta_{max}$. In the case of the more hydrophilic surface, e.g. $\theta = 68°$, the spilling occurs at a slightly larger normalized volume than that found in the simulations, as indicated by the vertical arrow. Afterwards, the lateral contact angle does not change until the drop collapse. Again, we think that the difference is probably caused by extrinsic pinning of the contact line due to morphological defects on the post vertical walls [126]. Instead, for more hydrophobic surfaces we do not see any evidence of spilling. In this case, the reason is the difficulty in producing large symmetric drops.

3.6 Conclusion

In this Chapter is described how we have studied the suspension of water drops on cylindrical pillars with circular and square cross sections and different wettabilities. The observed shapes are the result of the geometric pinning of the contact line to the pillar edge and can be accurately described in terms of the Gibbs condition. In the case of a circular profile, the contact line is pinned to the whole edge, while in the presence of corners, the contact line can spill along the vertical walls. Moreover, because of the pinning, an individual pillar can sustain much larger drops than a flat surface having the same surface area and wettability. To better understand pillar shape capability of sustaining larger drops, we evaluated that if V_{max} on the square pillar is normalized to D^3, where D is the diameter of a circle inscribed in square cross-section, this pillar is able to sustain larger drops with respect to a circular pillar of diameter D. Instead, if the volumes are normalized to $A^{3/2}$, where A is the upper surface of the pillars, the geometries more capable to sustain larger drops with the same A is the circular. Preliminary numerical results obtained with Surface Evolver, leave us to formulate the following conjecture, which generalizes this trend to regular polygons of N sides circumscribed to the same circle. On the basis of their $V_{max}/A^{3/2}$, the different pillar cross sections can be ranked according to the sequence: circle, ..., (N+1)-polygon, N-polygon, (N-1)-polygon, ..., square, triangle. Therefore fixed A and θ, the circular pillars are more capable of sustaining liquid drops.

Chapter 4

Morphological transitions of droplets wetting rectangular domains

In this Chapter is reported the results of comprehensive experiments and numerical calculations of interfacial morphologies of water confined to the hydrophilic top face of rectangular posts having different aspect ratios ℓ. A continuous evolution of the interfacial shape from a homogeneous liquid filament to a bulged filament and back is observed during changes in the liquid volume: above a certain threshold length of ℓ , the transition between the two morphologies is discontinuous and a bistability of interfacial shapes is observed. Additionally, we investigated the dynamic proprieties of this transition.

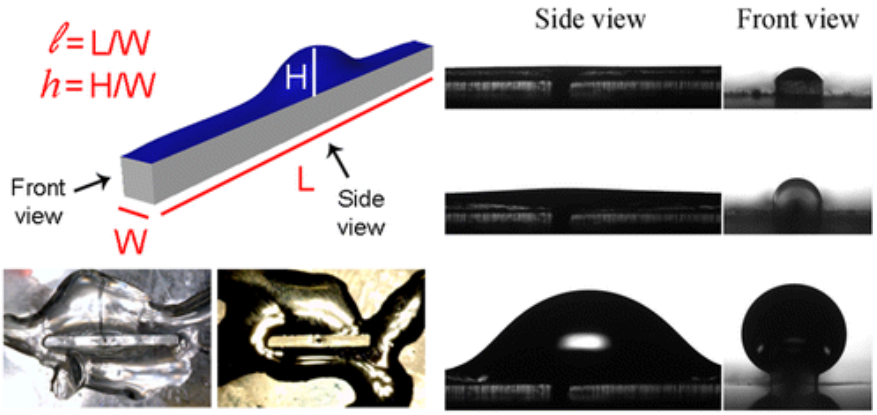

4.1 Introduction

As described in Chapter 1 instabilities of liquid filaments can be the origin of morphological transition. Gau et al. [19] observed experimentally a transition between a liquid filament with a homogeneous cylindrical cross section and a flat filament with a single bulge located in the center of the rectangular domains. In particular they did the experiment condensing water on hydrophilic stripes, without controlling and measuring the liquid volume adsorbed on the stripes . For this reason the results were mostly qualitative. Also, the influence of the length to width ratio of the stripes onto the character of the transition was not considered. In contrast, to the discontinuous morphological transition found on hydrophilic stripes of finite length [19], no abrupt changes in the equilibrium shape were observed for liquid droplets wetting the top of a square post as the liquid volume V was increased, as described in Chapter 3 [129]. This fact led us to conjecture the existence of a bifurcation point in terms of length to width ratio $\ell \equiv L/W$ of rectangular posts having length L and width W, which separates a regime of continuous transitions on 'short' posts with $\ell < \ell^*$ from a regime of discontinuous transitions on 'long' posts $\ell > \ell^*$. To verify this conjecture and to quantify the values of ℓ^*, we have performed systematic microfluidic experiments and numerical minimizations of the interfacial energy [130].
In detail, this Chapter can be divided in three parts: first, it is described the microfabrication procedure to obtain rectangular posts having hydrophobic walls and hydrophilic top surface. Then, experimental and numerical results are compared and finally, a preliminary work regarding the dynamic of the transition between the two states is presented.

4.2 Microfabrication of posts with hydrophobic and hydrophilic surfaces

A series of individual posts having rectangular cross-sections of different ratios ℓ have been fabricated by using a combination of photo and soft-lithographic techniques. Moreover, they showed hydrophobic vertical walls, hydrophilic top faces and a hole with diameter 150 μm in the center, as illustrated in Figure 4.2a. In this way the water film would be confined on the top face of the post by the

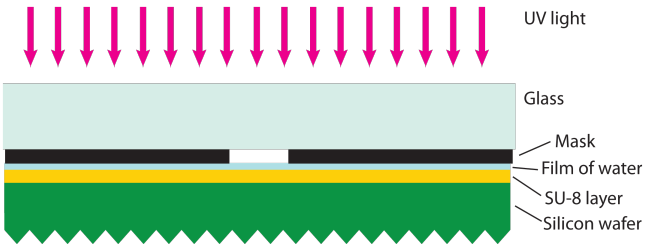

Figure 4.1: Scheme of the sample during the UV- exposure. Drop of water of few µL is deposited between the SU-8 film and the mask. The mask is attached to a glass slide to guarantee the flatness of the celluloid film.

wettability and on the edge by the pinning of the contact line. Therefore, as in the Chapter 3 at first we prepared some masters with different ℓ, then we replicated them by Double replica molding and finally we covered only the top surface with gold to give a hydrophilic character. Being made by silicon in the most part, before proceeding with the first PDMS replica, the master surfaces have to be functionalized with a monolayer of trichloroperfluorooctylsilane (FOTS) as described in Chapter 3, to facilitate the replica peeling.

4.2.1 Master production

At variance with the fabrication of Chapter 3, masters were produced by photolithography, using SU-8. Therefore, at first we prepared some different masks and then we realized the structures, as described in Chapter 2. In details, masks were printed on celluloid films by an appropriate printer with a resolution of 3600 dpi. Because of rectangular shapes, we did not find any particular problems about the resolution of the masks, and the final roughness of the edge of our structures has been estimated about 1 µm.
Regarding the details of the photolithography procedure, we used the SU-8 2050 spun on a silicon wafer specifically cleaned with water, acetone, isopropanol and by 30 minutes in UVO cleaner. To obtain thickness of 100-150 µm the film of SU-8 was spin-coated with a velocity of 1200 rpm (revolutions per minute) by the spincoater SCS P 6708/6712. After that, we left the samples stand for 2 hours to obtain a more uniform film spread on large area. Next, as described in the data sheet [78], after the pre-bake, we prepared the film for the UV-exposure. In details, the celluloid mask was fixed on a glass support and was laid down on the polymer film, putting a small drop of water between the two part to match

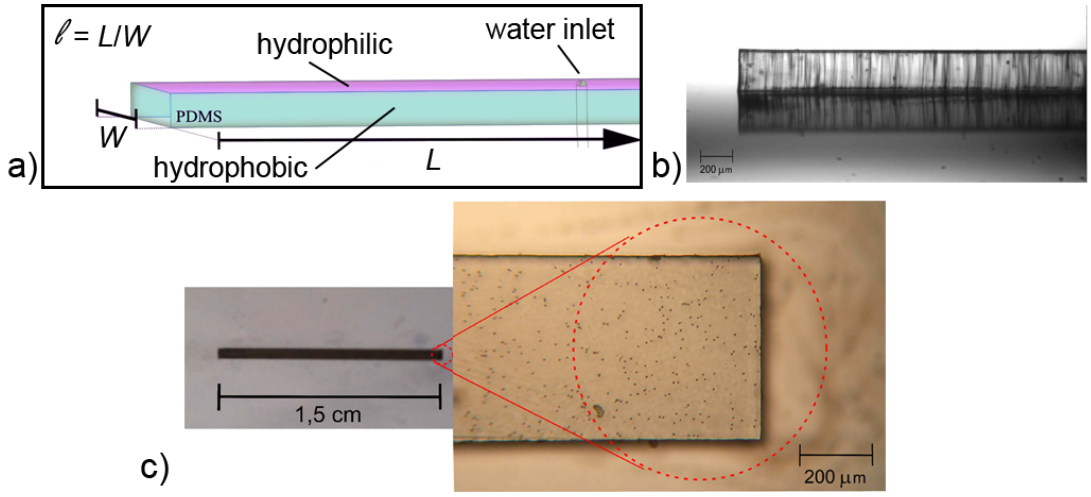

Figure 4.2: a) Scheme of the final rectangular post having hydrophobic walls and hydrophilic top surface. Pictures of the sample from b) side and c) top views.

the refraction index, as shown in Figure 4.1. In this way the Fresnel diffraction problems are significantly reduced [131]. The UV source is a mercury lamp with a power of 350 W. Before to arrive on the sample, the radiations is collimated and filtered to guarantee a beam with a diameter of 10 cm and a wavelength of 365 nm. As described in Chapter 2 the exposure time has to be tuned on the basis of different parameters and we evaluated experimentally that 40 seconds was a proper time to obtain structures with good quality. Then, we passed to the post-exposure bake and finally, to the development. With this procedure, we produced several posts made with SU-8 in relief on silicon substrate with a height of 150 µm, width W=500 µm, and ℓ= 5, 10, 15, 20, 25, and 30, as shown in Figure 4.2. A width of 500 µm was chosen because it is sufficiently small to neglect gravity safely and, at the same time, it allows the central hole to be made easily.

4.2.2 Soft-lithography

Positive copies of the SU8 masters in PDMS were then produced by a double replica molding process, in the same manner described in Chapter 3. However, they resulted hydrophobic with a contact angle of θ=110°, therefore it was not possible to spread the water on them. To modify their top face wettability exclusively, a thin gold layer with a thickness of about 200 nm was deposited by magnetron sputtering [132]. To protect the vertical walls during metal deposition,

Figure 4.3: Pictures of the post with ℓ=15 with the NOA 61 deposited on the border, a) before and b) after the gold sputtering. c) After removing the NOA the PDMS wall is still hydrophobic.

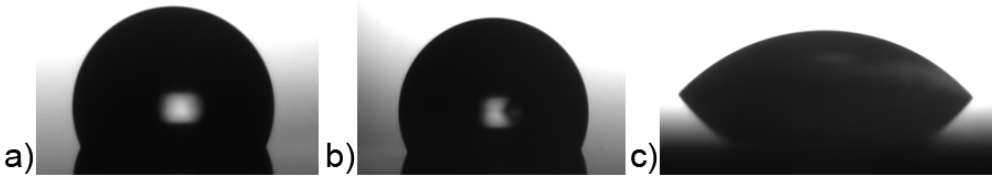

Figure 4.4: Contact angle measures of a flat PDMS surface before and after the UVO-cleaner exposure. a) native and b) protected PDMS shows a contact angle about 110°, while c) the non protect surface about 60°.

they were covered with a UV-curable optical adhesive, NOA 61 [133]. Particular care was taken so that NOA 61 touched only the vertical walls up to the edge (see Figure 4.3). Right before each measurement, the gold surface was activated in the UVO-cleaner and then the cured NOA 61 coating was peeled off. As result, the material contact angle on the top face was reduced to $\theta \approx 15°$ remaining stable for a couple of hours [134]. By the exposure of a flat surface of PDMS covered with a film of NOA of few millimeters, we checked that the cover part of the elastomeric polymer was not affected by the UVO cleaner and so the PDMS walls of the structures were still hydrophobic, as shown in Figure 4.4.

4.3 Experimental apparatus

The liquid profiles are recorded with the same apparatus described in Chapter 3, fixing the two cameras at 90°, to simultaneously observe the front and the side views of the rectangular posts [129]. The only difference concerned the way to increase and decrease the volume of water on the structures. The central hole of each post was connected at its extremity to a thin tube attached to a syringe pump (Harvard Apparatus, PHD2000) connected in series with a flow meter (by Fluigent). In this way, it was possible to accurately control the production of

a liquid layer on top of the post with a known volume. To achieve statistically robust results, we typically recorded 10 complete runs for each post. Starting from the spreading of a very thin liquid layer on the top face, we injected water until a maximum volume of $2 \div 3$ µL was reached and after that, we suck-up it with the same syringe pump. Every image was then analyzed off-line, by a home made program written in IDL (Interactive Data Language version 7), which can find the profile of the liquid layer from the difference of contrast between the drop (dark) and the background (light) and consequently, it evaluates the resulting maximal high of the water layer for every image. In effect, comparing this last parameter, we distinguished the water layer from filament and bulge state. Moreover, from the synchronization of the image sequence with the data saved from the flow-meter, it was possible to know the exact volume of water for every image with an error of about 50 nl.

4.4 Simulation details

Similarly to the work described in Chapter 3, the experimental results were compared with numerical simulations realized in collaboration with the group in the Max Plank "Dynamics of Complex Fluids" in Gottingen. The shapes of the droplets were calculated using Surface Evolver [128], fixing the contact line to the boundary of rectangular shape. In detail, for convenience, we employed the Bond number $Bo \equiv \rho\, g\, W^2/\gamma$ related to the width of the post to quantify the magnitude and sign of buoyancy forces. Here, ρ and γ denote the mass density and interfacial tension, respectively, of water and g the acceleration of gravity. As we were working with posts of width $W = 500\,\mu$m and water ($\rho = 1.0\ 10^3\,\mathrm{kg/m^3}$, $\gamma = 7.2\ 10^{-2}\,\mathrm{N/m}$), in this Chapter the Bond number is fixed, if not stated otherwise, to $\mathrm{Bo} = 0.0341$ in our numerical calculations.
To compare the experimental results with the simulations, we chose to normalize all the quantities to nondimensional values. In particular, the high of the water layer H was divided by the width W of the post and the volume by W^3, obtaining the reduce high $h{=}H/W$ and the reduce volume $v{=}V/W^3$, respectively.

4.5 Data elaboration

With all the posts studied in our experiments we observed a morphological transition of the liquid between a homogeneous filament and a filament with a central bulge as the volume was changed. Photographs of the experimentally observed liquid morphologies, as well as the numerically computed shapes, are shown in Figure 4.5. The observed shape transition is in agreement with previous experimental studies for liquid condensing on long highly wettable stripes [19]. However, depending on the length to width ratio ℓ of the post, different scenarios could be observed as the volume was changed. Starting at small volumes, the liquid was distributed on the top face of the post forming a flat layer, (Figure 4.5a). Upon increasing the volume, the liquid interface formed a homogeneous filament which displayed a uniform cross section close to the segment of a circle, (Figure 4.5b). Noticeable deviations of this almost homogeneous profile occured only in the proximity of the ends of the post and decay on a length scale comparable to the post width. As the volume kept on rising, the contour of the liquid interface in side view started to form a central bulge, which grew with the liquid volume. This process is characterized by a pronounced increase of the reduced height [120, 129] (Figure 4.5 c,d).

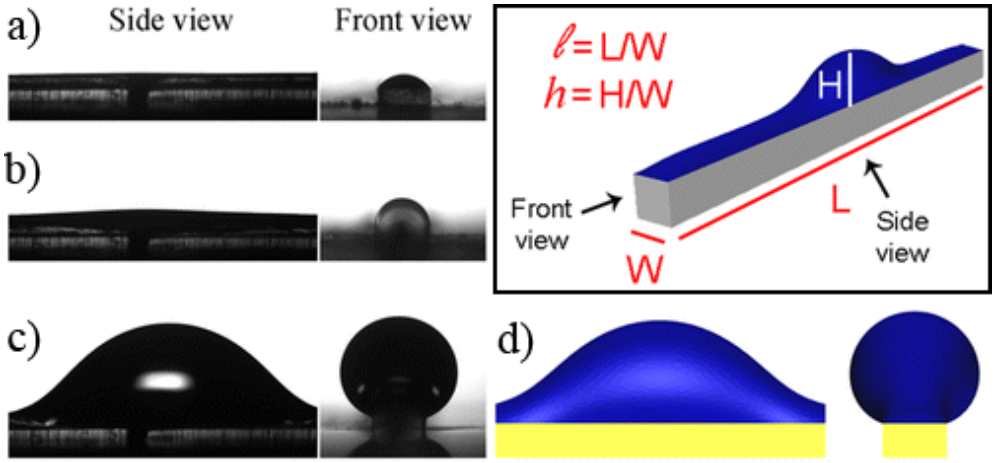

Figure 4.5: Bulged filament on a post of length L and width W. Panels a), b) and c): side and front views of the drop profile for different volumes on the post ℓ=30; panel d): numerical energy minimization of the drop. These volumes correspond to the large pink circles plotted in the graph of Figure 4.6.

The plot shown in Figure 4.6 displays the measured and the numerically calculated reduced height h for Bo = 0.0341 as a function of the reduced liquid volume

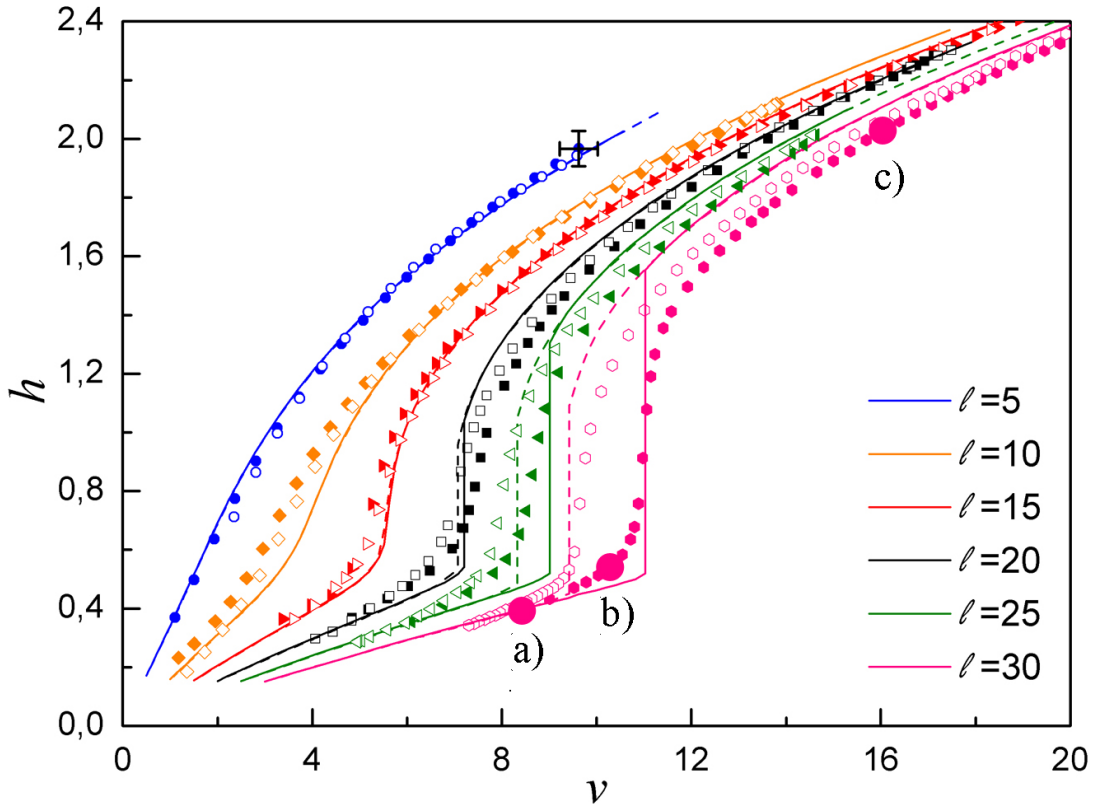

Figure 4.6: (color online) Reduced height $h = H/W$ of water layers deposited on rectangular posts of different ℓ as a function of the reduced liquid volume $v = V/W^3$. Full (empty) symbols represent the experimental data during liquid injection (extraction) in comparison to numerical minimizations during liquid injection (extraction) displayed as solid (dashed) lines. The volumes marked by bigger circles a),b),c) refer to the plates of Figure 4.5. The final point of ℓ=5 indicates the characteristic error bars of the experiment.

$v \equiv V/W^3$ for the six different posts employed in our experiments. For short posts ($\ell = 5,\ 10,\ 15$) all numerically obtained curves $h(v)$ plotted in Figure 4.6 display a smooth cross-over between the homogeneous and the bulged filament and it is not possible to make a clear distinction between both morphologies. Furthermore, the curves $h(v)$ for increasing and decreasing v are identical. Instead, for long posts,namely $\ell = 20,\ 25,\ 30$, $h(v)$ presents a discontinuous jump up ($v_\uparrow$) at increasing v and a jump down ($v_\downarrow$) at decreasing v. The opening of the hysteresis loop, i.e. the difference $\Delta v \equiv v_\uparrow - v_\downarrow > 0$, becomes larger as ℓ increases. Moreover, we found a quantitative agreement between experimental and simulation results of the reduced volumes related to the instabilities of the homogeneous filament and the bulged filament, as well as the width of the hysteresis loops.

4.5.1 Comparison between experimental and simulated data

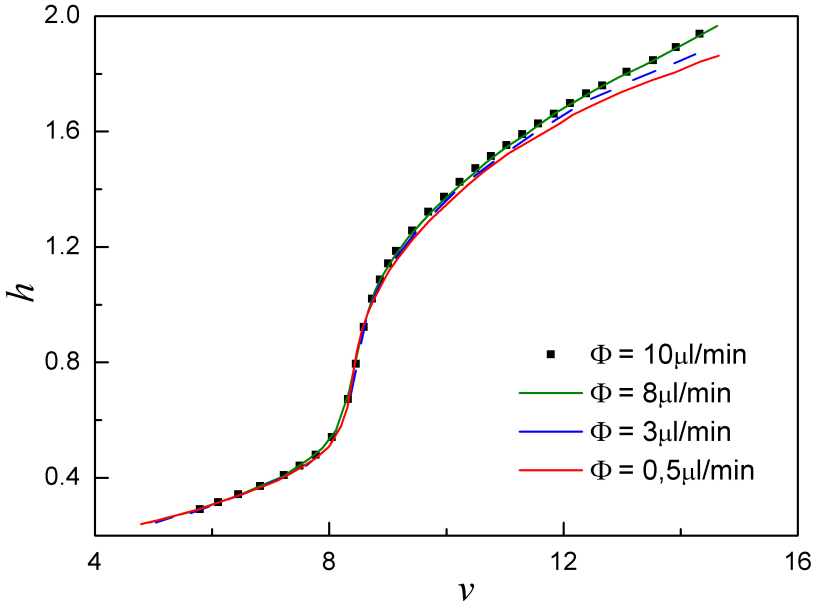

Figure 4.7: Maximum reduced height h of water films as a function of the dimensionless liquid volume v. The data refer to different flow rates and a rectangular post having ℓ=25.

The main difference between our experimental and numerical results is that the expected discontinuous transition are somewhat rounded in the experiments. There are several possible factors affecting the shape of the present experimental curves: liquid evaporation, spilling along the vertical walls [129] and surface defects which create deviations of the contact line position from the rectangular domain. Extensive and systematic tests have been carried out to evaluate their individual contribution. Figure 4.7 shows the maximum reduced height h of the liquid contour as a function of the reduced liquid volume v for a post having an aspect-ratio $\ell = 25$. The different curves refer to different flow rates Φ comprised between 0.5 and 10 μL/min, which represent the limits of our set-up. The curves show an increase in the final h as Φ increased. This difference is very likely due to evaporation, since the measurement at small flow rates requires more time. For this geometry, the acquisition time for a complete run are about 0.5 (10) minutes for the highest (lowest) Φ. Interestingly, the data corresponding to flow rates of 8 and 10 μL/min are practically coincident suggesting that, above Φ_{min}=8 μL/min, the evaporation effects become negligible. The exact value of Φ_{min} was found to depend on ℓ and was always less than 10 μL/min for all the posts used in this

study. To guarantee that the data plotted in 4.6 are not affected by evaporation, they were taken with $\Phi > \Phi_{min}$.

Figure 4.8 shows a sequence of frontal images taken on two posts having ℓ=25. The top images a)→d) refer to a post whose vertical walls have been exposed to UVO-cleaner, while the bottom ones e)→h) indicate a post whose vertical walls have been protected during the activation of the gold surface. Their behavior was dramatically different. In the former case, the liquid film collapsed as soon as the bulge state had been reached. Conversely, the other post can sustain a much larger liquid volume and there is clear evidence of overhangs detaching from the post edge. Again, the film profiles analyzed in 4.6 displayed frontal images that indicate pinning of the contact line to the post edges.

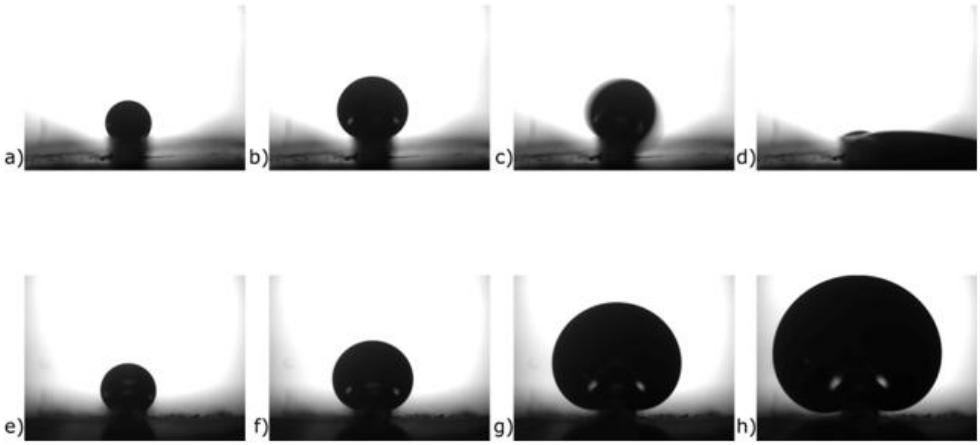

Figure 4.8: Frontal images taken at different volumes on posts having ℓ=25. Images a)→d) refer to a post whose vertical walls have been exposed to UV light. Images e)→h) refer to a post whose vertical walls have been protected from the action of UV light.

Finally, the top surface might present some morphological and/or chemical defects mainly due to a not uniform gold deposition. Results taken with posts of the same aspect ratios but having gold layers of quite different quality indicate that the more uniform surfaces presented more vertical transition. Figure 4.9 shows two runs of measures performed with two different sample having the same $\ell = 25$. Sample 1 (black square dots) showed a non-homogenous layer of gold, while Sample 2 (red circle dots) was characterized by gold deposition of good quality; the percentage of the surface area covered by gold were about 87% and 99%, respectively. Although the data in Figure 4.6 refer to the best gold films that we have obtained, we cannot exclude that the unavoidable presence

of inhomogeneities be responsible of the observed rounding. Actually, a similar argument was originally proposed to explain the observed rounding of the prewetting transition of quantum liquids on alkali metals [135, 136].

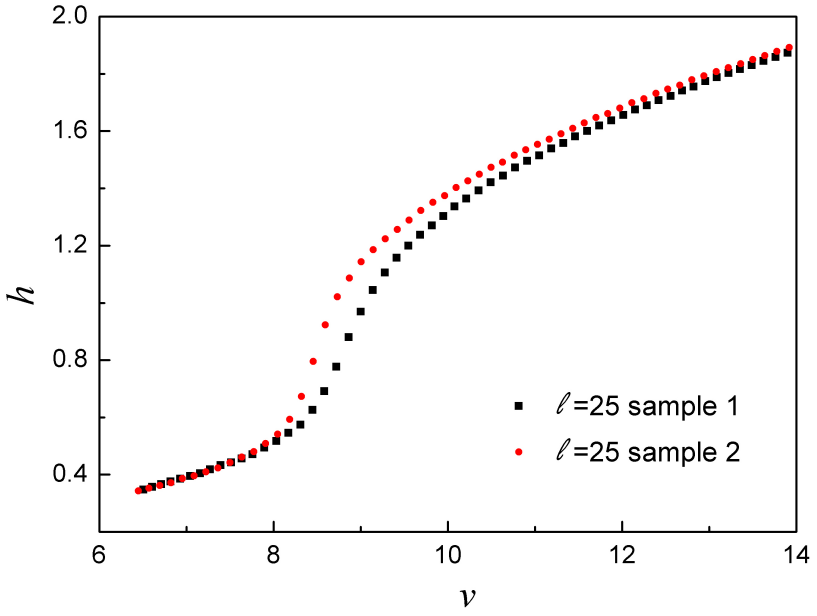

Figure 4.9: Maximum reduced height h of water films as a function of the dimensionless liquid volume v. The data refer to different samples having the same aspect ratio $\ell = 25$, with a not-homogenous (black square dots) and homogeneous (red circle dots) gold depositions.

4.5.2 Phase diagram

We point out that the experimental data, the numerical energy minimizations and the model calculations can be conveniently expressed in the form of a morphology diagram in terms of ℓ and v. The morphology diagram in Figure 4.10a displays regions where homogeneous and bulged filaments morphologies are mechanically stable. Inspection of the numerically determined stability boundaries in Figure 4.10 reveals a cusp-like bifurcation point at $\ell^* \simeq 16.0$ and $v^* \simeq 5.5$ and a tongue-shaped region of bistability for $\ell > \ell^*$. The energy minimizations for the morphology diagram in Figure 4.10a were carried out for $\mathrm{Bo} = 0$. A comparison to the case of $\mathrm{Bo} = 0.0341 \ll 1$ shows only minor differences with respect to the position of the bifurcation point and stability boundaries. Noticeable deviations are observed only for bulged filaments with large volumes. On short posts with $\ell < \ell^*$, no discontinuity in the evolution of interfacial shapes during changes in

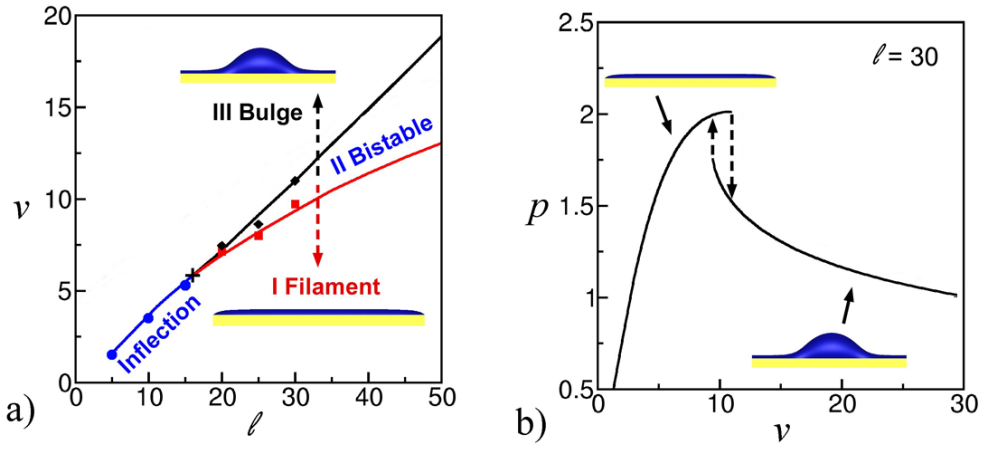

Figure 4.10: (color online) a) Morphology diagram in terms of the control parameter ℓ and v. Black and red lines indicate stability boundaries of homogeneous and bulged filaments, respectively, from numerical energy minimizations at Bo = 0 in comparison to experimental data points (symbols). The bifurcation point is indicated by (+), while the solid blue line (circles) represent the volume where the continuous $h(v)$ numerical (experimental) curves display an inflection point. b) Reduced Laplace pressure $p = P\,W/\gamma$ of the wetting liquid on the posts ℓ=30 as a function of v for Bo = 0 . Black lines indicate results of numerical energy minimizations. Solid (dashed) lines are mechanically stable (unstable) branches.

the volume is observed. For post with $\ell > \ell^*$, however, discontinuities in $h(v)$ appear and the range of reduced volumes can be divided into three regions. In region I corresponding to $v < v_\downarrow$, solely homogeneous filaments are mechanically stable, while in region III, with $v > v_\uparrow$, exclusively filaments with a central bulge are mechanically stable. In the intermediate region II, with $v_\downarrow \leq v \leq v_\uparrow$, a bistability between the two filament morphologies is observed.

Considering the reduced Laplace pressure $p \equiv P\,W/\gamma$ as a function of the reduced volume v from the numerical minimizations (see Figure 4.10b), it is possible to observe the presence of a discontinuity between the filament and the bulge state, which in turn increases with ℓ. As already pointed out by Gau et al. [19], the interfacial instability occurs for asymptotically long stripes $\ell \to \infty$ once the cross section of the homogeneous liquid filament reaches a semi-cylindrical shape with maximum Laplace pressure $p_{\max} = 2\,W/\gamma$. This is confirmed by our experiments where we indeed show that, on long posts, the local contact angle of the cross sectional contour of the homogeneous liquid filament never exceeds $\pi/2$.

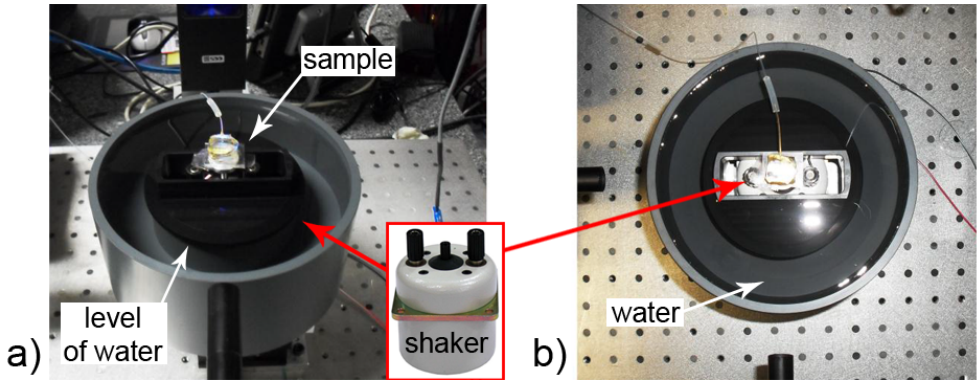

Figure 4.11: Pictures of side a) and top b) views of the sample holder. The shaker is contained inside of the PMMA box, which is filled of water in the bottom part.

4.6 Morphological transition induced by vibrations

In this study, to reduce dynamic effects, the volume was increased slowly, ensuring compatibility with evaporation effects. Both interfacial instabilities here described (filament and bulge states) are discontinuous on sufficiently long stripes and hence, the transition between them can be excite by capillary waves (see Chapter 1). These waves can also be exited externally, for example by forcing the sample to vertically oscillate at its resonance frequency. With the aim to observe the dynamic behavior of the transition, we made some preliminary measures, mounting the microstructures on a sample holder fixed on the shaker LDS V101, produced by Brüel & Kjær. This can oscillate in a vertical plane at frequency between 10 Hz and 10 kHz, giving a maximum force of 8.9 N and the maximum amplitude of oscillation about 2.5 mm. Figure 4.11 shows the sample holder from side an top views: the shaker is contained inside a PMMA (polymethilmetacrylate) box filled of water in the bottom part. During the measures the box is closed with a transparent cap to keep the humidity stable about 90% and so, to reduce the evaporation effect.

Experimentally, we pumped the water until it reached a volume between $v_{\downarrow} < v < v_{\uparrow}$, without reaching the bulge state. By applying vibration on the sample at the resonance frequency, we expected to see the morphological transition to the bulge state. However, it was not possible to calculate this quantity with the usual equation described by Rayleigh and Lamb [34], mainly because the shape of the water film and the bulge state could not be compared with a normal drop deposited on a flat surface. Therefore, we empirically scanned all the

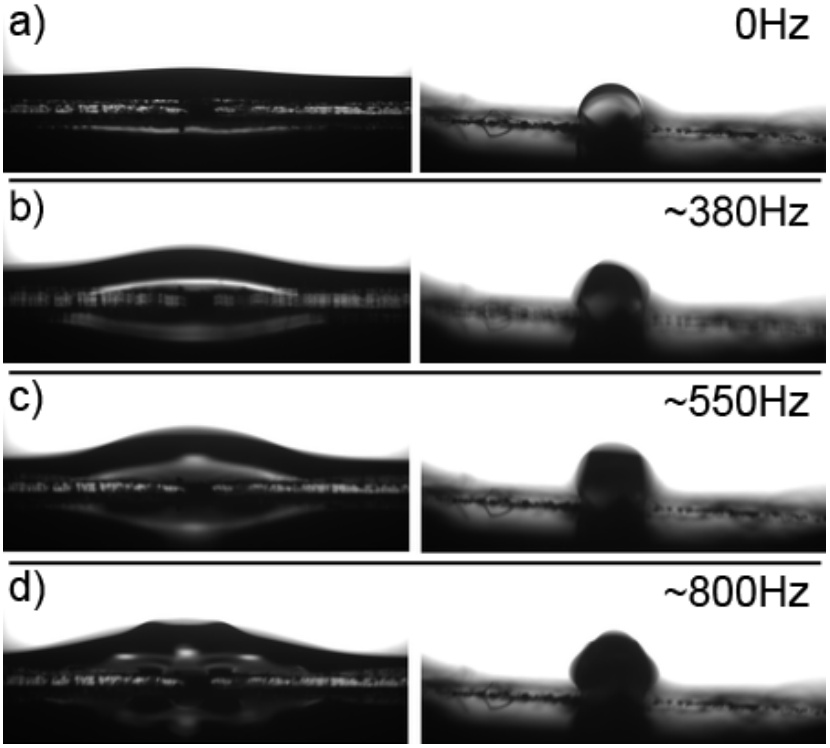

Figure 4.12: a) Droplet on a post with ℓ=25, in the channel state and with volume between $v_{\downarrow} < v < v_{\uparrow}$. Morphological transition to the bugle state induced by b) first , c) second and d) third harmonic resonance.

feasible frequency with the apparatus at fixed amplitude and vice-versa. For this preliminary study we used only microstructures with aspect ratio ℓ=10, 16, 25. In Figure 4.12 it is possible to observe an example of these observations. Since we did not dispose of a fast camera (frame rates greater than 1 kHz), we could only get qualitative results fom the images. In detail, we worked with a camera having a maximal frame rate of 17 fps.

4.6.1 Experimental results of the transition induced by vibration

In the study of the dynamical effect of the morphological transition, several parameters play an important role: basically the volume of the water film, aspect ratio ℓ, oscillation frequency and amplitude and probably the defects on the surfaces. For all of these factors, the resonance frequency has been found inside of a large interval with respect to the precision of the experimental apparatus (less than 1 Hz). In particular, for the sample with aspect ratio 16 and 25 we observed

I)	360÷450 Hz
II)	550÷600 Hz
III)	750÷900 Hz

Table 4.1: First (I), second (II) and third (III) order of resonance frequency of water on posts having ℓ=16, 25.

the transition at the same frequency. Also the first, second and third orders of resonance of the bulge state was observed at same frequencies, as shown in Table 4.1. While for ℓ=10 we have never observed the transition from filament to bulge state. These findings led us to consider that the transition induced by the vibration could be excited only for post larger than the bifurcation point. Indeed, in that case it is possible to observe the bistability of the two states at the same volume, as already described in Figure 4.10a.

Moreover, fixing the frequency at the resonance and changing the vibration amplitude, it was possible to notice a threshold under that the transition did not take place. Furthermore, increasing and decreasing the amplitude we discovered the presence of a hysteresis: the threshold from the filament to the bulge state was between 40÷60 μm, while to go back to the initial state it was necessary to arrive until 10÷30 μm, as shown in Figure 4.13.

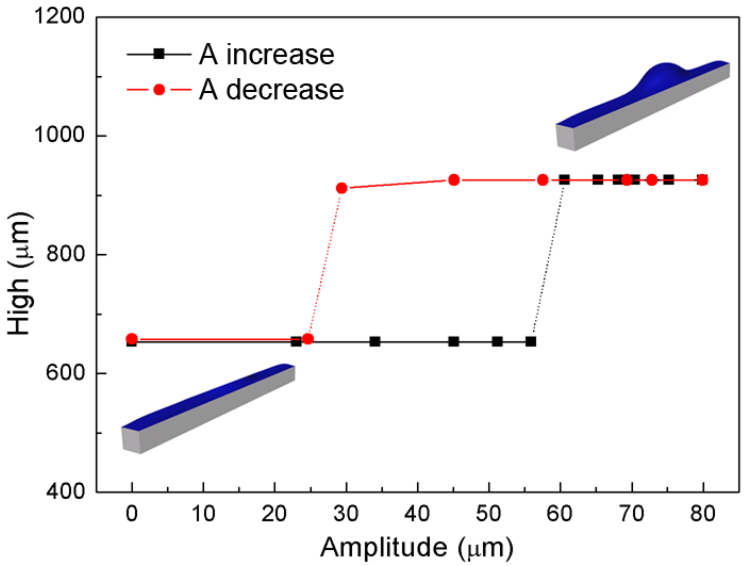

Figure 4.13: Preliminary measures of the maximal high H of the water film versus the oscillation amplitude A, using a post with ℓ=25. There is a hysteresis loop: increasing the amplitude the bulge is formed at about 55 μm, while decreasing the amplitude, the bulge state is stable until an amplitude of about 27 μm.

4.7 Conclusion

In this Chapter, we described the morphological transition of a film of water confined on rectangular surface. At first we realized samples having different aspect ratios by photo and soft lithography and then, we changed the wettability by applying a gold layer on their top surface protecting the lateral walls with NOA61. Moreover, like described in Chapter 3, the introduction of a microchannel with hole in the center of the post, allowed us to increase and decrease the water volume without perturbing the shape of the drop. Furthermore, the combination of the syringe pump with flow meter and the synchronization with the camera acquisitions increased the precision of the measures, comparing to the previous approaches of these types of studies [19, 137]. We observed that the transition between filament and bulge state occurs for all the aspect ratio that we investigated, but only for ℓ>16, there is the bistability of the two states for the same volume. Moreover, the hysteresis is more evident in structures with larger aspect ratio. The experimental results are in good agreement with the numerical simulations and the small disparities were justified with the presence of defects on the surfaces.

Furthermore, for the presence of hysteresis loop in the transitions, we made a preliminary study to understand the influence of the vibrations. We found that, fixing the volume between $v_{\downarrow}$ and $v_{\uparrow}$, it is possible to excite the system at the resonance frequency passing from the filament to the bulge state. Also, fixing the frequency and changing the amplitude of the vibrations, we discovered that in this case a hysteresis loop appears. In future, more detailed studies will be developed to better quantify these effects.

Chapter 5

Sliding droplets

This Chapter describes a work with the aim to study the different droplet motions on inclined patterned and homogeneous surfaces, having the same apparent contact angle. We observed that the pattern induces a stick-slip motion at the droplet, that results continuously deformed during the sliding. This behavior induces a friction between the droplet and the substrate, which causes a dissipation of energy at the contact line. Therefore, droplets slide faster on homogeneous surfaces, than on patter surfaces.
In detail, first, the microfabrication and characterization strategies is introduced. Following an experimental apparatus inspired by [49] is presented. It allowed us to observe the drops from two different orientations at the same time, using one single camera. Then, experimental data and some considerations about that are discussed.

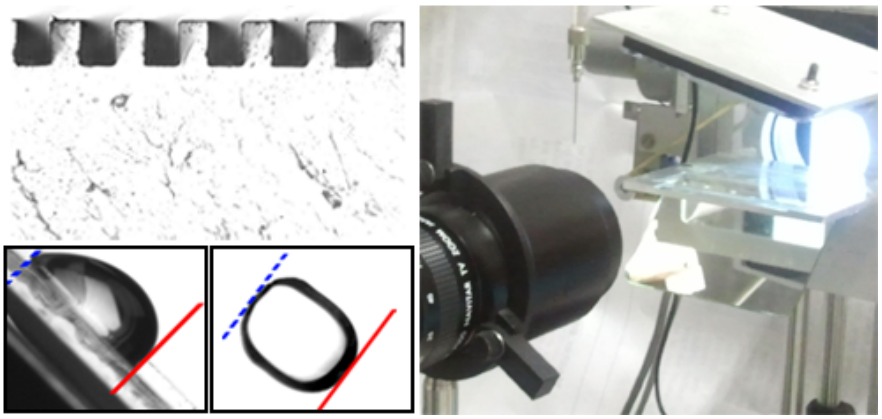

5.1 Introduction

Beyond the control of the shape of the droplet in open configuration channels, it is very important to control also their motion and during the last ten years many studies have been carried out in this sense. As described in the Introduction of this thesis, in literature there are three main solutions to control the droplet motion: by electrowetting [22], by SAWs (surface acoustic waves) and by mechanical oscillation induced externally of the device. The firsts two methods allow to control the droplets motion using complex devices, where the standard photo- and soft-lithography have to combine with electronics production strategies, increasing the producing costs and making the microfabrication more challenging.
The alternative method, which does not involve electric potentials, is the application of oscillation waves [138] to the substrate, by an external shaker. In particular, Brunet et al. [27] observed that applying vertical vibrations on a flat surface tilted at 45°, a droplet, initially pinned, can slide down and can slide up in antigravity direction. This happens because the vibration changes the local contact angles of the droplet and for particular amplitudes and frequencies, the contact angle hysteresis $\Delta\theta$, introduced in Chapter 1, can overcame the condition of sliding, allowing the drop to move up or down. Surprisingly, precise theoretical models to describe this phenomenon are still basically lacking. However, trying to replicate this kind of experiment in laboratory, we observed that perfect vibration control on nominal flat and homogenous surfaces is not so simple, because eventual defects or dirty parts can easily drift the droplets. To overcame this problem a pattern on the substrate may be introduced, indeed, it has been shown in closed microchannels, that patterned surfaces work like a rail for the droplets, as described from Baroud et al. [139]. With the aim to develop this possibility also in open microfluidic case, we studied the sliding of droplets on inclined chemically patterned surfaces. Therefore, in this preliminary study, gravity plays the role of driving force to move the droplets. The motion of a droplet on inclined surface can have two different contributions: the rolling motion, typical of super-hydrophobic surfaces and the sliding motion, observable in all other cases. Since 20 years the super-hydrophobic surfaces are studied, inspired by the lotus leaf effect for the self cleaning and friction proprieties. However, this kind of surface is characterized by a small contact angle hysteresis and thinking about possible

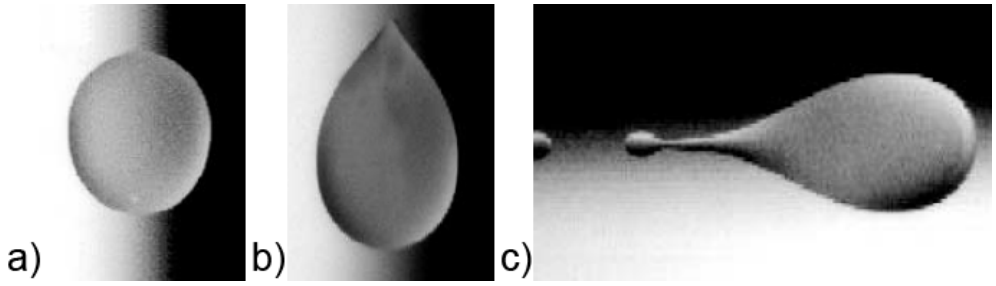

Figure 5.1: Droplets sliding down solid surfaces with a contact angle of about 50° [51], showing different regimes: a) rounded drop, b) corner, c) pearling drop. Motion is from top to bottom in a) and b), and from left to right in c).

application, the slipping control is very difficult to achieve. For this reason, in these last years a lot of research has been concentrated on surfaces where the most important contribution at the motion is the sliding. Podgorski et al. [51] in 2001 studied shapes and motions of droplets sliding down flat and homogeneous planes, using different liquids. They observed that droplets can assume different shapes depending on their capillary number Ca, as shown in Figure 5.1. At low Ca, they are delimited by a round and smooth contact line. At intermediate values they develop a corner at the trailing edge, with increasing velocity. At high Ca, they exhibit a cusped tail that emits smaller droplets (pearling transition). Moreover, in 2005 [49] the same group revisited the original experiment with a new improved experimental setup. In this second paper they confirmed the previous conclusions and better quantified the original considerations.
Apart from the case of homogeneous surfaces in literature there are no papers describing the behavior of droplets sliding on heterogeneous surfaces. With this frame, we started a new experimental work with the aim to study the sliding in this condition. In particular, we chose to produce surfaces having hydrophilic and hydrophobic stripes, as shown in Figure 5.2.

5.2 Microfabbrication of patterned chemically surfaces

To create chemically patterned surfaces we used the microcontact printing technique (μCP) on glass, described in Chapter 2.
The first step of the microfabrication process is the production by photolithography of masters with rectangular grooves of different sizes. Like in Chapter 4

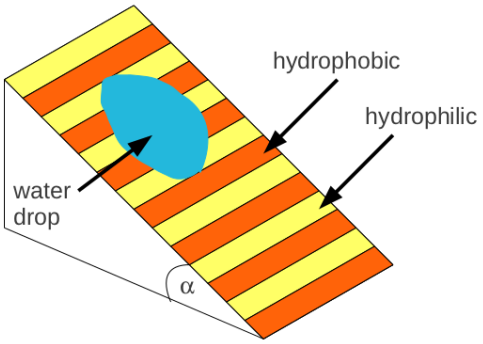

Figure 5.2: Cartoon of a sliding droplet on inclined patterned surface. α is the inclination angle of the surface, which is patterned with hydrophilic and hydrophobic stripes.

we used the SU-8 2050 as photoresist. We realized three different masters with rectangular grooves, having a length of 2 cm and width of 25, 50, 100 µm. We used two different types of masks (see Figure 5.3):

1. masks of ink printed on celluloid film with a resolution of 3600 DPI, for stripes of 100 and 50 µm;

2. masks of chromium on a soda-lime glass slide, produced by the Delta Mask company, for stripes of 25 µm.

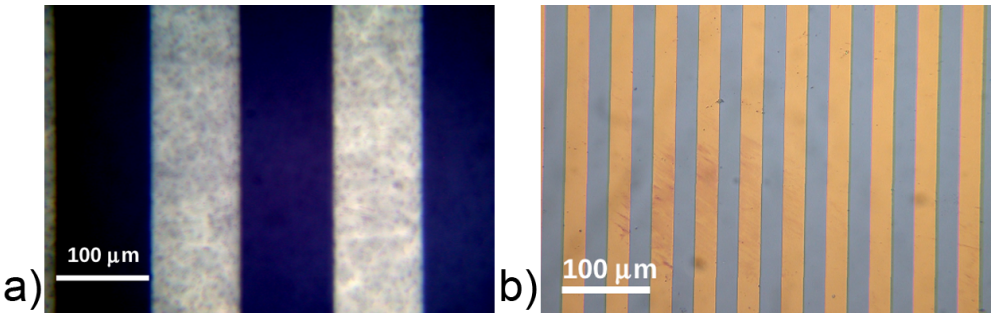

Figure 5.3: Masks for photolithography: a) mask with stripes of 100 µm and b) mask with stripes of 25 µm.

The parameters tuned in this relative master production and the relative characteristics of the structures are summarized in Table 5.1. We assumed the Datasheet provided by Microchem [78] and we optimized the parameters for our purpose. Figure 5.4 shows an example of the master produced.

After the production, we functionalized the master surfaces with a layer of

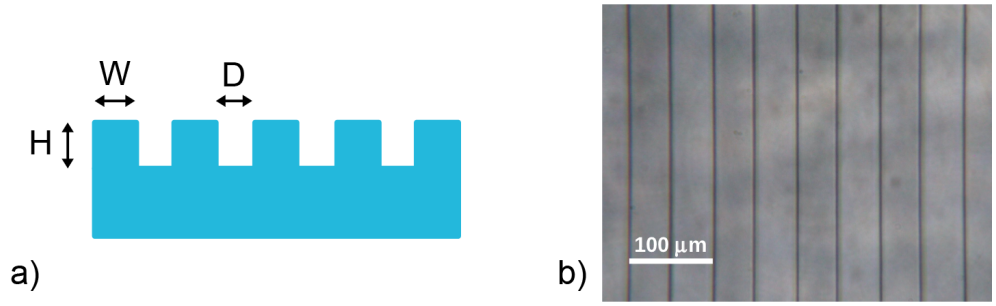

Figure 5.4: a) Scheme of the master produced and b) microscopy image of the SU-8 master with rectangular grooves of 50 µm width (W), 47 µm gap (D) and75 µm height (H).

Nominal width (µm)	spin velocity (rpm)	Exposure time (s)	Real width W (µm)	Gap D (µm)	Height H (µm)
100	1300	30	101±2	100±3	75±1
50	1300	30	50±3	47±2	75±1
25	1500	30	29±1	21±1	43.7±0.3

Table 5.1: SU-8 masters parameters.

trichloroperfluorooctylsilane (FOTS), as described in Chapter 3. They were replicated only once by standard replica molding with PDMS. At this point the molds were ready for the µCP process. Figure 5.5 shows an example of PDMS stamp. As described in Chapter 2, we recall that µCP is a soft lithographic technique for chemically patterning a surface: a PDMS mold is used as a stamp to transfer molecules dissolved in a solution, or "ink", on a substrate by the contact between the two parts (see Figure 2.12). We chose a solution of octadecyltrichlorosilane (OTS), provided by Sigma Aldrich, in toluene (0,5 mM) as "ink", and microscope glasses as substrates. PDMS samples were completely got soaked in OTS solution for 30-60 seconds. They were consequently dried and put in contact with cleaned glass substrate, previously activated by UVO-cleaner for 30 minutes. Finger pressure was exerted for 20-60 seconds paying attention to give an homogeneous pressure. Using the PDMS stamp with rectangular grooves, we created patterns with hydrophobic (OTS) and hydrophilic (glass) stripes. After having gently removed the mold, patterned glasses were placed on a hot plate at 70°C in order to evaporate the solvent. The best parameters used for every samples are empirically found and summarized in Table 5.2.

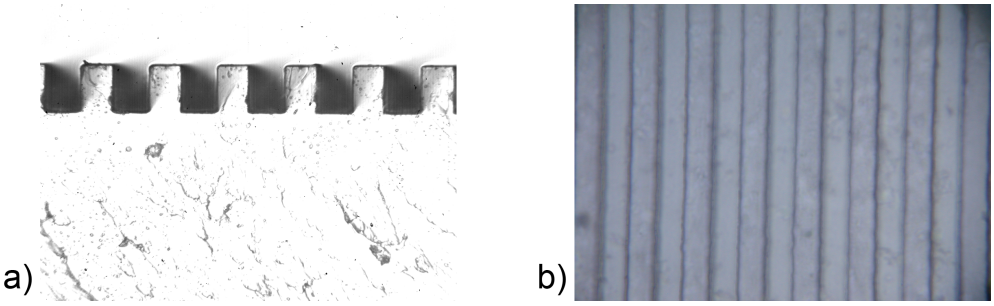

Figure 5.5: Photographs of a PDMS stamp with grooves 50 µm wide: a) lateral view and b) reflection microscope view.

5.2.1 Characterization of the patterns

The different wettability proprieties of the patterns between OTS and PDMS stripes can be exploited in order to characterize and to observe sample features with the condensation figure method [140]: water vapor condensation on hydrophobic and hydrophilic surfaces is different and, as a result, two different areas can be distinguished according to the size and distribution of the condensed droplets. As shown in Figure 5.6, some stripes are characterized by bigger droplets

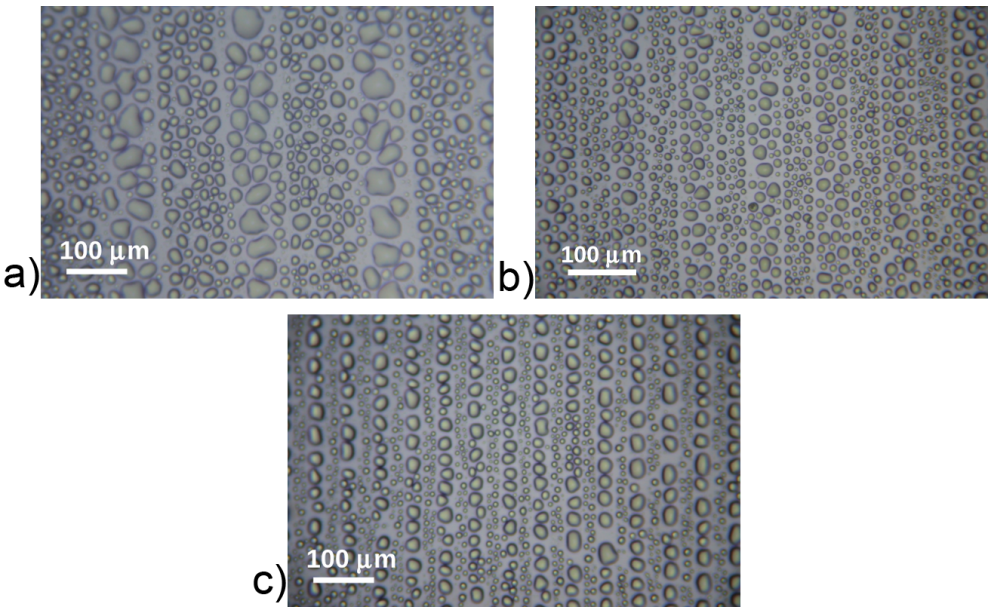

Figure 5.6: Examples of condensation figures on glass surfaces patterned with OTS: bigger droplets form on glass whereas smaller droplets on the OTS layer. These photographs refer to the four kinds of produced samples, presenting stripes a) 100 µm, b) 50 µm and c) 25 µof width.

(hydrophilic glass surface) while other stripes covered by smaller droplets (hy-

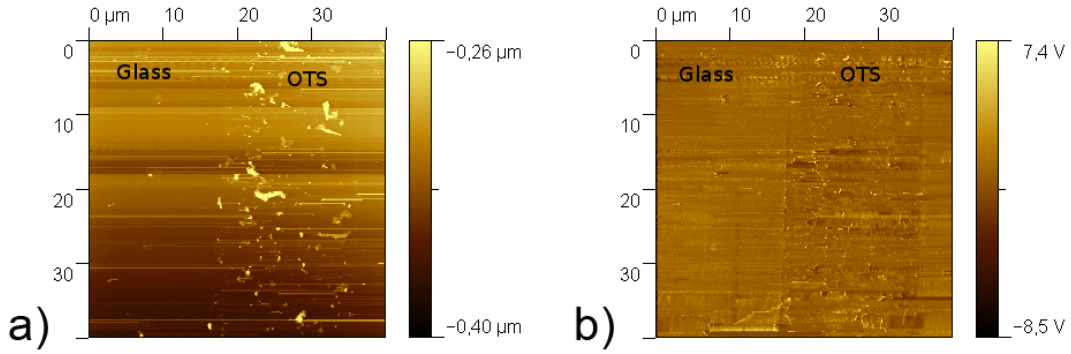

Figure 5.7: AFM scanning image of a surface patterned with almost 25 µm wide stripes: a) topographic mode, b) lateral force mode.

drophobic OTS layer). This is a simple and fast technique to measure the stripe width on the scale of tens of microns and to check if the patterned surfaces have relevant defects. Unfortunately this method does not provide informations about layer thickness, that we had to measure by Atomic Force Microscopy (AFM). In order to study our surfaces we used an AFM (Park scientific instruments autoprobe CP) both in topography and lateral force modes [141]. Two examples of a scanning outputs is shown in Figure 5.7, where the difference between OTS and glass is marked by the different color scales, which are related with the height and the hardness of the surface in topographic and lateral force modes, respectively. From them it is possible to observe that OTS and glass boundaries are well defined. However, OTS layer is not a single monolayer, probably because of molecular accumulation during the printing. Since these buildups are not higher than 100 nm, which is in any case much smaller than the dimensions of the typical drops used, we reasonably expected that these OTS layer irregularities would not affect drops motion. The main results of the surface characterization of the samples realized by µCP are listed in Table 5.2.

Stripes nominal width (µm)	Contact time (s)	OTS stripes width (µm)	Glass stripes width (µm)	OTS layer roughness (nm)
100	40	98±3	102±4	∼80
50	40	47±3	48±4	∼80
25	60	23±2	28±2	∼80

Table 5.2: Characterization parameters of the patterned surfaces.

In addition to the topographic characterizations we also performed a wettability test, to control if the behavior of our surfaces was coherent with the Cassie

Equation 1.14, which, in this case may be written in the following form:

$$\cos\theta' = f_{glass}\cos\theta_{glass} + f_{OTS}\cos\theta_{OTS} \tag{5.1}$$

where θ' is the apparent contact angle of the patterned surface, θ_{glass} and θ_{OTS} are contact angles of water droplets on a surfaces made of glass and OTS respectively, and f_{glass} (f_{OTS}) is the fraction of the glass (OTS) with respect to the whole wetted surface area.

Therefore we performed contact angle measures for all the surfaces we realized and we compared their values with those calculated on the basis of the Equation 5.1. To do that we had also to prepare OTS and glass homogenous surfaces. The former was obtained by cleaning a microscope glass with distilled water and isopropanol, then left in UVO cleaner for 30 minutes and finally immersed for 24 hours in a solution of OTS in toluene 5 mM. To simulate the μCP process on the glass surface, we washed it in toluene for about 6 minutes. This procedure was necessary because otherwise cleaned glass would have been different from glass stripes in patterned samples. Contact angle measurements of water drops on homogeneous surfaces are shown in Table 5.3. The area fractions of OTS and

Substrate	Static contact angle (°)
Glass	52.2 ± 2.2
OTS	118.2 ± 1.8

Table 5.3: Static contact angles on homogeneous surfaces.

glass on patterned surfaces were extracted from condensation figures, like the ones of Figure 5.6. The results is tabulated in Table 5.4, where predicted and direct measured values are compared. The agreement between theoretical θ'_{Th} and experimental θ'_{Exp} values constitutes a further proof of the good realization of our samples.

Nominal pattern size (μm)	f_{OTS}	f_{glass}	θ'_{Th} (°)	θ'_{Exp} (°)
100	0.49±0.02	0.51±0.03	85.4±1.6	84.8±3.2
50	0.49±0.05	0.51±0.04	85.6±2.2	83.2±3.0
25	0.45±0.04	0.55±0.04	82.9±2.2	81.9±5.6

Table 5.4: Static contact angles on heterogeneous surfaces: f theoretical predicted (θ'_{Th}) and measured values (θ'_{Exp}). f_{OTS} and f_{glass} are the fractions of total surface which exposed OTS and glass, respectively.

Moreover, let us outline that the three patterned surfaces show contact angles θ'_{Exp} between 81.9° and 84.8°. To compare the behavior of water droplets which slide on patterned and homogeneous surfaces having the same contact angles, we had to produce one more sample, having a homogeneous contact angle close to the values measured on the patterned surfaces. To do that we cleaned a glass slide with acetone, isopropanol and 30 minutes in UVO-cleaner and then we left it in a solution of Octyltrimethoxysilane (TMS) in toluene 5mM for 24 hours. Finally, we washed the sample with pure toluene for about 5 minutes and put it on hotplate at 70°C for half an hour. After the treatment, the glass showed a contact angle θ_{TMS} of $82° \pm 2°$. As required, this value was enough close to the apparent contact angles θ'_{Exp} measured on the patterned surfaces.

5.3 Experimental apparatus for sliding droplets

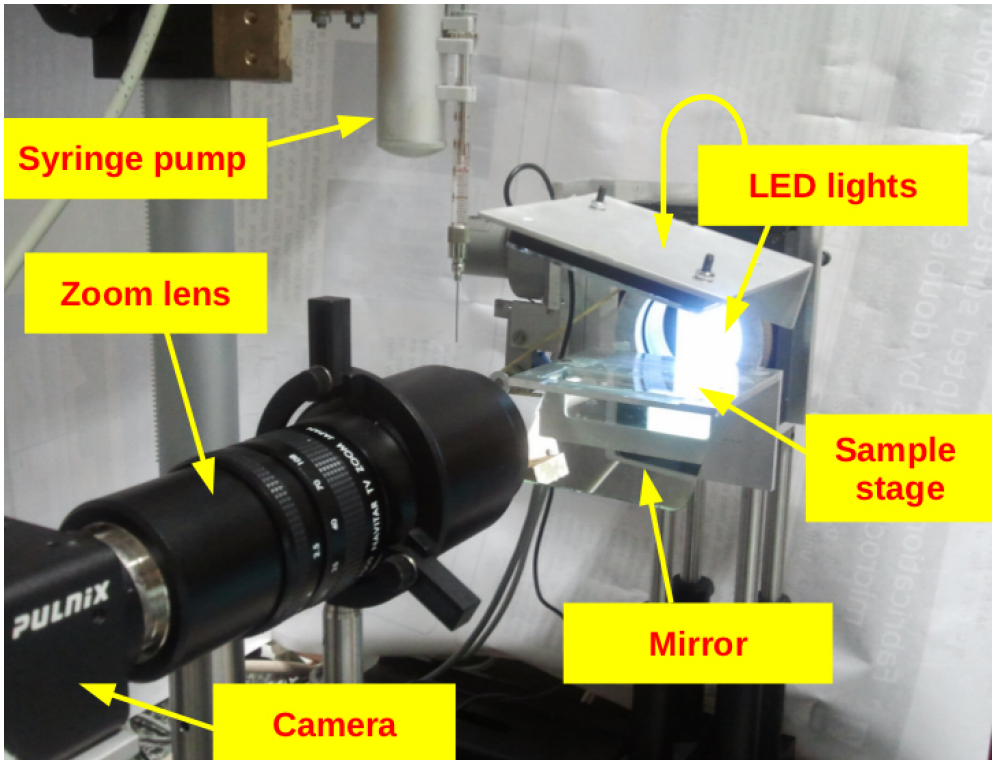

Figure 5.8: Experimental setup used to observed the sliding droplets.

The experimental apparatus is shown in Figure 5.8. Droplets of the desired volume are positioned on the surface through a syringe pump (World Precision Instruments, Inc.). The sample is placed on a tiltable support, whose inclination

can be set with a 0.1° accuracy. A mirror mounted under the sample stage at 45° with respect to the surface allows to view the contact line and the lateral side of the drop, simultaneously. The drop is lightened by two white LED backlights (Phlox): one of them is placed in front of the camera and the other is fixed upper the sample stage, to illuminate the droplet from the top. The sample stage, the mirror and the light above the drop rotate together, while the light behind the drop is fixed. Images are acquired by a CCD camera (Pulnix, TM1402CL, 30 frame per second) equipped with macro zoom lens (Navitar 7000). By zooming or dezooming the macro objective it is possible to observe both the whole motion of the drops and to focus on a droplet detail as, for instance, the contact angles. The frame grabber (SiliconSoftware, mE4AS1-PoCL), which connects the camera to the computer, allows to acquire image sequences of 4500 frames.
Experimentally, at first we fixed the inclination of the plane and then we deposited the drop of known volume by mean of the syringe pump. As expected, for small volume of the order of 20 μL the drop was pinned on the surface, while for high volume (>50 μL) it slided too fast for the frame rate range of our camera. Therefore, we finally chose to work with droplets of 30 and 40 μL.

5.3.1 Images acquisition

Once the drop has been deposited, it can be focalized with the desired magnification, by regulating the macro zoom. Image contrast and brightness can be adjusted acting on LED lights power and/or on the aperture of the zoom lens. In addition, the brightness can be digitally changed also in post processing using an apposite program of treatment and analysis of images, realized with LabVIEW.
It was possible to setup three different field of view, according to the magnification imposed through the zoom lens:

a) frames with a field of view of about 1×0.75 cm, necessary for seeing not only that the whole drop laying at rest, measuring static contact angles, when the plane is horizontal, but also the advancing and receding contact angles, when the plane is tilted (Figure 5.9a);

b) images of an area of approximately 3.5×2.6 cm, focusing only on the side view of a drop sliding down the tilted surface and traveling a distance of some centimeters, so that its motion law can be inferred (Figure 5.9b);

c) views of nearly 4×3 cm, with the capability of framing at the same time both side and bottom views, giving an idea of the three-dimensional shape of the drop. Moreover, the bottom view allows to reveal contact line movement and behavior (Figure 5.9c).

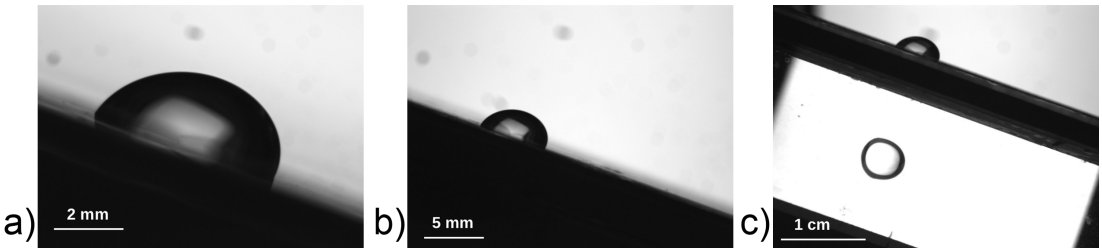

Figure 5.9: Three possible zooming of the same drop by our experimental apparatus.

Acquired sequences were then analyzed off line by a homemade programs, written in LabVIEW which gives in output front/rear contact angles and front/rear contact points for every frame; therefore the motion law and the drop length behavior can be reconstructed. The program at first finds the drop contour comparing the contrast difference between drop (dark) and background (bright). Then it fits the points found with polynomial of the fourth degree. Finally, using the function obtained, it calculates the contact angles and the contact points between surface and droplet, which will be discussed in following section.

5.4 Data elaboration of sliding droplets

The image sequences were analyzed from two different points of view: at first, we focused our attention on the behavior of water droplets sliding on the chemically patterned surfaces by varying progressively the patterning and then we compared the mean velocities of the droplets sliding on both patterned and homogeneous surfaces as a function of the inclination angle α of the plane.

5.4.1 Sliding droplets on patterned surfaces: stick-slip motion

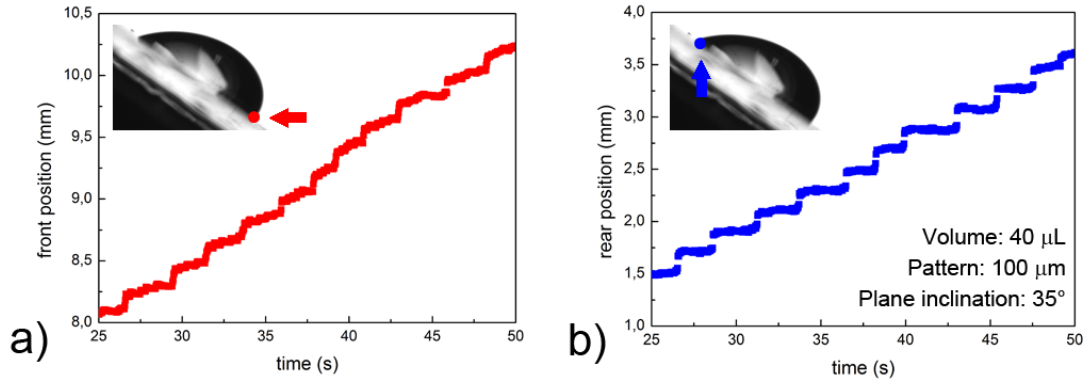

Figure 5.10: Motion law in the stick-slip regime: a) front and b) rear contact points. These data refers to the motion of a 40 µL water droplet on a patterned surface with stripes 100 µm wide, having a slope of 35°. Stick-slip is characterized by a space periodicity of 200 µm, the same as the pattern ones.

By observing the droplets during their sliding on the patterned surfaces we detected a distinctive feature of the sliding: the droplets moved with jerking motion that we refer as stick-slip motion. This was caused by the surface pattern, made of alternating hydrophilic and hydrophobic stripes; the influence of the different wetting materials on drops motion appears evident: glass stripes are traveled faster than OTS bands, as shown in Figure 5.10, where the position of both the front and the rear contact points are plotted as a function of the time. Moreover, comparing panels *a* and *b* of Figure 5.10, it is possible to notice that the two contact points exhibit rather different trends:

- the front contact point travels hydrophobic and hydrophilic bands with different velocities. Glass stripes are crossed faster than OTS stripes: OTS hydrophobicity represents an energetic barrier to drops motion (see Figure 5.10a);

- the rear part is pinned on a glass stripe and when the front slides down a sufficient distance, the front bulge attracts the rear part, which jumps on the subsequent glass stripe (see Figure 5.10b).

In both cases, *space* periodicity is the same as the pattern periodicity; on the contrary, *time* periodicity generally changes during the motion: steps can be taken

with different velocities.

Moreover, stick-slip makes the drop *shape* not to be constant, as Figures 5.12 and 5.13 depict: the drop elongates when the front advances, because at the same instant the rear is pinned; subsequently the droplet contracts as the rear makes a sudden step forward. Therefore, the drop lengths "oscillates", generally without following a regular continuous behavior: length increases and then suddenly diminishes, as plotted in the examples in Figure 5.11. This characteristic trend may be drastically changed, depending both on the surface pattern and on the drop instantaneous speed. In any case, the variations of the droplets length are of the same order of magnitude as the pattern stripe dimensions.

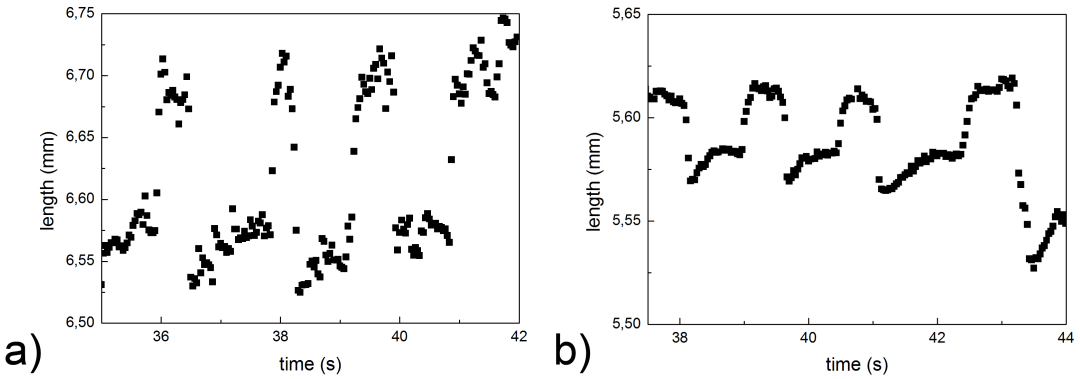

Figure 5.11: Two examples of oscillations of drops length in the stick-slip regime: a) a 40 µL water drop on a surface patterned with bands of 100 µm, tilted of 35°; b) a 30 µL water drop on a patterned with stripes 25 µm wide, with an inclination of 37.3°. The difference between maximum and minimum length is of the order of the texture stripes width.

5.4.2 Sliding droplets on patterned and homogeneous surfaces

After having evaluated the stick-slip behavior, we compared the mean velocities of sliding, taken for patterned and homogeneous surfaces, with the aim to evaluate the pattern influence. Kim et al. [142] observed that a droplet which slides on tilted plane, moves with constant velocity. Moreover, fixed the fluid, this velocity is directly proportional to the plane inclination α and to the static contact angle θ of the surface. Therefore, to consider the possible influence of the pattern, we had to compare the velocities related to patterned and homogeneous surfaces sliding at the same θ. In particular, we used the three patterned surfaces real-

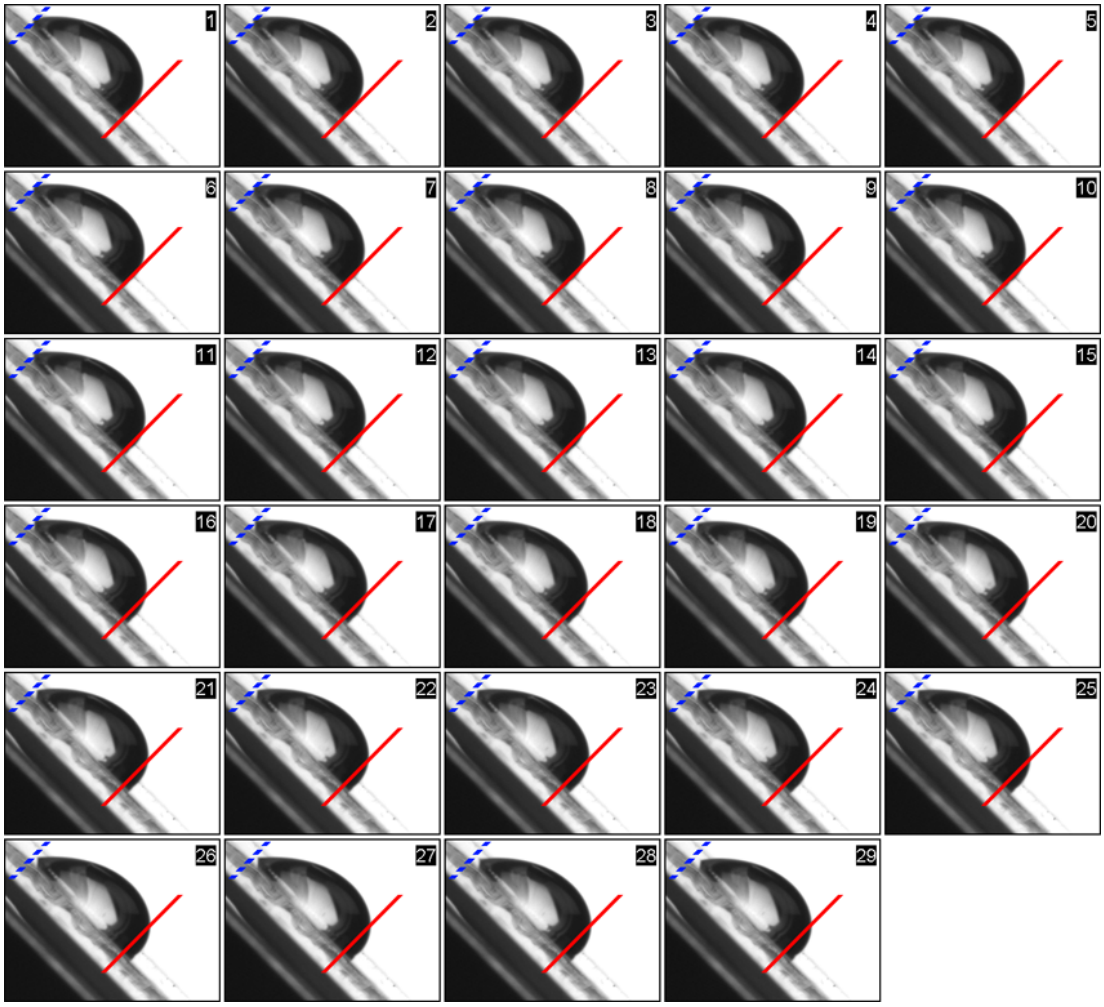

Figure 5.12: Sequence of side view of a 30 µL water drop in the stick-slip regime on a surface patterned with stripes of 100 µm, inclined by 45°. Time interval between two consecutive frames is 1/30 s. The continuous red and the dashed blue lines indicate the front and the rear contact points in the frame 1, respectively. The lines are kept fixed in other frames to underline the droplet motion. In particular, the droplet front proceeds, for a while the rear contact position does not change, until frame 18 (elongation), where it takes a sudden step of almost 200 µm (contraction). This new position is maintained up to frame 29 (elongation), where the rear jumps again (contraction).

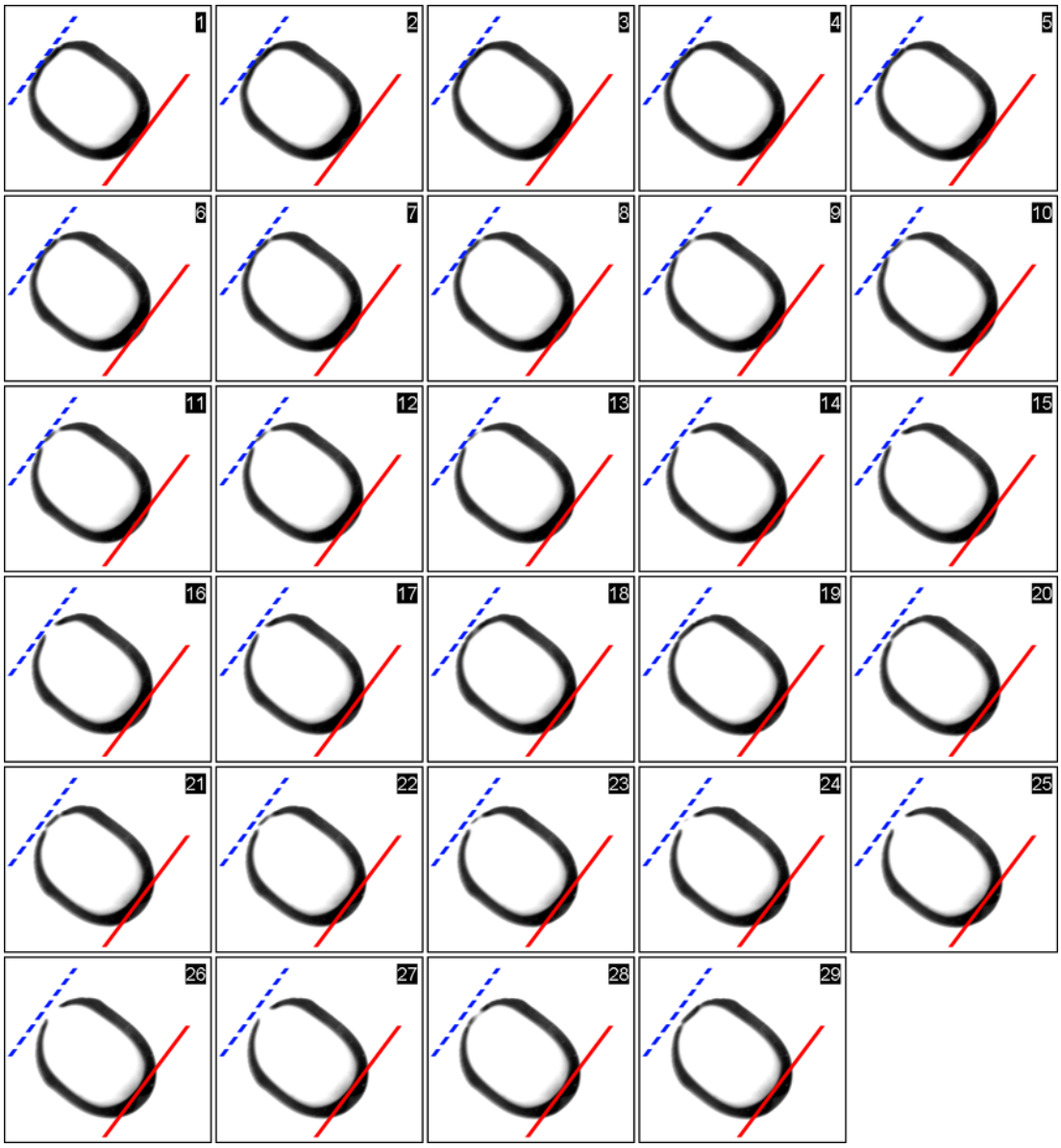

Figure 5.13: Sequence of contact line (bottom view) of a 30 µL water droplet in the stick-slip regime on a surface patterned with stripes of 100 µm, with a slope of 45°. Time gap between two successive frames is 1/30 s. These images correspond to the frames in Figure 5.12. Like in that case, the continuous red and the dashed blue lines indicate the front and the rear contact points in the frame 1, respectively. In some frames the rear part of the contact line is not visible because it becomes very thin and the contrast is not enough high. However the rear position can be determined through the comparison with the corresponding side view.

ized, which showed contact angles of $81^\circ \div 84^\circ$ and the homogeneous glass surface functionalized with TMS ($\theta_{TMS} = 82^\circ \pm 2^\circ$). Considering the contact angle errors listed in Table 5.2, we could consider that all had the same static contact angle. In Figure 5.14 the mean velocity U is plotted as a function of the increasing inclination angle of the plane, for the different patterned and homogeneous surfaces. As expected the U grows with α, but there is a large different between the heterogeneous and the homogeneous cases. In particular, in the heterogeneous cases, U is always smaller than in the second case, although the apparent contact angle was the same (about 82°). Such behavior was found also for 40 µL drops.

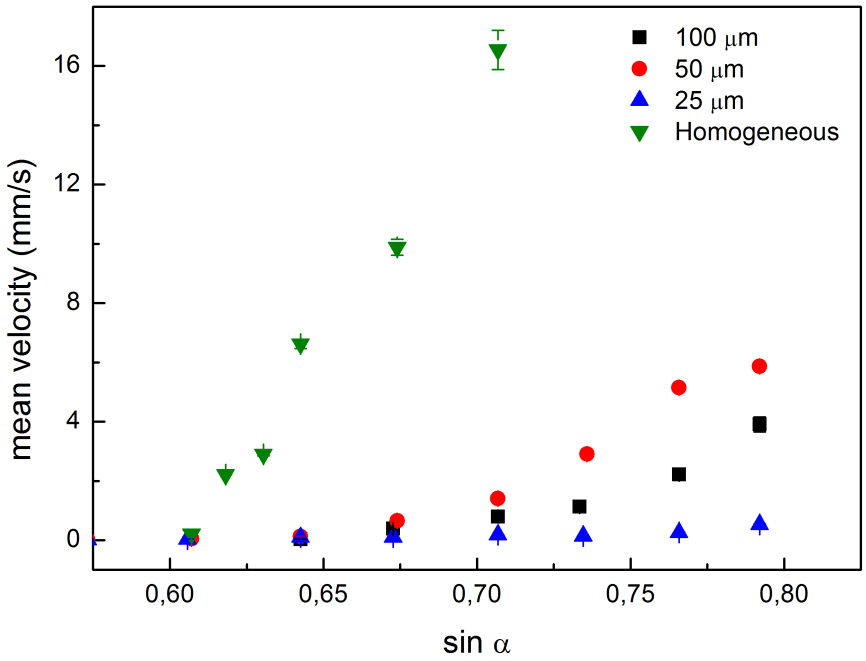

Figure 5.14: Mean velocities as a functions of inclination angles α: velocities are much lower on patterned surfaces than on homogeneous surfaces. This graph refers at volume drops of 30 µL.

5.5 Dissipation at the contact line

A comparison between the motion on homogeneous and heterogeneous surfaces revealed strong differences in the mean velocities at the same inclination angle of the plane α, as shown in Figure 5.14. In detail, we observed that for a given contact angle θ, the mean velocity is always much slower on heterogeneous surfaces than on homogeneous substrate. This is not predicted by the model introduced

by Kim et al. [142], suggesting that, it is due to the presence of the pattern. In particular, we think that these different velocities are caused by the dissipation on the contact line of the droplet, which is continuously deformed during the sliding on patterned surface. In other words, we think that the deformation of the contact line during the stick-slip introduces an extra-friction between droplet and substrate, missing on the homogeneous surface.

5.6 Conclusions

Inspired by the work of Limat et al. [51], we compared the behavior of sliding droplets on homogeneous and chemically patterned surfaces, with the aim to control their motion. In particular, in this Chapter we described how we optimized an usual apparatus for contact angle measures, to a more articulated setup, allowing to record the droplet motion from two different points of view at the same time, notably droplet profile and contact line. Then we realized different chemically patterned surfaces by microcontact printing procedure, comprising master production (through photolithography), PDMS stamp realization (by replica molding) and microcontact printing. The final result was a set of micropatterned surfaces featuring hydrophobic stripes (OTS layer zones) alternated with hydrophilic stripes (uncoated glass bands) and different stripe widths. Moreover, we functionalized a glass surface in homogeneous manner, in order to obtain a surface having the same contact angle of the patterned ones previously described ($\theta \simeq 82°$).
By observing droplets sliding on patterned surfaces, we noticed that they showed the stick-slip motion, which featured the same space periodicity of the texture. As a consequence, drop shapes were not constant, but it were subjected to discontinuous oscillations, causing the contact lines to be continuously modified during the motion.
Finally, we showed that, for a given static static contact angles, the droplet mean velocity was much slower on heterogeneous surfaces than on homogeneous substrate. We tried to give a reasonable interpretation of that effect, ascribing to the dissipation on the contact line. To validate this insight, we will compare our results with Lattice Boltzmann numerical simulations.

With this work, we demonstrated that chemical patterns strongly affect drop

dynamics and we can state that a surface with areas of different wettability can be employed to facilitate the control of drop motion. Taking inspiration from the work of Brunet et al. [27], described in the Introduction of this Chapter, we also aim to couple the patterned surfaces and the oscillation provided by an external shaker. In detail, the oscillation system will provide the driving force to move the droplets, which can follow patterns drawn on the surface. We think that this idea promises to be a suitable way to easily and completely control the dynamics of the drops both on horizontal and tilted surfaces.

Chapter 6

Droplet production in T-junction device

This Chapter presents the generation of droplets using T- shape junctions, following the approaches of [62, 64, 66]. The attention has been focused on the tuning of the correct parameters necessary to produce control sequences of droplets with narrow distribution in size. In detail, this Chapter describes the microfabrication strategies used to produce the devices, their characterization and the interaction with the liquids, focusing on the swelling problem of PDMS microchannels. Finally, some results regarding the distribution in size of the droplets are presented.

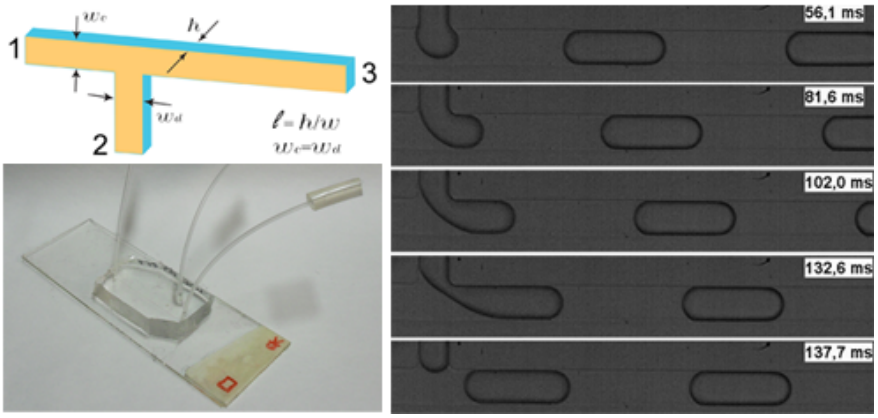

6.1 Introduction

In the previous Chapters we discussed droplets in open microfluidic systems, however in literature the droplet production is more diffused in closed microchannel and different types of geometry are used, as illustrated in Chapter 1. Despite a so large diffusion of these systems, the control of the droplets in microchannels is not completely understood. With the aim to study the influence of different channel geometries on the droplets manipulation, we considered, at first, their generation with T-shape junction devices.

6.2 Microfabbrication of T-junction devices

We made microfluidic devices, characterized by different height h, having T-shape junction to produce water droplets in an organic phase, namely "oil". In particular, we realized T-junctions, where the channel width of the dispersed and continuous phase (w_c and w_d respectively) had the same dimensions equals to 50 μm, as shown in Figure 6.1. The production process followed the same double step approach described in Chapter 4: first, we made SU-8 masters by photolithography and then we obtained the final samples in PDMS by double replica molding. Finally, the channels were closed with a glass slide covered with a thin layer of PDMS (about 40 μm) and three polyethylene tubes were fixed as inlets. Following sections desribes in details the sample production.

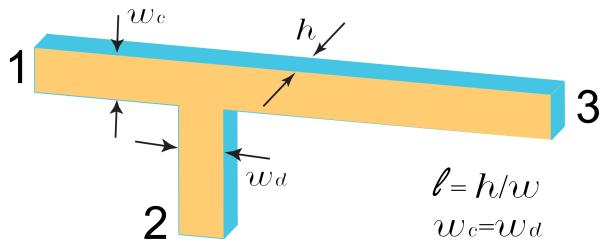

Figure 6.1: Scheme of a T-junction device. Normaly oil and water are pumped from inlet 1 and 2, respectively. While the inlet 3 is used to transport the produced droplets. w_c, w_d and h are the widths and the height of the channels.

6.2.1 T-shape master production by photolithography

The photolithography process is realized following the same procedure described in Chapter 4. In particular, for this case we used masks, provided by Delta Mask, realized depositing on glass a thin chrome film [143]. As in the previous cases, the entire master production was performed in an ISO-7 clean room. At first we cleaned the silicon wafer and then we spun SU-8 2050 at different rpm (revolutions per minute) to obtain different film thickness (see Table 6.1 for details). Then, the samples were prebaked on hot plate for about 5 min at 60°C and for about 25 min at 90 °C to evaporate the solvent of the photoresist. Next, they were aligned on a mask and exposed to UV-light (365 nm) for 30 sec. During the alignment of the mask, a small drop of water was put in the gap between the mask and the resist layer to ensure a small change of the refractive index, as described in Chapter 4. During the exposure phase the polymerization starts in the exposed regions of the SU-8. Further, polymerization was catalyzed by heat during the post exposure bake for 5 min at 60 °C and then for 15 min at 90 °C. After that, the non polymerized photoresist was washed by MicroChem's SU-8 Developer for about 10 minutes. Afterwards a hard bake at 100 °C for about 30 min was finally carrier out, leading to a higher robustness of the sample. During all the baking steps the temperature was increased and decreased using thermal ramps, in order to avoid mechanical stress in the photoresist layer due to the large temperature gradient. Finally, the sample was treated trichloroperfluorooctylsilane (FOTS) to create an anti-sticking layer allowing to peel off the PDMS replica in the next step, as described in Chapter 3. With this method we were able to realized positive SU-8 masters; therefore the microchannels were digged in the SU-8 films and we had to use double replica molding to obtain the PDMS devices, as described in the following section.

6.2.2 Replica molding and closing channels

The masters made in this way, were replicated by standard double replica molding technique as described in Chapters 3 and 4. Differently from that case, we did not put any metallic wire to create the input channel, rather we applied three holes to the second replica, one for each inlet. Every channel was closed with glass slide covers with a thin film of PDMS. In detail, the glasses were cleaned

using distilled water, acetone, ethanol and UVO-cleaner (30 minutes) and then, were spin coated (1500 rpm) with PDMS to obtain a thickness of about 40 µm. Next, they were placed on a hot plate for about 10 minutes at 80°C to ensure that the PDMS was almost completely cured. To activate both PDMS surfaces, we placed the glass slides and the PDMS structure, with the punched holes, in the UVO-cleaner for 1 min. The resulting hydroxyl groups on the two surfaces were then able to form covalent bonds and so, the surfaces were put into contact. To support the formation of the bonds, heat (100°C for 2 h) and small pressure (about 150 mbar) were applied. In this way we guaranteed homogeneous wetting properties on all the inside borders. Finally, the polyethylene tubes with an inside diameter of 0.5 mm and an outside diameter of 1 mm were fixed inside the holes previously made. The inlet tubes inserted were sealed with PDMS. The result can be summarized and visualized in Figure 6.2.

We produced three T-junctions ($T1$, $T2$, $T3$), summarized in Table 6.1, with

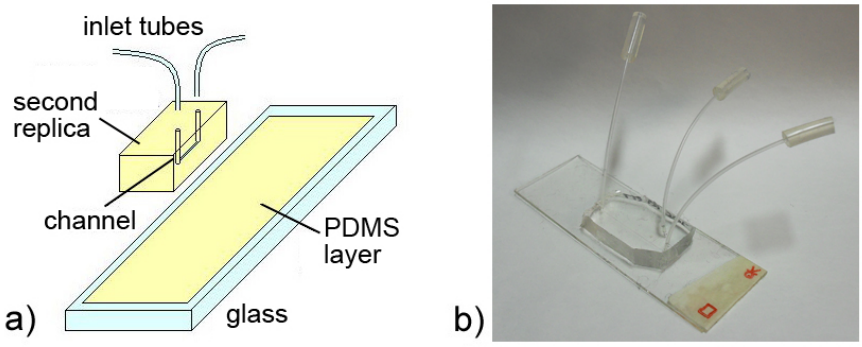

Figure 6.2: a) Scheme and b) picture of a T-junction produced by soft-lithography.

channels having different aspect ratio ℓ, between height h and width w (ℓ=h/w) to study the swelling effect. The height h of the channels summarized in Table 6.1 were measured by the profilometer Tencor P10.

	Spin velocity (rpm)	Exposure (s)	w (µm)	h (µm)	ℓ
$T1$	6500	30	50	16	0.32
$T2$	3500	30	50	23	0.46
$T3$	1500	30	50	44	0.88

Table 6.1: Channel production parameters.

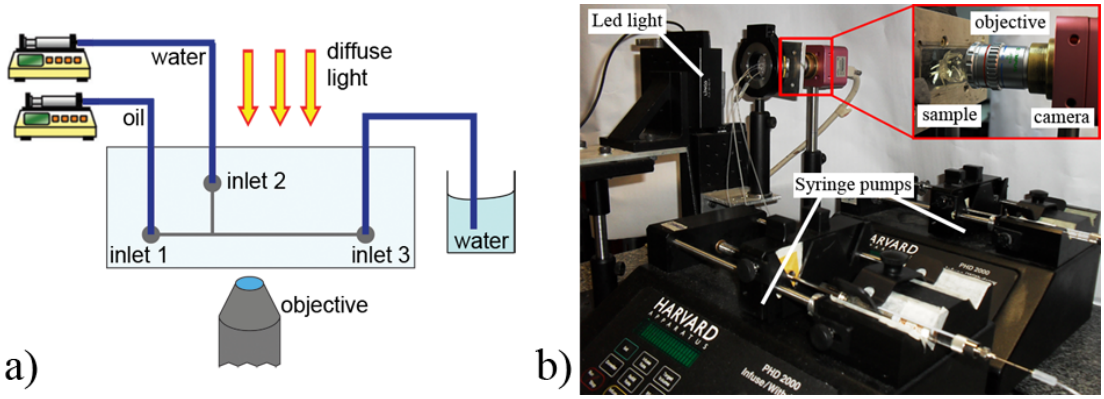

Figure 6.3: a) Schematic overview and b) picture of the experimental setup. Two syringe pumps are connected to the inlets 1 and 2, while the inlet 3 is connected to a tube which ends in a glass beaker with distilled water.

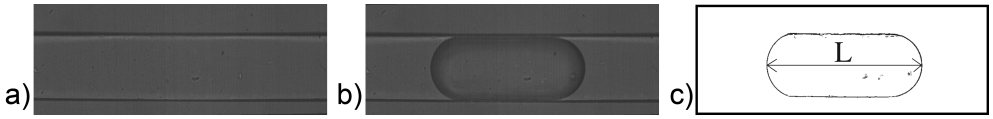

Figure 6.4: Principal steps of image processing: a) image of a empty channel; b) image of a droplet inside the channel; c) from them difference the droplet edges is obtained, which is used to calculate its length.

6.3 Experimental setup

The experimental apparatus is shown in Figure 6.3. It is composed by a CMOS camera (MV-D1024E Camera Link) mounting a 40× objective (phase contrast Olympus LWDCD Plan) assembled just behind the device. The device is fixed at a specific support movable by three translator stages and it is illuminated by a white led backlight. The image is observed in real time in a computer setup. A software manages the camera properties setting both the time exposition and the lag time between two frames, changing consequently the frame rate at which the camera works. Then, the image sequences were analyzed off-line with a homemade program realized with LabVIEW. All the images of every sequence are subtract to the channel without droplets. At this point, their lengths are measured evaluating a threshold between dark (droplet border) and white pixels, as shown in Figure 6.4. The final droplet length of every sequence L, is calculated as the average of the droplets detected.

The microfluidic device is filled by two syringe pumps (Harvard apparatus PHD2000) connected to the inlets of the microchannels to flow oil and water,

represented in Figure 6.1 as 1 and 2, respectively. Moreover, during the experiment, we used also MFCS-Maesflow pump from Fluigent, that delivers high accuracy pressure control in a microchannels (0.1% of full scale) and measures the resulting flow (up to 7 µL/min) [144]. In particular, the version present in the laboratory has four indipendent feed channels and can monitor a range of pressures between 0 and 25 mbar relative to atmospheric pressure, with a stabilization time less than 1 second. The pressure control, usually very critical working at so small pressure variations, is reliable thanks to special patented technology, based on the management of air pressure instead of the water pressure: the gas is pressurized in the same container with the liquid, therefore, controlling the gas pressure, also the water pressure is automatically controlled.

The MFCS pump was used to characterize the channel resistances during the swelling (see Section 6.5). In detail, we applied a pressure gradient between the inlet 3 and the inlets 1 and 2, producing a flow, as shown in Figure 6.5. Measuring the flow, we were able to calculate the channel resistance in analogy to Ohm's law, described in Chapter 1. For the smallest channel (w=16 µm) the pressure supplied by MFCS pump was too small to drive a measurable flow and pressures above 25 mbar were needed. Therefore, for this channel, we used a manual valve to impose pressures up to 600 mbar.

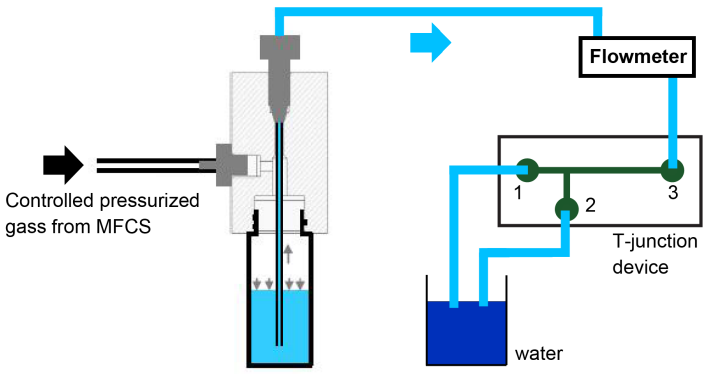

Figure 6.5: Schematic overview of the experimental setup for the channel resistance characterization.

6.4 Fluids used

To produce water droplets, we had to choose an organic solution as continuous phase and we chose hexadecane (provided by Sigma-Aldrich) for several reasons. The channel walls, made of PDMS, are hydrophobic and hexadecane has a low surface tension ($\gamma = 26.952$ mN/m), that enable to wet the channels [145]. Moreover hexadecane has a small viscosity (2.89 mPa s at 27 °C) compared to other fluids normally used for this application (e.g. mineral oil) [145]. Furthermore its surface tension can be easily adjusted using Span 80 as surfactant.
An undesired property of hexadecane is that it swells PDMS, as most of the organic solvents (see Chapter 2). Dangla et al. [2] suggested that because of the swelling, the channel diameter can decrease as much as 30%. This work was done using channels with $w = 1$ mm and $h = 50$ µm (ℓ=h/w=0.05) . However, we were not sure that this conclusion was valid also in our microchannels, having them an aspect ratios larger than one order of magnitude(see Table 6.1). Therefore, we decided to evaluate, on a quality level, their swelling ratio. To do that, we considered that the fluidic resistance R, defined in Chapter 1, is a function of the channel geometry and so it can be used to estimate the channel deformation. We measured the resistances of our channels before and after the swelling, using MFCS-Maesflow setup connected as described in Figure 6.5. Moreover, the same strategy was used to find which was the time needed for the swelling to reach equilibrium. This was relevant because it was the minimal waiting time prior to start the droplet production.
We mixed hexadecane with Span 80 for reducing the surface tension [146]. In this way, hexadecane can wet PDMS surfaces much better and the droplet production is facilitated. In fact, we experimentally observed that without surfactant it was not possible to create stable droplets. Another surfactant effect is the change of the surface tension γ between hexadecane and water. In particular, it decreases from 58.0mN/m (no surfactant) to 3.2mN/m, measured at the critical micelle concentration (0.03 wt.%) [146]. Changing the surface tension, also the capillary number Ca is modified. As described in Chapter 1, Ca is a critical parameter to drive the droplet breaks-up from squeezing to dripping regime.
In all the experiments presented we used a concentration of 0.2 wt.% of Span 80 in hexadecane. This value was chosen after having tried different concentrations.

At smaller concentration, the droplet production was not stable and, with larger concentration, a lot of micelle were observed, meaning that part of the surfactant was not necessary. For this concentration $\gamma = 3.2$ mN/m, because over the critical micelle concentration, the Span 80 do not have effect on it [146].

6.5 Swelling measures and droplet observations

At first we evaluated the swelling ratio of PDMS microchannels due to hexadecane. Once quantified the problem, we started to produce water droplets in hexadecane, observing the two main regimes of droplet formation in T-junction: squeezing and dripping. Finally, we generated droplets with various lengths and evaluated them monodispersity.

6.5.1 Swelling of PDMS

Swelling of the channel in time

To investigate the time scale for the swelling of PDMS, we measured the volumetric flow of hexadecane through the microchannel $T3$ with a height of 44 µm, applying a constant pressure of 25 mbar. Figure 6.6 shows how the equilibrium shape is reached after 10 minutes. As we believe that this equilibrium time is characteristic for all channel geometries and to ensure a complete swelling, we pumped pure hexadecane for at least 20 min before starting with the droplet production.

Measurement of the hydrodynamic diameter

We measured the hydraulic resistance R for both water and hexadecane, passing through the three different channels. To do that we applied various difference of pressures in the channel ΔP and we measured the resultant flows Q. Then, we plotted ΔP as a function of Q and fitted the collected data with a linear function. Being R the slope of the fit, we found two different hydraulic resistances of the channel for water R_w and hexadecane R_{hex}. Since the viscosity of the two liquids were known for the measured temperature (T = 27°C), we assumed that the changes were due to a change of the hydraulic radius r caused by the swelling of PDMS. Considering the Hagen-Poiseuille Equation 1.3, the ratio between the

radius before r_0 and after r the swelling process can be calculated as:

$$[htbp]\frac{r}{r_0} = \left(\frac{R_w}{R_{hex}}\frac{\mu_{hex}}{\mu_w}\right)^{1/4} \tag{6.1}$$

where μ_{hex} and μ_w are the dynamic viscosity of hexadecane and water, respectively. In Table 6.2 are reported the values obtained on the three channels. It is possible to observe that, the swelling ratio is higher on the channel having the highest aspect ratio ($T3$, $\ell = 0.88$), while there is not so much difference between the other two channels ($T1$, $\ell = 0.32$ and $T2$, $\ell = 0.46$). Probably this is due to the fact that glass slides prevent the channel from changing geometry and so the swelling is not homogeneous. But the real final channel shape is rather trapezoidal with a curvature on the walls bending inwards into the channel (see Figure 6.7). This explains the fact that, for smaller heights, meaning in turn smaller ℓ, less swelling is observed.

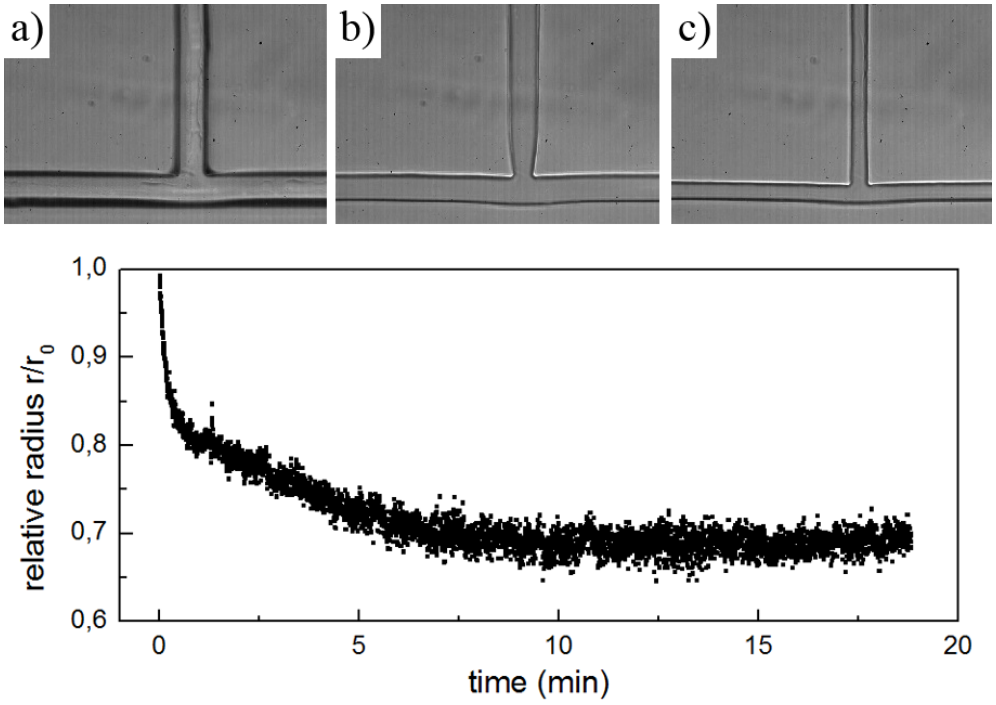

Figure 6.6: (Top) T-shape junction of PDMS filled with hexadecane. In the pictures the channel width is reduced by the swelling as in contact with hexadecane: a) before the contact b) after 22 s c) after 50 min. (Bottom) Relative radius (r/r_0) of the channel measured during the swelling.

Since the global channel resistance increases significantly with the decreasing of r, we chose to work with the channel having original width of 23 μm, to reduce

the stability problems of the devices. We observed that the maximum pressure applicable in these channels was of about 3 bars. For higher flow rates, the channels did not damage, but the connecting tubes detached from the PDMS devices.

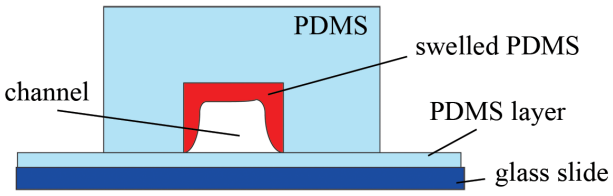

Figure 6.7: (Color online) Schematic possible swelling of the channel, in red (dark) is drawn the swelled PDMS.

	$\ell = h/w$	R_w $[\frac{\text{mbar}\cdot\text{min}}{\mu L}]$	R_{hex} $[\frac{\text{mbar}\cdot\text{min}}{\mu L}]$	r/r_0
$T1$	0.32	52±1	399±160	0.8±4
$T2$	0.46	20.1±0.1	148±2	0.8±0.2
$T3$	0.88	4.89±0.03	101±10	0.6±1

Table 6.2: Comparison of hexadecane induced swelling for channels of different ℓ.

6.6 Droplet production and analysis

In this section some preliminary results of the droplet production by T-junction device are presented. At first, the procedure used to acquire the image sequences is described, then we evaluated the squeezing and the dripping regimes of droplet breaks-up at the different Ca and finally, the droplet lengths are analyzed as a function of the flow rates.

6.6.1 Generating droplets of water in hexadecane

To start the filling of channels and guarantee a clomplete swelling before producing droplets, we followed this procedure: at first, a polyethylene tube is connected to the inlet 1 from one side and to the syringe from di other. Moreover, it is filled with 30 µL of pure hexadecane, while the syringe is filled with hexadecane and Span 80 (at 0.2 wt.%), as shown in Figure 6.8a. Prior to the droplet production, a hexadecane flow of 1 µL/min swells the PDMS channel walls for at least 20 minutes (see Figure 6.8b). At this point, water is inserted using a low flow rate

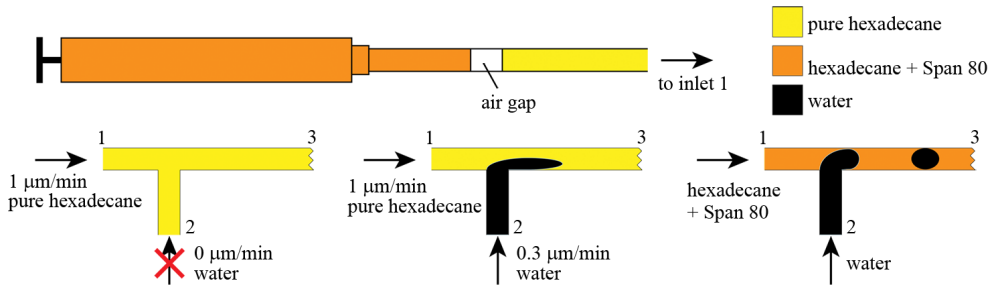

Figure 6.8: Scheme of the T-junction during the first filling of the liquid before to start the droplet production. a) The syringe was filled with hexadecane and Span 80, while the tube onlty with pure exadecane, leaving a gap of air to do not mix the two fluids. In this way, it was possible to fill the channel b) at first with pure hexadecane, c) then with water and d) finally with hexadecane with Span 80, without disconnect the tubes.

of 0.3 µL/min to stabilize the pressure at the T-junction before the arrival of hexadecane with Span 80 (Figure 6.8c). When hexadecane with Span 80 fluxes, the formation of stable droplets is observed (Figure 6.8d). During the image acquisition, hexadecane flow rate was kept constant and the water flow was increased step by step waiting 5 minutes after every change, to be sure that the droplet production was stable. Then, after acquired the foreseen image sequences for one flow rate of hexadecane, this rate was increased too and the flow of water was set to the minimal rate again. Water flow was then increased step by step. This procedure was performed for several combinations of flow rates and for each combination of them, a sequence of 700 images was acquired using the digital camera, setting a frametime of 3.06 ms and an exposure time of 2.02 ms, acquiring in consequence about 196 fps. Finally, the image sequences were analyzed by the program describe in Section 6.3 to obtain the droplet lengths.

6.6.2 Discussion of squeezing and dripping regimes

At a first view of the acquired image sequences, it was possible to distinguish between the two regimes of droplet breaks-up: squeezing and dripping, showed on left and right sides of Figure 6.9, respectively. In particular, in the squeezing regime, the forming droplet fills the entire channel and afterwards, the increasing excess pressure deforms the droplet until leads to break-up. While, in the dripping case, the shear stress pushes the droplet that do not touch the opposite channel wall.

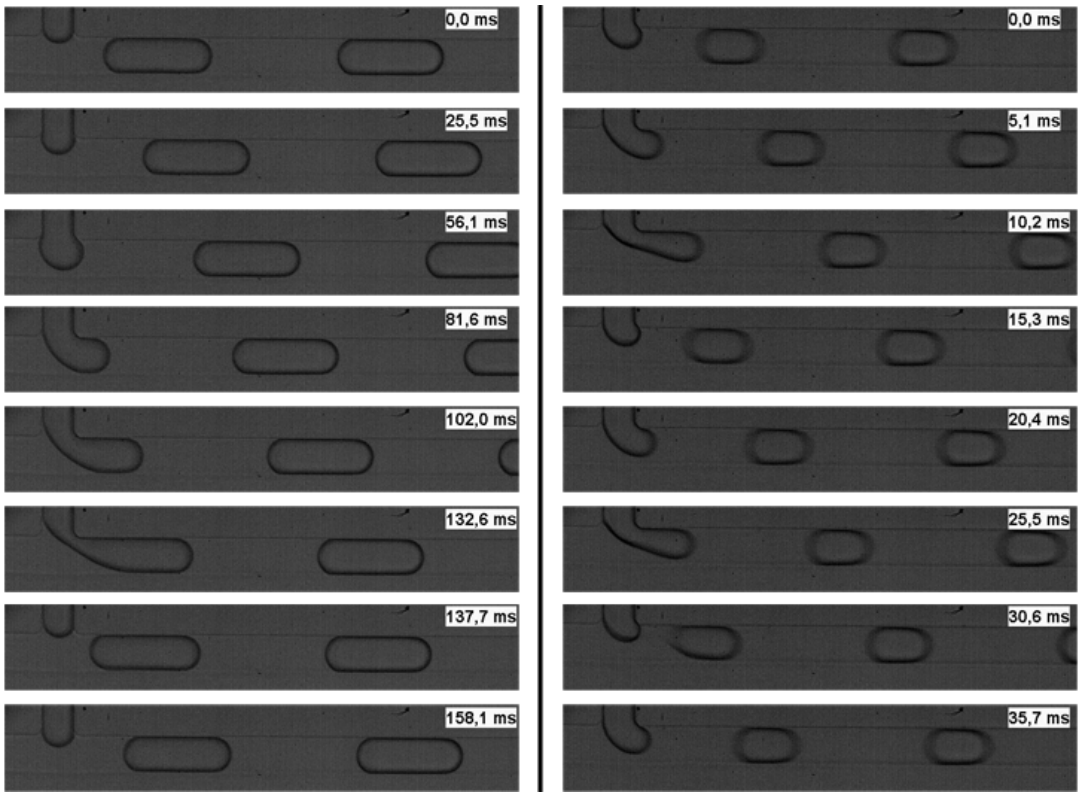

Figure 6.9: On the left side it is reported an example of squeezing at the flow rates $Q_d = 20$ nl/min and $Q_c = 400$ nl/min is shown. On the right side is presented an example of dripping with the flow rates $Q_d = 10$ nl/min and $Q_c = 850$ nl/min.

To verify if our results were consistent with the critical capillary number for the transition from squeezing to dripping introduced in Chapter 1 (Ca^*=0.015), we calculated Ca for our systems. Because this value depends from the cross section of the channel, we needed a good estimation of that after the swelling process. Therefore, we considered the hydraulic radius of the original channels r_0 and we calculated the new hydraulic radius after the swelling r, using the analysis described in Section 6.5.1. Therefore, the Ca values for our systems was calculated as:

$$Ca = \frac{\mu_c Q_c}{\gamma (\pi r^2)} \tag{6.2}$$

where γ is the surface tension between water and hexadecane with Span 80 (3.2 mN/m), Q_c and μ_c are the flow and the viscosity of the continuous phase, respectively. Therefore, in the squeezing regime illustrated on left side in Figure 6.9, Ca was 0.008, while in the dripping on right side, Ca was 0.017. The two values are

respectively smaller and larger than the critical capillary number $Ca^* = 0.015$ [65], confirming the validly of our consideration.

6.6.3 Analysis of the droplet lengths

The droplet length L was calculated as the average of all the detected droplets for every sequence. This analysis showed that the droplets produced in our T-junction can be reasonably considered monodispersed with standard deviations σ comprised between 2% and 5% of L. Figure 6.10 shows an example of this Gaussian distribution. Having verified that our droplets were sufficiently mono-

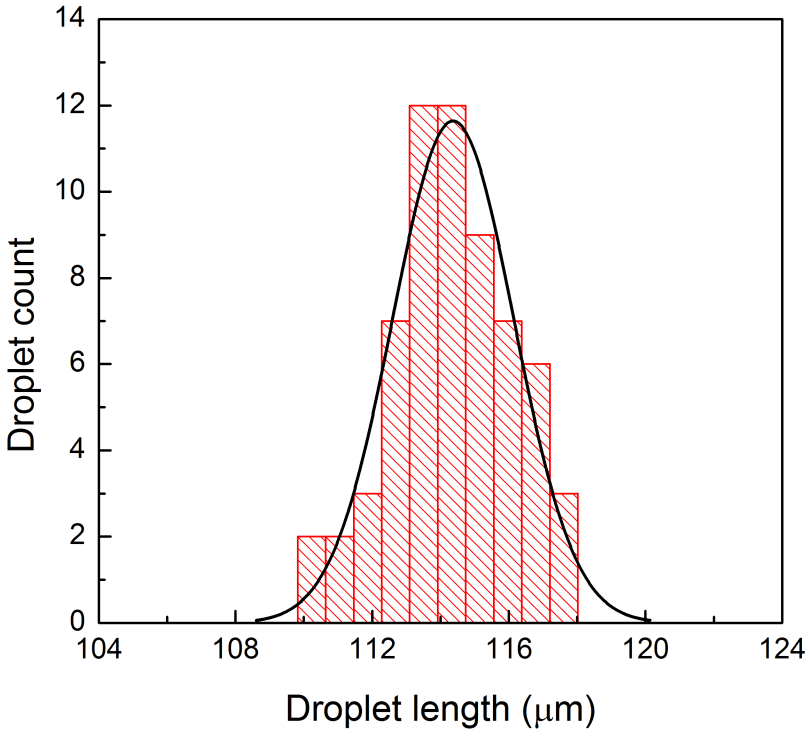

Figure 6.10: The histogram shows the total number of droplets detected in one of the image sequences and fitted with the Gaussian function (continuous line). The average length L is 114.4 μm and standard deviation σ is 1.8 μm. The droplets were produced with the flow rate combination Q_c = 600 nL/min and Q_d = 150 nL/min.

dispersed, we observed the relation between their lengths and the flow rates. The results are shown in Figure 6.11. It is possible to observe that smaller flow ratios (Q_d/Q_c) result in smaller droplets and that higher flow rates of the continuous phases, represented by different symbols, seem to lead to smaller droplets.
Working with this channel, it has been possible to produce droplets with lengths

from 70 to 350 μm. The limitation was given by the maximal camera speed; as a matter of fact, using the CMOS camera described in Section 6.3, it was not possible to acquire faster images than the which indicated, because we would not see the dynamics inside the channels.

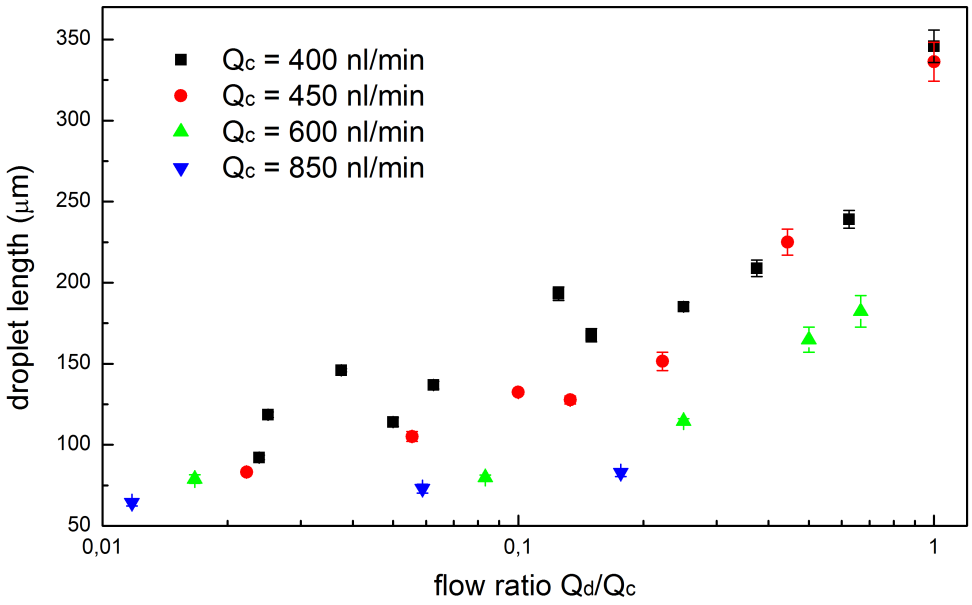

Figure 6.11: Droplet length as function of flow ratio Q_d/Q_c using different flow rates.

6.7 Conclusions

This Chapter describes a work focused to define all the ingredients necessary to produce monodisperse droplets at different flow rates. To do that we fabricated three types PDMS T-junctions with different aspect ratios, by photo- and soft-lithographic techniques. Their geometry was investigated during the swelling caused by the hexadecane. In particular, we fixed the time necessary to reach an equilibrium shape and we observed the swelling for three different microchannels, highlighting that it is larger for channels with larger aspect ratio ℓ.Considering that, we chose the channel $T2$, with a height of 23 μm, because it did not appreciably swell and it was large enough for avoiding problems of filling related to the hydraulic resistance. This channel was used to produce monodisperse droplets of different size.

After the development of this reliable protocol for production of droplets in T-shape junction, we started to study their interaction with obstacles, as innovative way for tuning their break-up. As introduced in Chapter 1, posts and defects inside of microchannel can induced the droplets break-up. Indeed, for inducing the splitting, the most common way consists in crashing droplets on post placed in a center of the channels over a critical of velocity [71, 147]. We believe that the droplet break-up can be achieved also using obstacles placed on the side of the channel, for example like those described in Appendix B. In this case the break-up might be introduced by the deformation that the droplet suffered in proximity of the obstacles. Figure 6.12 shows a preliminary experimental results of this kind of break-up, which is obtained using a rectangular obstacles placed on the border of the channel. The aim of our study will be to compare the different strategies to split droplets, considering which is the most efficient.

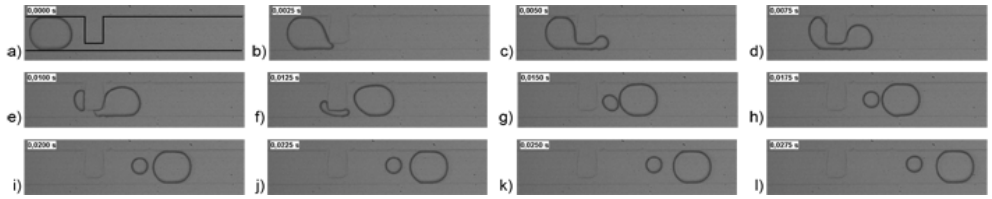

Figure 6.12: Droplet break-up in proximity of a rectangular obstacle placed on the border of the channel.

Chapter 7

Changing the wetting of thiolene microfluidic materials

In all the works presented in the previous Chapters, wetting plays a crucial role for reaching the objectives set. Sometimes it is fundamental to have the possibility to tune the wettability proprieties of a material in a versatile way. In this regard, this Chapter presents a functionalization method for the control of the wettability of thiolene resins, in particular of the commercial available Norland Optical Adhesives, commonly named NOA. In particular , treatment of open surfaces or closed microchannels with chlorosilane derivatives are shown. Moreover, the experimental findings are confirmed by the fabrication of a Y-junction device that works as a passive valve for water streams.

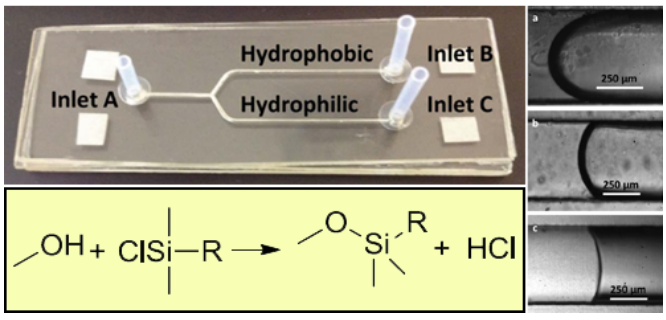

7.1 Introduction

In Chapter 6, we described the production of water droplets in organic phase. To do this, we choose to work with PDMS microchannels, which presents a hydrophobic character. While, as introduced in Chapter 1, to generate emulsion of organic phase in water, it is necessary to make channels with hydrophilic materials: these are examples of single emulsions, where one single phase is dispersed in the other. In microfluidics it is also possible to generate double emulsion droplets, conveniently combining the wettability proprieties of the microchannels [148]. This means that it is possible to create for example water droplets, covered with an oil layer and finally immersed in a water phase. To do this, the are two possibilities: microchannels are made of two different materials, one hydrophilic and the other hydrophobic [149], or the wettability of the material used is arbitrary changed in different parts of the microchannel [150, 151]. For these reasons, from the microfabrication point of view, it is very important to have different strategies to tune the wetting of the typical materials used in microfluidics.

The material always present in the microfabrication strategies described in the previous Chapter is PDMS. Despite it is also the most common material in microfluidics, the elastic nature and the swelling problem reduce its range of application. Other current materials for microfluidic applications are the thiolene resins (ThR) and in particular the Norland Optical Adhesive, known as NOA, described in Chapter 2. Compared to PDMS, NOA presents distinctive characteristics, such as i) a greater solvent resistance to swelling; ii) a much higher elastic modulus; iii) a smaller autofluorescence background; iv) impermeability to air and water vapor [91]. For these reasons, a variety of microfluidic devices have been made with ThR, to exploit the aforementioned features [88, 90, 133, 152–156].
Regarding the wettability proprieties, NOA presents a slightly hydrophilic behavior, being the contact angle about 70° and despite its large diffusion, only few papers investigate the possibility to tune its wetting [153, 154]. Moreover, in these works, oxidation of open ThR surface by exposure to either oxygen plasma or short wavelength UV radiation, decreased the water contact angle of the resin which however, may recover slowly to the initial value. In this chapter, we present a simple and stable post-functionalization protocol to tailor the wettability of NOA surfaces, using chlorosilane chemistry [157]. In detail, hydrophilic

and hydrophobic surfaces were obtained both in open and closed chip geometries.

7.2 NOA composition

There are various formulations of NOA, which are different in their mechanical properties and curing time, but have the same chemical composition. In this work we chose NOA81 and NOA63 mainly because, the first has a very short curing time, compared to other NOA products and the second is optimized to prepare thick pieces.
A mixture of 1,1,1-tris(mercaptomethyl)- propane (1), trimethylolpropane diallyl ether (2), isophorone diisocyanate ester (3) and benzophenone photoinitiator (PI) is generally accepted for NOA products [156], as shown in Figure 7.1. The exposure to UV radiation (365nm) causes the production of a radical on the PI, the formation of thiolene bonds (between 1 and 2) and thiourethane bonds (between 1 and 3) are expected to happen, while the hydroxyl group in 2 should in principle survive and be available for post-functionalization. Figure 7.2 reports the 3750-2000 cm^{-1} region of the FT-IR spectra of a thin layer of NOA81 undergoing successive exposition to UV radiation [158]. The progressive disappearance of the bands at 2572 and 3084 cm^{-1}, assigned to the S-H and allyl C-H stretching, respectively, confirm the polymerization route described. The area at around 3500 cm^{-1}, typical for the stretching of hydroxide groups, presents somewhat weak peaks that are more difficult to evaluate, but appear not to be influenced by the exposition.

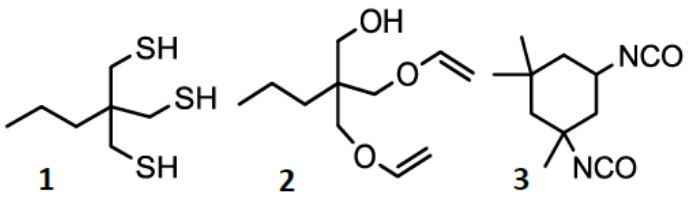

Figure 7.1: NOA components: 1,1,1-tris(mercaptomethyl)-propane (1), trimethylolpropane diallyl ether (2) and isophorone diisocyanate ester (3).

The presence of hydroxide groups on surfaces is typical for many inorganic materials, such as silicone or glass. A typical reaction used to anchor organic molecules to such surfaces is the condensation of hydroxide groups with chlorosilanes, yielding a siloxane bond with the release of hydrochloric acid, as reported in Figure 7.3.

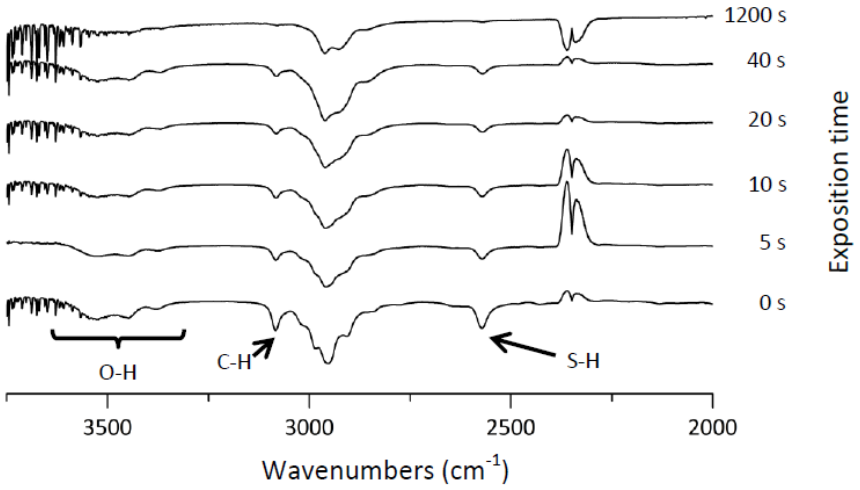

Figure 7.2: FT-IR spectra of NOA 81 resin upon UV exposition at 354 nm for different amounts of time. The disappearence of signals at 2572 cm-1 (S-H stretching) and those at 3084 cm-1 (C-H bonds stretching on allyl groups) is due to the thiol-ene polymerization reaction.

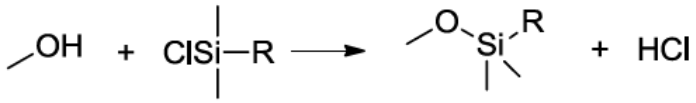

Figure 7.3: General scheme of condensation reaction of a chlorosilane with an hydroxide group.

In chapters 5 we used this strategy to functionalize glass surfaces with octadecyltrichlorosilane (OTS) in order to get a hydrophobic character. On the other hand, chlorosilanes with polyethylene glycol moieties can be used to get a hydrophilic character at the material. Having considered that, we thought to change the wettability of NOA surface using these molecules; in particular we chose OTS (from Sigma-Aldrich) and 2-methoxy(polyethylenoxy) propyl trichlorosilane (or PTS, from ABCR GmbH).

7.3 Microfabrication details

To test experimentally our considerations, we prepared three types of samples to functionalize: 1) NOA spin coated on glass slides, 2) microchannels made with NOA and 3) Y-junction to demonstrate a possible application of this work, see Figure 7.4.

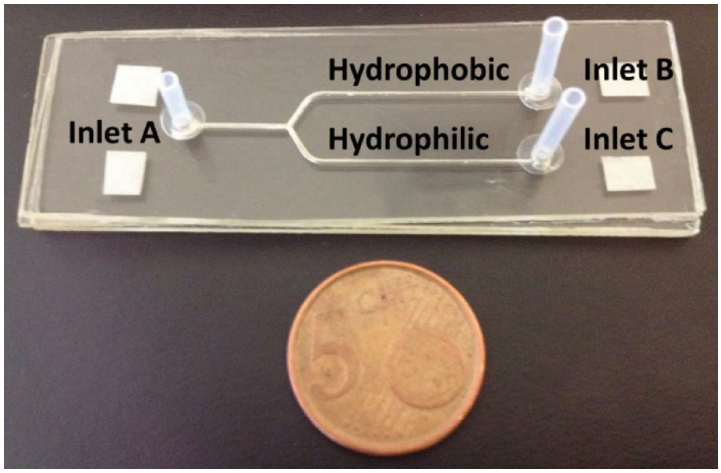

Figure 7.4: Y-junction demonstrator chip. The bottom channel, leading to inlet C, was treated with PTS to become hydrophilic. The one leading to inlet B was treated with OTS to become hydrophobic.

1) NOA on glass slides

NOA81 was spin coated on glass slides at 3000 rpm (revolutions per minute) and exposed to UV irradiation at 365 nm for 30 min using a 150 W lamp. The UV curing was followed by an overnight thermal annealing at 50 °C on a conventional heating plate. Following this procedure we realized three samples. Two of them were treated with OTS and PTS solutions, following described, while the third was used to compare the results (prestine sample). In parallel, solutions of OTS and PTS in toluene (5% v/v) were prepared. The first two flat NOA81 surfaces were dipped for 15 min in the solution of interest, then thoroughly rinsed with toluene, isopropanol and dried under a nitrogen flow. Finally, the samples obtained were used to measure their static contact angles and the results are reported in next section.

2) Fabrication of NOA microchannels

In order to test the functionalization procedure also on closed channels, two microchannels with a rectangular cross section (500×200 μm) were fabricated by double replica molding of SU-8 master produced by photolithography technique [91]. At first, we obtained its negative replica in PDMS, which was used as a mold to realize the final channel with NOA63. In this last case the polymer curing was performed by UV-exposure. To close the microchannel, a film of NOA63 was spun on a transparent plastic foil and the two parts were sealed

together. The functionalization was carried out by filling the channels with the solutions described above for about 5 min, followed by rinsing with toluene and isopropanol, and drying with a nitrogen flow.

3) Fabrication of the Y-junction

We produced a demonstrator device with a Y-shape junction, see Figure 7.4 [157]. The channel corresponding to the intlet B was treated with OTS, while the other chennel corresponding to the intlet C, with PTS. In this way, an incoming water stream from A should be forced to flow through the hydrophilic channel. In order to treat the two channels with different chlorosilanes, a steady nitrogen flow was plugged into inlet C, while the OTS solution was injected with a syringe into inlet B. The nitrogen flow assured that accidental extra-volumes of chlorosilane solution could flow towards inlet A, rather than contaminate the surfaces of the other channels. The chlorosilane solution was left in contact with the conduit walls for 5 min, and then removed with a syringe, while toluene was flushed through inlet A without stopping the nitrogen flow. After extensive flushing with toluene, the nitrogen flow was moved to inlet A and the PTS solution was injected through inlet C. In this case, the extra amount of PTS solution would flow towards inlet B, where the conduit had previously been functionalized.

7.4 Characterizations and results

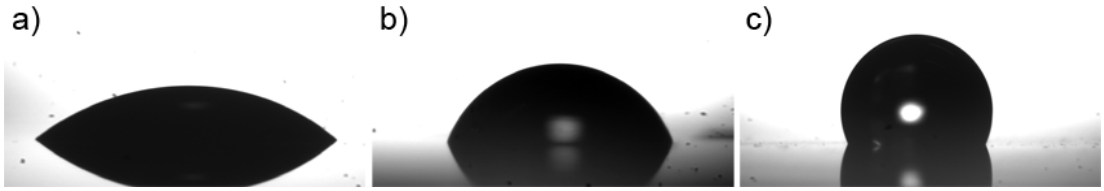

Figure 7.5: Profiles of water droplets deposited on ThR surfaces: a) PTStreated; b) untreated; c) OTS-treated.

Flat ThR model samples, functionalized with OTS and PTS, were characterized by water drop contact angle. Figure 7.5 shows three examples of profiles recorded: ThR surface treated with PTS (a), untreated (b) and treated with OTS (c). Contact angle values are reported in Table 1. The experiment was repeated on more than three samples and once a month over a three month period, in order to study the stability in time of the functionalized surfaces. As

it is possible to see from Table 7.1, the functionalization procedure enabled the modulation of the NOA contact angle, which was shown at about 70°C (untreated surface), at about 45°C (PTS-treated surface) and at about 110°C (OTS-treated surface). The standard deviations of these data was relatively low, suggesting a homogeneous functionalization of the surfaces. Additionally, water contact angles changed slightly over the months, without any monotonic tendency towards the starting values.

Pristine NOA			
Sample n°	Month 0 contact angle (°)	Month 1 contact angle (°)	Month 2 contact angle (°)
1	70 ± 2	69 ± 1	74 ± 2
2	68 ± 2	69 ± 1	72 ± 1
3	72 ± 2	75 ± 1	71 ± 1
PTS-treated			
Sample n°	Month 0 contact angle (°)	Month 1 contact angle (°)	Month 2 contact angle (°)
1	44 ± 3	46 ± 1	46 ± 3
2	49 ± 3	50 ± 2	53 ± 2
OTS-treated			
Sample n°	Month 0 contact angle (°)	Month 1 contact angle (°)	Month 2 contact angle (°)
1	114 ± 3	115 ± 3	111 ± 3
2	110 ± 2	111 ± 3	106 ± 6
3	111 ± 2	110 ± 2	113 ± 2

Table 7.1: Observed water contact angles, calculated by averaging 5 measures carried out on random positions over the sample having a size of 2×2 cm. The errors reported were calculated as the standard deviation and so they are a way to quantify the surface uniformity.

The experimental setup described in Chapter 6 was employed to observe the water–air meniscus during the filling of closed channels. In detail, using the Fluigent pump we blocked the water/air meniscus inside the channel to measure its contact angle at lateral border, as shown in Figure 7.6. The results are reported in Table 7.2; the measured contact angles were practically the same of the ones obtained in open configuration. Additionally, we measured the filling velocity of the water in the empty channel. Since it is basically influenced by the static contact angle, we expected to observe different behaviors for different treated channels. In detail, we applied a constant different of pressure of 15 mbar and we measured the

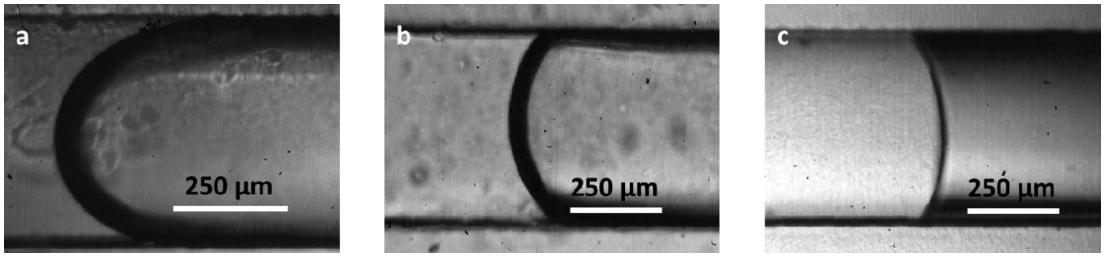

Figure 7.6: Water contact angle at the water–air meniscus in a microchannel: a) PTS-treated; b) untreated; c) OTS-treated. Water enters the conduit from the left in all the pictures.

meniscus velocities. The results are listed in Table 7.2, reporting, as expected, that the meniscus moving faster in the hydrophilic channels (PTS-treated) and slower in the hydrophobic ones (OTS-treated).

		Contact angle (°)	**Filling rate ($mm\,s^{-1}$)**
Channel 1	Pristine	70±5	4.6±0.1
	OTS-treated	112±5	2.2±0.2
Channel 2	Pristine	72±5	4.7±0.1
	PTS-treated	40±5	5.6±0.1

Table 7.2: Static water contact angles at the water–air interface and filling rates measured upon application of a 15 mbar pressure to the water flow.

An application of the functionalized surfaces so far described was developed by treating two "arms" of a NOA-made Y-junction with different chlorosilanes, thus obtaining their hydrophilic and hydrophobic characters. A scheme of this device is shown in Figure 7.4. Water was pumped into inlet A and once at the junction, it passed through the hydrophilic channel and stopped in the hydrophobic one. Figure 7.7 shows a series of frames with a water front at the Y-junction. This device can work as a static valve. However, we observed that once the channel C was full of water, channel B started filling; this happened because of the pinning of the meniscus at the outlet, which was made with Teflon (which shows hydrophobic character).

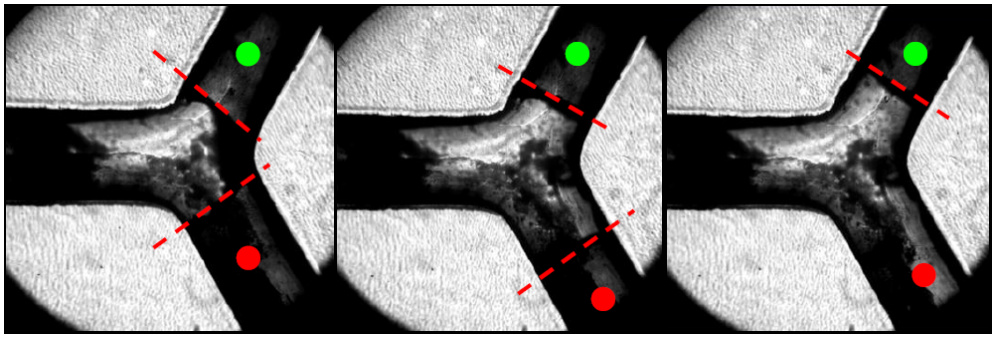

Figure 7.7: (color online) Water behaviour at the Y-junction. The red dot indicates the hydrophilic channel, whereas the green dot indicates the hydrophobic one. The water front, where visible, is highlighted by a red dashed line.

7.5 Conclusions

This Chapter it described a stable and versatile strategy that allows the modification of NOA surface in order to control its wettability. In particular, chlorosilane/–OH interfacial chemistry was used to control the resin surface wettability by choosing different trichlorosilane derivatives. In detail, we used OTS and PTS to get hydrophobic and hydrophilic characters, respectively. We observed that the water contact angles were stable for months, keeping the samples in ambient conditions.

The method was also successfully employed to modify closed channels and was proved useful for the fabrication of passive microfluidic valves. We think that this general strategy can be expanded to other chlorosilanes to create a variety of functional surfaces especially useful for generating multiphasic droplets in microfluidic devices.

Conclusions

In this thesis, we have investigated interfacial phenomena related to microfluidics of droplets, both in case of open and closed devices. Indeed, despite their huge diffusion, these systems present several open questions that are due to the complexity of the interfacial phenomena which are involved. One of the most important goals in microfluidics of droplets, is the their complete motion control. For achieve this, it is crucial to know the device surface proprieties, both from chemical and physical point of view. For this reason, we have firstly studied the different shape of droplets confined on pillars having circular and square cross sections and different wettabilities. For the realization of the sample, we first prepared masters by micro-EDM and then we made the final structures by soft-lithography with PDMS. We observed that, in the case of a circular profile, the contact line is pinned to the whole edge, as predicted by the Gibbs criteria, while in the presence of corners, the contact line can spill along the vertical walls.
Another important effect involving droplets confined on elongate structures, is the morphological transition that was experimentally and numerically illustrated in Chapter 4. For this study we realized rectangular posts having hydrophobic walls and hydrophilic top surface, combining different materials and microfabrication techniques. In detail, we observed that the morphological transition between the two states, filament and bulge, occurs for all the aspect ratios ℓ, but only for $\ell > 16$, it is shown a bistability of the two states at the same volume. The experimental results were in good agreement with the numerical simulations. Furthermore, we started to investigate the dynamic of the transition, induced by oscillations, observing that for post with $\ell > 16$, it is possible to induce the transition by the oscillation, without change the volume.

Moreover, with the aim to control the droplet motion, we compared the behavior of sliding droplets on homogeneous and chemically patterned surfaces. In particular, glass surfaces were functionalized with organic molecules by microcontact printing, in order to obtain patterns of hydrophilic and hydrophobic stripes. On these surfaces, droplets show the stick-slip motion, which causes the deformation of their shapes. Comparing this behavior with sliding droplets on homogeneous surfaces, we observed that the stick-slip introduces an extra friction imputable to the dissipation of energy at the contact line. To validate this insight, we will compare our results with Lattice Boltzmann numerical simulations.
Also in closed microfluidic systems, the droplets can be manipulated by posts and obstacles placed inside channels. With the aim to study these effects, in the work described in Chapter 6 we focused the attention to define all the ingredients necessary to produce monodisperse droplets at different flow rates, using T-shape junctions. Working with water and organic phases in PDMS devices, we investigated the swelling problem, which causes deformation of the channels. After the development of a reliable protocol for production of droplets in T-junction, we started to study their interaction with obstacles, as innovative way for tuning their break-up.
Finally in Chapter 7 is presented a stable and versatile method which allows to change the wetting proprieties of thiolene resins. In particular we focused on NOA, a commercial available resin, which presents a contact angle of 70°. Using chlorosilane chemistry, we changed its wettability to a more hydrophilic and to hydrophobic contact angles. Additionally, we demonstrated that this strategy can be apply both to open and closed microfluidic devices.

Concluding, we would like to stress that the interest on droplet microfluidics has been enormously and rapidly growing at least for the last decade despite of a detailed, quantitative comprehension of the basic mechanisms underlying the control of microdroplets.
Partially inspired by these considerations we tried to follow a systematic approach for studying the properties of the interfaces, based from one hand on the development of suitable microfabrication strategies, and from the other hand on the comparison of the experimental results to the numerical simulation and predictions.

We do believe that this route may reveal very promising also for the new challenges in multiphase fluids under confinement for which it is the time of more quantitative and comprehensive methods involving physical, chemical, and engineering details.

Appendix A

Contact angle measure

The contact angles presented in this thesis are measured with a homemade apparatus, which is showed in Figure A.1a. It is composed of a high resolution camera (MANTA G-146B), equipped with a telecentric objective. The sample is positioned on a sample stage and its vertical and horizontal positions could be finely adjusted with manual translation stages. A droplet of 1 µL is gently placed on the surface, by a syringe, having capacity of 500 µL (provided by SGE Analytical Science), mounted on a vertical syringe pump (provided by World Precision Instruments). The drop is illuminated by a LED blue backlight (provided by CCS America), which aligned with the telecentric objective, allows a good contrast of the droplet shape. In particular, the droplet appears completely black on the white background, as shown in Figure A.1b. The images collected are analyzed off line by a homemade program, written with LabVIEW (by Na-

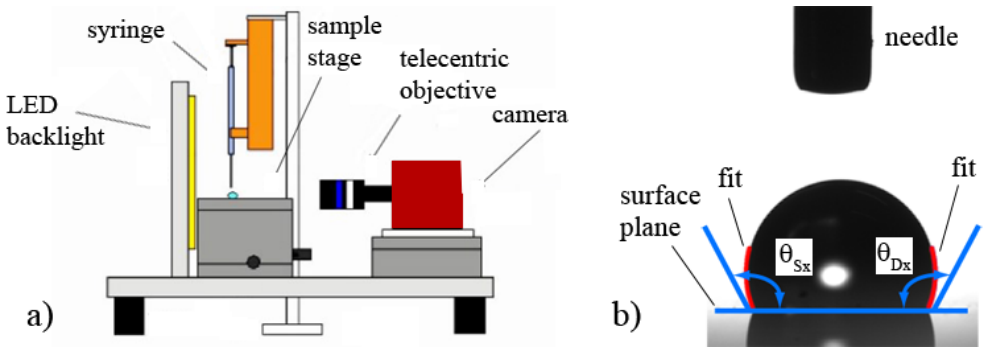

Figure A.1: a) Scheme of the homemade apparatus used in this thesis to measure the contact angles; b) example of droplet placed on flat surface. The contact angle is evaluated as the mean value between θ_{Sx} and θ_{Dx}.

tional Instruments). In detail, the program finds the droplet profile, comparing the pixel grayscales of the image with a threshold previously fixed. Then, it fits the profile with two polynomial functions of tunable degree, one for the left and one for the right side of the droplet and calculates the derivates in the points of intersection between the fits and the surface plane. The two contact angles are evaluated from the slope of the derivatives, as shown in Figure A.1b. In order to characterize a surface, it is necessary to collect data from at least five droplets in different positions on that surface, such as, the final contact angle is represented by the mean of the different value obtained from every droplet. In this way, the standard deviation of the measure is representative of the surface uniformity.

Appendix B

Capillary filling in patterned microchannels

In this Appendix there are illustrated the results of a systematic experimental work aimed to investigate the shape of air/water meniscus moving in microchannel patterned with different geometric posts. First, the microfabrication procedure and the experimental setup are introduced and then some quantitatively results are presented.

B.1 Introduction

One of the most critical steps working with microfluidic devices is their filling. Indeed, it is highly probable the formation of bubbles which can compromise the correct operation. Normally, this occurs when the liquid meniscus finds an obstacle during the first filling of the channel. For this reason, in recent years the filling of microchannels, patterned with posts or ridges, has been the subject of intensive work motivated by the rich phenomenology observed in numerical simulations [44, 159] and by its technological interest, e.g. design of micro-injection molding in capillaries [160] and of channel geometries which prevent air bubbles [161].

As already described in Chapter 1, although several numerical works have been made on the pinning in microchannels, from the experimental point of view this problem has not been analyzed quantitatively. For this reason, we started to study the behavior of a water/air meniscus moving in microchannels with obsta-

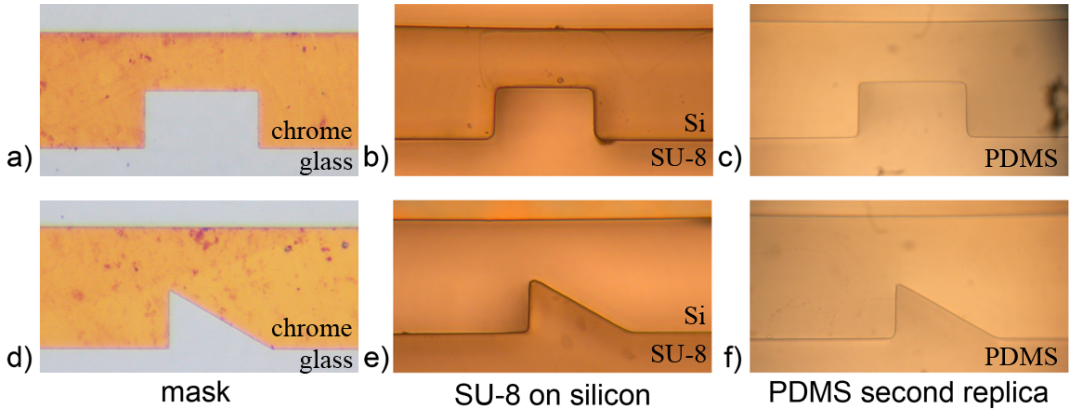

Figure B.1: Images of microchannels drawn on mask a) d), reproduced with SU-8 b) e) and replicated with PDMS c) f) having rectangular and triangular posts.

cles of different shapes: rectangular and asymmetric triangular.

B.2 Microfabrication of PDMS microchannels

We produced two types of microfluidic devices, with an obstacle inside having rectangular and asymmetric triangular shapes. In particular, we used the same double step approach described in Chapter 6: first, we made SU-8 masters by photolithography and then we obtained the final samples in PDMS by double replica molding. Finally, the channels were closed with a glass slide having a thin layer of PDMS (about 40 μm) and two polyethylene tubes were fixed as inlet and outlet. Figure B.1 shows the chromium masks, the SU-8 masters and the final PDMS channels in proximity to the obstacles. The realized channels showed a square cross section of 100x100 μm and the inside posts extended until half of the width of the channel (50 μm).

B.3 Experimental setup

To observe the meniscus advancing inside of the channel, we used the same optical setup described in Chapter 6.
During the data acquisition we wanted to observe the shape of meniscus advancing as function of the difference of pressure inside the channel. For this reason we chose to fill the channel using the Microfluidic Control System (MFCS) provided by Fluigent, described in Chapter 6, instead of a normal syringe pump.

The acquired images have been processed using a homemade program written with the Interactive Data Language programming language (IDL) [162]. In particular, it allows to detect the meniscus along a line previously selected, comparing the brightness of every pixel of the line with a fixed threshold. In this way it was possible to retrace the meniscus position for every image.

B.4 Characterization of the meniscus shape in patterned microchannels

We evaluated the pressure difference inside a microchannel, necessary for the water/air meniscus to overcome the posts. The channels were kept in an oven at 80 °C for at least 2 hours to dry completely their surface. Then, we filled the channels at a fixed pressure which remain unchanged until the meniscus stopped somewhere. At this point, we increased the pressure of steps of 1 mbar, waiting again that it stopped. Figure B.2a shows the image sequences acquired with of water/air meniscus, moving on rectangular post and increasing the pressure. Convex meniscus shape is due to the channel hydrophobicity. Figure B.3a shows the plot of the meniscus position, evaluated halfway between the post and the top channel border, as function of the difference of pressures applied. Comparing Figures B.2a and B.3a, it is possible to see that the meniscus stops when it finds the post, however 7 mbar are sufficient to move it. While in case of the pinning at the end of the post, it is necessary to increase the pressure up to 15 mbar to observe the depinning. Before this pressure, the meniscus increases the curvature, but without dethatching from the obstacle.

The same evaluation was done for the channel with triangular post. Additionally, in this case we tried to pump the water from both directions, as shown in Figure B.2b,c. As seen in the Figure B.3b, the difference of pressure necessary to overcame the obstacle is different for the two directions: when the meniscus moves from right to left it needs a higher pressure (22 mbar), while when it moves from left to right the pressure required is lower (15mbar). This is due to the different shapes of the obstacle that the meniscus finds during the filling and confirms the simulation results described in [44]. Moreover, looking more carefully at the image sequence it is possible to notice that the meniscus are not pinned exactly on the edge, but slightly under it, as expected from the simulation results of the

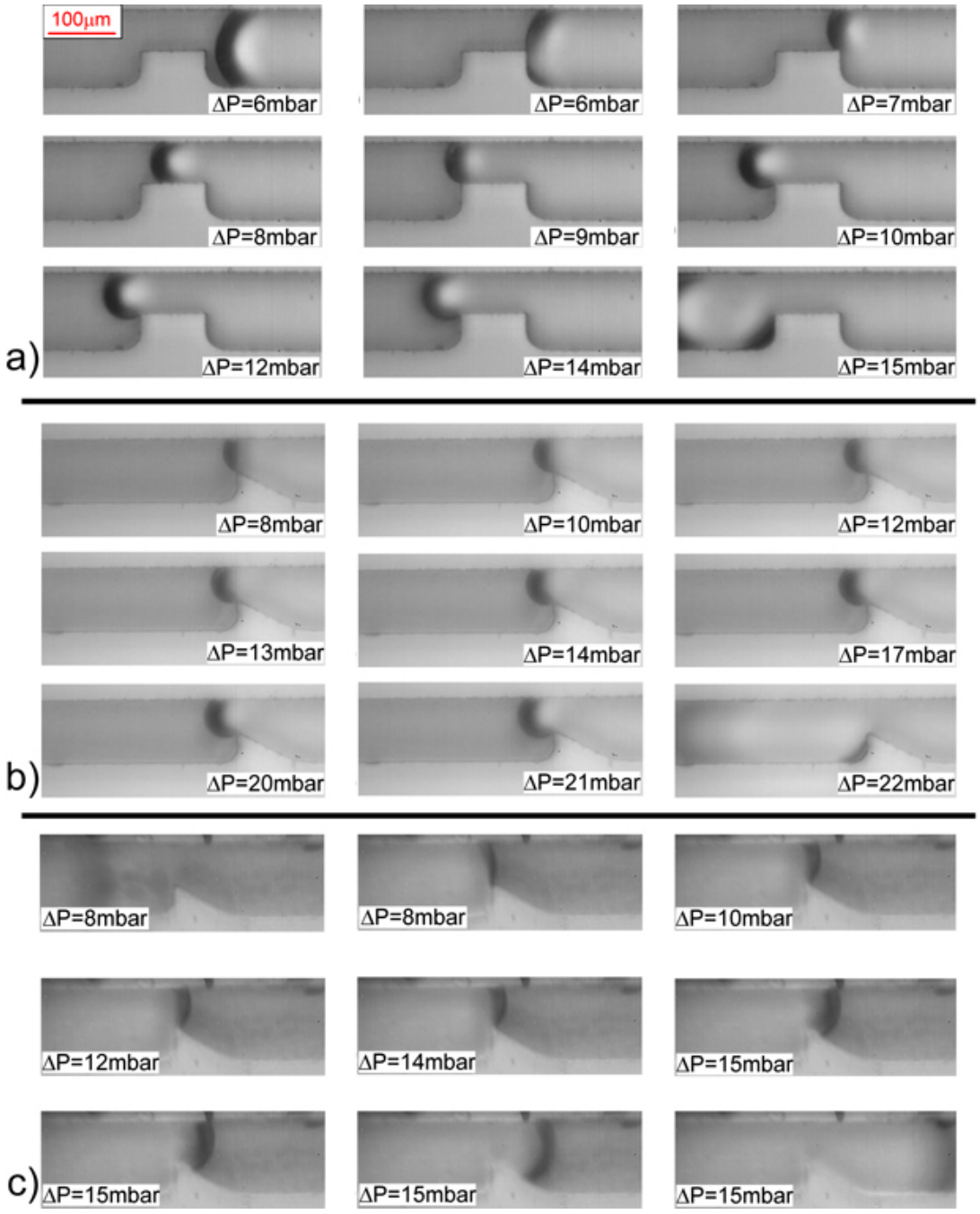

Figure B.2: Image sequence show the advance of the meniscus along the channels with rectangular a) triangular b) c) obstacles. In particular, in this last case, water is pumped from right b) and from left c).

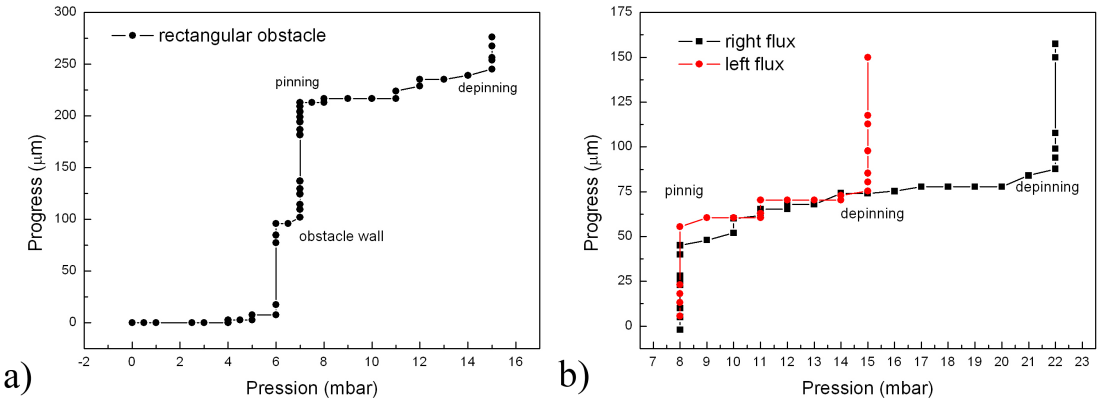

Figure B.3: Space which the meniscus covered as function of the difference of pressures applied; in particular, graphs are related to channels with rectangular a) and triangular b) obstacles, filling from the two directions.

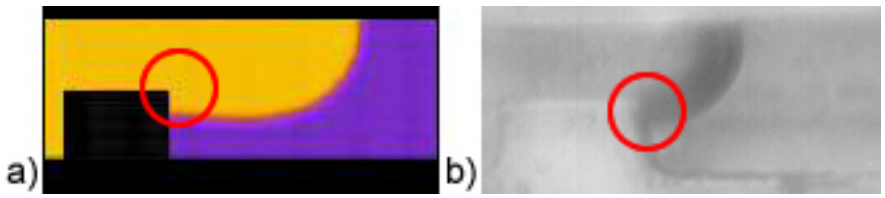

Figure B.4: Comparison between simulation a) and experimental b) results of the meniscus shape stopped by the obstacle.

group of Prof. Biferale [47], as shown in Figure B.4.

B.5 Conclusions

This Appendix describes a quantitatively work to confirm the simulation results presented in literature and to evaluate the efficiency of our experimental apparatus. In detail, we realized an experimental study of the meniscus shape in proximity of the obstacles and as expected, we observed that the pinning effect strongly depend on the post geometry, proving the Lattice-Boltzmann simulation results.

The experimental procedure and the reproducibility of the manufacturing process can be considered well established. Therefore, particular attention will be paid to combine this kind of patterned channels with droplet microfluidic studies, with the aim to observe the interaction between droplets and different types of obstacles.

Bibliography

[1] J. Bibette, F.L. Calderon, and P. Poulin. *Rep. Prog. Phys.*, 62:969–1033, 1999.

[2] R. Dangla, F. Gallaire, and C.N. Baroud. *Lab Chip*, 10:2032–2045, 2010.

[3] V. Chokkalingam, B. Weidenhof, M. Krämer, W.F. Maier, S. Herminghaus, and R. Seemann. *Lab Chip*, 10:1700–1705, 2010.

[4] C. Zhang, J. Xu, and W. Maand W. Zheng. *Biotechnol Adv.*, 24:243–284, 2005.

[5] G.F. Christopher and S.L. Anna. *J. Phys. D Appl. Phys.*, 40:R319–R336, 2007.

[6] N. Pannacci, H. Bruus, D. Bartolo, I. Etchart, T. Lockhart, Y. Hennequin, H. Willaime, and P. Tabeling. *Phys. Rev. Lett.*, 101:164502, 2008.

[7] J. Goyon, A. Colin, G. Ovarlez, A. Ajdari, and L. Bocquet. *Nature*, 454:84–87, 2008.

[8] M. Zhang, J. Wu, X. Niu, W. Wen, and P. Sheng. *Phys. Rev. E*, 78:066305, 2008.

[9] R. Seemann, M. Brinkmann, T. Pfohl, and S. Herminghaus. *Rep. Prog. Phys.*, 75:016601, 2012.

[10] Nanoscribe - True 3D Laser Lithography. `http://www.nanoscribe.de/`.

[11] `http://summertomato.com/tag/mayonnaise/`.

[12] S.Y. Teh, R. Lin, L.H. Hung, and A.P. Lee. *Lab Chip*, 8:198–220, 2008.

[13] N. Pannacci, H. Bruus, D. Bartolo, I. Etchart, T. Lockhart, Y. Hennequin, H. Willaime, and P. Tabeling. *Phys. Rev. Lett.*, 101:164502, 2008.

[14] N. Bremond, A.R. Thiam, and J. Bibette. *Phys. Rev. Lett.*, 100:024501, 2008.

[15] M. Prakash and N. Gershenfeld. *Science*, 315:832–835, 2007.

[16] M. Rauscher, S. Dietrich, and J. Koplik. *Phys. Rev. Lett.*, 98:224504, 2007.

[17] R. Ledesma-Aguilar, R. Nistal, A. Hernández-Machado, and I. Pagonabarraga. *Nat. Mater.*, 10:367–371, 2011.

[18] R. Seemann, M. Brinkmann, E.J. Kramer, F.F. Lange, and R. Lipowsky. *Proc. Natl. Acad. Sci. U.S.A.*, 102:1848–1852, 2005.

[19] H. Gau, S. Herminghaus, P. Lenz, and R. Lipowsky. *Science*, 283:46–49, 1999.

[20] L.Y. Yeo and J.R. Friend. *Biomicrofluidics*, 3:012002, 2009.

[21] S.C.C. Shih, H. Yang, M.J. Jebrail, R. Fobel, N. McIntosh, O.Y. Al-Dirbashi, P. Chakraborty, and A.R. Wheeler. *Anal. Chem.*, 84:3731–3738, 2012.

[22] F. Mugele and J.C. Baret. *J. Phys.: Condens. Matter*, 17:R705–R774, 2005.

[23] N.A. Mousa, M.J. Jebrail, H. Yang, M. Abdelgawad, P. Metalnikovand, J. Chen, A.R. Wheeler, and R.F. Casper. *Sci. Transl. Med.*, 1:368–373, 2009.

[24] S.Srigunapalan, I.A. Eydelnant, C.A. Simmons, and A.R. Wheeler. *Lab Chip*, 12:369–375, 2012.

[25] M. Vallet, M. Vallade, and B. Berge. *EPJ B*, 11:583–591, 1999.

[26] T.D. Luong and N.T. Nguyen. *Langmuir*, 2(3):217–225, 2010.

[27] P. Brunet, J. Eggers, and R.D. Deegan. *The European Physical Journal Special Topics*, 166(1):11–14, 2009.

[28] E. Singer. Novel chip for monitoring breast cancer. *MIT Tech. Rev.*, 2009.

[29] P.K. Kundu, I.M. Cohen, and D.R. Dowling. *Fluid Mechanics - Fifth edition.* Elsevier, 2012.

[30] P. Tabeling. *Introduction to Microfluidics.* Oxford University Press, 2005.

[31] A.E. Kamholz and P. Yage. *Biophys. J.*, 80:155–160, 2001.

[32] P.J.A. Kenis, R.F. Ismagilov, and G.M. Whitesides. *J. Micromech. Microeng.*, 285:83–85, 1999.

[33] M.R. Bringer, C.J. Gerdts, H. Song, J.D. Tice, and R.F. Ismagilov. *Phil. Trans. R. Soc. Lond.*, 362:1087–1104, 2004.

[34] P.G. de Gennes, F. Brochard-Wyart, and D. Quere. *Capillarity and Wetting Phenomena.* Springer, 2004.

[35] C. Cramer, P. Fischer, and E.J. Windhab. *Chemical Engineering Science*, 59:3045–3058, 2004.

[36] C. Schäfle, M. Brinkmann, C. Bechinger, P. Leiderer, and R. Lipowsky. *Langmuir*, 26:11878–11885, 2010.

[37] A. Klingner and F. Mugele. *J. Appl. Phys.*, 95:2918–2920, 2004.

[38] J.C. Baret, M.M. J. Decré, S. Herminghaus, and R. Seemann. *Langmuir*, 23:5200–5204, 2007.

[39] K. Khare, S. Herminghaus, J.C. Baret, B.M. Law, M. Brinkmann, and R. Seemann. *Langmuir*, 26:12997–13006, 2007.

[40] T. Young. *Phil. Trans. R. Soc. Lond.*, 95:65–87, 1805.

[41] R.N. Wenzel. *Ind. Eng. Chem.*, 28:988–994, 1936.

[42] A.B.D. Cassie and S. Baxter. *Trans. Faraday Soc.*, 40:546–551, 1944.

[43] Y.T. Cheng, D.E. Rodak, C.A. Wong, and C.A. Hayden. *Nanotechnology*, 17:1359–1362, 2006.

[44] H. Kusumaatmaja, C.M. Pooley, S. Girardo, D. Pisignano, and J.M. Yeomans. *Phys. Rev. E*, 77:067301, 2008.

[45] B.M. Mognetti and J.M. Yeomans. *Soft Matter*, 6:2400–2402, 2010.

[46] F. Diotallevi, L. Biferale, S. Chibbaro, G. Pontrelli, F. Toschi, , and S. Succi. *Eur. Phys. J. special topics*, 171:237–243, 2009.

[47] Courtesy of L. Biferale - Department of Physics & CAST, University of Rome "Tor Vergata".

[48] C.G.L. Furmidge. *J. Coll. Sci.*, 17:309–324, 1962.

[49] N. Le Grand, A. Daerr, and L. Limat. *J. Fluid Mech.*, 541:293–315, 2005.

[50] S. Suzuki, A. Nakajima, M. Sakai, J. Song, N. Yoshida, Y. Kameshima, and K. Okada. *Surf. Sci.*, 600:2214 – 2219, 2006.

[51] T. Podgorski, J. M. Flesselles, and L. Limat. *Phys. Rev. Lett.*, 87:036102, 2001.

[52] S.R. Annapragada, J.Y. Murthy, and S.V. Garimella. *Int. J. Heat Mass Tran.*, 55:1466 – 1474, 2012.

[53] Y.Y. Koh, Y.C. Lee, P.H. Gaskell, P.K. Jimack, and H.M. Thompson. *Eur. Phys. J. S.T.*, 166:117–120, 2009.

[54] A.K. Das and P.K. Das. *Langmuir*, 25:11459–11466, 2009.

[55] M.T. Guo, A. Rotem, J.A. Heymanab, and D.A. Weitz. *Lab Chip*, 12:2146–2155, 2012.

[56] S. Xu, Z. Nie, M. Seo, P. Lewis, E. Kumacheva, H. A. Stone, P. Garstecki, D.B.Weibel, I. Gitlin, and G.M. Whitesides. *Angew. Chem.*, 117:734–738, 2005.

[57] C. Priest, S. Herminghaus, and R. Seemann. *Appl. Phys. Lett.*, 88:024106, 2006.

[58] T. Thorsen, R.W. Roberts, F.H. Arnold, and S.R. Quake. *Phys. Rev. Lett.*, 86:4163–4166, 2001.

[59] T. Nisisako, T. Torii, T. Takahashi, and Y. Takizawa. *Adv. Mater.*, 18:1152–1156, 2006.

[60] S. Yeom and S. Y. Lee. *EXP. Therm. Fluid Sci.*, 35:387–394, 2011.

[61] S.L. Anna, N. Bontoux, , and H.A. Stone. *Appl. Phys. Lett.*, 82:364–366, 2002.

[62] A. Gupta and R. Kumar. *Microfluid. Nanofluid.*, 8:799–812, 2010.

[63] A. Gupta and R. Kumar. *Phys. Fluids*, 22:122001, 2010.

[64] M. De Menech, P. Grastecki, F. Jousse, and H.A. Stone. *J. Fluid Mech.*, 595:141–161, 2008.

[65] G.F. Christopher, N.N. Noharuddin, J.A. Taylor, and S.L. Anna. *Phys. Rev. E*, 78:036317, 2008.

[66] P. Garstecki, M.J. Fuerstman, H.A. Stone, and G. M. Whitesides. *Lab Chip*, 6:437–446, 2006.

[67] L.W. Schwartz, H.M. Princen, and A.D. Kiss. *J. Fluid Mech.*, 172:259–275, 1986.

[68] A.L. Hazel and M. Heil. *J. Fluid Mech.*, 470:91–114, 2002.

[69] F. Jousse, G.P. Lian, R. Janes, and J. Melrose. *Lab Chip*, 5:645–656, 2005.

[70] X. Niu, S. Gulati, J.B. Edel, and A.J. deMello. *Lab Chip*, 8:1837–1841, 2008.

[71] S. Protière, M.Z. Bazant, D.A. Weitz, and H.A. Stone. *EPL*, 92:54002, 2010.

[72] M. Kunieda, B. Lauwers, K.P. Rajurkar, and B.M. Schumacher. *Annals of the CIRP*, 54:64–87, 2005.

[73] D.T. Pham, S.S. Dimov, S. Bigot, A. Ivanov, and K. Popov. *J. Mater. Process. Tech.*, 149:50–57, 2004.

[74] K.P. Rajurkar, G. Levy, A. Malshe, M.M. Sundaram, Hu X. McGeough, J., R. Resnick, A.E. De Silva, S. Piltz, and U. Doll. *Annals of the CIRP*, 55:643–666, 2006.

[75] M.J. Madou. *Fundamentals of microfabrication: the science of miniaturization (Second edition).* CRC press, 2002.

[76] P. Abgrall, C. Lattes, V. Conédéra, X. Dollat, Colin S., and A.M. Gué. *J. Micromech. Microeng.*, 16:113–121, 2006.

[77] A.D. Stroock, S.K.W. Dertinger, A. Ajdari, I. Mezic, H.A. Stone, and G.M. Whitesides. *Science*, 295:647–651, 2002.

[78] SU-8 50-100 Data Sheet. `http://microchem.com/`.

[79] Y. Xia and G.M. Whitesides. *Annu. Rev. Mater. Sci.*, 28:153–184, 1998.

[80] D. Bodas and C. Khan-Malek. *Sensor Actuator B Chem.*, 123:368–373, 2007.

[81] E. Delamarche, H. Schmid, B. Michel, and H. Biebuyck. *Adv. Mater.*, 9:741–746, 1997.

[82] SYLGARD 184 Data Sheet. `http://www.dowcorning.com`.

[83] J.N. Lee, C. Park, and G.M. Whitesides. *Anal. Chem.*, 75:6544–6554, 2003.

[84] A.R. Abate, D. Lee, T. Do, C. Holtze, and D.A. Weitz. *Lab Chip*, 8:516–518, 2008.

[85] Y. Huang, P. Castrataro, C.C. Lee, and S.R. Quake. *Lab Chip*, 7:24–26, 2007.

[86] G.S. Fiorini, R. Lorenz, J.S. Kuo, and D.T. Chiu. *Anal. Chem.*, 76:4697–4704, 2004.

[87] Norland Products website. `https://www.norlandprod.com/`.

[88] Z.T. Cygan, J.T. Cabral, K.L. Beers, and E.J. Amis. *Langmuir*, 21:3629–3634, 2005.

[89] C.E. Hoyle and C.N. Bowman. *Angew. Chem. Int. Ed.*, 49:1540–1573, 2010.

[90] C. Harrison, J.T. Cabral, C.M. Stafford, A. Karim, and E.J. Amis. *J. Micromech. Microeng.*, 14:153–158, 2004.

[91] D. Bartolo, G. Degré, P. Nghe, and V. Studer. *Lab Chip*, 8:274, 2008.

[92] N.T. Nguyen and Wereley. S.T. *Fundamentals and Applications of Microfluidics*. Artech House Publishers, 2002.

[93] Y. Xia, M. Mrksich, E. Kim, and G.M. Whitesides.

[94] N.L. Jeon, k. Finnie, k. Branshaw, and R.G. Nuzzo. *Langmuir*, 13:3382–3391, 1997.

[95] G.P. López, H. A. Biebuyck, C.D. Frisbie, and G.M. Whitesides. *Science*, 260(5108):647–649, 1993.

[96] K.R. Finnie, R. Haasch, and R.G. Nuzzo. *Langmuir*, 16:6968–6976, 2000.

[97] C.D. James, R.C. Davis, L. Kam, H.G. Craighead, M. Isaacson, and W. Turner, J.N. Shain. *Langmuir*, 14:741–744, 1998.

[98] Y. Xia, E. Kim, X.M. Zhao, J.A. Rogers, M. Prentiss, and G.M. Whitesides. *Science*, 273:347–349, 1996.

[99] Y. Xia, J.J. McClelland, R. Gupta, D. Qin, X.M. Zho, L.L. Sohn, R.J. Celotta, and G.M. Whitesides. *Adv. Mater.*, 9:147–149, 1997.

[100] J.C. McDonald, D.C. Duffy, J.R. Anderson, D.T. Chiu, H. Wu, O.J.A. Schueller, and G.M. Whitesides. *Electrophoresis*, 21:27–40, 2000.

[101] S. Shibuichi, T. Onda, N. Satoh, and K. Tsuji. *J. Phys. Chem.*, 100:19512–19517, 1996.

[102] M. Sun, C. Luo, L. Xu, H. Ji, Q. Ouyang, D. Yu, and Y. Chen. *Langmuir*, 21:8978–8981, 2005.

[103] A. Pozzato, S. Dal Zilio, G. Fois, D. Vendramin, G. Mistura, M. Belotti, Y. Chem, and M. Natali. *Microelectron. Eng.*, 83:884–888, 2006.

[104] P. Roach, N.J. Shirtcliffe, and Newton M.I. *Soft Matter*, 4:224–240, 2008.

[105] X. Feng and Jiang. L. *Adv. Mater.*, 18:3063–3078, 2006.

[106] F. C. Cebeci, Z.Z. Wu, L. Zhai, R.E. Cohen, and M.F. Rubner. *Langmuir*, 22:2856–2862, 2006.

[107] C.W. Extrand, S.I. Moon, P. Hall, and D. Schmidt. *Langmuir*, 23:8882–8890, 2007.

[108] R. Wang, K. Hashimoto, A. Fujishima, M. Chikuni, E. Kojima, A. Kitamura, M. Shimohigoshi, and T. Watanabe. *Nature*, 388:431–432, 1997.

[109] H.S. Lim, J.T. Han, D. Kwak, M. Jin, and K. Cho. *J. Am. Chem. Soc.*, 128:14458–14459, 2006.

[110] D. Dattilo, L. Armelao, G. Fois, G Mistura, and M. Maggini. *Langmuir*, 23:12945–12950, 2007.

[111] T.L. Sun, H.A. Liu, W.L. Song, X. Wang, L. Jiang, L. Li, and D.B. Zhu. *Angew. Chem., Int. Ed.*, 43:357–360, 2004.

[112] Q. Fu, G.V. Rama Rao, S.B. Basame, D.J. Keller, K. Artyushkova, J.E. Fulghum, and G.P. López. *J. Am. Chem. Soc.*, 126:8904–8905, 2004.

[113] A. Podestá, G. Bongiorno, P.E. Scopelliti, S. Bovio, P. Milani, C. Semprebon, and G. Mistura. *J. Phys. Chem. C*, 113:18264–18269, 2009.

[114] J. Drelich, J.L. Wilbur, J. D. Miller, and G.M. Whitesides. *Langmuir*, 12:1913–1922, 1996.

[115] S. Brandon, N. Haimovich, E. Yeger, and A. Marmur. *J. Colloid Iterf. Sci.*, 263:237–243, 2003.

[116] M. Morita, T. Koga, H. Otsuka, and A. Takahara. *Langmuir*, 21:911–918, 2005.

[117] Y. Chen, b. He, J. Lee, and N.A. Patankar. *J. Colloid Iterf. Sci.*, 281:458 – 464, 2005.

[118] J.Y. Chung, J. P. Youngblood, and C.M. Stafford. *Soft Matter*, 3:1163–1169, 2007.

[119] H. Kusumaatmaja, R. J. Vrancken, C. W. M. Bastiaansen, and J.M. Yeomans. *Langmuir*, 24:7299–7308, 2008.

[120] C. Semprebon, G. Mistura, E. Orlandini, G. Bissacco, A. Segato, and J.M. Yeomans. *Langmuir*, 25:5619–5625, 2009.

[121] J.F. Oliver, C. Huh, and S.G. Mason. *Journal of Colloid and Interface Science*, 59:568 – 581, 1977.

[122] C.W. Extrand. *Langmuir*, 21:10370–10374, 2005.

[123] J. Zhang, X. Gao, and L. Jiang. *Langmuir*, 23:3230–3235, 2007.

[124] J. Du, S. Michielsen, and H.J. Lee. *Langmuir*, 26:16000–16004, 2010.

[125] T.S. Wong, A.P.H. Huang, and C.M. Ho. *Langmuir*, 25:6599–6603, 2009.

[126] C.W. Extrand. *Langmuir*, 18:7991–7999, 2002.

[127] Yevgeniy V. Kalinin, Viatcheslav Berejnov, and Robert E. Thorne. *Langmuir*, 25:5391–5397, 2009.

[128] Kenneth A. Brakke. *Exp. Math.*, 1:141–165, 1992.

[129] T. Tóth, D. Ferraro, E. Chiarello, M. Pierno, G. Mistura, G. Bissacco, and C. Semprebon. *Langmuir*, 27:4728–4742, 2011.

[130] D. Ferraro, C. Semprebon, T. Tóth, E. Locatelli, M. Pierno, G. Mistura, and M. Brinkmann. *Langmuir*, 28:13919–13923, 2012.

[131] Y.J. Chuang, F.G. Tseng, and W.K. Lin. *Microsyst. Technol.*, 8:308–313, 2002.

[132] M. Mattox. *Handbook of Physical Vapor Deposition (PVD) Processing - Second Edition*. Elsevier, 2010.

[133] M. Natali, S. Begolo, T. Carofiglio, and G. Mistura. *Sens. Actuators B*, 8:492–494, 2008.

[134] M.L. White. *J. Phys. Chem.*, 68:3083–3085, 1964.

[135] E. Cheng, G. Mistura, H.C. Lee, M.H.W. Chan, C. Cole, M.W. Carraro, W.F. Saam, and F. Toigo. *Phys. Rev. Lett.*, 70:1854–1857, 1993.

[136] G. Mistura, H.C. Lee, and M.H.W. Chan. *J. Low Temp. Phys.*, 96:221–244, 1994.

[137] A. Checco, Y. Cai, O. Gang, and B.M. Ocko. *Ultramicroscopy*, 106:703–708, 2006.

[138] X. Noblin, A. Buguin, and F. Brochard-Wyart. *Eur. Phys. J. Special Topics*, 166:7–10, 2009.

[139] P. Abbyad, R. Dangla, A. Alexandrou, and C.N. Baroud. *Lab Chip*, 11:813–821, 2011.

[140] G.P. López, H.A. Biebuyck, C.D. Frisbie, and G. M. Whitesides. *Science*, 206:647–649, 1993.

[141] H.J. Butt, B. Cappella, and M. Kappl. *Surf. Sci. Rep.*, 59:1–152, 2005.

[142] H.Y. Kim, H.J. Lee, and B.H. Kang. *J. Colloid Interf. Sci.*, 247:372–380, 2002.

[143] Delta Mask - Chorme Masks. `http://www.deltamask.nl/`.

[144] FLUIGENT. `http://www.fluigent.com/`.

[145] DBBST GmbH - Dortmund Data Bank. `http://ddbonline.ddbst.de/`.

[146] J.H. Xu, S.W. Li, J. Tan, Y.J. Wang, and G.S. Luo. *Langmuir*, 22:7943–7946, 2006.

[147] D.A. Weitz D.R. Link, S.L. Anna and H.A. Stone. *Phys. Rev. Lett.*, 92:054503, 2004.

[148] T. Nisisako, S. Okushima, and T. Torii. *Soft Matter*, 1:23–27, 2005.

[149] S. Okushima, T. Nisisako, T. Torii, and T. Higuchi. *Langmuir*, 20:9905–9908, 2004.

[150] V. Barbier, M. Tatoulian, H. Li, F. A. Khonsari, A. Ajdari, and P. Tabeling. *Langmuir*, 22:5230–5232, 2006.

[151] M. Seo, C. Paquet, Z. Nie, S. Xu, and E. Kumacheva. *Soft Matter*, 3:986–992, 2007.

[152] L. Brigo, T. Carofiglio, C. Fregonese, F. Meneguzzi, G. Mistura, M. Natali, and U. Tonellato. *Sens. Actuators B*, 130:447–482, 2008.

[153] L.H. Hung, R. Lin, and A. P. Lee. *Lab Chip*, 8:983–987, 2008.

[154] B. Levaché, A. Azioune, M. Bourrel, V. Studer, and D. Bartolo. *Lab Chip*, 12:3028–3031, 2012.

[155] T. Carofiglio, P. Donnola, M. Maggini, M. Rossetto, and E. Rossi. *Adv. Synth. Catal.*, 350:2815–2822, 2008.

[156] E. Rossi, T. Carofiglio, A. Venturi, A. Ndobe, M. Muccini, and M. Maggini. *Energy Environ. Sci.*, 4:725–727, 2011.

[157] S. Silvestrini, D. Ferraro, T. Tóth, M. Pierno, T. Carofiglio, G. Mistura, and M. Maggini. *Lab Chip*, 12:4041–4043, 2012.

[158] S. Silvestrini. *Microfluidic Devices: Compact Laboratories from Design to Application*. PhD thesis, 2012.

[159] S. Chibbaro, E. Costa, D.I. Dimitrov, F. Diotallevi, A. Milchev, D. Palmieri, G. Pontrelli, and S. Succi. *Langmuir*, 25:12653–12660, 2009.

[160] F. Goldschmidtboeing, M. Rabold, and P. Wojas. *J. Micromech. Microeng.*, 16:1321–1330, 2006.

[161] D. S. Kim, K-C. Lee, T. H. Kwon, and S. S. Lee. *J. Micromech. Microeng.*, 12:236–246, 2002.

[162] ITT Product Services. `http://www.ittvis.com/ProductServices/IDL.aspx/`.

PUBLICATIONS

Langmuir

ARTICLE

pubs.acs.org/Langmuir

Suspension of Water Droplets on Individual Pillars

T. Tóth,[†] D. Ferraro,[†] E. Chiarello,[†] M. Pierno,[†] G. Mistura,[*,†] G. Bissacco,[‡] and C. Semprebon[*,§]

[†]Dipartimento di Fisica G.Galilei, Università di Padova, via Marzolo 8, 35131 Padova, Italy

[‡]Department of Mechanical Engineering, Technical University of Denmark, Produktionstovet, 2800 Kgs-Lyngby, Denmark

[§]Max Plank Institute for Dynamic and Self-Organization, Bünsenstrasse 10, 37073 Göttingen, Germany

ABSTRACT: We report results of extensive experimental and numerical studies on the suspension of water drops deposited on cylindrical pillars having circular and square cross sections and different wettabilities. In the case of circular pillars, the drop contact line is pinned to the whole edge contour until the drop collapses due to the action of gravity. In contrast, on square pillars, the drops are suspended on the four corners and spilling along the vertical walls is observed. We have also studied the ability of the two geometries to sustain drops and found that if we compare pillars with the same characteristic size, the square is more efficient in pinning large volumes, while if we normalize the volumes to pillar areas, the opposite is true.

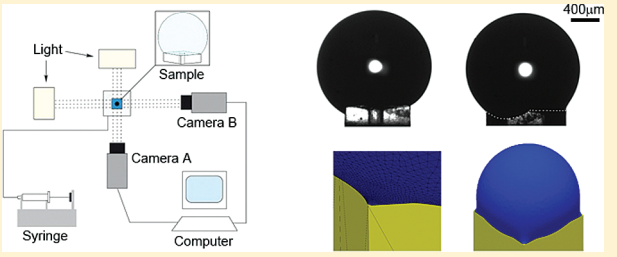

1. INTRODUCTION

A very active field of research in materials science is the realization of surfaces with controlled wettability. By playing with the surface chemical composition and its morphology, it is possible to significantly enhance its hydrophobic (hydrophilic) character, which is usually quantified by the apparent contact angle (Θ) that a water drop forms with the surface. In the past few years, a large variety of superhydrophobic (superhydrophilic) surfaces have been realized, which present a contact angle $\Theta > 150°$ [1−4] ($\Theta < 10°$ [5−7]). More interesting for potential applications is the realization of smart coatings, which can change their wettability when subject to specific external stimuli, like light[8−10] or temperature.[11−13] An essential feature in all of these realizations is the presence of a rough surface.

If the roughness is isotropic, a drop deposited on the surface assumes an almost hemispherical shape and the apparent contact angle is the same as measured in any direction. If the roughness is not isotropic, e.g. parallel grooves, the drop is elongated and the apparent contact angle depends on the direction of observation. Recent studies have focused on the wetting properties of anisotropic patterned surfaces. It was observed that even relatively simple surface topographies such as grooves with a rectangular cross section exhibit a large variety of different wetting morphologies.[14] Analogously, chemically heterogeneous flat surfaces formed by alternating hydrophilic/hydrophobic stripes[15−17] and geometrically structured surfaces characterized by parallel microscopic grooves[18−20] show pronounced anisotropic contact angle hysteresis and elongated drops. To better analyze this anisotropy, we have investigated the wetting of a water drop deposited on top of a single rectangular pillar having a length much longer than its width.[21] The orthogonal contact angle is found to increase with the drop volume; instead the parallel angle practically does not change and coincides with the intrinsic values of the corresponding surfaces.

To further characterize this phenomenology, we have extended our original study to individual pillars of submillimetric size having different cross sections (circular and square). In this case, the drop shape is dominated by the pinning of the contact line to the whole edge contour, which satisfies the Gibbs inequality condition. This geometric condition states that because of the pinning of the contact line, the maximum contact angle (Θ_{max}), which can be measured at a sharp solid edge having an aperture Φ, is equal to $\Theta_{max} = \Theta + (180° - \Phi)$, where Θ is the equilibrium contact angle on the flat surface away from the edge (see Figure 1a). Classic experiments[22] on the equilibrium of liquid drops bound on macroscopic circular cylinders with sharp edges confirmed the validity of the Gibbs condition. These measurements have been recently extended to the study of the suspension of liquid drops by a single frustoconical asperity having a top circular surface of millimeter size.[23] It was established that for the suspension of a drop not only the contact line must be pinned but also that the vertical component of the surface tension must be of sufficient magnitude to hold unsupported liquid against the downward pull of gravity. The stability of drops at the edges of similar asperities was also investigated by pressing the drop with a superhydrophobic surface and was characterized in terms of the critical pressure necessary to depin the contact line.[24] More recently, the profile of liquid drops at the tip of a cylindrical fiber with a submillimiter radius was studied.[25] Finally, the wetting behavior of individual nanostructures with diameters down to the sub-100 nm scale was quantified, and it

Received: January 11, 2011
Revised: February 22, 2011
Published: March 16, 2011

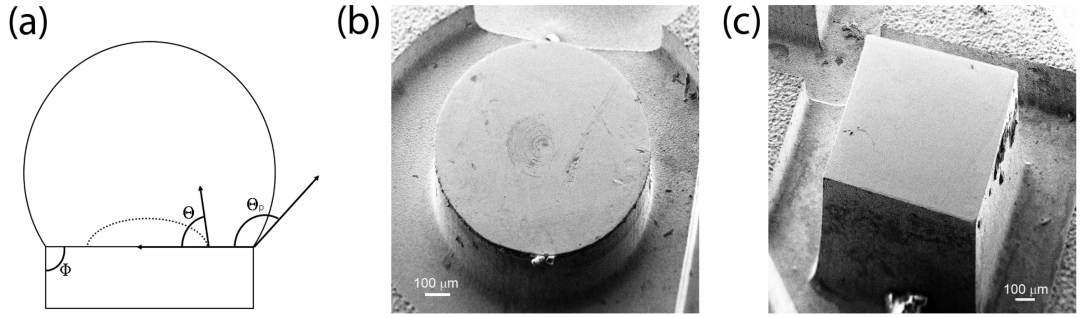

Figure 1. (a) A cross-section of a drop atop a single model pillar showing characteristic angles. SEM view of the circular pillar (b) and of the square pillar (c).

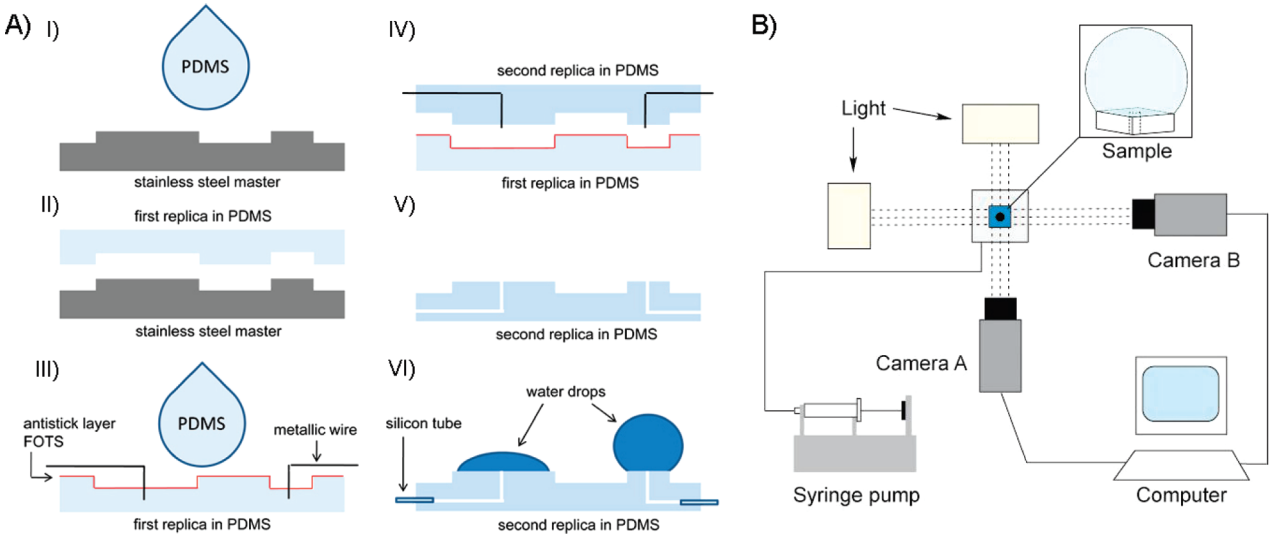

Figure 2. (A) Fabrication process of the pillars in PDMS. (B) Schematic drawing of the optical setup used to image the water drops.

was found that the macroscopic pinning behavior is preserved for nanostructures with dimensions down to about 200 nm.[26] Understanding the pinning of the contact line to geometric edges is essential to explain the numerous morphological wetting transitions observed at ring-shaped surface domains.[27] It is also necessary to design effective superhydrophobic surfaces[28] and to control and enhance the maximum advancing contact angle on surfaces micropatterned with circular polymer rings.[29]

A common feature in all of these studies is the presence of asperities having circular cross sections.[22−29] The aim of this work is instead to provide a first analysis of the profiles of water drops pinned to geometric pillars that have corners. In the following, we present the results of systematic experiments and numerical calculations of the shape of drops deposited on single pillars of different cross sections, from the highly symmetric circular section to the square one, and various wettabilities. After a brief description of the experimental and numerical techniques employed in this study, we present and comment on the main results of our work.

2. METHODOLOGY

A series of individual cylindrical pillars having a characteristic height of 200 μm were fabricated on a stainless steel flat substrate. Pillar geometries were characterized by different shapes (circular and square) and sizes (diameter D = 800 μm and side L = 800 μm, respectively) and have been produced by means of microelectrical discharge machining (μEDM), operated in milling mode. μEDM is a thermal process for contactless material removal of electrically conductive materials.[30] In μEDM the machining of conductive materials is performed by a sequence of electrical discharges occurring in an electrically insulated gap between the tool electrode and the sample. The minimum machinable feature size and maximum accuracy are on the order of 10 and 1 μm, respectively. The morphology of the pillars has been characterized with the profile meter and the scanning electron microscope (SEM). Figure 1 shows magnified views of the two pillars. The root mean squared surface roughness of the top face was less than 1 μm, that of the vertical walls about 3 μm, and finally, that of the contour edge roughness 2 μm.

By a standard double replica molding process, positive copies in polydimethilsiloxane (PDMS) of the stainless steel master were fabricated (see Figure 2A). At first, a negative copy in PDMS was casted by simply pouring over the master a mixture of the prepolymer and the curing agent and then heating the whole system in an oven for 1 h at 80 °C (steps I and II). With the help of a microscope, thin metallic wires (diameter ∼150 μm) were vertically inserted at the center of each cavity (step III). Then, a second replica of PDMS was performed on this assembly in the same manner as the first process (step IV). Before casting, an

dx.doi.org/10.1021/la2001249 |*Langmuir* 2011, 27, 4742–4748

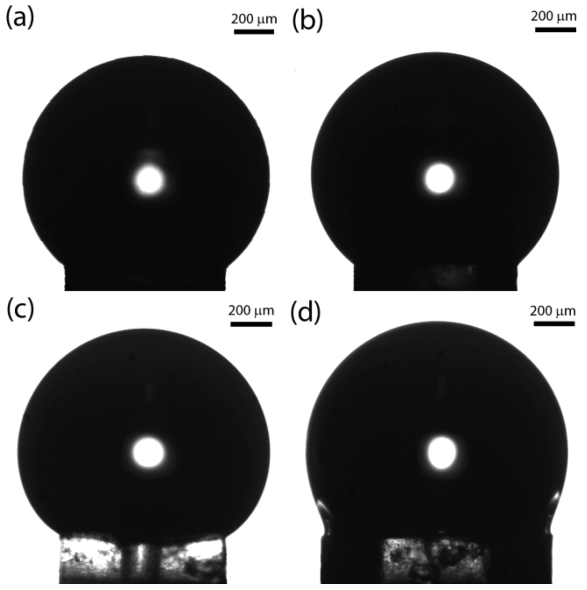

Figure 3. Typical images of water drops on a circular (a, b) and on a square (c, d) cylinder taken from two different directions. Images a and b are taken along two orthogonal directions ($\Theta = 64°$), while image c (d) represents a side (diagonal) view ($\Theta = 68°$).

antistick monolayer of trichloroperfluorooctysilane (FOTS) was evaporated onto the template as a release agent. After solidification, the PDMS layer was peeled off, the wires were gently taken off, and thin tubes were fixed at the extremity of each hole (step V). By connecting them to a syringe pump, a water flow could be induced through the central hole to form a small drop on top of the pillar (step VI). In this way it was possible to easily control the production of drops of known volume. We soon discarded the standard deposition of sessile drops because of a series of drawbacks: (i) the procedure was highly erratic given the small size of the pillar and its hydrophobic nature and (ii) the volume could not be varied continuously. A similar procedure was adopted in the original work by Mason and co-workers,[22] the only difference being that they used much larger pillars by a factor ≥ 10.

The wettability of these pillars was changed by exposure to UV light. The treatment of the PDMS surface was carried out in a commercial ultraviolet/ozone (UVO) cleaner. We found that after 3 h (45 min) in the UVO, the contact angle Θ (see Figure 1a) on flat, untreated PDMS samples decreased from 115° to around 60° (80°), the actual value being explicitly indicated in each case. This change was not permanent: it was stable for a couple of hours and then the surface recovered its initial wetting character on a time scale of several days. The data on the treated surfaces were taken right after the extraction from the UVO and very quickly (within 2 h) to bypass this recovery. To make sure that the surface recovery was negligible, contact angle measurements on flat portions of the sample were taken before and after each acquisition sequence.

Water drop profiles were recorded with the custom-built apparatus schematically shown in Figure 2B. The sample was positioned in the middle and its vertical position could be finely adjusted with a manual translational stage. A small drop of increasing volume V of Milli-Q water was produced on the top face of each pillar with a syringe pump. The drop was illuminated by two back-light collimated LED sources. The drop profile was simultaneously viewed from two different orientations with two high-resolution cameras. In this study, they were oriented at right angles to probe the symmetry of the drop and, with the non-circular pillars, in such a way as to view the drop from one side and from one corner. Figure 3 shows some typical images recorded on a circular and a square pillar. The cameras mounted telecentric lenses, which guarantee a better contrast and a more faithful reproduction of the drop shape. In order to get statistically sound results, we typically recorded at least five complete runs for each pillar, starting from the formation of a tiny drop at the center until the final collapse of the enlarged drop due to gravity. After each sequence, the surface was dried with absorbant paper and by blowing with pure nitrogen. The profile of each image was then analyzed off-line. For each volume, the contact angle was deduced from a fit of the profile. The profiles have been derived from differences in the grayscale values along the horizontal direction. In correspondence of each corner, a window was selected that defined the baseline and the actual area for the polynomial fit. The contact angles have been calculated from the slope of the fit in correspondence of the contact line. The corresponding error was estimated to be typically $\pm 3°$, unless otherwise stated.

Droplet shapes were calculated using the public domain software Surface Evolver, developed by Brakke,[31] which determines the shape of the interface by minimizing the total interfacial energy. In this program the liquid−vapor interface is represented by a mesh of small triangles. Setting the liquid−vapor surface energy equal to unity, the total interfacial energy of the droplet becomes the area of the liquid−vapor interface subtracted by the area of the wet surface multiplied by the cosine of the local equilibrium contact angle. Mechanical equilibria are obtained from a numerical minimization of the total interfacial energy under the constraint of a constant liquid volume using a conjugate gradient descent. The area of the wet part of the surface is calculated from appropriate line integrals along the contact line. For the purpose of these calculations, we only account for liquid configurations which exhibit the same symmetry as the underlying pillar geometry; i.e., horizontal translations of the center of mass of the liquid are completely suppressed. This simplification of the problem allows us to consider only one-eighth of the whole system as obtained by cutting the pillar and the droplet along the vertical symmetry planes of the square pillar. The same symmetry has been also maintained in the case of circular pillars. Different pillar geometries imply different protocols to manage the local constraint, which must be satisfied by the various elements of the contact line. The essential feature in the numerical calculation is that the contact line is always free to move on a surface until it reaches a pinning edge. The Gibbs inequality is then applied to those parts of the contact line that coincide with the edge. As long as the local contact angle on the pillar (Θ_p) is less than the maximum angle (Θ_{max}) derived from the Gibbs condition, the corresponding portion of the contact line is pinned to the edge (see Figure 1a). As the liquid volume is increased, Θ_p augments until it reaches Θ_{max}. After a further addition of liquid, $\Theta_p > \Theta_{max}$, the contact becomes free to move along the adjacent surface and eventually finds a new equilibrium position or keeps on moving, indicating a collapse of the drop along the vertical direction. In the latter case, the corresponding volume will represent the maximum liquid volume V_{max} which can be sustained by the pillar. We studied both the cases of zero and nonzero gravity. In the latter case, the size of the simulated pillars were adjusted to the size of the experimental system.

dx.doi.org/10.1021/la2001249 |*Langmuir* 2011, 27, 4742–4748

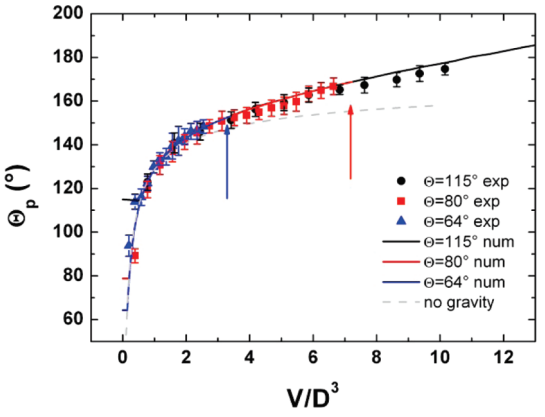

Figure 4. Contact angle as a function of the normalized volume of water drops on circular pillars having different surface wettabilities and a diameter $D = 800\ \mu$m. Symbols refer to experiments, the continuous line to numerical simulations, and the dashed line to theoretical calculation for an hemispherical drop.

3. RESULTS

First we analyze the most symmetrical case of a drop deposited on a cylindrical pillar having a circular cross-section. This geometry was originally studied by Mason and co-workers in their classic work devoted to the stability of axis symmetric sessile drops of various liquids[22] and more recently by Extrand.[23] When $\Theta > 90°$, the maximum angle predicted by the Gibbs condition at a right edge (i.e., $\Phi = 90°$) is $\Theta_{max} > 180°$. In the absence of gravity, the contact angle on the pillar Θ_p tends to the limiting value 180° at finite volumes V, while for macroscopic systems angles above 180° can be obtained because of the distortion induced by gravity. Actually, $\Theta_{max} > 180°$ have been found, even though they have been not measured directly.[23] When $\Theta < 90°$, Θ_{max} is expected to be less than 180° at a right edge. If the volume V exceeds that corresponding to Θ_{max}, the contact line suddenly jumps and spreads spontaneously down the vertical wall. Our results are consistent with such a phenomenology. Regardless of the surface wettability, the drops have a symmetric shape with the contact line pinned to the circular edge. Figure 4 summarizes the contact angle measurements on a cylindrical pillar having a diameter $D = 800\ \mu$m. It shows the contact angle on the pillar Θ_p as a function of the drop volume divided by D^3 for three different wetting surfaces. The measured dependence of the contact angle on drop volume nicely follows the curves derived from Surface Evolver taking gravity into account (see continuous lines). For each curve, the final point corresponds to the maximum volume of a stable sessile drop: at higher volumes, the drops collapse. Again, the experimental data for these characteristic volumes agree, within experimental errors, with those derived from the numerical simulations (see vertical arrows in Figure 4). The corresponding contact angle values Θ_{max} are also quite consistent with the Gibbs prediction. Actually, $\Theta_{max} = 148° \pm 3°$ ($\Theta_{max} = 167° \pm 3°$) for a surface with $\Theta = 64° \pm 4°$ ($\Theta = 80° \pm 4°$). On the untreated PDMS pillar, the simulation yields a monotonically increasing Θ with the normalized drop volume well above 180°. Experimentally, we find instead $\Theta_{max} = 175° \pm 4°$. We believe that one reason for the observed difference is the difficulty of producing large symmetric drops. Actually, the quoted value for Θ_{max} corresponds to the largest volume that presents a symmetric profile. For larger drops, contact angles above 180° were observed but only on one side of the pillar (see, for example, photo a in Figure 5). Furthermore, in the case of symmetric drops, it was impossible to directly measure contact angles above 180°, because the depth of field of our objectives was much larger than the drop size.

As a useful comparison, in Figure 4 we have also plotted (see the dashed line) the volume of an hemispherical drop having a circular contact line of diameter D and forming a contact angle Θ_p as derived from the geometric formula[22]

$$\frac{V}{D^3} = \frac{\pi}{24}\frac{(1-\cos\Theta_p)^2}{\sin^3\Theta_p}(2+\cos\Theta_p) \qquad (1)$$

which is valid in the absence of gravity. As expected, at small volumes the data agree with this estimate, while for $V/D^3 \geq 1.2$, eq 1 underestimates the actual contact angles. In other words, gravity acts to flatten the central portion of the drop and increases the pinned contact angle.

Let us now consider the novel case of a geometric pillar with a square cross-section. Figure 6 shows the numerical and experimental profiles of drops of different volumes as viewed along the side (panel a, right) and the diagonal (panel a, left) of a moderately hydrophilic pillar with a side $L = 800\ \mu$m. The full symbols represent the experimental profiles for different volumes, while the continuous lines indicate the corresponding calculated profiles. The smallest drop displays the profile of a hemispherical cap with an angle Θ, indicating that the (circular) contact line has not reached the sides of the pillar. As V is increased, the liquid front reaches the side edges and pins. However, the regions close to the corners are still dry. On further increasing V, the liquid remains pinned to the lateral edges and the lateral contact angle increases. When this angle passes the Gibbs maximum angle, the contact line depins from the edge and slightly moves down the vertical walls. When the contact line reaches the corners, the constrains of the boundary conditions are modified and the contact line is then allowed to move downward along the corner edge. When this movement occurs, it is interpreted as the equivalent instability which takes place on the circular pillar, leading to the collapse of the droplet. Loosely speaking, we can say that the drop is suspended by the whole edge contour on the circular pillar and only by the four corners on the square pillar. A more detailed description of the shape evolution near the edges, as derived from the numerical calculations, is displayed in panel b of Figure 6. The continuous lines represent the evolution of the lateral profile of a drop pinned to the edge. The dashed curves indicate the corresponding profiles as viewed along the diagonal. They show a not simple variation of the profile near the solid surface. This is more clearly seen in panel d of Figure 6, which shows a magnified view of a drop near the corner of a square pillar with $L = 800\ \mu$m calculated for $\Theta = 68°$. More interesting is the behavior observed from the side view, which clearly displays a pronounced spilling of the drop down the vertical wall. The profiles shown in the graphs of Figure 5 indicate a very good agreement between the experimental and numerical data up to the intermediate volumes (blue data, $V/L^3 = 2.6$). For larger values (orange data, $V/L^3 = 3.6$), deviations from a symmetric shape start to be clearly observable in the experimental profiles. However, the main difference is the amount of spilling found: in the simulation the contact line moves down the lateral wall much more than in the experiment. We think that this is due to two different factors. First of all, no symmetry breaks and other instability mechanisms related to in-plane shifts of the center of mass are considered in the

dx.doi.org/10.1021/la2001249 |*Langmuir* 2011, 27, 4742–4748

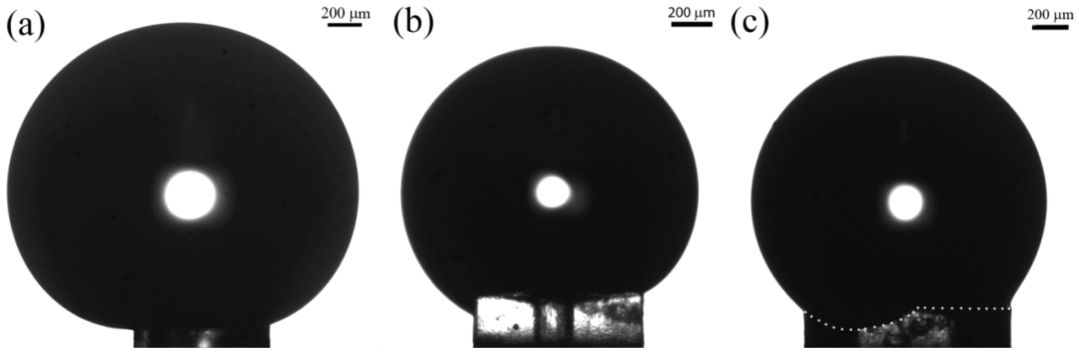

Figure 5. Images of asymmetric water drops on a circular pillar with $\Theta = 115°$ (a) and side view (b) and diagonal view (c) of a square pillar with $\Theta = 68°$.

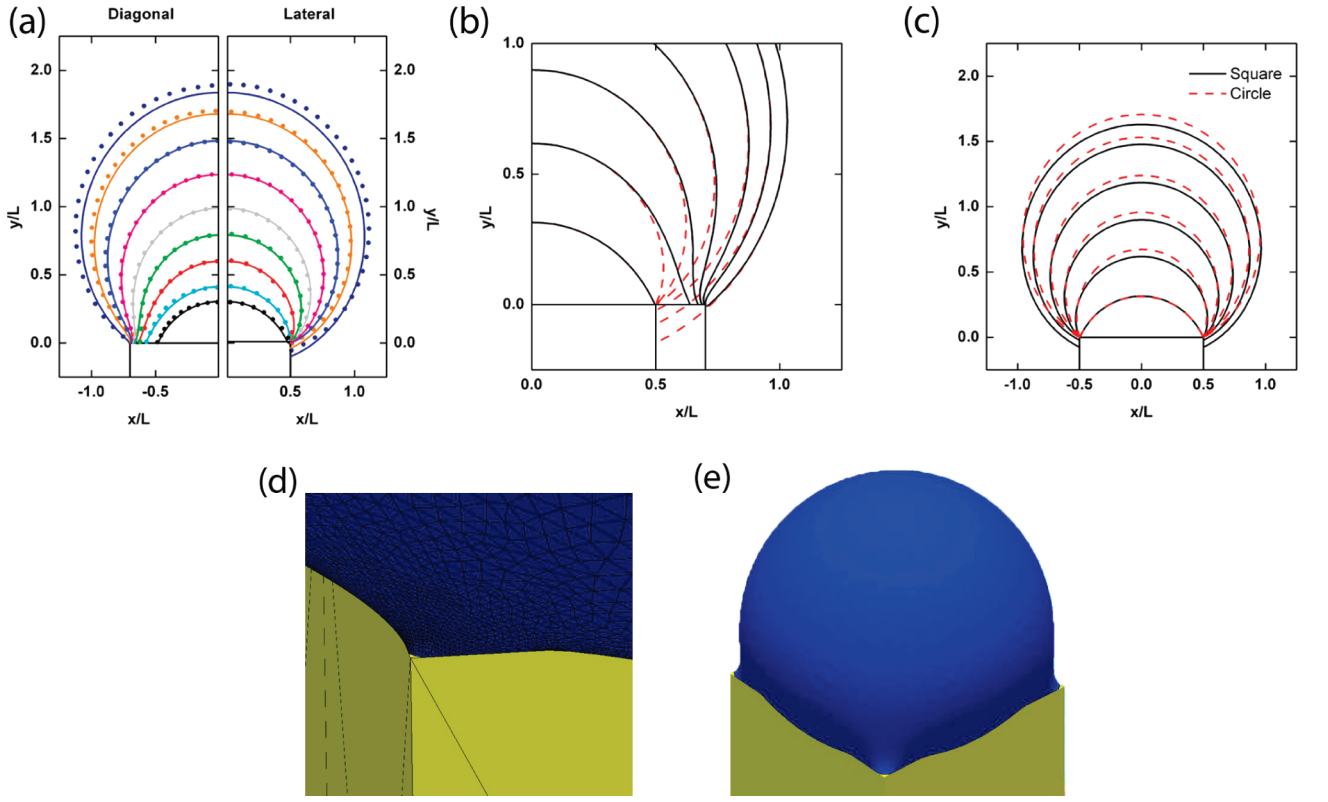

Figure 6. Profiles of drops of different volumes deposited on a pillar having a square section of side $L = 800$ μm and a contact angle $\Theta = 68°$. (a) Experimental (dotted lines) and numerical (continuous lines) profiles along the diagonal and lateral views. (b) Evolution of the numerical profiles near a corner displayed along the side (red dashed lines) and diagonal (black continuous lines) views. (c) Lateral view of whole numerical profiles of drops deposited on square and circular pillars having the same characteristic size (L or D). (d) Three-dimensional magnified view of a drop near the corner of a square pillar with $\Theta = 68°$. (e) Spilling of a drop atop a square pillar with $\Theta = 46°$.

calculations. As already stated, experimentally it is very difficult to produce a symmetric large drop. The profile shown in Figure 6a corresponds to one of the most symmetric drop we produced, the more common outcome being the asymmetric profile displayed in Figure 5b,c, characterized by significant spilling but only on one side. Second, the vertical walls of the real pillars are not smooth but present some roughness, which favors the pinning of the contact line.[28]

Although the spilling of the drop along the vertical walls is arguably the most evident difference between a drop sustained by a square pillar and a circular one, Figure 6c shows that it is also possible to distinguish the pinning behavior of the two pillars by just looking at the lateral views of the drop profiles. In general, the flattening of a drop is caused by gravity. On a square pillar the drop is more flattened than on a circular one because the rotational symmetry is lost. This is more evident for surfaces with high wettability, because the elongation in the diagonal direction is more pronounced.

Another way to account for the pinning behavior is to use the contact angle. Figure 7 shows the contact angle Θ_p measured laterally on a square pillar as a function of the drop volume divided by L^3 for three different wetting surfaces. Again, the continuous lines represent the results of the numerical simulations. At variance with the circular pillar, once Θ_p reaches the

dx.doi.org/10.1021/la2001249 |*Langmuir* 2011, 27, 4742–4748

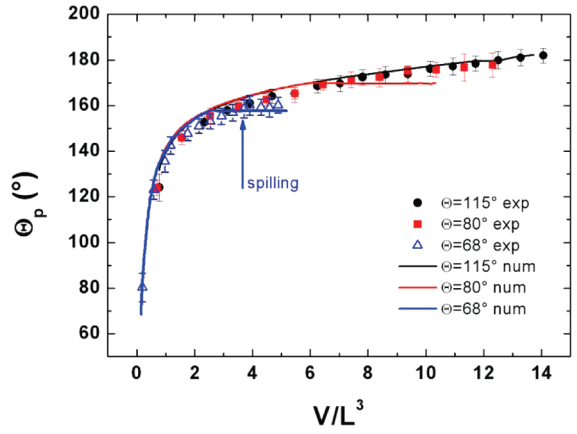

Figure 7. Lateral contact angle as a function of the normalized volume of water drops on a square pillar having different surface wettabilities and a side $L = 800\ \mu$m. Symbols refer to experiments and continuous lines to numerical simulations.

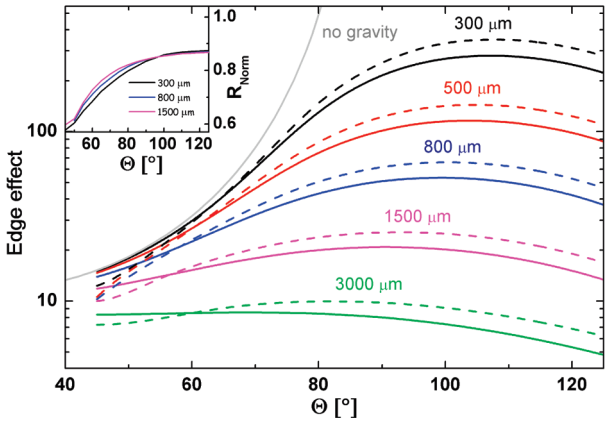

Figure 8. Calculated edge effects for circular (continuous lines) and square (dashed lines) pillars having different characteristic sizes (D or L) as a function of their surface wettability. The gray line corresponds to the ideal case of a drop on a circular pillar in the absence of gravity. Inset: ratio of the normalized maximum volumes on square and on circular pillars of three different sizes as a function of their surface wettability.

critical value Θ_{max}, the drop does not fall down but spills over the edge and the contact line gets pinned somewhere along the vertical sides, as previously discussed. The drop remains suspended, and further increases in volumes can be accommodated at the same critical angle by simply moving the contact line downward. This explains the horizontal segment seen in the numerical curves. Eventually, the drop will tumble down when the spilling region extends itself and touches the corners. Interestingly, in this case the droplet recovers the spherical symmetry in the case of no gravity or the full rotational symmetry for a finite size, which was lost when the contact line started pinning to the side edge, the corner still being dry. The experimental points nicely agree for $\Theta_p < \Theta_{max}$. In the case of the more hydrophilic surface, e.g. $\Theta = 68°$, the spilling occurs at a slightly larger normalized volume than that found in the simulations, as indicated by the vertical arrow. Afterward, the lateral contact angle does not change until the drop collapse. Again, we think that the difference is probably caused by extrinsic pinning of the contact line due to morphological defects on the pillar vertical walls.[28] We must also add that the numerical results are quite sensitive to the pillar contact angle: a change by a couple of degrees in Θ yields a relative variation in V/L^3 by more than 20%. Taking into account the uncertainty in the measurement of the pillar wettability, we conclude that the experimental and numerical results are in a satisfactory agreement. Instead, on more hydrophobic pillars we do not see any evidence of spilling because the required V/L^3 must be so large that it becomes very difficult to produce symmetric drops. The situation changes substantially on hydrophilic pillars. The image in Figure 6e shows the numerical profile of a drop atop a square pillar with $\Theta = 45°$, where the spilling along the side walls is quite evident.

An alternative to Θ_{max} to quantify the pinning to the pillar is the so-called edge effect (E),[22] which is defined as the fractional increase in the equilibrium drop volume $E = (V_{max} - V_1)/V_1$, where V_1 (V_{max}) is the volume of the drop pinned to the edge and characterized by an angle $\Theta_p = \Theta$ ($\Theta_p = \Theta_{max}$). According to this definition, in the circular geometry the contact line is totally pinned along the edge, while in the square geometry the contact line pins only in the middle point of each side. Figure 8 displays the E values calculated with Surface Evolver for pillars with circular (continuous lines) and square (dashed lines) cross sections of different sizes and in a wettability range useful for applications. The action of gravity is to flatten the droplets. It then affects not only the maximum volume V_{max} but also V_1, which can be remarkably smaller than that of the equivalent hemispherical cap when the size of the pillar becomes comparable with the capillary length. Accordingly, these two characteristic volumes were calculated by taking into account gravitational effects. The gray continuous line represents the edge factor for a circular pillar in the absence of gravity, with V_{max} and V_1 derived from formula 1. It obviously diverges for Θ approaching 90°, i.e., for Θ_{max} approaching 180°, while for smaller Θ it is very close to the value calculated with Surface Evolver for a circular pillar with $D = 300\ \mu$m. In the presence of gravity, E depends also on the pillar size, and our numerical results show a broad maximum that occurs between 90° and 110° according to the pillar size. Our results are markedly different from the original calculations by Mason et al. based on the Bashforth−Adams tables,[22] which show a sharp cusp for $\Theta = 90°$. The reason is rather simple: these latter calculations consider sessile drops flattened by gravity where the maximum contact angles are limited to the value of 180°. This assumption is certainly correct for drops deposited on flat surfaces but it breaks down for drops suspended to single asperities, where larger contact angles can be achieved.[23] Comparing the results between the two shapes, in the range of contact angles and sizes here considered, the circular geometry presents a larger E for Θ less than about 60°, regardless of the post size, while for larger Θ the square geometry dominates. However, the area A of the pillar top face is different in the two cases. To better compare the ability of pillars having the same A but different shape to sustain liquid drops, in the inset of Figure 8 we display the ratio R_{Norm} between the respective normalized maximum volumes on a square and on a circular pillar as a function of the pillar wettability for three different sizes (D or L). The normalized volume is defined as $V_{max}/A^{3/2}$. For the characteristic sizes used in our experiment, we find that this ratio is always smaller than 1, suggesting that, area A being equal, the circular pillar is more capable to sustain large water drops than a square one for any Θ. We reach the same conclusion if we refer the maximum volume to the perimeter p of the pillar edge through the adimensional ratio V_{max}/p^3. Numerically, the new ratio R'_{Norm}

dx.doi.org/10.1021/la2001249 |*Langmuir* 2011, 27, 4742–4748

will be equal to that plotted in the inset of Figure 8 times $(\pi/4)^{3/2}$.

Preliminary numerical results obtained with Surface Evolver for a triangular pillar are consistent with the data just discussed. In particular, if V_{max} on the triangular pillar is normalized to D^3, where D is the diameter of a circle inscribed in the equilateral triangular cross-section, this pillar is able to sustain larger drops with respect to a circular pillar of diameter D and a square pillar of side D. If the volumes are instead normalized to $A^{3/2}$, one finds that the geometries more capable to sustain large drops with the same A are, in decreasing order, circle, square, triangle. It is then tempting to formulate the following conjecture, which generalizes this trend to regular polygons of N sides circumscribed to the same circle. On the basis of their $V_{max}/A^{3/2}$, the different pillar cross sections can be ranked according to the sequence circle, ..., $(N + 1)$-polygon, N-polygon, $(N - 1)$-polygon, ..., square, triangle, the circle (triangle) being the more (less) capable of sustaining a liquid drop and all other pillar parameters like A and Θ being the same.

In conclusion, we have systematically studied the suspension of water drops on cylindrical pillars having circular and square cross sections and different wettabilities. The observed shapes are the result of the geometric pinning of the contact line to the pillar edge and can be accurately described in terms of the Gibbs condition. In the case of a circular profile, the contact line is pinned to the whole edge, while in the presence of corners, the contact line can spill along the vertical walls. Because of this pinning, an individual pillar can sustain much larger drops than a flat surface having the same surface area and wettability. Furthermore, a circular pillar is more capable of sustaining large drops than a square one having the same cross-section area.

AUTHOR INFORMATION

Corresponding Author

*E-mail: giampaolo.mistura@unipd.it (G.M.), ciro.semprebon@ds.mpg.de (C.S.).

ACKNOWLEDGMENT

This work was partially supported by Padua University through project CPDA077281/07 and by Fondazione CARIPARO (MISCHA project, bando 2008, and Progetti Dottorati 2009). We thank Alessandro Pozzato and Gianluca Grenci for the SEM characterization of the stainless steel master. We acknowledge many clarifying discussions with Francesco Ancilotto, Martin Brinkmann, and Enzo Orlandini.

REFERENCES

(1) Shibuichi, S.; Onda, T.; Satoh, N.; Tsuji, K. *J. Phys. Chem.* **1996**, *100*, 19512.
(2) Sun, M.; Luo, C.; Xu, L.; Ji, H.; Ouyang, Q.; Yu, D.; Chen, Y. *Langmuir* **2005**, *21*, 8978.
(3) Pozzato, A.; Dal Zilio, S.; Fois, G.; Vendramin, D.; Mistura, G.; Belotti, M.; Chen, Y.; Natali, M. *Microelectron. Eng.* **2006**, *83*, 884.
(4) Roach, P.; Shirtcliffe, N. J.; Newton, M. I. *Soft Matter* **2008**, *4*, 224.
(5) Feng, X.; Jiang, L. *Adv. Mater.* **2006**, *18*, 3063.
(6) Cebeci, F. C.; Wu, Z. Z.; Zhai, L.; Cohen, R. E.; Rubner, M. F. *Langmuir* **2006**, *22*, 2856.
(7) Extrand, C. W.; Moon, S. I.; Hall, P.; Schmidt, D. *Langmuir* **2007**, *23*, 8882.
(8) Wang, R.; Hashimoto, K.; Fujishima, A.; Chikuni, M.; Kojima, E.; Kitamura, A.; Shimohigoshi, M.; Watanabe, T. *Nature* **1997**, *388*, 431.
(9) Lim, H. S.; Han, J. T.; Kwak, D.; Jin, M.; Cho, K. *J. Am. Chem. Soc.* **2006**, *128*, 14458.
(10) Dattilo, D.; Armelao, L.; Fois, G.; Mistura, G.; Maggini, M. *Langmuir* **2007**, *23*, 12945.
(11) Sun, T. L.; Liu, H. A.; Song, W. L.; Wang, X.; Jiang, L.; Li, L.; Zhu, D. B. *Angew. Chem., Int. Ed.* **2004**, *43*, 357.
(12) Fu, Q.; Rao, G. V. R.; Basame, S. B.; Keller, D. J.; Artyushkova, K.; Fulghum, J. E.; Lopez, G. P. *J. Am. Chem. Soc.* **2004**, *126*, 8904.
(13) Podestà, A.; G. Bongiorno, G.; P. E. Scopelliti, P. E.; S. Bovio, S.; Milani, P.; Semprebon, C.; Mistura, G. *J. Phys. Chem. C* **2009**, *113*, 18264.
(14) Seemann, R.; Brinkmann, M.; Kramer, E. J.; Lange, F. F.; Lipowsky, R. *Proc. Natl. Acad. Sci. U. S. A.* **2005**, *102*, 1848.
(15) Drelich, J.; Wilbur, J. L.; Miller, J. D.; Whitesides, G. M. *Langmuir* **1996**, *12*, 1913.
(16) Brandon, S.; Haimovich, N.; Yeger, E.; Marmur, A. *Colloid Interface Sci.* **2003**, *263*, 237.
(17) Morita, M.; Koga, T.; Otsuka, H.; Takahara, A. *Langmuir* **2005**, *21*, 911.
(18) Chen, Y.; He, B.; Lee, Y.; Patankar, N. A. *J. Colloid Interface Sci.* **2005**, *281*, 458.
(19) Chung, J. Y.; Youngblood, J. P.; Stafford, C. M. *Soft Matter* **2007**, *3*, 1163.
(20) Kusumaatmaja, H.; Vrancken, R. J.; Bastiaansen, C.W. M.; Yeomans, J. M. *Langmuir* **2008**, *24*, 7299.
(21) Semprebon, C; Mistura, G.; Orlandini, E.; Bissacco, G.; Segato, A.; Yeomans, J. M. *Langmuir* **2009**, *25*, 5619.
(22) Oliver, J. F.; Huh, C.; Mason, S. G. *J. Colloid Interface Sci.* **1977**, *59*, 568.
(23) Extrand, C. W. *Langmuir* **2005**, *21*, 10370.
(24) Zhang, J.; Gao, X.; Jiang, L. *Langmuir* **2007**, *23*, 3230.
(25) Du, J.; Michielsen, S.; Lee, H. J. *Langmuir* **2010**, *26*, 16000.
(26) Wong, T. S.; Huang, A. P. H.; Ho, C. M. *Langmuir* **2009**, *25*, 6599.
(27) Schäfle, C.; Brinkmann, M.; Bechinger, C.; Leiderer, P.; Lipowsky, R. *Langmuir* **2010**, *26*, 11878.
(28) Extrand, C. W. *Langmuir* **2002**, *18*, 7991.
(29) Kalinin, Y. V.; Berejnov, V.; Thorne, R. E. *Langmuir* **2009**, *25*, 5391.
(30) Kunieda, M.; Lauwers, B.; Rajurkar, K.; Schumacher, B. M. *Ann. CIRP* **2005**, *54/2*, 599.
(31) Brakke, K. *Exp. Math* **1992**, *1*, 141.

Langmuir

Article

pubs.acs.org/Langmuir

Morphological Transitions of Droplets Wetting Rectangular Domains

Davide Ferraro,[†] Ciro Semprebon,[‡] Tamara Tóth,[†] Emanuele Locatelli,[†] Matteo Pierno,[†] Giampaolo Mistura,*[,†] and Martin Brinkmann*[,§]

[†]CNISM and Dipartimento di Fisica G. Galilei, Università di Padova, via Marzolo 8, 35131 Padova, Italy

[‡]Max Planck Institute for Dynamic and Self-Organization, Am Fassberg 17, D-37077 Göttingen, Germany

[§]Experimental Physics, Saarland University, 66123 Saarbrücken, Germany

Supporting Information

ABSTRACT: We report the results of comprehensive experiments and numerical calculations of interfacial morphologies of water confined to the hydrophilic top face of rectangular posts of width W = 500 μm and lengths between $L = 5W$ and $30W$. A continuous evolution of the interfacial shape from a homogeneous liquid filament to a bulged filament and back is observed during changes in the liquid volume. Above a certain threshold length of $L^* = 16.0W$, the transition between the two morphologies is discontinuous and a bistability of interfacial shapes is observed in a certain interval of the reduced liquid volume V/W^3.

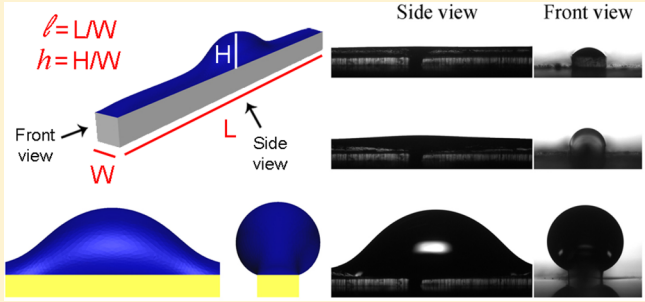

Interfacial shapes and instabilities of small liquid droplets wetting chemically or topographically structured surfaces have been widely studied in recent years, motivated both by practical applications and by fundamental questions.[1−4] Effects of interfacial tension are dominant on length scales below the capillary length and can be utilized to control small amounts of liquid passively by specifically designed wettability patterns[1,3,4] or surface topographies.[5] It has also been demonstrated in electrowetting experiments that morphological transitions of droplets on substrates with suitably shaped electrodes or surface geometry can be employed to actuate liquids in microfluidic applications.[6−8]

In particular, condensation experiments on hydrophilic stripes reported a transition between a liquid filament with a homogeneous cylindrical cross section and a flat filament with a single bulge located in the center of the rectangular domain.[1] However, these experiments were mostly qualitative because they did not control and measure the liquid volume adsorbed to the stripes. Also, the influence of the length to width ratio of the stripes on the character of the transition was not considered. In contrast to the discontinuous morphological transition found on hydrophilic stripes of finite length,[1] no abrupt changes in the equilibrium shape were observed for liquid droplets wetting the top of a square post as the liquid volume V was increased.[9] This fact led us to conjecture the existence of a bifurcation point in terms of the length to width ratio $l \equiv L/W$ of rectangular posts having length L and width W, which separates a regime of continuous transitions on "short" posts with $l < l^*$ from a regime of discontinuous transitions on "long" posts $l > l^*$. To prove this conjecture and to quantify the values of l^*, we have performed systematic microfluidic experiments and numerical minimizations of the interfacial energy.

A series of individual posts having rectangular cross sections of different ratios l, hydrophobic vertical walls, hydrophilic top faces, and a through hole with diameter 150 μm in the center have been fabricated by using a combination of photolithographic and soft-lithographic techniques. Master copies of the posts with a characteristic height of 150 μm, width W = 500 μm, and l = 5, 10, 15, 20, 25, and 30 are made in SU8 by standard photolithography. A width of 500 μm was chosen because it is sufficiently small to neglect gravity safely and, at the same time, it allows the central hole to be made easily. Positive copies of the SU8 masters in poly(dimethilsiloxane) (PDMS) are then produced by a double replica molding process (details in ref 9). The PDMS posts are hydrophobic with a contact angle of θ_0 = 110° for water. To modify their top face wettability exclusively, a thin gold layer with a thickness of about 200 nm is evaporated by magneto-sputtering. To protect the vertical walls during metal deposition, they are covered with a UV-curable optical adhesive, NOA 61.[10] Particular care is taken so that NOA 61 touches only the vertical walls up to the edge. Right before each measurement, the gold surface is activated in a commercial ultraviolet/ozone cleaner, and then the cured NOA 61 coating is peeled off. As a result, the material contact angle on the top face is reduced to $\theta_0 \approx 15°$ and remains stable for a couple of hours. The central hole of each post is connected at its extremity to a thin tube attached to a syringe pump connected in series with a flow meter. In this

Received: July 16, 2012
Revised: August 31, 2012
Published: September 4, 2012

way, it is possible to control the production of a liquid layer on top of the post with a known volume easily. This combination of techniques used in wetting and microfluidic experiments[9,11] represents a major improvement compared to previous approaches.[1,12,13]

The liquid profiles are recorded with a custom-made apparatus.[9] To achieve statistically robust results, we typically record 10 complete runs for each post. Starting from the spreading of a very thin liquid layer on the top face, we inject liquid until a maximum volume of 2 to 3 μL is reached, and after that, we extract it with the same pump. The profile of the liquid morphology in each image is then analyzed off-line.

Shapes of pinned droplets are numerically computed using the public domain software Surface Evolver.[14] The free-liquid interface is represented by a mesh of small triangles spanning the nodes. Mechanically stable interface configurations are obtained by minimizing the sum of interfacial and gravitational energy, which is a function of the coordinates of the nodes. Futhermore, a fixed liquid volume is enforeced during energy minimization, representing an integral constraint to the shape of the liquid interface. Nodes belonging to the three-phase contact line are subject to a local constraint because their motion is restricted to the boundary of the rectangular domain.

For convenience, we will employ the Bond number, $Bo \equiv \rho g W^2/\gamma$, related to the width of the post to quantify the magnitude and sign of buoyancy forces. Here, ρ and γ denote the mass density and interfacial tension, respectively, of water, and g denotes the acceleration of gravity. Because we are working with posts of width $W = 500$ μm and water ($\rho = 1.0 \times 10^3$ kg/m^3, $\gamma = 7.2 \times 10^{-2}$ N/m), the Bond number is fixed, if not stated otherwise, to $Bo = 0.0341$ in our numerical calculations. In our convention, the positive sign is related to the acceleration of gravity pushing the liquid down on the post.

Minimization steps include a combination of conjugate gradient descent steps and refinements of the triangulated interface. The droplet volume is increased or decreased in steps of 5%, and typically, each volume change is followed by 200 combined steps to evolve the system sufficiently close to a local energy minimum. In the vicinity of a bifurcation point, the number of gradient descent steps is increased to ensure a good convergence of the shape.

With all of the posts studied in our experiments, we observe a morphological transition of the liquid between a homogeneous filament and a filament with a central bulge and vice versa as the volume is changed. Photographs of the experimentally observed liquid morphologies as well as the numerically computed shapes are shown in Figure 1. The observed shape transitions are in agreement with previous experimental studies for liquid condensing on long, highly wettable stripes.[1] For a further quantitative comparison with the numerically computed interfacial shapes, we extract from each image the reduced height $h \equiv H/W$, where H is the maximal height of the liquid interface above the top face of the post. Because liquid accumulates in the central region of the stripe during the transition, h represents a suitable order parameter that distinguishes between the two liquid morphologies.

Depending on the length to width ratio l of the post, different scenarios can be observed as the volume is changed. Starting at small volumes, the water distributes evenly on the top face of the post, forming a flat layer (cf. Figure 1a). Upon increasing its volume, the water adopts the shape of a homogeneous filament with a uniform cross section close to a circular segment (Figure 1b). Noticeable deviations of this

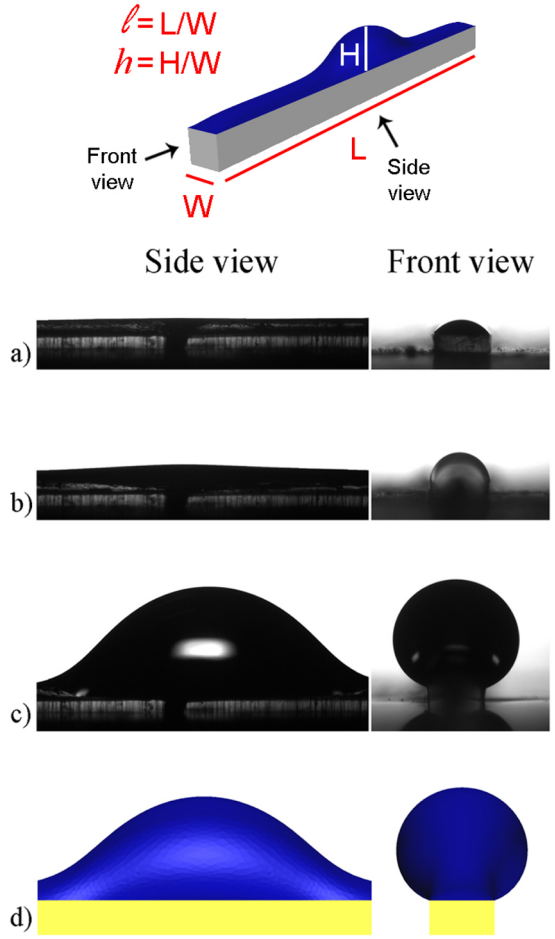

Figure 1. (Top) Bulged filament on a post of length L and width W. (a–c) Side and front views of the drop profile for different volumes on the post, $l = 30$. (d) Numerical energy minimization of a drop for the same parameters as in c). These volumes correspond to the large pink circles plotted in Figure 2.

almost homogeneous profile occur only in the vicinity of the ends of the post and decay on a length scale comparable to the post width. As the volume keeps rising, the contour of the water interface in side view starts to form a central bulge, which grows with the volume. This process is characterized by a pronounced increase in the reduced height[9,11] (Figure 1c,d).

The plot shown in Figure 2 displays the measured and numerically calculated reduced height h for $Bo = 0.0341$ as a function of the reduced volume $v \equiv V/W^3$ for the six different posts employed in our experiments. Continuous (dashed) lines indicate the results of our numerical computations during the injection (extraction) of water. Full (empty) symbols represent the experimental data during injection (extraction). For short posts ($l = 5$, 10, and 15), all numerically obtained curves $h(v)$ plotted in Figure 2 display a smooth crossover between the homogeneous and the bulged filament, and it is not possible to make a clear distinction between both morphologies. Furthermore, curves $h(v)$ for increasing and decreasing v are identical. In agreement with this numerical finding, the corresponding experimental data points do not show any noticeable difference between increasing and decreasing volumes. Instead, for long posts ($l = 20$, 25, and 30), $h(v)$ presents a discontinuous increaase at $v_\uparrow$ with increasing v and a decrease at $v_\downarrow$ with decreasing v. The opening of the hysteresis

dx.doi.org/10.1021/la302854t | Langmuir 2012, 28, 13919–13923

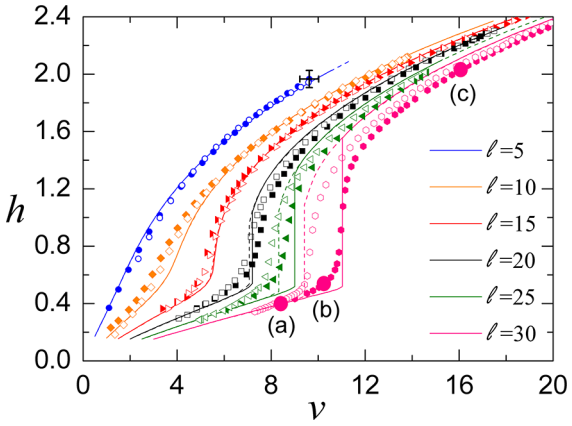

Figure 2. Reduced height $h = H/W$ of a water layer deposited on rectangular posts of various l as a function of the reduced volume $v = V/W^3$. Full (empty) symbols represent the experimental data during injection (extraction) in comparison to numerical minimizations during injection (extraction) displayed as solid (dashed) lines. The reduced volumes marked by pink circles refer to the plates of Figure 1. The final point of $l = 5$ indicates the characteritsic error bars of the experiment.

loop (i.e., the difference $\Delta v \equiv v_\uparrow - v_\downarrow > 0$) becomes larger as l increases. This behavior is also seen in the experimental data points in Figure 2 for long posts. In particular, we find quantitative agreement of the reduced volumes related to the instabilities of the homogeneous filament and the bulged filament, as well as the width of the hysteresis loops.

The main difference between our experimental and numerical results is that the expected discontinuous transitions are somewhat rounded in the experiments. Extensive and systematic tests tend to exclude the fact that the experimental data in Figure 2 are affected by liquid evaporation or spilling along the vertical walls[9] (Supporting Information). Although these data refer to the best gold films that we have obtained, we cannot exclude the fact that the unavoidable deviations from the ideal plane rectangular top face in the production process are responsible for the observed rounding. Actually, a similar argument was originally proposed to explain the observed rounding of the prewetting transition of quantum liquids on alkali metals.[16,17]

The results of our experiments, the numerical energy minimizations, and the model calculations can be conveniently expressed in the form of a morphology diagram in terms of the length to width ratio l and the reduced volume v. The morphology diagram in Figure 3 displays regions where homogeneous and bulged filament morphologies are mechanically stable.

An inspection of the numerically determined stability boundaries in Figure 3 reveals a cusplike bifurcation point at $l^* \simeq 16.0$ and $v^* \simeq 5.5$ and a tongue-shaped region of bistability for $l > l^*$. These curves were determined by varying the volume in small steps at a fixed l and locating the volume yielding the minimum energy. The energy minimizations for the morphology diagram in Figure 3 were carried out for zero gravity conditions $Bo = 0$. A comparison to the case of $Bo = 0.0341 \ll 1$ shows only minor differences with respect to the position of the bifurcation point and stability boundaries. Noticeable deviations are observed only for bulged filaments with large volumes. The experimentally measured data points of the morphology transitions displayed as symbols in Figure 3a

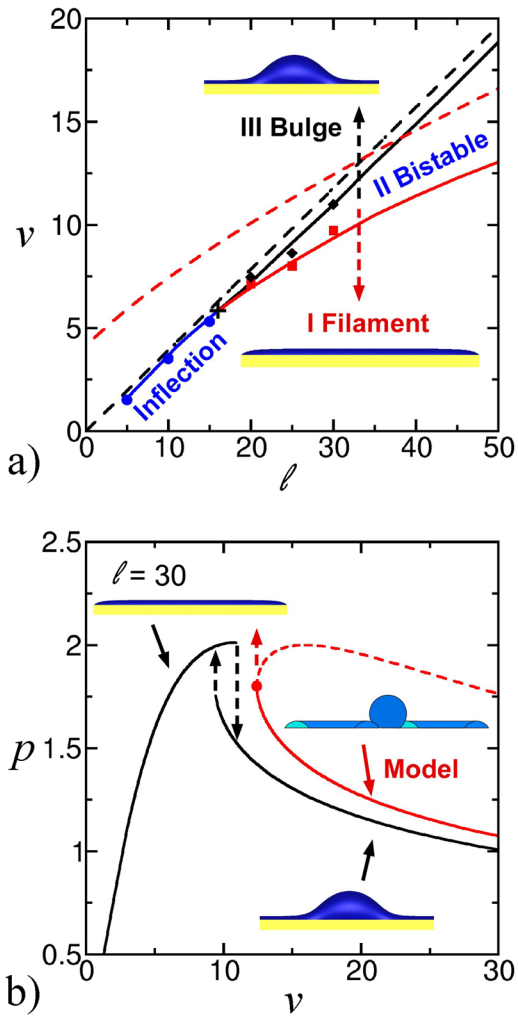

Figure 3. (a) Morphology diagram in terms of the control parameter length to width ratio l and the reduced volume v. Solid red and black lines indicate stability boundaries of homogeneous and bulged filaments, respectively, in the absence of gravity ($Bo = 0$) from numerical energy minimizations in comparison to experimental data points (symbols). Dashed black and red lines are estimates of the stability limits (main text). The bifurcation point is indicated by (+), and the solid blue line (circles) represents the volume where the continuous $h(v)$ numerical (experimental) curves display an inflection point. (b) Reduced Laplace pressure $p = PW/\gamma$ of the wetting liquid on the posts $l = 30$ as a function of v for $Bo = 0$. Black lines indicate the results of numerical energy minimizations in comparison to the approximation (red lines). Solid (dashed) lines are mechanically stable (unstable) branches.

match the results of the energy minimizations for zero gravity $Bo = 0$ very well. They are located as the inflection points of the corresponding experimental curves.

On short posts with $l < l^*$, no discontinuity in the evolution of interfacial shapes during changes in the volume is observed. For posts with $l > l^*$, however, discontinuities in $h(v)$ appear and the range of reduced volumes can be divided into three regions. In region I, corresponding to $v < v_\downarrow$, solely homogeneous filaments are mechanically stable, whereas in region III, with $v > v_\uparrow$, exclusively filaments with a central bulge are mechanically stable. In intermediate region II, with $v_\downarrow \leq v \leq v_\uparrow$, a bistability between the two filament morphologies is observed (Figure 3a). For large l, $v_\uparrow$ grows linearly with l. As already pointed out by Gau et al.,[1] the interfacial instability

dx.doi.org/10.1021/la302854t | Langmuir 2012, 28, 13919−13923

occurs for asymptotically long stripes $l \to \infty$ once the cross section of the homogeneous liquid filament reaches a semicylindrical shape (i.e., the maximum Laplace pressure $p_{max} = 2W/\gamma$). This is confirmed by our experiments where we indeed find that, on long posts, the local (pinned) contact angle of the cross-sectional contour of the homogeneous liquid filament never exceeds $\pi/2$. The reduced volume of the semicylindrical filament provides the asymptotic form

$$v_{\uparrow} = \frac{\pi}{8} l + O(l^0) \tag{1}$$

of the line limiting the stability of homogeneous filaments to large volumes.

The bulging instability of the homogeneous filament can be easily explained from the self-amplifying variations of the Laplace pressure in response to a longitudinal redistribution of liquid volume beyond P_{max}. A comparison of the stability criterion (eq 1) to the numerically obtained values of $v_{\uparrow}$ shows a constant offset for $l \to \infty$. This constant offset is readily explained by a lack of volume in the terminal parts of the observed liquid shape as compared to that of the ideal homogeneous filament with a constant cylindrical cross section.

The derivation of an approximate criterion for the inverse transition from the bulged filament to the homogeneous filament is more involved. The central bulge can be approximated by a spherical cap with an opening angle of $\alpha_s > \pi/2$ and a base area of diameter W. The flat homogeneous filaments wetting the remaining part of the post are represented by cylindrical segments with an opening angle α_c and total length L. Similar to the argument used to determine the mechanical stability of the homogeneous filament, we now consider the stability of the model interface with respect to an exchange of liquid volume between the cap and the cylindrical segment. The condition of mechanical equilibrium demands an identical Laplace pressure in both the spherical cap and the extending flat filaments and yields a relation between angles α_s and α_c. This relation is then employed to construct the set of possible equilibrium shapes in the model.

This explicit construction of the model equilibrium shapes allows no solution for a given reduced liquid volume v smaller than a certain value v_{min}. Above this value, two possible solutions exist that can be distinguished by their Laplace pressures. The full stability analysis based on the compressibilities $\kappa = \partial V/\partial P$ of the spherical cap and the cylindrical segments shows that the solution with the smaller pressure is stable with respect to an exchange of volume between cap and cylindrical segment. Hence, the value of v_{min} should correspond to the point $v_{\downarrow}$ where the bulged filament looses stability and transforms into a homogeneous filament.

Figure 3b shows the reduced pressure $p \equiv PW/\gamma$ as function of the reduced volume v both from the numerical minimizations (black solid line) and the solution branches of the present model (red lines). Solid lines in Figure 3b denote stable branches, and the dashed line corresponds to unstable solutions. The minimum volume (red circle) clearly exceeds the volume of instability obtained from our numerical minimizations. A comparison of the minimum volume criterion for different l with the stability lines from our numerical minimizations shows that v_{min} systematically overestimates the smallest reduced volume where mechanically stable bulged filaments exist (cf. also the dashed and solid red line in the morphology diagram in Figure 3a). The reduced volume v_{min} and l satisfy an implicit equation that can be only solved for v_{min} in the asymptotic limit $l \to \infty$ with the result

$$v_{\downarrow} = \left(\frac{128\pi}{2187}\right)^{1/4} l^{3/4} + O(l^{-1/4}) \tag{2}$$

In comparison to the linear dependence of the estimate (eq 1) for the instability line of the homogeneous filament, the instability line of the bulged filament (eq 2) displays a relatively slow increase with l in the limit $l \to \infty$

It is instructive to compare the morphologies adhering to the perfectly wettable top face of a rectangular post to morphologies wetting an ideally infinite stripe of finite wettability. On the basis of numerical energy minimizations, a similar morphological transition has been found on partially wetting stripes[15,18] and was later confirmed by electrowetting experiments.[6] The major difference in the present system is that the liquid adhering to an infinitely long stripe of finite wettability extends only to a finite fraction of the stripe. In contrast to the bulged filaments described in this work, the bulge morphology on an infinitely long partially wettable stripe does not extend in the form of flat filaments to either side. Discontinuous morphological transitions and a bistability of shapes during changes in the volume are found for material contact angles of $\theta_0 \lesssim 39.2°$ whereas a gradual transformation between both morphologies occurs for $\theta_0 \gtrsim 39.2°$. This demonstrates that the longitudinal confinement of the liquid on the highly wettable posts is responsible for the formation of stable bulged filaments.[18]

In this study, the volume was increased as slowly as possible to ensure compatibility with evaporation effects and to reduce dynamic effects. Both interfacial instabilities described in this article are discontinuous on sufficiently long stripes and, hence, will inevitably excite damped capillary waves. These waves can also be excited externally through vertically vibrating the sample at its resonance frequency. We expect to observe a nontrivial response of the liquid interface close to the bifurcation point, $l^* = 16.0$, as a result of the highly nonharmonic energy landscape.

■ ASSOCIATED CONTENT

Supporting Information

Maximum reduced height of water films as a function of the dimensionless liquid volume. Front views taken at different volumes on posts. Maximum reduced height of water films as a function of the dimensionless liquid volume. This material is available free of charge via the Internet at http://pubs.acs.org.

■ AUTHOR INFORMATION

Corresponding Author

*E-mail: giampaolo.mistura@unipd.it; martin.brinkmann@ds.mpg.de.

Notes

The authors declare no competing financial interest.

■ ACKNOWLEDGMENTS

Funding from BP International within the ExploRe research program is gratefully acknowledged. Planning of this work was facilitated by a Vigoni exchange program between the Ateneo Italo-Tedesco and the German Academic Exchange Service (DAAD). Finally, we thank Dr. Tiziana Cesca for the gold evaporation.

REFERENCES

(1) Gau, H.; Herminghaus, S.; Lenz, P.; Lipowsky, R. Liquid morphologies on structured surfaces: from microchannels to microchips. *Science* **1999**, *283*, 46−49.

(2) Kataoka, D. E.; Troian, S. M. Patterning liquid flow on the microscopic scale. *Nature* **1999**, *402*, 794−797.

(3) Schäfle, C.; Brinkmann, M.; Bechinger, C.; Leiderer, P.; Lipowsky, R. Morphological wetting transitions at ring-shaped surface domains. *Langmuir* **2010**, *26*, 11878−11885.

(4) Ledesma-Aguilar, R.; Nistal, R.; Hernández-Machado, A.; Pagonabarraga, I. Controlled drop emission by wetting properties in driven liquid filaments. *Nat. Mater.* **2011**, *10*, 367−371.

(5) Seemann, R.; Brinkmann, M.; Kramer, E.; Lange, F.; Lipowsky, R. Wetting morphologies at microstructured surfaces. *Proc. Natl. Acad. Sci. U.S.A.* **2005**, *102*, 1848−1852.

(6) Klingner, A.; Mugele, F. Electrowetting-induced morphological transitions of fluid microstructures. *J. Appl. Phys.* **2004**, *95*, 2918−2920.

(7) Baret, J. C.; Decré, M. M. J.; Herminghaus, S.; Seemann, R. Transport dynamics in open microfluidic grooves. *Langmuir* **2007**, *23*, 5200−5204.

(8) Khare, K.; Herminghaus, S.; Baret, J. C.; Law, B. M.; Brinkmann, M.; Seemann, R. Switching liquid morphologies on linear grooves. *Langmuir* **2007**, *26*, 12997−13006.

(9) Tóth, T.; Ferraro, D.; Chiarello, E.; Pierno, M.; Mistura, G.; Bissacco, G.; Semprebon, C. Suspension of water droplets on individual pillars. *Langmuir* **2011**, *27*, 4728−4748.

(10) Natali, M.; Begolo, S.; Carofiglio, T.; Mistura, G. Rapid prototyping of multilayer thiolene microfluidic chips by photopolymerization and transfer lamination. *Lab Chip* **2008**, *8*, 492−494.

(11) Semprebon, C.; Mistura, G.; Orlandini, E.; Bissacco, G.; Segato, A.; Yeomans, J. M. Anisotropy of water droplets on single rectangular posts. *Langmuir* **2009**, *25*, 5619−5625.

(12) Checco, A.; Gang, O.; Ocko, B. M. Liquid nanostripes. *Phys. Rev. Lett.* **2006**, *96*, 056104(1−4).

(13) Checco, A.; Cai, Y.; Gang, O.; Ocko, B. M. High resolution noncontact AFM imaging of liquids condensed onto chemically nanopatterned surfaces. *Ultramicroscopy* **2006**, *106*, 703−708.

(14) Brakke, K. A. The Surface Evolver. *Exp. Math.* **1992**, *1*, 141−165.

(15) Brinkmann, M.; Lipowsky, R. Wetting morphologies on substrates with striped surface domains. *J. Appl. Phys.* **2002**, *92*, 4296−4306.

(16) Cheng, E.; Mistura, G.; Lee, H. C.; Chan, M. H. W.; Cole, M. W.; Carraro, C.; Saam, W. F.; Toigo, F. Wetting transitions of liquid-hydrogen films. *Phys. Rev. Lett.* **1993**, *70*, 1854−1857.

(17) Mistura, G.; Lee, H. C.; Chan, M. H. W. Hydrogen adsorption on alkali-metal surfaces-wetting, prewetting and triple-point wetting. *J. Low Temp. Phys.* **1994**, *96*, 221−244.

(18) Lipowsky, R.; Brinkmann, M.; Dimova, R.; Haluska, C.; Kierfeld, J.; Shillcock, J. Wetting, budding, and fusion-morphological transitions of soft surfaces. *J. Phys.: Condens. Matter* **2005**, *17*, S2885−S2902.

Lab on a Chip

Cite this: *Lab Chip*, 2012, **12**, 4041–4043

www.rsc.org/loc

TECHNICAL INNOVATION

Tailoring the wetting properties of thiolene microfluidic materials†

Simone Silvestrini,[a] Davide Ferraro,[b] Tamara Tóth,[b] Matteo Pierno,[b] Tommaso Carofiglio,[a] Giampaolo Mistura*[b] and Michele Maggini*[a]

Received 9th June 2012, Accepted 23rd July 2012
DOI: 10.1039/c2lc40651a

A post functionalization method for the control of the wettability of thiolene resins of the NOA family is presented. Treatment of open model surfaces or closed microchannels with chlorosilane derivatives resulted in dramatic changes in the behaviour of droplets and streams contacting the surfaces. The experimental findings are confirmed by the fabrication of a Y-junction device that works as a passive valve for water streams.

Introduction

Thiolene resins (ThR) have been extensively used to fabricate microdevices because of their good solvent resistance, rapid curing procedures, biocompatibility and strong adhesion to metal and glass substrates.[1] The fabrication process is highly facilitated by the availability of ThR under the brand name NOA (Norland Optical Adhesives by Norland Products Inc.). They are commercialized as single-component resins that polymerize upon exposure to UV light in a wide range of thicknesses, without inhibition by oxygen.[2] If compared to polydimethylsiloxane (PDMS), the most used elastomer in soft-lithography, ThR present distinctive characteristics, such as i) a greater solvent resistance to swelling; ii) a much higher elastic modulus (typically, orders of magnitude); iii) a smaller auto-fluorescence background and iv) impermeability to air and water vapor.[3] Therefore, a variety of microfluidic devices have been made with ThR to exploit the aforementioned features.[3–11] Wettability represents a key factor in microfluidic applications, such as the production and handling of droplets,[12] but only few reports address its tuning.[8] In these works, oxidation of open ThR by exposure to either oxygen plasma or short wavelength UV radiation, decreased the water contact angle of the resin which, however, may recover slowly to its initial value.

Here we report a simple post-functionalization protocol to tailor the wettability of NOA surfaces in an ample interval of contact angles by using chlorosilane chemistry. Hydrophilic and hydrophobic surfaces were obtained both in open and closed chip geometries.

[a]*Department of Chemical Sciences and ITM-CNR, University of Padova, Via Marzolo 1, 35131 Padova, Italy. E-mail: michele.maggini@unipd.it; Tel: +39 0498275662*
[b]*CNISM and Department of Physics and Astronomy, University of Padova, Via Marzolo 8, 35131 Padova, Italy. E-mail: giampaolo.mistura@unipd.it; Tel: +39 0498277020*

† Electronic supplementary information (ESI) available: (S1) preparation of NOA surfaces; (S2) ATR-IR spectra of surface-modified NOA81 powders; (S3) fabrication of the Y-junction chip; (S4) movie of a passive valve demonstrator device. See DOI: 10.1039/c2lc40651a

Experimental

Thiolene-based (liquid) monomers solutions are available from Norland Products under the acronym NOA. Various formulations exist, differing in their mechanical properties, curing time, viscosity and refractive index. In this work we chose NOA81 mainly because it has very short curing times, if compared to other NOA products. A mixture of 1,1,1-tris(mercaptomethyl)-propane (**1**), trimethylolpropane diallyl ether (**2**) and isophorone diisocyanate ester (**3**) is generally accepted for NOA products (see Scheme 1).[11] Thiolene bonds (between **1** and **2**) and thiourethane bonds (between **1** and **3**) are expected to form upon UV irradiation, while the hydroxyl group in **2** should in principle survive the thiolene reaction and be available for post-functionalization.

ThR surfaces were prepared by spin coating NOA81 precursors over 3″ × 1″ microscope slides (Corning Inc.), followed by curing with UV light (365 nm) for 30 min and thermal annealing overnight at 50 °C (see the ESI,† section S1, for detailed spin coating procedure). Solutions of octadecyltrichlorosilane (OTS, from Sigma-Aldrich) and 2-methoxy(polyethylenoxy)propyl trichlorosilane (PTS, from ABCR GmbH) were prepared in HPLC-grade toluene (5% v/v) in a round bottomed flask. Flat ThR surfaces were dipped for 15 min in the solution of interest, then thoroughly rinsed with toluene, isopropanol and dried under a nitrogen flow. In order to test the functionalization procedure on closed channels, two microchannels with a rectangular cross section (500 × 200 μm) were fabricated by double replica molding of an SU-8 master.[13] At first, we obtained its negative in PDMS, which was used as a

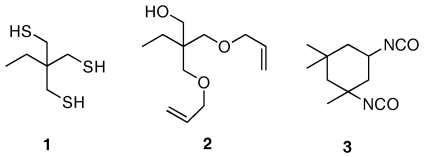

1 2 3

Scheme 1 NOA81 components.

mold for the channel in ThR. A film of ThR was then spun on a transparent plastic foil and the two parts sealed. The silanization was carried out by filling the channels with the same solutions described above, followed by rinsing with toluene and isopropanol, and drying with a nitrogen flow.

Demonstrator devices, in which an incoming fluid stream is forced to meet a Y-shaped junction and flow through either a hydrophilic or a hydrophobic conduit, were produced (Fig. 1). In order to treat the two channels with different chlorosilanes, a steady nitrogen flow was plugged into inlet C, while a OTS toluene solution was injected with a syringe through inlet B. The nitrogen flow assured that accidental extra-volumes of chlorosilane solution could flow towards inlet A, rather than contaminate the surfaces of the other channel. The chlorosilane solution was left in contact with the conduit walls for 5 min, and then removed with a syringe, while toluene was flushed through inlet A without stopping the nitrogen flow. After extensive flushing with toluene, the nitrogen flow was moved to inlet A and the PTS solution was injected through inlet C. In this case, any extra amount of OTS solution would flow towards inlet B, where the conduit had previously been functionalized.

Flat ThR model samples, functionalized with OTS and PTS, were characterized by sessile water drop contact angle (WCA). Water drop profiles were recorded with a custom-made apparatus.[13] In order to get statistically sound results, at least five drops, deposited randomly over the surface, were analyzed. A similar experimental setup was also employed to observe the water–air meniscus during the filling of closed channels with water at a pressure of 15 mbar. Both the angle of the meniscus at the channel wall and the filling rate were measured before and after functionalization. The demonstrator chip was also characterized during filling with water in the same way.

Results and discussion

Fig. 2 displays the profiles of the water drops recorded on open ThR model surfaces treated with PTS (a), untreated (b) and treated with OTS (c). WCA values are reported in Table 1. The experiment was repeated once a month over a three month period, in order to study the stability of the functionalized surfaces. Both the WCA mean values and the standard deviations (σ) for each measurement are reported, the latter assessing the homogeneity of the surface.

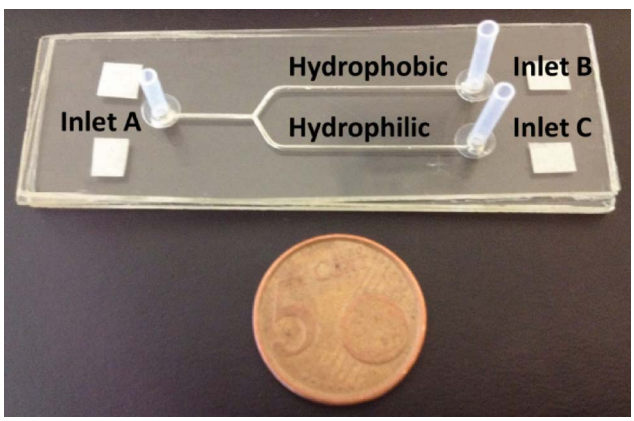

Fig. 1 Y-junction demonstrator chip. The bottom channel, leading to inlet C, was treated with PTS to become hydrophilic. The one leading to inlet B was treated with OTS to become hydrophobic.

Fig. 2 Profiles of water droplets deposited on ThR surfaces: a) PTS-treated; b) untreated; c) OTS-treated.

ATR-IR spectra, collected on pulverized samples of ThR resin, are reported in the ESI† (section S2). They confirm the presence of aliphatic chains on the resin surface upon OTS treatment. On the other hand, the absorptions of oxyethylene groups of PTS moieties could not be detected clearly, because they were covered by those of the ThR bulk. In any case, the functionalization procedure described above enabled the modulation of the ThR WCA which was modified from about 70° (untreated surface) to about 45° (PTS-treated surface) or 110° (OTS-treated surface). The standard deviation of the WCA data was low, albeit larger on treated surfaces than on pristine ones, suggesting a homogeneous functionalization of the surfaces. Additionally, WCAs changed slightly over months, without any monotonic tendency towards the starting values. Mixtures of OTS and PTS were also tested to tune surface wettability for intermediate contact angles. Unfortunately, this approach gave contact angle values affected by a high standard deviation, suggesting segregation of the chlorosilanes on the polymer surface.

The behavior of the water–air meniscus in a closed channel results from the interplay of geometry and surface wettability. Indeed, treatment of ThR closed channels with OTS or PTS resulted in the modification of the shape of the static meniscus (Fig. 3), as well as of its velocity during filling of the channel at constant pressure. These phenomena were assayed by taking images of the advancing water–air meniscus, both before and after the functionalization of the channels (Table 2). The observed WCA values closely resemble those measured on open model surfaces; also the filling rate was affected accordingly.

Table 1 Observed water contact angles (WCA), calculated by averaging 5 measurements carried out on random positions over the sample having a size of 2 × 2 cm. Standard deviations (σ) are reported as a way to assess the uniformity of the surfaces

Pristine ThR surface						
Months passed	0		1		2	
Sample no	WCA (°)	σ (°)	WCA (°)	σ (°)	WCA (°)	σ (°)
1	70	2	69	1	74	2
2	68	2	69	1	72	1
3	72	2	75	1	71	1
PTS-treated ThR surface						
Months passed	0		1		2	
Sample no	WCA (°)	σ (°)	WCA (°)	σ (°)	WCA (°)	σ (°)
1	44	3	46	1	46	3
2	49	3	50	2	53	2
OTS-treated ThR surface						
Months passed	0		1		2	
Sample no	WCA (°)	σ (°)	WCA (°)	σ (°)	WCA (°)	σ (°)
1	114	3	115	3	111	3
2	110	2	111	3	106	6
3	111	2	110	2	113	2
4	107	3	108	1	98	1

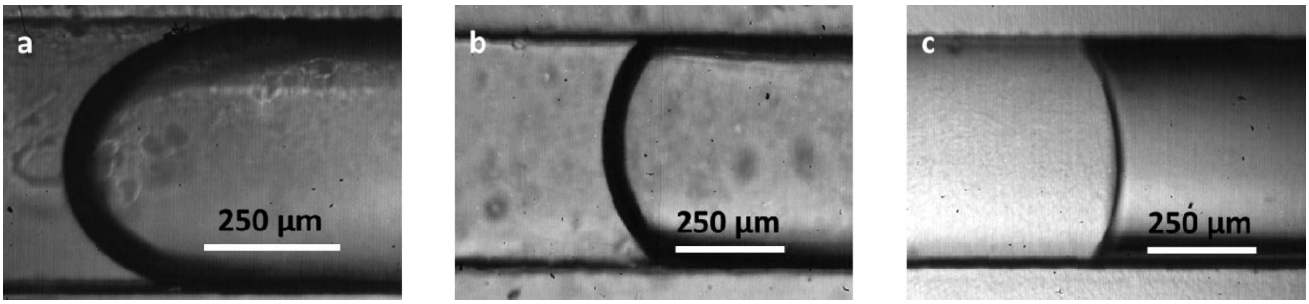

Fig. 3 Water contact angle at the water–air meniscus in a microchannel: a) PTS-treated; b) untreated; c) OTS-treated. Water enters the conduit from the left in all pictures.

Table 2 Static water contact angles at the water–air interface and filling rates measured upon application of a 15 mbar pressure to the water flow

		Contact angle (°)	Filling rate (mm s^{-1})
Channel 1	Pristine	70 ± 5	4.6 ± 0.1
	OTS-treated	112 ± 5	2.2 ± 0.2
Channel 2	Pristine	72 ± 5	4.7 ± 0.1
	PTS-treated	40 ± 5	5.6 ± 0.1

The differences in the interaction of water fronts with hydrophobic and hydrophilic channels, that have been reported so far, were exploited in the Y-junction demonstrator shown in Fig. 1 that was made according to the procedure reported in the ESI,† section S3. The demonstrator, equipped with one hydrophobic and one hydrophilic arm, worked as a passive valve by directing selectively water flows through the hydrophilic channel (see ESI,† section S4, for a video that shows a water front crossing the Y junction in the direction of the hydrophilic arm exclusively).

Conclusions

In summary, we have demonstrated a practical method for functionalizing thiolene resins of the NOA family that complement PDMS for the fabrication of microfluidic devices. Chlorosilane/–OH interfacial chemistry was used to control the resin surface wettability by choosing different trichlorosilane derivatives. The contact angle did not change for samples stored under ambient conditions for months. The method was successfully employed to modify closed channels and proved useful for the fabrication of passive microfluidic valves. We envisage that this general strategy, in principle, can be expanded to other chlorosilanes to create a variety of functional surfaces especially useful for handling droplets and multiphasic flows.

Acknowledgements

Fondazione CARIPARO (MISCHA project), University of Padova (PRAT 2009) and MUR (PRIN 20085M27SS) are gratefully acknowledged for financial support.

References

1 (*a*) C. E. Hoyle and C. N. Bowman, *Angew. Chem., Int. Ed.*, 2009, **48**, 4900; (*b*) C. E. Hoyle and C. N. Bowman, *Angew. Chem., Int. Ed.*, 2010, **49**, 1540.
2 J. T. Cabral, S. D. Hudson, C. Harrison and J. F. Douglas, *Langmuir*, 2004, **20**, 10020.
3 D. Bartolo, G. Degré, P. Nghe and V. Studer, *Lab Chip*, 2008, **8**, 274.
4 C. Harrison, J. Cabral, C. M. Stafford, A. Karim and E. J. Amis, *J. Micromech. Microeng.*, 2004, **14**, 153.
5 Z. T. Cygan, J. T. Cabral, K. L. Beers and E. J. Amis, *Langmuir*, 2005, **21**, 3629.
6 L. Brigo, T. Carofiglio, C. Fregonese, F. Meneguzzi, G. Mistura, M. Natali and U. Tonellato, *Sens. Actuators, B*, 2008, **130**, 477.
7 M. Natali, S. Begolo, T. Carofiglio and G. Mistura, *Lab Chip*, 2008, **8**, 492.
8 (*a*) L.-H. Hung, R. Lin and A. P. Lee, *Lab Chip*, 2008, **8**, 983; (*b*) B. Levaché, A. Azioune, M. Bourrel, V. Studer and D. Bartolo, *Lab Chip*, 2012, **12**, 3028.
9 S. Martínez-Crespiera, E. Ionescu, M. Schlosser, K. Flittner, G. Mistura, R. Riedel and H.F. Schlaak, *Sens. Actuators, A*, 2011, **169**, 242.
10 T. Carofiglio, P. Donnola, M. Maggini, M. Rossetto and E. Rossi, *Adv. Synth. Catal.*, 2008, **350**, 2815.
11 E. Rossi, T. Carofiglio, A. Venturi, A. Ndobe, M. Muccini and M. Maggini, *Energy Environ. Sci.*, 2011, **4**, 725.
12 (*a*) S. Y. Teh, R. Lin, L.-H. Hung and A. P. Lee, *Lab Chip*, 2008, **8**, 198; (*b*) X. Niu, F. Gielen, J. B. Edel and A. J. deMello, *Nat. Chem.*, 2011, **3**, 437.
13 T. Tòth, D. Ferraro, E. Chiarello, M. Pierno, G. Mistura, G. Bissacco and C. Semprebon, *Langmuir*, 2011, **27**, 4742.

Curriculum Vitae Davide Ferraro

Name and Surname:	Davide Ferraro
Born:	07/10/1985 in Este (Padova), Italy
Address:	Università di Padova Via Marzolo, 8 35131 Padova, Italy
Phones:	+39-347-2479698 +39-049-8277181
E-Mail:	dav.ferraro@gmail.com

Education

2010 - present	PhD student in Materials Science and Engineering, University of Padova (Italy), Department of Physics. Ph.D. defense expected in January 2013.
2007 - 2009	M. Sc. Materials Science and Engineering, University of Padova (Italy), *Cum Laude.*
2004 - 2007	B. Sc. Materials Science, University of Padova (Italy).

Summer school

[1] Dynamics in soft condensed matter, Cargèse (France), August 2-13, 2010.

[2] Micro Mechanical Systems Design and Manufacture at DTU, Lyngby (Denmark), June 20 - July1, 2011.

Research Experience

2010 - present	Research in the laboratory of Prof. Giampaolo Mistura and dott. Matteo Pierno (LaFSI) on "Fabrication of open and closed microfluidic devices for wetting studies"**,** University of Padova, Department of Physics, Padova (Italy)
2009	Master thesis in the laboratory of Prof. Giampaolo Mistura - University of Padova, Department of Physics, Padova (Italy). Title of the Master Thesis *"*Fabrication of patterned microchannels to study the capillary filling*".*
2007	Undergraduate level research in the laboratory of Prof. Giampaolo Mistura - University of Padova , Department of Physics, Padova (Italy) Title of the Bachelor Thesis: *"*Fabrication of a microfluidics damper by soft-lithography".

Teaching Experience

2011 - 2012	Tutor Junior to the first year students of Chemistry, Optics and Materials Science. These are extra-lessons given to first year students who need help in chemistry and physics.
2010 - 2011	Teaching Assistant for Physics Laboratories.

I have also supervised Master and Bachelor students in their lab interns. My task was to help the young students during the experiments, have scientific discussion with them and their supervisors.

Skills and Interests

Microfabrication:	Photo-lithography (with SU-8 and NOA, a thiolene resin), Soft-lithography (in particular Double Replica molding and micro-Contact Printing with PDMS), micro-Electro Discharge Machining (micro-EDM) and various surface functionalizations with the aim to produce open and closed microfluidic chips, chemically and physically patterned surfaces. To characterize the samples I have mainly used optical microscopy and profilometer.
Wetting:	I am interested in droplets: - confined in structures having different shapes and wetting properties; - sliding on chemically and/or physically patterned surfaces; - pinned to nanopatterned (hairy) surfaces to study the petal effect; - moving on vibrating surfaces.
Microfluidics:	Droplet microfluidics, Flow control and Pressure control in Microsystems;
Software:	LabView (elaboration data), Origin, Latex, Photoshop, Illustrator, Dreamweaver, MS Office;
Languages:	Italian (mother tongue), English (oral: good, written: advance), French (basics).

Publications

[1] T. Tóth, **D. Ferraro**, E. Chiarello, M. Pierno, G. Mistura, G. Bissacco, C. Semprebon, Suspension of water droplets on individual pillars. *Langmuir* 2011, 27, 4728.

[2] S. Silvestrini, **D. Ferraro**,T. Tóth, M. Pierno, T. Carofiglio, G. Mistura, M. Maggini, Tailoring the wetting properties of thiolene microfluidic materials. *Lab chip* 2012, 12, 4041.

[3] **D. Ferraro**, C. Semprebom, T. Tóth, E. Locatelli, M. Pierno, G. Mistura, M. Brinkmann, Morphological transitions of droplets wetting rectangular domains. *Langmuir* 2012, 28, 13919.

[4] **D. Ferraro**, T. Tóth, M. Pierno, G. Mistura, G. Fois, B. Tripathi, G. L. W. Cross, Wetting properties of micropatterned hairy surfaces. In preparation.

[5] **D. Ferraro**, T. Tóth, M. Pierno, G. Mistura, Capillary filling in patterned microchannels. In preparation.

[6] **D. Ferraro**, S. Varagnolo, P. Fantinel, M. Pierno, G. Mistura, Sliding of droplets on micropatterned surfaces. In preparation.

Conference Participations

[1] **D.Ferraro**, T.Toth, M.Pierno, G.Mistura, G.Bissacco, Capillary filling in patterned microchannels, International Soft Matter Conference, Granada (Spain) July 5-8 2010 (Poster).

[2] **D. Ferraro**, T. Tóth, E. Locatelli, M. Pierno, G. Mistura, C. Semprebom, M. Brinkmann, Morphological transitions of droplets wetting rectangular posts, Microfluidics 2012, EMBL Heidelberg (Germany), July 25-27 2012 (Poster).

[3] **D. Ferraro**, T. Tóth, E. Locatelli, M. Pierno, G. Mistura, C. Semprebom, M. Brinkmann, Morphological transitions of droplets wetting rectangular posts, Microflu' 2012, EMBL Heidelberg (Germany), December 03-05 2012 (Poster).

Ringraziamenti (Acknowledgment)

Siamo alla fine, manca solo qualche correzione qua e là, quindi è tempo di passare ai ringraziamenti.
Innanzi tutto voglio ringraziare Matteo Pierno e Giampaolo Mistura, perché due supervisori così non si trovano dappertutto. Grazie a Matteo perché un giorno di Marzo mi ha telefonato per chiedermi se avessi avuto intenzione di fare il dottorato, riempiendomi di orgoglio, anche se non ne ero ancora per niente convinto. Grazie perché mi ha seguito in maniera sempre attenta, ma anche affettuosa in questi tre anni e perché durante la scrittura di questa tesi mi ha supportato, anche facendomi penare ... ma per un'ottima causa. Grazie infinite poi anche a Giampaolo, perché mi ha insegnato un modo di fare ricerca e pianificare le attività che, guardandomi intorno, reputo tra i migliori. Grazie anche per le infinite discussioni e per essere sempre stato disponibile a spiegarmi le cose anche più di una volta! Grazie di nuovo ad entrambi perché oltre supervisori, sono stati anche educatori e hanno badato alla mia formazione, prima che all'attività in laboratorio.
Un ringraziamento speciale va poi a Giorgio Delfitto, una tra le persone che mi mancheranno di più quando me andrò via dal LaFSI. Grazie per tutti gli oggetti elettronici (vedi alimentatori, cavi, ...), grazie per essersi sempre seduto accanto a me in laboratorio tutte le volte che avevo un problema e grazie per i bei momenti passati insieme fuori dal laboratorio, tra sciate, spritz e bombardini. Grazie poi a Michele Merano per aver portato pazienza e non aver ancora comprato quel benedetto tavolo che mi avrebbe costretto a smontare tutti gli esperimenti. Gra-

zie a Emanuele Locatelli per i momenti fuori e dentro il laboratorio e perché, da buon teorico, mi ha aiutato a capire diversi concetti, che per uno scienziato dei materiali a volte sono un po' difficili. Grazie anche a Gaurav Jayaswal, ormai qui da un anno, per avermi fatto conoscere un'altra cultura e un'altra cucina.
Andando poi indietro all'inizio del dottorato, non posso non ringraziare con cuore e affetto Tamara "Tami" Tòth, che dopo essersi ambientata mi ha insegnato come vivere la quotidianità in laboratorio e con la quale formavamo una coppia davvero affiatata! Grazie poi a Luca Porcelluzzi, il tesista anziano, che quando sono arrivato al LaFSI mi ha accolto e coinvolto come un amico di vecchia data. Grazie perché in poco tempo ho passato con lui tantissimi bei momenti e perché è anche merito suo se ho conosciuto Maria Chiara.
Procedendo con ordine, un ringraziamento affettuoso va a Francesca "Frà" Tesser che, con la sua semplicità nel fare scelte importanti, mi ha convinto che l'estero non è poi un posto così lontano. Grazie poi a Paolo Fantinel e Silvia Varagnolo che, una volta arrivati al LaFSI, si sono lasciati subito coinvolgere sia dal punto di vista lavorativo che umano. Grazie perché avete contribuito, e non poco, alla buona riuscita di questa tesi. Entrambi hanno ora deciso di iniziare il dottorato, quindi gli faccio un grande in bocca al lupo, con l'augurio che sia una bella esperienza, come lo è stata per me. Grazie infinite anche a Enrico "Henry" Chiarello, sempre disponibile e attento nell'aiutarmi con il suo preziosissimo supporto informatico. Senza di lui probabilmente starei ancora analizzando immagini di gocce che cambiano forma, che scivolano, che corrono, ... insomma non so se avrei avuto il tempo di fare tutte le cose descritte in questa tesi. Grazie a Sebastian Eckart, che con la sua semplicità ha conquistato il LaFSI non appena arrivato. Grazie perché sei quasi impazzito dietro a quelle maledette gocce nei canali che "swellavano" e perché il tuo aiuto è stato determinante per la buona riuscita di questa tesi. Grazie anche a Paolo "Paolone" Sartori, che da quando è arrivato non ha fatto altro che passare ore e ore in laboratorio cercando di migliorare tutto quello che incontrava. Grazie perché anche lui ha contribuito con alcuni risultati di questa tesi, osservando cose non troppo evidenti con lo spirito e l'iniziativa giusta. Molte grazie anche a Veronica Fitti e Veronica Schiocchet, le "Veroniche", che si stanno dannando l'anima per avere dei bei, oltre che buoni, risultati dai loro esperimenti. Grazie poi a Daniele Filippi, che dopo essere venuto a chiedermi diverse volte le attività in corso in laboratorio, ha seguito il mio consiglio di andare direttamente

col Mist, che come previsto, gli proposto una tesi su un argomento completamente nuovo. Grazie poi a tutta la schiera di tesisti triennali che sono passati e stanno passando per il LaFSI: Andrea "lo juventino" Cerea, Elia Marazzolo che riusciva ad addormentarsi mentre gli parlavo, Gianmatteo Cossu che parlava in italiano a Tami, ma si faceva rispondere in inglese, Damiano Quagliati, Francesca Tessari, Nicola Dal Bianco, i fratelli Giovanni e Giulio Benetti, Michele Gintoli, Marco Grison, Filippo Dall'Armellina e gli ultimi arrivati, Gianluca Dalle Rive e Valdo Chilese. Sperando di non essermi dimenticato nessuno, ringrazio tutti perché, anche se per brevi periodi di permanenza, hanno contribuito a farmi passare una bella esperienza al LaFSI.
Grazie davvero Gruppo LaFSI, spero di trovare un ambiente altrettanto bello, piacevole e stimolante, dove sto andando. In ogni caso, spero che questo non sia un addio, ma un arrivederci!

Uscendo dal laboratorio e camminando per i corridoi del dipartimento, un ringraziamento molto affettuoso va ad Adriana "Adri" Schiavon, che è sempre stata molto di più di una segretaria. Grazie perché è sempre stata disponibile per qualsiasi cosa e perché non si è mai tirata indietro dal viziarmi di Tiramisù e salami di cioccolato. Grazie poi a Renzo Storti e Luca Bacci, i tecnici dell'altra ala, perché anche loro sono sempre stati disponibili e mi hanno sempre offerto il loro supporto con un sorriso. Un grazie speciale va poi anche a tutto il gruppo Niobato di Litio. In modo particolare a Marco Bazzan, per avermi prestato un sacco di componenti ottiche e per le innumerevoli bevute offerte, a Maria Vittoria "Vic" Ciampolillo per i momenti fuori dal dipartimento, ma anche per il supporto nell'uso del forno e dello sputtering e Annamaria "Anna" Zaltron, per aver portato pazienza quando le portavo via l'obiettivo. Grazie poi a Boris Kalinic per le spatterate di oro.
Uscendo poi dal dipartimento, devo assolutamente ringraziare Michele Maggini e Simone Silvestrini per la piena disponibilità garantitemi nel prestarmi solventi organici di ogni genere e la pompa a siringa che ho tenuto per mesi. Grazie poi per la stretta collaborazione, già forte prima che io arrivassi e che si è ulteriormente consolidata durante il mio dottorato, che ha portato ad alcuni dei risultati descritti in questa tesi. Grazie poi a Ciro Semprebon e Martin Brinkmann, per averci accolti a Gottingen in varie occasioni, per le discussioni scientifiche e per aver supportato i nostri esperimenti con le loro simulazioni, parzialmente de-

scritte anche in questa tesi. Un grazie molto speciale va poi a Nicola Rossetto, che prima da studente, poi da compagno di dottorato e infine da coinquilino ha condiviso con me questi otto anni di università patavina. Grazie perché durante il dottorato, anche senza collaborare direttamente, abbiamo condiviso tantissime discussioni scientifiche, che mi hanno aiutato nei lavori descritti in questa tesi. Usciamo quindi dall'ambiente universitario, ringraziando i miei cari coinquilini e coinquiline, che hanno sicuramente contribuito alla buona riuscita di questa tesi di dottorato. In particolare, Mauro, Giulia, Sara e Alberto per avermi accolto nella mia prima esperienza fuori casa e Nicole, Simona, Nicola di nuovo, e Greshia perché con loro mi sono trovato davvero bene in questo ultimo anno e sarà davvero un dispiacere andare via da casa Pertile. Grazie poi a tutti gli amici padovani e non che mi hanno supportato in questi tre anni.

Dulcis in fundo, siamo ai ringraziamenti più cari. Ringrazio mamma e papà perché mi hanno supportato e sopportato in questi tre anni. Grazie soprattutto a mamma, perché quando ho deciso di andare a vivere fuori casa, anche se con diverse difficoltà iniziali, ha accetto la mia scelta. Grazie a Linda per essermi sempre stata vicina in questi anni e per avermi sempre fatto venire voglia di tornare a casa nei week-end per vederla. Grazie a zia Lucia e zio Paolo, che mi sono sempre stati vicini a me e alla famiglia, soprattutto in questo ultimo periodo di grandi traslochi e cambiamenti. Grazie anche a nonna Maria, perché ha sempre pregato per me e questo da parte sua è uno dei regali più grandi che mi potesse fare. In generale, grazie a tutta la FAMIGLIA in generale, perché in questi ultimi anni, in quelli passati e in quelli futuri, siete stati e sarete sempre un esempio di vita da portare con me.

Infine, manca un solo ringraziamento fondamentale. Grazie Maria Chiara, perché da quella sera in Prato della Valle, in cui ho iniziato a conoscerla, ha lasciato il segno, continua a lasciarlo e continuerà a farlo, spero per tanto tanto tempo. Grazie a Maki, perché in questi tre anni di dottorato mi ha sopportato nei momenti difficili, in cui ero stanco, antipatico e incazzoso. Grazie perché ha condiviso con me i momenti belli e le mie soddisfazioni personali, con piena e felice sincerità. Grazie anche per avermi spronato a fare cose, che magari non avrei fatto e che poi mi sono piaciute, vedi per ultimo il corso di salsa. Grazie perché in queste ultime

settimane di stress per la scrittura di questa tesi, mi è stata vicina, sopportandomi, coccolandomi e aiutandomi, come nessuno avrebbe saputo fare meglio.

Sperando di non aver dimenticato nessuno, vi ringrazio di nuovo tutti!